

AN INTEGRATED GPS/INS/BARO AND RADAR
ALTIMETER SYSTEM FOR AIRCRAFT
PRECISION APPROACH LANDINGS

THESIS

ROBERT A. GRAY
GS-12, USAF

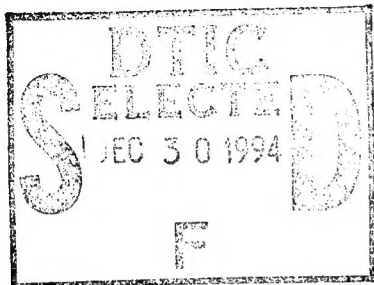
AFIT/GE/ENG/94D-13

This document has been approved
for public release and unlimited
distribution is authorized

DEPARTMENT OF THE AIR FORCE
AIR UNIVERSITY
AIR FORCE INSTITUTE OF TECHNOLOGY

Wright-Patterson Air Force Base, Ohio

19941228 059



AN INTEGRATED GPS/INS/BARO AND RADAR
ALTIMETER SYSTEM FOR AIRCRAFT
PRECISION APPROACH LANDINGS

Accesion For		
NTIS CRA&I	<input checked="" type="checkbox"/>	<input type="checkbox"/>
DTIC TAB	<input type="checkbox"/>	<input type="checkbox"/>
Unannounced	<input type="checkbox"/>	
Justification	
By	
Distribution /	
Availability Under		
Dist	Avail. end / or	Specified
A-1		

THESIS

ROBERT A. GRAY
GS-12, USAF

AFIT/GE/ENG/94D-13

Approved for public release; distribution unlimited

Approved for public release; distribution unlimited

The views expressed in this thesis are those of the author and do not reflect the official policy or position of the Department of Defense or the U.S. Government.

**AN INTEGRATED GPS/INS/BARO AND RADAR ALTIMETER SYSTEM
FOR AIRCRAFT PRECISION APPROACH LANDINGS**

THESIS

Presented to the Faculty of the Graduate School of Engineering

of the Air Force Institute of Technology

Air University

In Partial Fulfillment of the

Requirements for the Degree of

Master of Science in Electrical Engineering

Robert A. Gray, B.S.E.E.

GS-12, USAF

December 1994

Approval for public release; distribution unlimited

Preface

My love of avionics first began when I enlisted as an Air Force technician and worked on the Cobra Ball aircraft at Shemya Island, Alaska when I was nineteen years old. Twelve years have since passed and I have seen the navigation area grow exponentially with the advent of the GPS. This thesis will focus on optimally combining an INS, GPS, Baro altimeter and Radar altimeter using an extended Kalman filter for aircraft precision landing approaches.

I have met some great classmates at AFIT: 2LT Brian Bohenek, Capt Peter Eide, Capt Curtis Evans, Capt Gordon Griffin, Capt Ki Ho Kang, Major Scott Phillips and 2LT Michael Veth. Thank-you for accepting me as your "civilian" friend. I wish you all the best in your military careers, and hope we will see each other again in the future (maybe a 10 or 20 year reunion?).

Thanks to my ASIRT 'PIT' colleagues at Wright Laboratories: Capt Joseph Solomon and Capt "Gus" Gustafson for giving me advice and keeping me on-track during this thesis. Special thanks to Stan Musick for taking the time to explain MSOFE, PROFGEN, MPLOT, etc., and to Major Bob Lashlee for allowing me time to finish this thesis (holding off the TDYs and allowing me to borrow "his" laptop computer for my many nights of thesis editing).

Thanks to Maj Randy Paschall, Mr Phil Hanselman, Mr David Zann, Col "Stan" Lewantowicz and Dr John D'Azzo for approving my "paperwork" so I could complete my education at AFIT.

I also would like to thank my committee members, Lt Col Bob Riggins and Capt Ron Delap for aiding me in my AFIT education and reviewing this thesis research effort. I especially would like to thank Dr Peter Maybeck for his constant, sincere support and spiritual help throughout the thesis development. Dr Maybeck is truly a very unique person with very special gifts. Thank-you for being my advisor and accepting this thesis topic.

I want to thank my wife Mary for her patience and motivational speeches that kept me on track. For better and for worse, she was always there! Finally, I want to send out lots of love to my two children Karen and David. It wasn't easy seeing Daddy leaving to "go to school" on weekends and holidays. Thank-you Karen and David for all your hugs and kisses, it really helped. Now that Dad's school is over lets get back to having some family fun together!

Table of Contents

	Page
Preface	ii
Table of Contents.....	iii
List of Figures.....	viii
List of Tables	xiii
Abstract.....	xvi
I. Introduction	1-1
1.1 Background.....	1-4
1.2 Key Terms	1-4
1.3 Literature Review	1-6
1.3.1 GPS (Stand-Alone)	1-6
1.3.2 CPGPS (Stand-Alone)	1-6
1.3.3 GPS, DGPS or CPGPS Integrated with an INS Using a Kalman Filter	1-7
1.4 Problem.....	1-8
1.5 Problem Statement.....	1-9
1.6 Past Research.....	1-9
1.7 Scope	1-9
1.8 Assumptions	1-1
1.9 Summary.....	1-15
II. Background.....	2-1
2.1 Introduction.....	2-1
2.1.1 Notation	2-1
2.2 Ring Laser Gyro (RLG) Strapdown INS	2-1
2.3 Barometric Altimeter.....	2-3

	Page
2.4 Global Positioning System (GPS)	2-3
2.4.1 GPS Space Segment	2-4
2.4.2 GPS Control Segment.....	2-4
2.4.3 GPS User Segment	2-4
2.5 Radar Altimeter	2-5
2.6 Instrument Landing System (ILS) Precision Approach.....	2-6
2.7 Reference Frames	2-7
2.7.1 Inertial Frame (x^i, y^i, z^i).....	2-9
2.7.2 Earth Frame (x^e, y^e, z^e)	2-9
2.7.3 Geographic Frame (x^g, y^g, z^g) = (E, N, U).....	2-9
2.7.4 Navigation Frame (x^n, y^n, z^n).....	2-9
2.7.5 Body Frame (x^b, y^b, z^b).....	2-12
2.8 Reference Frame Transformations.....	2-12
2.8.1 Inertial Frame to Earth Frame.....	2-13
2.8.2 Earth Frame to Geographic Frame.....	2-13
2.8.3 Earth Frame to Navigation Frame.....	2-14
2.8.4 Geographic Frame to Navigation Frame.....	2-14
2.8.5 Geographic Frame to Body Frame.....	2-14
2.8.6 Navigation Frame to Body Frame.....	2-15
2.9 Kalman Filter Theory.....	2-15
2.9.1 What is a Kalman Filter?	2-15
2.9.2 Kalman Filter Example.....	2-16
2.9.3 Linear Kalman Filter.....	2-20
2.9.4 Linearized and Extended Kalman Filtering	2-23
2.10 Summary.....	2-26
III. Design Methodology and Error Models	3-1

	Page
3.1 Introduction to MSOFE	3-1
3.1.1 MSOFE Computer Requirements	3-2
3.2 Introduction to PROFGEN	3-3
3.3 The LSM Computer Model	3-5
3.4 LSM Model Description	3-9
3.4.1 The Inertial Navigation System (INS) Model.....	3-11
3.4.1.1 The 93-State LN-93 Error Model.	3-11
3.4.1.2 The 39-State INS Truth Model.	3-12
3.4.1.3 The 11-State INS Filter Model.	3-13
3.4.1.4 INS Measurement Model.....	3-13
3.4.2 Radar Altimeter Model.	3-14
3.4.3 The Global Positioning System (GPS) Model.....	3-15
3.4.3.1 The 30-State GPS Truth Model	3-15
3.4.3.2 The 2-State GPS Filter Model	3-17
3.4.3.3 GPS Measurement Model.....	3-18
3.5 Chapter Summary	3-20
IV. Results and Analysis.....	4-1
4.1 The Tanker (KC-135) flight profile	4-3
4.2 Satellite Vehicle Data Using SEM 3.6	4-5
4.3 Development of The Three INS's	4-7
4.4 Filter Tuning Example.....	4-11
4.5 Radar Altimeter/Baro/GPS Aiding of the 0.4 nm/hr, 2.0 nm/hr and 4.0 nm/hr INS	4-14
4.5.1 Case I and Case II - 0.4 nm/hr INS	4-14
4.5.2 Case III and Case IV - 2 nm/hr INS	4-16
4.5.3 Case V and Case VI - 4 nm/hr INS.....	4-17

	Page
4.6 Radar Altimeter/Baro/GPS Aiding of the 0.4 nm/hr, 2.0 nm/hr and 4.0 nm/hr INS using an Additional Single Pseudolite during the Landing Approach	4-18
4.6.1 Cases VII, VIII and IX - Pseudolite But No Radar Altimeter.....	4-19
4.6.2 Cases X, XI and XII - Pseudolite and Radar Altimeter	4-22
4.7 Example of 0.4 nm/hr, 2.0 nm/hr and 4.0 nm/hr INS Drift during a Loss of GPS Measurement for 1/8 Schuler Period.....	4-23
4.8 Performance Example of a 4.0 nm/hr INS during Two Periods of GPS Measurement Loss with Radar Altimeter Aiding during the Final Approach.	4-25
4.9 Chapter Summary	4-26
V. Conclusions and Recommendations.....	5-1
5.1 Introduction.....	5-1
5.2 Conclusions	5-2
Appendix A. Error State Definitions for the LSM Truth and Filter Models.....	A-1
Appendix B. Dynamics Matrices and Noise Values	B-1
B.1 Definition of Dynamics Matrices	B-1
B.2 Elements of the Process Noise and Measurement Noise Matrices	B-5
Appendix C. PROF_IN Input File.....	C-1
Appendix D. Tanker Flight Profiles	D-1
Appendix E. FORTRAN Source Code, Ephemeris Data and Almanac Files.....	E-1
Appendix F. SEM 3.6 Dilution of Precision Plots.....	F-1
Appendix G. Kalman Filter Error State Example Plots	G-1
Appendix H. Case I, 0.4 nm/hr INS, Error State Plots (Baseline).....	H-1
Appendix I. Case II, 0.4 nm/hr INS, Error State Plots using a Radar Altimeter	I-1
Appendix J. Case III, 2.0 nm/hr INS, Error State Plots (Baseline)	J-1

	Page
Appendix K. Case IV, 2.0 nm/hr INS, Error State Plots using a Radar Altimeter	K-1
Appendix L. Case V, 4.0 nm/hr INS, Error State Plots (Baseline)	L-1
Appendix M. Case VI, 4.0 nm/hr INS, Error State Plots using a Radar Altimeter	M-1
Appendix N. Case VII, 0.4 nm/hr INS, Error State Plots using a single Pseudolite.....	N-1
Appendix O. Case VIII, 2.0 nm/hr INS, Error State Plots using a single Pseudolite.....	O-1
Appendix P. Case IX, 4.0 nm/hr INS, Error State Plots using a single Pseudolite.....	P-1
Appendix Q. Case X, 0.4 nm/hr INS, Error State Plots using Radar Altimeter and a single Pseudolite.....	Q-1
Appendix R. Case XI, 2.0 nm/hr INS, Error State Plots using Radar Altimeter and a single Pseudolite.....	R-1
Appendix S. Case XII, 0.4 nm/hr INS, Error State Plots using Radar Altimeter and a single Pseudolite.....	S-1
Appendix T. Case XIII, XIV and XV, 0.4, 2.0 and 4.0 nm/hr INS with a Single GPS Outage	T-1
Appendix U. Case XVI, 4.0 nm/hr INS with Two GPS Outage using a Radar Altimeter	U-1

List of Figures

	Page
Figure 1 - 1. Instrument Approach Procedures, Wright-Patterson AFB, OH.....	1-14
Figure 1 - 2. Navigation Reference System (NRS)	1-16
Figure 1 - 3. Landing System Model (LSM) Simulation.....	1-16
Figure 2 - 1. Elementary Radar Altimeter Block Diagram.....	2-6
Figure 2 - 2. Standard ILS Characteristics and Terminology.....	2-8
Figure 2 - 3. Inertial Frame.....	2-10
Figure 2 - 4. Earth Frame.....	2-10
Figure 2 - 5. Geographic Frame.....	2-11
Figure 2 - 6. Navigation Frame	2-11
Figure 2 - 7. Body Frame.....	2-12
Figure 2 - 8. Conditional Density of Position Based on Measured Value z_1	2-16
Figure 2 - 9. Conditional Density of Position Based on Measurement z_2 Alone	2-18
Figure 2 - 10. Conditional density of position based on data z_1 and z_2	2-18
Figure 3 - 1. Overall Landing System Model (LSM) Description.....	3-4
Figure 3 - 2. Truth and Filter Model Block Diagram	3-8
Figure 4 - 1. CEP curves for the 0.4 nm/hr, 2.0 nm/hr and 4.0 nm/hr INS	4-10
Figure 4 - 2. Plot Legend	4-12
Figure 4 - 3. Top View of Tanker Precision Approach	4-20
Figure 4 - 4. Side View of Tanker Precision Approach	4-21
Figure C - 1. PROF_IN Input File for PROFGEN.....	C-2
Figure D - 1. Latitude, Longitiude and Altitude of the Tanker Profile	D-2
Figure D - 2. 3-D Position, Wander Azimuth and Velocity of the Tanker Profile.....	D-3
Figure D - 3. X, Y and Z Velocity of the Tanker Profile	D-4
Figure D - 4. Roll, Pitch and Heading Changes of the Tanker Profile	D-5

	Page
Figure E - 1. FORTRAN source code "ADDSV.for"	E-2
Figure E - 2. Sample from National Geodetic Office True Ephemeris Data	E-4
Figure E - 3. SEM 3.6 Almanac Data File (051994.al3) Used For: 21 May 94.	E-5
Figure F - 1. GDOP and PDOP	F-3
Figure F - 2. HDOP and VDOP	F-4
Figure F - 3. TDOP and SV Bearing/Elevation	F-5
Figure F - 4. SV Rise/Set and Number of Visible SVs	F-6
Figure F - 5. Elevation/Time	F-7
Figure G - 1. North, West and Azimuth Tilts (Conservative Q-tuning)	G-2
Figure G - 2. North, West and Azimuth Tilts (Non-Conservative Q-tuning)	G-3
Figure G - 3. North, West and Vertical Velocity (Conservative Q-tuning)	G-4
Figure G - 4. North, West and Vertical Velocity (Non-Conservative Q-tuning)	G-5
Figure H - 1. Latitude and Longitude Error.....	H-2
Figure H - 2. Aircraft Altitude and Baro-Altimeter Error.....	H-3
Figure H - 3. Latitude, Longitude and Aircraft Altitude Error.....	H-4
Figure H - 4. North, West and Azimuth Tilt Errors	H-5
Figure H - 5. North, West and Vertical Velocity Errors.....	H-6
Figure H - 6. GPS User Clock Bias and GPS User Clock Drift.....	H-7
Figure I - 1. Latitude and Longitude Error.....	I-2
Figure I - 2. Aircraft Altitude and Baro-Altimeter Error	I-3
Figure I - 3. Latitude, Longitude and Aircraft Altitude Error.....	I-4
Figure I - 4. North, West and Azimuth Tilt Errors	I-5
Figure I - 5. North, West and Vertical Velocity Errors.....	I-6
Figure I - 6. GPS User Clock Bias and GPS User Clock Drift.....	I-7
Figure J - 1. Latitude and Longitude Error.....	J-2
Figure J - 2. Aircraft Altitude and Baro-Altimeter Error	J-3

	Page
Figure J - 3. Latitude, Longitude and Aircraft Altitude Error	J-4
Figure J - 4. North, West and Azimuth Tilt Errors	J-5
Figure J - 5. North, West and Vertical Velocity Errors.....	J-6
Figure J - 6. GPS User Clock Bias and GPS User Clock Drift.....	J-7
Figure K - 1. Latitude and Longitude Error.....	K-2
Figure K - 2. Aircraft Altitude and Baro-Altimeter Error	K-3
Figure K - 3. Latitude, Longitude and Aircraft Altitude Error	K-4
Figure K - 4. North, West and Azimuth Tilt Errors	K-5
Figure K - 5. North, West and Vertical Velocity Errors.....	K-6
Figure K - 6. GPS User Clock Bias and GPS User Clock Drift.....	K-7
Figure L - 1. Latitude and Longitude Error.....	L-2
Figure L - 2. Aircraft Altitude and Baro-Altimeter Error	L-3
Figure L - 3. Latitude, Longitude and Aircraft Altitude Error	L-4
Figure L - 4. North, West and Azimuth Tilt Errors	L-5
Figure L - 5. North, West and Vertical Velocity Errors.....	L-6
Figure L - 6. GPS User Clock Bias and GPS User Clock Drift.....	L-7
Figure M - 1. Latitude and Longitude Error.....	M-2
Figure M - 2. Aircraft Altitude and Baro-Altimeter Error	M-3
Figure M - 3. Latitude, Longitude and Aircraft Altitude Error	M-4
Figure M - 4. North, West and Azimuth Tilt Errors	M-5
Figure M - 5. North, West and Vertical Velocity Errors.....	M-6
Figure M - 6. GPS User Clock Bias and GPS User Clock Drift.....	M-7
Figure N - 1. Latitude and Longitude Error.....	N-2
Figure N - 2. Aircraft Altitude and Baro-Altimeter Error	N-3
Figure N - 3 Latitude, Longitude and Aircraft Altitude Error	N-4
Figure N - 4 North, West and Azimuth Tilt Errors	N-5

	Page
Figure N - 5. North, West and Vertical Velocity Errors.....	N-6
Figure N - 6. GPS User Clock Bias and GPS User Clock Drift.....	N-7
Figure O - 1. Latitude and Longitude Error.....	O-2
Figure O - 2. Aircraft Altitude and Baro-Altimeter Error	O-3
Figure O - 3. Latitude, Longitude and Aircraft Altitude Error	O-4
Figure O - 4. North, West and Azimuth Tilt Errors	O-5
Figure O - 5. North, West and Vertical Velocity Errors.....	O-6
Figure O - 6. GPS User Clock Bias and GPS User Clock Drift.....	O-7
Figure P - 1. Latitude and Longitude Error.....	P-2
Figure P - 2. Aircraft Altitude and Baro-Altimeter Error	P-3
Figure P - 3. Latitude, Longitude and Aircraft Altitude Error	P-4
Figure P - 4. North, West and Azimuth Tilt Errors	P-5
Figure P - 5. North, West and Vertical Velocity Errors.....	P-6
Figure P - 6. GPS User Clock Bias and GPS User Clock Drift.....	P-7
Figure Q - 1. Latitude and Longitude Error.....	Q-2
Figure Q - 2. Aircraft Altitude and Baro-Altimeter Error	Q-3
Figure Q - 3. Latitude, Longitude and Aircraft Altitude Error	Q-4
Figure Q - 4. North, West and Azimuth Tilt Errors	Q-5
Figure Q - 5. North, West and Vertical Velocity Errors.....	Q-6
Figure Q - 6. GPS User Clock Bias and GPS User Clock Drift.....	Q-7
Figure R - 1. Latitude and Longitude Error.....	R-2
Figure R - 2. Aircraft Altitude and Baro-Altimeter Error	R-3
Figure R - 3. Latitude, Longitude and Aircraft Altitude Error	R-4
Figure R - 4. North, West and Azimuth Tilt Errors	R-5
Figure R - 5. North, West and Vertical Velocity Errors.....	R-6
Figure R - 6. GPS User Clock Bias and GPS User Clock Drift.....	R-7

	Page
Figure S - 1. Latitude and Longitude Error.....	S-2
Figure S - 2. Aircraft Altitude and Baro-Altimeter Error	S-3
Figure S - 3. Latitude, Longitude and Aircraft Altitude Error	S-4
Figure S - 4. North, West and Azimuth Tilt Errors	S-5
Figure S - 5. North, West and Vertical Velocity Errors.....	S-6
Figure S - 6. GPS User Clock Bias and GPS User Clock Drift.....	S-7
Figure T - 1. Latitude Error.....	T-2
Figure T - 2. Longitude Error.....	T-3
Figure T - 3. Aircraft Altitude Error	T-4
Figure T - 4. Baro-Altimeter Error.....	T-5
Figure T - 5. North Tilt Errors	T-6
Figure T - 6. West Tilt Errors	T-7
Figure T - 7. Azimuth Tilt Errors.....	T-8
Figure T - 8. North Velocity Errors	T-9
Figure T - 9. West Velocity Errors	T-10
Figure T - 10. Vertical Velocity Errors.....	T-11
Figure T - 11. GPS User Clock Bias Error	T-12
Figure T - 12. GPS User Clock Drift Error.....	T-13
Figure U - 1. Latitude and Longitude Error.....	U-2
Figure U - 2. Aircraft Altitude and Baro-Altimeter Error	U-3
Figure U - 3. Latitude, Longitude and Aircraft Altitude Error	U-4
Figure U - 4. North, West and Azimuth Tilt Errors	U-5
Figure U - 5. North, West and Vertical Velocity Errors.....	U-6
Figure U - 6. GPS User Clock Bias and GPS User Clock Drift.....	U-7

List of Tables

	Page
Table 1 - 1. Typical avionics equipment found on commercial or DOD aircraft	1-2
Table 1 - 2. Cost Comparison of Stand-Alone vs. Embedded INS-GPS	1-2
Table 1 - 3. Case I-XI Thesis Integration Comparisons	1-3
Table 1 - 4. Precision Approach Accuracy Requirements at Decision Heights	1-5
Table 2 - 1. 2σ Precision ILS Approach Criteria at Decision Height	2-7
Table 3 - 1. PROFGEN Segments for "Tanker" Flight Profile	3-6
Table 3 - 2. PROFGEN Flight Profile Outputs	3-7
Table 3 - 3. References for the Sub-Matrices of the LSM Truth and Filter	3-10
Table 4 - 1. Case I-IX Integration Comparisons	4-2
Table 4 - 2. Case X-XI Integration Comparisons	4-2
Table 4 - 3. Precision Approach Accuracy Requirements at Decision Heights	4-3
Table 4 - 4. Category I, II and III Decision Height Profile Times	4-5
Table 4 - 5. Satellite Vehicles Chosen During Simulation	4-7
Table 4 - 6. MSOFE Initial System Covariance Parameters for 0.4/2.0/4.0 nm/hr INS	4-8
Table 4 - 7. Q-Values for N, W and Az Tilts (Before and After Tuning)	4-13
Table 4 - 8. Q-Values for N, W and Vertical Velocity (Before and After Tuning) ..	4-13
Table 4 - 9. Case I and Case II 1σ Latitude, Longitude and Altitude Errors	4-15
Table 4 - 10. Precision Landing Category Predicted To Achieve	4-16
Table 4 - 11. Case III and Case IV 1σ Latitude, Longitude and Altitude Errors	4-17
Table 4 - 12. Precision Landing Category Predicted To Achieve	4-17
Table 4 - 13. Case V and Case VI 1σ Latitude, Longitude and Altitude Errors	4-18
Table 4 - 14. Precision Landing Category Predicted To Achieve	4-18
Table 4 - 15. Case VII, Case VIII and Case IX Configurations	4-19
Table 4 - 16. Averaged True Error Reduction Using a Single Pseudolite	4-21

	Page
Table 4 -17. Precision Landing Category Predicted To Achieve	4-22
Table 4 - 18. Case X, Case XI and Case XII Configurations	4-22
Table 4 - 19. Averaged True Error Reduction, Case I-II-III vs. Case X-XI-XII	4-23
Table 4 - 20. Averaged True Error Reduction, Case II-IV-VI vs. Case X-XI-XII	4-23
Table 4 - 21. Averaged True Error Reduction, Case VII-VIII-IX vs. Case X-XI-XII.	4-23
Table 4 - 22. Precision Landing Category Predicted To Achieve	4-23
Table 4 - 23. Case XVI 1s Latitude, Longitude and Altitude Errors.....	4-26
Table 4 -24. Precision Landing Category Predicted To Achieve	4-26
Table 4 - 25. Averaged True Error % Change, Case VI vs. Case XVI	4-26
Table 4 - 26. Summary of Cases I - VIII: Precision Approach Requirements Met....	4-27
Table 4 - 27. Summary of Cases IX - XVI: Precision Approach Requirements Met	4-27
Table A - 1. 39-State INS System Model: First 20 States.....	A-2
Table A - 2. 39-state INS System Model: Second 19 States.....	A-3
Table A - 3. 30-State GPS System Model.....	A-4
Table A - 4. 13-State Reduced-Order Filter Model	A-5
Table B - 1. Notation of Variables used in Tables B - 2 to B - 4	B-2
Table B - 2. Elements of the Dynamics Submatrix	B-3
Table B - 3. Elements of the Dynamics Submatrix	B-4
Table B - 4. Elements of the Dynamics Submatrix	B-5
Table B - 5. Elements of the Dynamics Submatrix	B-5
Table B - 6. Elements of Truth Model Process Noise Submatrix for the INS Truth Model.....	B-6
Table B - 7. Elements of Truth Model Process Noise for GPS States.....	B-6
Table B - 8. Filter Process Noise Q Values for Case 1 (using 0.4 nm/hr INS).....	B-7
Table B - 9. Filter Process Noise Q Values for Case 2 (using 2.0 nm/hr INS).....	B-7
Table B - 10. Filter Process Noise Q Values for Case 3 (using 4.0 nm/hr INS).....	B-7

	Page
Table B - 11. Truth and Filter Measurement Noise R Values for Cases 1-3	B-8
Table E - 1. Template for Understanding Figure E - 2	E-1

Abstract

Currently, the Department of Defense (DOD) and the commercial airline industry are utilizing the Instrument Landing System (ILS) during aircraft landings for precision approaches. The replacement system for the aging ILS was thought to be the Microwave Landing System (MLS). Instead, use of the Global Positioning System (GPS) is now thought to be a viable replacement for ILS precision approaches. The majority of current precision landing research has exploited “stand-alone” GPS receiver techniques. This thesis instead explores the possibilities of using an extended Kalman filter (EKF) that integrates an Inertial Navigation System (INS), GPS, Barometric Altimeter, Pseudolite and Radar Altimeter for aircraft precision approaches. Thesis results show that integrating the INS, GPS, Barometric Altimeter and Radar Altimeter meets Federal Aviation Administration (FAA) requirements for a Category I precision approach. Thesis results also show that integrating the INS, GPS, Barometric Altimeter, Radar Altimeter and a single Pseudolite meets FAA requirements for a Category II precision approach.

AN INTEGRATED GPS/INS/BARO AND RADAR ALTIMETER SYSTEM FOR AIRCRAFT PRECISION APPROACH LANDINGS

I. Introduction

Current Department of Defense (DOD) and commercial aircraft utilize the Instrument Landing System (ILS) during landings for precision approaches [19,22]. The replacement system for this aging ILS was thought to be the Microwave Landing System (MLS). Instead, use of the Global Positioning System (GPS) is now thought to be a viable replacement for aircraft ILS precision approaches.

The DOD and Department of Transportation (DOT) are under extreme pressure from military users and the commercial airline market to "find a way" to certify GPS for precision landing approaches [2,20,55,64,67]. Using GPS for precision landing approaches instead of using an additional MLS receiver, clearly makes sense from a cost/benefit perspective. First, GPS will eventually be installed on all the DOD's major weapon systems (aircraft, ships, etc.) and eventually be installed on commercial transports [21]. Second, if a MLS receiver does not have to be purchased by the DOD or commercial airlines, billions of dollars would be saved. For example, if only the F-16 system program office (SPO) could integrate their 2000 aircraft with existing GPS and INS properly, the F-16 SPO could conservatively save \$250 million dollars, since no additional MLS receiver will have to be purchased [37]. Studies also have shown the use of GPS on commercial transports will save airlines an estimated 6 billion dollars annually. The DOD would also benefit from substantial dollar savings. Civil aviation aircraft can also benefit from the use of GPS and GPS-aided inertial systems for non-precision and precision approaches, provided that the total system cost is not prohibitive for such aircraft. In an effort to reduce costs, airlines are looking for ways GPS can save operating costs. The author believes that in order for GPS to be certified on civil and DOD aircraft, not only must GPS meet the accuracy requirements, but the *integrity* of the GPS must not be in question. The author also believes that a GPS combined with an INS can meet both the accuracy and integrity requirements of the FAA for precision approaches.

If one currently looks at how the majority of FAA certified precision approach aircraft are equipped with avionics black boxes, one would typically see the following shopping list of Table 1 - 1:

Quantity (each)	Nomenclature
1	Barometric altimeter
1 to 3	Inertial Navigation System
1	Radar altimeter
1*	Global Positioning System*
---	* = predicted to be installed by 1998

Table 1 - 1. Typical avionics equipment found on commercial or DOD aircraft

Present-day INS systems on board most commercial and DOD aircraft are medium accuracy (1.0 nm/hr CEP) stand-alone systems at a cost of about \$100,000 per unit. The author believes that the present-day stand-alone INS could be replaced by a single integrated INS-GPS black-box which will utilize barometric and radar altimeter measurements to meet and exceed FAA requirements at a reduced cost; see Table 1 - 2 for cost comparisons [37,62,61]. The reduction in cost is found by replacing the current medium 1.0 nm/hr accuracy INS with a less accurate, 2-4 nm/hr INS tightly coupled with a carrier-phase differential GPS. Table 1 - 2 does not show additional integration cost savings of an off-the-shelf GPS-INS which will *already* contain a host Kalman filter algorithm. A further advantage to such a proposed system is that the INS can reduce carrier-phase ambiguities, and GPS integrity monitoring techniques can be employed

Black-box	Single INS	Triple INS	Single Embedded INS- GPS	Triple Embedded INS- GPS
Baro altimeter	\$20K	\$20K	\$20K	\$20K
INS	\$100K	\$300K	---	---
Radar altimeter	\$30K	\$30K	\$30K	\$30K
GPS	\$25K	\$25K	---	---
Embedded INS- GPS	---	---	\$60K	\$180K
Total	\$175K	\$375K	\$110K	\$230K

Table 1 - 2. Cost Comparison of Stand-Alone vs. Embedded INS-GPS

using a centralized Kalman filter. Another advantage of an embedded INS-GPS black-box is that it contains a Kalman filter "tuned" to the specific INS-GPS hardware.

In order for GPS to replace ILS for non-precision and precision approaches, areas associated with accuracy, coverage, integrity, availability and aircraft integration must be studied and understood. Because a GPS differential-carrier-phase model was unavailable at the onset of this thesis, the author will instead use a P-Code GPS model, *with and without* the accurate radar altimeter. The *beauty* of the radar altimeter is it is designed to do one thing -- give height measurements referenced above the ground. It is no secret that during an aircraft landing, incorporation of height above ground data is of utmost importance, yet most commercial and military aircraft do not integrate radar altimeter information using a Kalman filter. Instead, the author is aware that most military and commercial airlines have purchased the radar altimeter, but it is only used in a stand-alone mode. Another reason to integrate the radar altimeter height above ground measurements, is that typically code phase GPS suffers most in the *vertical* channel due to satellite vehicle geometry than when compared with GPS horizontal position errors. The author is aware that not all aircraft (particularly civil aviation aircraft) can afford the use of a radar altimeter; instead, the use of a GPS pseudolite (used during aircraft final approach) will be compared. This thesis will take a first-cut look at comparing the following integrated systems containing a low and medium accuracy INS:

Case I	Case II	Case III	Case IV	Case V	Case VI	Case VII	Case VIII	Case IX
Barometric Altimeter								
0.4 nm/hr CEP INS	0.4 nm/hr CEP INS	2.0 nm/hr CEP INS	2.0 nm/hr CEP INS	4.0 nm/hr CEP INS	4.0 nm/hr CEP INS	0.4 nm/hr CEP INS	2.0 nm/hr CEP INS	4.0 nm/hr CEP INS
P-Code GPS								
----	Radar Altimeter	----	Radar Altimeter	----	Radar Altimeter	Pseudolite	Pseudolite	Pseudolite

Table 1 - 3. Case I-IX Thesis Integration Comparisons

1.1 Background

After much review of the past years' technical publications, it appears that very few "integrated" GPS/INS studies have been accomplished with regard to implementing precision landing approaches. Instead, the majority of research has exploited "stand-alone" GPS receiver techniques (Differential GPS (DGPS) or Carrier-phase GPS (CPGPS)) [53,66,26,5,51,12,30,34]. Only two publications described an integrated mechanization using an Inertial Navigation System (INS) [30,34].

No technical papers were noted using a radar altimeter, INS and GPS measurements with a Kalman filter. The author chose to use a radar altimeter because the radar altimeter can provide vertical (altitude) measurements to the Kalman filter which otherwise would not be utilized. Integration techniques for precision approaches normally fail because the vertical channel accuracy requirements are not met (despite the use of a barometric altimeter to stabilize the vertical channel of the INS). The accuracy of most radar altimeters can meet the vertical precision approach requirements typically to Category I requirements (see Section 1.2, Table 1 - 4) [28]. Another benefit of the radar altimeter is it can be used in ground collision avoidance algorithms. Because the radar altimeter is equipped on most commercial airline and DOD aircraft, and because the radar altimeter shows great potential for aiding an aircraft during precision approaches using a Kalman filter, it was chosen to be utilized in this thesis. The author believes that pseudolites (active pseudo- "satellites" precisely stationed along the approach runway path) show great potential in allowing the host aircraft's Kalman filter access to a superb ranging device to eliminate vertical errors. These are currently being investigated by a number of researchers [12], and so they will also be considered in this performance analysis. It was also noted that though a wide variety of integration techniques exist (fuzzy logic, neural networks, least squares, etc.), only Kalman filter integration techniques were found to be actively in use for current aircraft precision approach research and development.

1.2 Key Terms

Global Positioning System: A satellite-based navigation and time system designed, developed and maintained by the U.S. Department of Defense (DOD) [17]. Accuracy: Stand-alone (no-aiding) GPS is typically 16 meters (military) and 100 meters (commercial) spherical error probable (SEP).

Differential GPS (DGPS): A ground-based GPS receiver (accurately surveyed) uplinks error corrections to nearby (< 150 nautical miles) aircraft, thus reducing common errors. Accuracy: 3 meters (military and commercial) SEP.

Carrier-Phase GPS (CPGPS): A new receiver technique which is able to measure the incoming satellite-transmitted GPS signal to a fraction of a wavelength. Accuracy: < 30 centimeters (military and commercial), $1-\sigma$.

Inertial Navigation System (INS): A self-contained dead-reckoning system that utilizes internal gyroscopes and accelerometers to navigate. Typical medium accuracy: 1-3 nautical-miles/hour circular error probable (CEP).

Kalman Filter: A recursive computer algorithm that uses sampled-data measurements to produce optimal estimates of states of a dynamic system, under the assumptions of linear system models and white Gaussian noise models. Developed by R.E. Kalman in the early 1960s, *A New Approach to Linear Filtering and Prediction Problems* [35].

Aircraft Precision Landing: Formally defined by the Federal Aviation Administration (FAA) in [22] as Category I, II or III precision approach. See Table 1 - 4 [36].

Precision Approach Parameters (in feet, all 1-sigma values)		
Category	Azimuth	Elevation
I	+/- 28.1	+/- 6.8
II	+/- 8.6	+/- 2.8
III	+/- 6.8	+/- 1.0

Table 1 - 4. Precision Approach Accuracy Requirements at Decision Heights

Instrument Landing System (ILS): Current land-based navigation aide used to guide aircraft safely for final approach airport landings [22,36].

Microwave Landing System (MLS): Proposed land-based replacement navigation aide for the ILS [36,43].

1.3 Literature Review

The following is a brief discussion of eight technical papers published in 1993-1994 [53,66,26,5,51,12,30,34]. The eight technical papers were reviewed and summarized in three categories: (1) DGPS (stand-alone), (2) CPGPS (stand-alone) and (3) GPS, DGPS or CPGPS integrated with an INS using a Kalman filter.

1.3.1 DGPS (Stand-Alone)

[53]. Commercial code tracking differential GPS (DGPS) landing system, using narrow correlator receivers in the ground reference station and avionics, configured to drive an ILS autoland flight control system with ILS "look alike" deviation signals, successfully guided a BOEING 737 to 31 successful "hands off" landings. No landings are aborted because of equipment failure, and conservative estimates of lateral and vertical total system error fell within Category III for both the approach and touchdown segments of the landings with substantial margin. Pilots commented that DGPS approach paths seemed noticeably straighter than what they had experienced with ILS coupled approaches. Performance results were based on predicted FAA "tunnel" requirements.

[66]. A commercial code tracking Novatel Model 951R GPS card is utilized, along with DGPS corrections. A total of 43 approaches are flown at Atlantic City, NJ. The Novatel receiver is a 10-channel, narrow correlator which outputs data at a 5 Hz rate. Category I vertical requirements are met.

1.3.2 CPGPS (Stand-Alone)

[26]. The theoretical use of carrier-phase for Category I, II and III approaches is discussed. Mathematical equations describing single, double and triple differencing techniques are derived for use with pure carrier-phase GPS receivers.

[5]. The theoretical use of carrier-phase GPS and solving the carrier-phase cycle ambiguity is discussed. The author describes situations in which use of only L1 band cannot guarantee Category III integrity and reliability. Use of pseudolites (GPS "satellites" based on the ground at precisely known locations) to carry out a continuous landing approach is mentioned.

[51]. The NASA Ames Research Center conducted theoretical research to develop and demonstrate carrier-phase DGPS algorithms for approach and landing. The theoretical research is put to test by actually flight testing the algorithms and navigation

systems using a King Air 200 aircraft and an Ashtech P-12 GPS receiver. In 11 of 12 approaches, integer ambiguities (See Note below) are resolved at a minimum distance of 2.7 km from landing, with the solution being maintained through touchdown. However, in 5 of the 12 final approach and landing segments, wrong integers are determined. Continuing work is necessary to achieve "robust" integer-ambiguity resolution without the use of pseudolites.

Note: The GPS carrier frequencies (L1 and L2) are in the L-band (1.2 to 1.6 GHz) [27]. The wavelength range of the L-band is therefore 18 to 25 centimeters. The observed carrier-phase quantity is a measure of the phase-shift; that is, it represents only a fractional part of one wavelength [27]. The total phase-range measurement at some time epoch t would then be equal to this fractional part, Φ_{frac} , plus an integer number of phase cycles from the initial time, t_0 , to the time epoch t (which is continuously measured and compensated by the receiver), $\Phi_{\text{int}}(t_0, t)$, plus an integer phase ambiguity term N [27]. Note that $\Phi_{\text{int}}(t_0, t_0)$ represents the receiver's initial estimate of the number of integer phase cycles [27]. The integer ambiguity term, sometimes referred to as the cycle ambiguity, is the difference between the true integer count at time t and the current integer count at time t measured by the receiver [27]. The total phase can then be represented from [27]:

$$\Phi_{\text{total}}(t) = \Phi_{\text{frac}}(t) + \Phi_{\text{int}}(t_0, t) + N(t) \quad (1.1)$$

For more information about carrier-phase GPS terminology, see [27,6].

[12]. Stanford University provided flight test results of a carrier-phase GPS, using pseudolites along the airport approach path. Flight test results are compared to data from independent laser measuring equipment. The "Kinematic GPS" achieved centimeter accuracy throughout all flight tests (between 5 and 30 centimeters, $1-\sigma$ = one standard deviation). The estimated cost to outfit a runway with pseudolites for Category III precision is stated at less than \$100K.

1.3.3 GPS, DGPS or CPGPS Integrated with an INS Using a Kalman Filter

[30]. A carrier-phase, double differential GPS and an INS are integrated using a centralized Kalman filter (post-processed after flight). Through the analysis of flight test data, it is shown that the GPS/INS position data agrees at the centimeter-level ($1-\sigma$) with the GPS-only carrier-phase receiver position. The ability of the INS to detect and correct cycle slips is also demonstrated for system integrity and reliability concerns.

[34]. An INS and a commercial GPS are integrated using a Kalman filter and flight tested in Germany. The requirements for automatic landing systems (accuracy, integrity and availability) are discussed in this paper. INS/GPS integration performance results are on the order of 1 meter accuracy. The performance of this system would meet Category III ILS specifications and could be used at airports not equipped with a ground-based GPS or ILS.

1.4 Problem:

In the case of aircraft integration, very few "integrated" GPS/INS studies have been accomplished with respect to implementing precision landing approaches. Instead, the majority of research has explored stand-alone GPS receiver (mostly using uplinked GPS differential signals to reduce atmospheric and selective availability errors). The benefit of "stand-alone" is most definitely the cost-savings of such a scheme. The disadvantage is, GPS as a stand-alone is not an error-proof system. It is a complicated system devised of three main segments: (1) space, (2) control and (3) user. Of the three parts the "user" segment is most vulnerable and is susceptible to using bad satellite vehicle (SV) range data or terrorist jamming (or unintentional jamming) if it is operating as a "stand-alone" system. During a precision landing, the navigation solution, that is, the input control signal(s) to the autopilot (for autoland), must be of highest integrity to be FAA certified.

Instead of stand-alone GPS techniques, this thesis will *integrate* stand-alone systems (INS/GPS/Baro/Radar Altimeter) using an extended Kalman filter. With this powerful integration of available sensor measurements, it then is possible to perform *residual monitoring* [40] (a possible follow-on to this thesis). Residual monitoring would be utilized as a "reasonableness" check of the incoming GPS measurements so that the overall navigation solution processed by the INS/GPS Kalman filter integration is of highest integrity. In short, use of an INS/GPS Kalman Filter integration **and** residual monitoring would be exploited to try to meet all FAA requirements with regard to accuracy, integrity, coverage, availability and continuity for precision landing operations. This thesis will only look at using an extended Kalman filter to meet FAA precision approach *accuracy* requirements.

The user's GPS receiver would make use of the good high-frequency INS information. Also, the highly accurate low-frequency GPS information would be used to offset the long term errors of the INS (i.e., errors due to gyro drift). A GPS and an INS, when integrated properly, are nearly perfect complements of one another.

1.5 *Problem Statement:*

This thesis concentrates on setting up reliable models for a medium (1 nm/hr CEP) and low accuracy INS (4 nm/hr CEP), GPS (4 channel receiver, 5m vertical and 4m horizontal precision, 1σ), Baro Altimeter (50 - 150ft, 1σ), and Radar altimeter (1% of altitude ± 1 ft, 1σ). This thesis also develops a generic precision approach flight profile (using PROFGEN [47]) that encompasses a majority of aircraft types. Lastly, this thesis utilizes a single ground-based SV (pseudolite) and available true post-processed ephemeris data [14], instead of prior FORTRAN orbit functions used at AFIT [58,3,45,50,27]. Once all the above elements are in place, the Multimode Simulation for Optimal Filter Evaluation (MSOFE) [48] is utilized to perform extended Kalman Filter integration analysis.

1.6 *Past Research:*

The past research at the Air Force Institute of Technology (AFIT) began with the generation of computer models for INS, GPS and Range/Range-Rate System (RRS), as well as the development of an integration scheme to blend the information from these three independent sources into a single navigation solution. The choice for blending measurement information is an extended Kalman filter (EKF). The overall navigation system developed by the early research became known as the Navigation Reference System (NRS) [45,50] model. This thesis will use pieces of the NRS model previously developed by researchers at AFIT. A fighter profile provided by Wright Laboratories [47] is used initially to ensure that the *modified* NRS model, (from this point on, we will call the *modified* NRS model the “Landing System Model” (LSM)) closely resembles prior AFIT research results.

1.7 *Scope:*

Itemizing the majority of the thesis tasks yields:

- a. Review prior AFIT thesis of Mosle (GE 93D) and Negast (GE 91D).
- b. Research current aircraft ILS Category I, II and III precision approach techniques and performance specifications. (Translate required performance specifications/capabilities into the development of the INS/GPS integration for this project).

- c. Interview pilots and Air Traffic Control personnel who have "real-world" experience in precision landing modes of operation. [Literature readings can never give all the information needed to understand a problem fully. Since real-world knowledge (from military and commercial pilots) is available, it makes sense to search it out].
- d. Create a realistic scenario and flight profiles of an autoland at Wright-Patterson AFB, OH. PROFGEN [47] will be utilized to create a trajectory that will represent a generic transport aircraft from take-off to a precision approach landing. This flight profile will be called "Tanker" since its attributes closely resemble those of a KC-135 tanker (Boeing 707) aircraft.
- e. Find/synthesize a "truth model" (a complete, complex mathematical *error* state model that portrays true system behavior very accurately). An *error* state model is chosen, as opposed to a total state model, because an error model is more adequately represented as linear and because it involves slower dynamics than a total state model for an INS; essentially all terrestrial navigation system Kalman filters are based upon error state models [40]. The NRS model of Mosle is used by extracting from the NRS truth and filter models, the doppler-aided velocity measurements and the transponder (RRS) measurements. Replace the current MSOFE NRS algorithms that "simulate" satellite vehicle (SV) ephemeris data by instead using true SV ephemeris data acquired directly from the National Geodetic Office. Modify Mosle's MSOFE NRS code to accept radar altimeter measurements. This *modified* NRS code that accepts radar altimeter measurement will be called the "Landing System Model (LSM). (Unfortunately, due to the many unknowns of the proposed integration mechanization and the time limitations of this thesis, only a first-cut approach at a radar altimeter model is incorporated).
- f. Linearize the truth model (if necessary).
- g. Conduct a performance analysis of each proposed Kalman filter (of item (e) above), driven by measurements derived from the truth model of the real system. [Repeat step (h) below as necessary].
- h. "Tune" each filter (of step (g) above) to provide the best possible performance.
- i. Generate a Monte Carlo analysis of designs (of step (h)) that show the most promise.
- j. Conduct a performance/computer loading tradeoff analysis -- then select a design.

- k. Implement the chosen design to be used in the final system against a realistic profile of step (d). Perform checkout and final tuning of the system.
- l. Analyze results and identify real world implementation issues.
- m. Compare performance results found from this thesis to benchmark(s) of today's ILS, MLS, and GPS (stand-alone).

1.8 Assumptions:

All theses are limited by the assumptions made, and no research can be adequately evaluated unless these assumptions are clearly defined [45]. This section outlines the assumptions that have been made in this thesis.

- 1. All work has been conducted through computer simulation. The "real" world in the simulation is modeled as a full-order truth error-state model. The full-order truth and filter models are presented Chapter 3.
- 2. The INS platform is assumed to be stabilized with a barometric (baro) altimeter. An INS platform is unstable without an outside measurement source in the vertical channel [9]. While a baro altimeter is not the only way to stabilize a platform, it is a commonly used method. The use of the baro altimeter is included in the modeling of the system. The majority of commercial and military aircraft utilize a radar altimeter in a stand-alone mode for terminal approaches to a runway. This thesis will instead exploit the radar altimeter as an independent measurement device feeding an extended Kalman filter. The radar altimeter measurements will be utilized at altitudes below 3000 feet above ground level (AGL). In summary, this thesis will use both the barometric *and* radar altimeter measurements.
- 3. A sample period of one second has been chosen (unless otherwise noted) for the EKF. The sample period refers to how often the GPS and radar altimeter measurements will be brought into the EKF. Past AFIT research has used a variety of sample periods, varying from two to ten seconds [45,50]. The decision to use one second sample period is based primarily on the typical availability of the GPS measurement in the real world. Though the author is aware of a few GPS receivers which output measurements at a rate of ten

times a second (10 Hz), a one second sample period is chosen as a good, representative design choice.

4. The computer simulations have been developed using a program called Multi-mode Simulation for Optimal Filter Evaluation (MSOFE) [48]. MSOFE is well-established Air Force software to develop and test Kalman filter algorithms.
5. The computer-simulated flight profile has been generated by the program PROFGEN [47]. PROFGEN is designed to work with MSOFE to provide the necessary data files to simulate dynamic flight profiles.
6. The plotted outputs are generated by the commercial software package MATLAB [60].
7. The SV ephemeris data using System Effectiveness Model (SEM) [18] software was obtained from the Coast Guard BBS. The ephemeris data is post-processed by the U.S. Department of Commerce, National Geodetic Information Branch [14].
8. Ephemeris data was incorporated into PROFGEN's binary output "FLIGHT" profile by making adaptations to existing [57] FORTRAN source code.
9. The four SVs chosen to range during operation of MSOFE and the FLIGHT profile are chosen based on the indicated results of the System Effectiveness Model (SEM3.6) software from [18] based on position dilution of position (PDOP) criteria less than two (2).
10. The simulation software, MSOFE and MATLAB, has been coded to run in double precision to increase the numerical stability and precision of the simulation. MSOFE software utilizes a U-D factorization algorithm to increase the numerical stability in the Kalman filter measurement update equations [48,41].
11. The MSOFE runs are conducted using 15-run Monte Carlo analyses. While a larger batch size for the Monte Carlo analysis would be preferable, this value has been chosen to keep the computational burden of the thesis within reasonable bounds, while maintaining adequate confidence that the resulting sample statistics properly reflect the true underlying statistics.

12. Taylor series approximations truncated at first order are used for linearizing nonlinear equations in the NRS and LSM filter. Perturbations about a nominal trajectory will be established in each case.
13. It will be assumed for this thesis that, when radar altimeter measurements are available, the earth's surface will be modeled as flat and referenced approximately to the INS indicated altitude (referenced to WGS-84 ellipsoid). This assumption will definitely have to be "upgraded" to a more realistic radar altimeter scenario at a later time by possibly using a database that contains "height of terrain" for specific locations on the earth.
14. The INS will have had a "normal" 8-minute alignment and nominal flight of sixty (60) minute duration prior to the terminal approach phase under investigation. "Normal" also means the INS has not been degraded nor enhanced by any means.
15. Four SV are always available, with an average PDOP of 2.1.
16. The transport aircraft flight profile will:

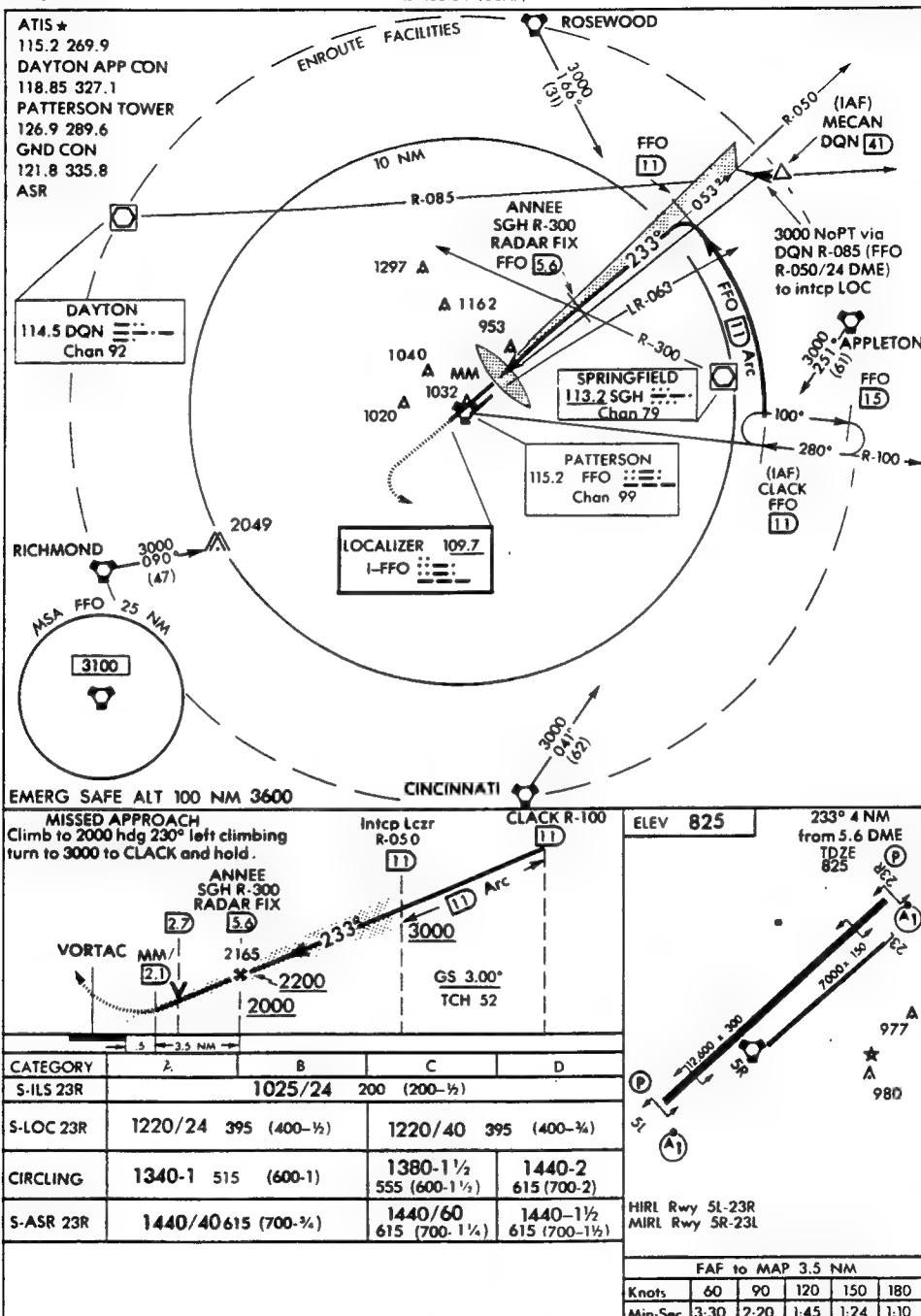
- a. Always be at less than 0.9g during entire flight.
- b. Have a takeoff speed of 150 knots.
- c. Have a landing speed of 133 knots at a 3 degree glideslope.
- d. Airspeed above 10,000 will always be greater than 250 knots.
- e. Change altitude at a rate 4000 ft/min (maximum).
- f. Follow the approach plate of Figure 1 - 1 [15].

The approach plate of Figure 1 - 1 is rather cryptic unless one is a trained pilot. Figure 1 - 1 shows two top views of the Wright-Patterson runway, and a side view for a landing specifically on runway 23R. The aircraft is transitioned to the Wright-Patterson (FFO) procedure track, approximately 11 nm from the runway. The aircraft then follows the arc-turn to heading 233°. During inbound transition, the aircraft must maintain a minimum altitude of 3000 ft MSL. At approximately 5.6 nm from the VORTAC DME station, the aircraft maintains a minimum of 2200 ft MSL which is the *glide slope intercept altitude*. At approximately 0.5 nm from the runway end, the pilot's VORTAC DME would indicate 2.1 nm. The aircraft continues its 3° ILS glideslope to touchdown. Figure 1 - 1 shows that FFO is only certified for a Category I precision approach. The lower left corner of Figure 1 - 1 shows, "S-ILS 23R 1025/24 200." This information

94118
ILS RWY 23R

336
AL 108.04 (USAF)

WRIGHT-PATTERSON AFB (KFFO)
DAYTON, OHIO



ILS RWY 23R

39°50'N-84°03'W

DAYTON, OHIO
WRIGHT-PATTERSON AFB (KFFO)

Figure 1 - 1. Instrument Approach Procedures, Wright-Patterson AFB, OH

states that it is a "Precision, straight-in to Runway 23 (right-hand side); the decision height (DH) MSL is 1025 ft with prevailing visibility (runway visible range in 100's feet) of 24." "Height of DH above touchdown zone (HAT) is 200 feet." For a precision ILS approach, the pilot:

- Transitions to the ILS Localizer Course from the published approach procedure
 - Tunes the ILS and monitors the proper identifier during the entire approach
 - Sets the published localizer course prior to localizer course interception
- Accomplishes the Approach
 - Once the localizer course is intercepted, maintains glide slope interception altitude until reaching the glide slope intercept point.
 - Maintains a complete instrument cross-check throughout the approach, with increased emphasis on the baro altimeter and radar altimeter (decision height (DH) is based on the altimeters).
 - Establishes a systematic scan for the runway environment prior to reaching DH.
 - Continues descent to DH.

Note: The precision ILS approach must be discontinued if the localizer course becomes unreliable, or anytime full-scale deflection of the pilot's control display indicator (CDI) occurs on final approach [16]. The pilot must not descend below localizer minimums if the aircraft is more than one dot (half scale) below or two dots (full scale) above the glide slope. If the glide slope is recaptured to within the above tolerance, descent may be continued to DH.

A block diagram of the NRS [45] is shown in Figure 1 - 2, Navigation Reference System (NRS). A block diagram of the LSM is shown in Figure 1 - 3. A "walk-through" of Figure 1 - 3 can be found in Chapter 3, Section 3.2.

1.9 Summary

This chapter has given a brief overview of the thesis plan to develop an integrated GPS/INS/Baro and Radar Altimeter System for aircraft precision approaches. Past research, the scope of this project, and all assumptions were presented. In Chapter 2, the reference frames utilized in this project are presented, along with INS, GPS, baro altimeter and radar altimeter subsystems, and Kalman filtering algorithms are discussed.

Navigation Reference System (NRS)

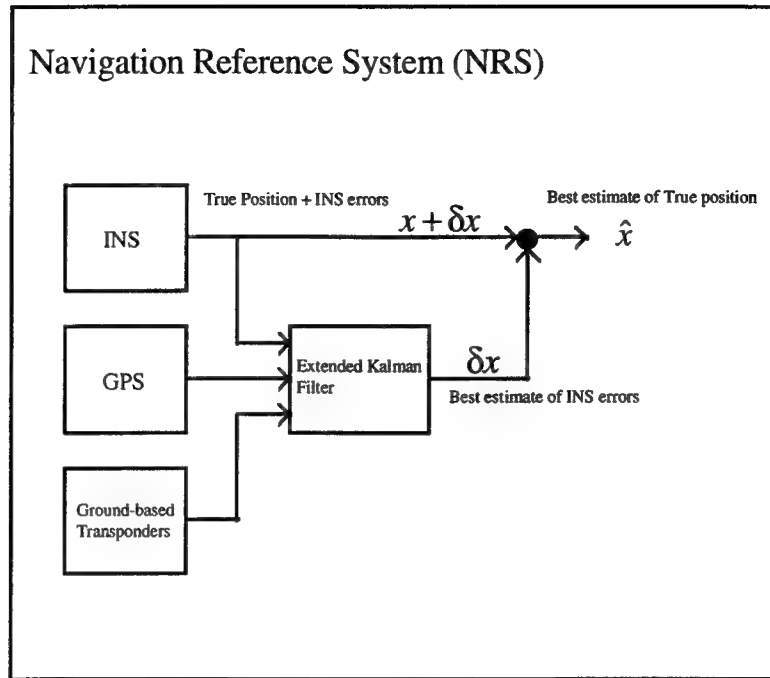


Figure 1 - 2. Navigation Reference System (NRS)

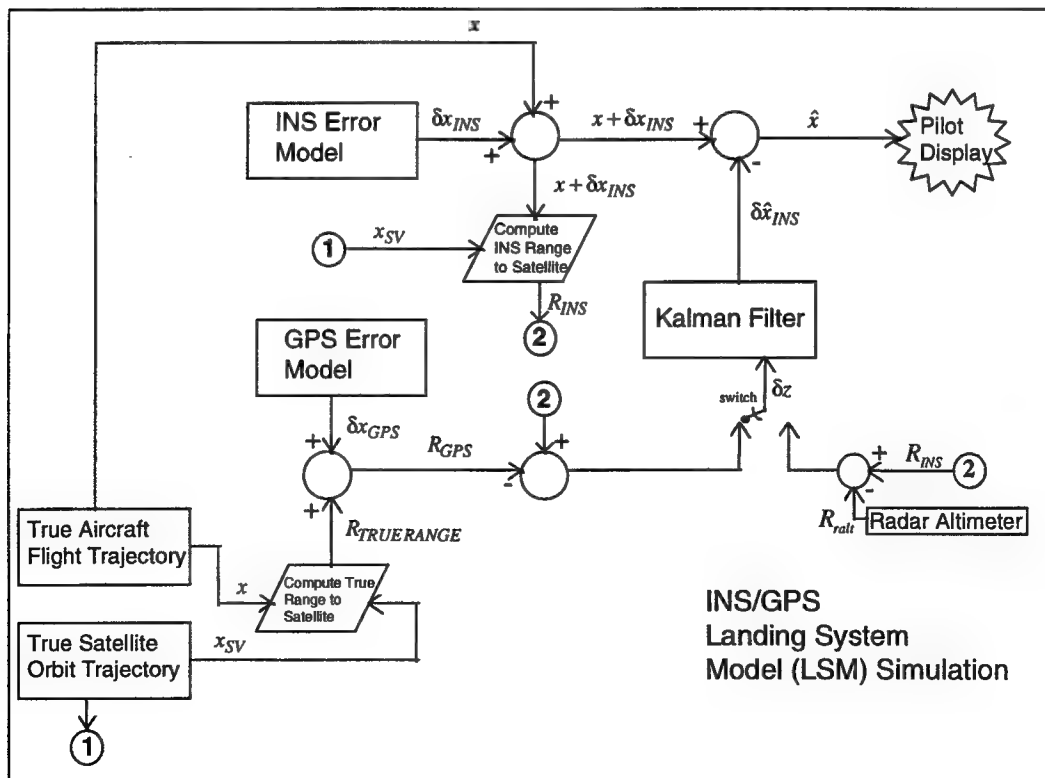


Figure 1 - 3. Landing System Model (LSM) Simulation

Chapter 3 introduces and develops the landing system model (LSM). Chapter 4 discusses the results and analysis of the LSM. Chapter 5 summarizes the research and presents recommendations and conclusions based on results presented in Chapter 4.

II. Background

2.1 Introduction

This section presents basic theory of a ring laser gyro (RLG), Inertial Navigation Systems (INS), Global Positioning System (GPS), barometric altimeter and the radar altimeter. ILS precision approach information will also be presented. Fundamental Kalman filter and extended Kalman filter (EKF) theory will also be discussed. A more rigorous development of many of the Kalman filter subjects can be found in [40,41,42]. A quick review of notation usage in Section 2.1.1 may be advantageous before reading further in this chapter.

2.1.1 Notation

Notation used in this thesis will attempt to maintain consistency with [40] Deterministic and stochastic processes alike will be indicated by the roman typeface. Vectors will be displayed in bold-faced type, \mathbf{x} , whereas scalars will be normal type, x . Matrices will be displayed in bold-upper case \mathbf{X} . A particular realization of a variable will be displayed in italics, \mathbf{x} .

2.2 Ring Laser Gyro (RLG) Strapdown INS:

In order to "navigate" well, one must find a solution to the following layman's "navigation" problem [32]:

- Where am I? (Present position)
- In which direction is my destination? (Relative bearing)
- How far is it to my destination? (Distance to go)
- How fast *and* in what direction am I going? (Velocity)

A ring laser gyro strapdown inertial navigation system can easily find the solution to the above questions.

By definition [33], an *inertial navigator* is a self-contained, dead-reckoning navigation aid using inertial sensors, a reference direction, and initial or subsequent fixes to determine direction, distance, and speed; single integration of acceleration provides speed information and a double integration provides distance information.

From [9], strapdown systems are characterized by their lack of a gimbal support structure. An advantage of strapdown vs. the gimbaled is that a strapdown has no moving

platform keeping a "stable element" level. Eliminating gimbals (i.e. reducing moving parts) translates to a higher mean time between failure (MTBF), and typically lower production costs. Also, if a gyro fails in a strapdown system, that one gyro can be replaced; in a gimbaled system, the entire inertial measurement unit (IMU) would have to be replaced. A disadvantage strapdown has vs. gimbaled is that the platform is physically "strapped-down" to the dynamic body in question, thus the gyroscopes, accelerometers and strapdown computer algorithms must be able to "keep-up" with whatever harsh dynamic environment to which it is attached. Accuracy is often lower also.

The strapdown system is mechanized by mounting three gyros and three accelerometers directly to the vehicles for which the navigation function is to be provided. An onboard digital computer keeps track of the vehicle's attitude with respect to some reference frame based on information from the gyros. The computer is thus able to provide the coordinate transformation necessary to coordinatize the accelerometer outputs in a computational reference frame.

RLG construction typically consists primarily of an optical cavity, a laser device, three or four mirrors, a prism, and a pair of photo detectors [58,54]. According to [58,54,29], the RLG operates as follows: the laser gyro detects and measures angular rates by measuring the frequency difference between two contra-rotating (laser) beams [29]. The two laser beams circulate in the "ring" cavity simultaneously. Mirrors are used to reflect each beam around an enclosed area. The resonant frequency of a contained laser beam is a function of its optical path length. Consequently, the two laser beams have the same frequencies when the gyro is at rest. If the cavity is rotating in an inertial sense, the propagation times of the two light beams are different. The delay manifests itself in the form of a phase shift between the two beams, and the phase shift is detected by a pair of photo detectors [58,54]. The magnitude of the phase shift provides a direct indication of the angular rate of rotation of the instrument with respect to inertial space [58,54]. The laser gyro is an unconventional gyro since it does not have a spinning rotor. Devices of this type are extremely reliable due to the absence of moving parts [58, 54].

Specific force is measured by accelerometers. The most common accelerometers to date have been devices which are sophisticated variations of the simple pendulum [58,9]. The motion of the internal mass is related to the inertially referenced motion of the instrument case by Newton's second law of motion [58]. However, to obtain the correct measure of inertial acceleration, the effects of local gravity must be removed from the measured specific force [9, 52].

In summary, inertial navigation principles, have been well understood for many years [9]. The author has always been fascinated at the cost and complexity of some

INSs, of how technicians and engineers continually try to "tweak", upgrade and massage its sensor components. In this brief INS introduction the author has mentioned many things, one of them is that the INS solves our *navigation problem*, and it does so on its own. A system self-contained, which does not need outside help, cannot be jammed and does not emit radiation that otherwise could be detected (for military purposes). The INS typically outputs data at a 50 Hz rate. Amazingly, INS prices keep dropping (\$127K (gimbaled INS) in 1990, now \$65K (RLG INS) in 1994 - with double the reliability!

2.3 Barometric Altimeter:

A shortcoming of any INS is the instability present in the vertical channel which (in the absence of aiding information) results in unbounded error growth in vertical position and velocity [3,9,25,52]. This inherent instability is controlled by vertical channel aiding. Such aiding is frequently accomplished in vertical position information provided from a barometric altimeter. This external altitude information has the effect of stabilizing the vertical channel [9].

There are many ways to measure the altitude of an aircraft; probably the simplest is with a barometric altimeter [16]. The pressure of the Earth's atmosphere decreases as height above the earth increases. Barometric altimeters are designed to output altitude relative to the pressure difference. For example, if the barometric scale is referenced to 29.92" Hg (sea level, standard conditions) and the instrument is supplied with a static pressure of 20.58" Hg (pressure at 10,000 feet, standard conditions), the altimeter should output 10,000 feet. The pressure difference between the sea level and 10,000 feet on a standard day is 9.34 inches of mercury [16]. Barometric altimeters are most inaccurate when ascending or descending at rapid rates (especially noted with fighter aircraft) but are relatively low cost.

2.4 Global Positioning System (GPS)

GPS navigation presents opportunity for standardized worldwide civil aviation operations using a common navigation receiver [23]. GPS is a space-based positioning, velocity and time system that has three major segments: Space, Control and User.

2.4.1 GPS Space Segment

The GPS *Space Segment* is composed of 24 satellites in six orbital planes. The satellites operate in near-circular 20,200 km (10,900 NM) orbits at an inclination angle of 55 degrees and with \approx 12-hour period. The spacing of satellites in orbit is arranged so that a minimum of five satellites will be in view to users worldwide, with a position dilution of precision (PDOP) of six or less. PDOP is a measure of the error contributed by the geometric relationships of the GPS satellites as seen by the GPS receiver [17]. PDOP is mathematically defined as:

$$PDOP = (\sigma_x^2 + \sigma_y^2 + \sigma_z^2)^{1/2} \quad (2.1)$$

where σ_x^2 , σ_y^2 and σ_z^2 are the variances of the x , y and z pseudorange measurement position errors [17]. Each satellite transmits on two L band frequencies, L1 (1575.42 MHz) and L2 (1227.6 MHz). L1 carries a precise (P) code and a coarse/acquisition (C/A) code. L2 carries the P code. A navigation data message is superimposed on these codes. The same navigation data message is carried on both frequencies.

2.4.2 GPS Control Segment

The *Control Segment* has five monitor stations, three of which have uplink capabilities. The monitor stations use a GPS receiver to track all satellites in view passively and thus accumulate ranging data from the satellite signals. The information from the monitor stations is processed at the Master Control Station (MCS) to determine satellite orbits and to update the navigation message of each satellite. This updated information is transmitted to the satellites via the ground antennas, which are also used for transmitting and receiving satellite control information.

2.4.3 GPS User Segment

The *User segment* consists of an antenna and receiver processors that provide positions, velocity and precise timing to the respective user. Computing the user's positional information typically requires simultaneous solution of the following four nonlinear position equations [17]:

$$\begin{aligned}
(x_1 - u_x)^2 + (y_1 - u_y)^2 + (z_1 - u_z)^2 &= (R_1 - C_B)^2 \\
(x_2 - u_x)^2 + (y_2 - u_y)^2 + (z_2 - u_z)^2 &= (R_2 - C_B)^2 \\
(x_3 - u_x)^2 + (y_3 - u_y)^2 + (z_3 - u_z)^2 &= (R_3 - C_B)^2 \\
(x_4 - u_x)^2 + (y_4 - u_y)^2 + (z_4 - u_z)^2 &= (R_4 - C_B)^2
\end{aligned}$$

where the pseudo range, $R_{i=1,2,3,4}$ to each satellite is defined as

$$\begin{aligned}
R_1 &= C\Delta t_1 \\
R_2 &= C\Delta t_2 \\
R_3 &= C\Delta t_3 \\
R_4 &= C\Delta t_4
\end{aligned}$$

and

C = speed of light

$\Delta t_{i=1,2,3,4}$ = time signals transmitted by the i-th satellite

$x_{i=1,2,3,4}$, $y_{i=1,2,3,4}$, $z_{i=1,2,3,4}$ are respective i-th satellite positions

u_x , u_y , u_z is the user position the GPS user equipment is solving numerically and recursively
 C_B = the user clock bias (user equipment solves)

Normally the user equipment needs to acquire and maintain lock on four satellites in order to compute a 3-D position fix [44] and the clock bias C_B . The GPS pseudorange between the user and each satellite is computed based on knowledge of time (the master GPS clock) and the unique signal format which is broadcast by each satellite. Once the four pseudo-ranges are known, a recursive algorithm is solved to compute the user's position [44]. See [17] for further references.

2.5 Radar Altimeter

A radar altimeter provides measurement of absolute clearance over all types of terrain [28]. System operation is based on the precise measurement of the time required for an electromagnetic energy pulse to travel from the aircraft to the terrain below and to return. An elementary block diagram (transmitter, receiver, range computer, height indicator) is shown in Figure 2 - 1.

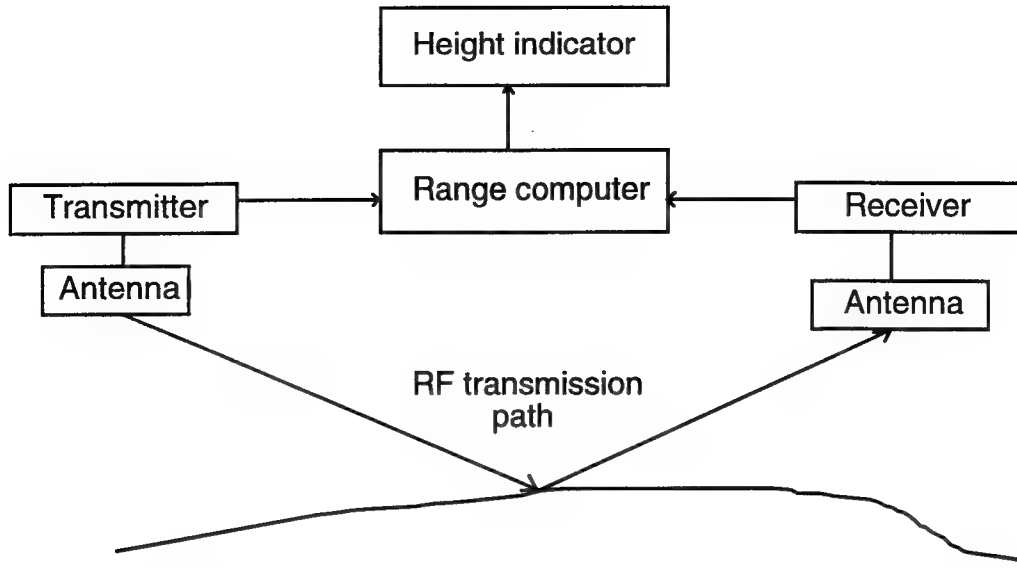


Figure 2 - 1. Elementary Radar Altimeter Block Diagram

Radar altimeters are normally all-weather devices. Performance specifications ($3-\sigma$) are typically $\pm [3\text{ft} + 3\% \text{ of altitude range}]$, with $\pm 30^\circ$ pitch and $\pm 45^\circ$ roll maneuverability at above ground level (AGL) heights, which typically vary from 0 feet to 10,000 feet.

2.6 *Instrument Landing System (ILS) Precision Approach*

An *instrument approach*, by definition [33], is the process of making an approach to a landing by the use of navigation instruments without dependence upon direct visual reference to the terrain. The *Instrument Landing System (ILS)* is designed to provide an approach path for exact alignment and descent of an aircraft on final approach to a runway [16]. The ground equipment consists of two highly directional transmitting systems, and along the approach, three (or fewer) marker beacons. The directional transmitters are known as the localizer and glide slope transmitters. See Figure 2 - 2.

The *localizer* transmitter, operating on one of the 40 ILS channels within the frequency range of 108.10 MHz to 111.95 MHz, emits signals which provide the pilot with course guidance to the runway centerline in the horizontal plane. The localizer signal is usable and accurate to a range of 18 nautical miles (NM) from the localizer antenna unless otherwise depicted on the Instrument approach procedure (IAP) [16]. See Figure 2 - 2.

The ultra high frequency *glide slope* transmitter, operating on one of the 40 ILS channels within the frequency range 329.15 MHz to 335.00 MHz, radiates its signals primarily in the direction of the localizer front course, i.e., so as to measure angular

vertical displacement from the desired glide path, as seen from the side. The glide slope signal is usable to a distance of 10 NM unless otherwise depicted on the Instrument approach procedure (IAP) [16].

A *marker beacon* light and (or) aural tone may be included in the cockpit display to indicate aircraft position along the localizer. The marker beacons are identified by continuous dashes for the outer marker, alternating dashes and dots for the middle marker, and continuous dots for the inner marker. See Figure 2 - 2. Precision ILS Approaches follow the 2σ decision height accuracy shown in Table 2 - 1, 2σ Precision ILS Approach Criteria at Decision Height.

<u>ILS Precision Category</u>	<u>Horizontal Accuracy</u>	<u>Vertical Accuracy</u>
1	± 56.1 ft	± 13.5 ft
2	± 17.1 ft	± 5.6 ft
3	± 13.5 ft	± 2.0 ft

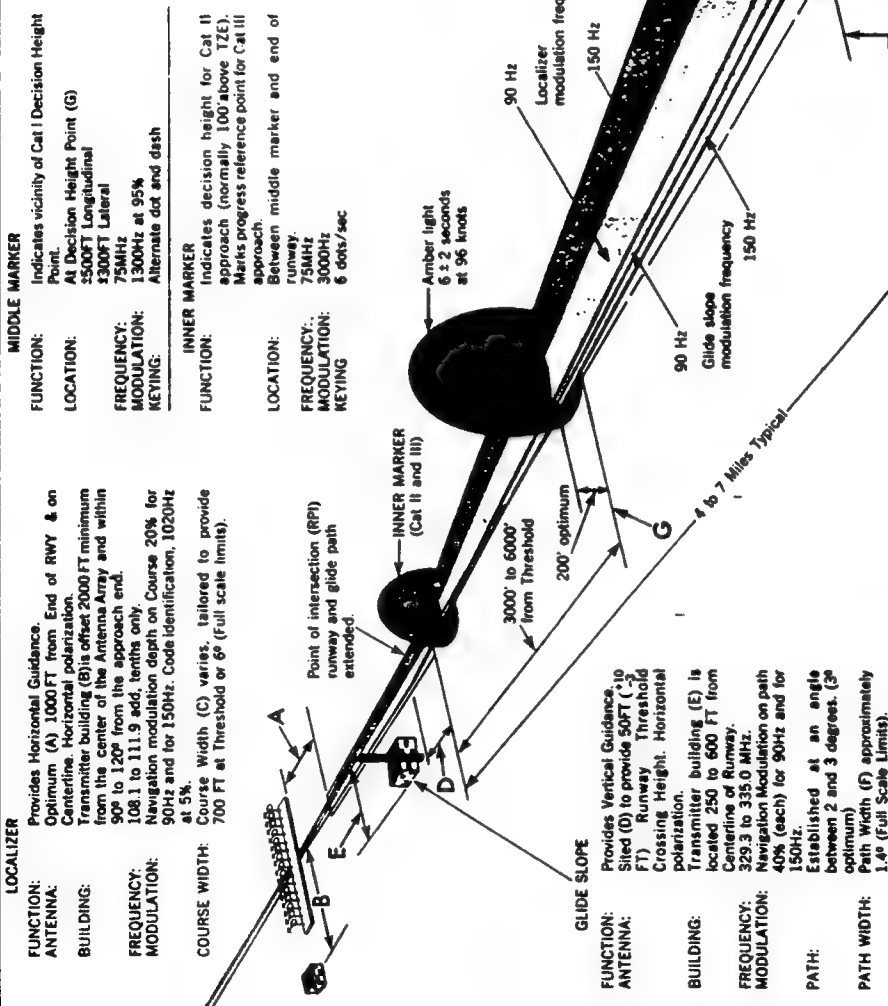
Table 2 - 1. 2σ Precision ILS Approach Criteria at Decision Height

2.7 *Reference Frames*

A navigation "solution" has significance only if the corresponding frame in which the solution is expressed is clearly understood [58]. While the preceding statement may seem obvious, it cannot be overemphasized. Consider that a typical INS "owner's manual" defines *earth frame*, *true frame*, *computer frame*, *platform frame*, *sensor frame*, *accelerometer frame* and the *body frame* [58,38]. From a student's perspective this may at first be overwhelming, but to make matters worse, another INS vendor may well define every frame mentioned above, such as "*earth frame*" in an entirely *different* manner! Therefore, the frames used in this project, along with coordinate transformations, will briefly be discussed (all reference frame figures with permission from [7]).

ILS STANDARD CHARACTERISTICS AND TERMINOLOGY

ILS APPROACH CHARTS SHOULD BE CONSULTED TO OBTAIN VARIATIONS OF INDIVIDUAL SYSTEMS



NOTE:
Compass locators, rated at 25 watts output, 200 to 415 kHz, are installed at some outer markers and middle markers. A 1020 Hertz tone, modulating the carrier about 95%, is keyed with the first two letters of the ILS identification on the outer locator and the last two letters on the middle locator. At some locators, simultaneous voice transmissions from ATC facilities are provided, with appropriate reduction in identification percentage.

Figure 2 - 2. Standard ILS Characteristics and Terminology.

2.7.1 *Inertial Frame* (x^i, y^i, z^i)

An inertial frame is an orthogonal, right-handed coordinate system; its origin is coincident with the earth's center-of-mass and the frame is oriented as follows. The x^i, z^i plane lies in the earth's equatorial plane and does not rotate with respect to the fixed stars. The y^i axis projects from the earth's center-of-mass directly through the North pole. The inertial frame is depicted by the $[x^i, y^i, z^i]$ frame shown in Figure 2 - 3.

2.7.2 *Earth Frame* (x^e, y^e, z^e)

The earth frame or “earth-centered-earth-fixed” (ECEF) frame is an orthogonal, right-hand coordinate system; its origin is coincident with the earth's center-of-mass, with the x^e, z^e plane located in the earth's equatorial plane. The z^e axis is aligned with the Greenwich meridian and rotates at exactly the earth rate, Ω , about the y^e axis, which projects from the earth's center-of-mass directly through the North pole. The Earth frame is depicted as $[x^e, y^e, z^e]$ in Figure 2 - 4.

2.7.3 *Geographic Frame* (x^g, y^g, z^g) = (E, N, U)

The geographic frame or “local-level” frame is an orthogonal, right-handed coordinate system; its origin is at the location of the INS (or the user), and its axes are aligned with the East, North and Up directions [E, N, U]. The geographic frame remains perpendicular to the earth's surface with respect to the earth's gravity field as the user moves over the Earth. The geographic frame is depicted as either $[x^g, y^g, z^g]$ or $[E, N, U]$ in Figure 2 - 5.

2.7.4 *Navigation Frame* (x^n, y^n, z^n)

The navigation frame or “local-level-wander-azimuth” frame is an orthogonal, right-hand coordinate system; its origin is at the location of the INS (or the user). This frame coincides with the geographic frame when the wander angle, α equals 0° . The wander angle is a computed angle between a “scribe mark” on a wander azimuth angle platform and North. For gimbaled systems, the platform is purposely not commanded to seek North, due to the high platform angular rates that this would require in polar regions, with resulting performance degradation [3,58]. The navigation frame is denoted as $[x^n, y^n, z^n]$ shown in Figure 2 - 6.

INERTIAL FRAME (x^i, y^i, z^i)

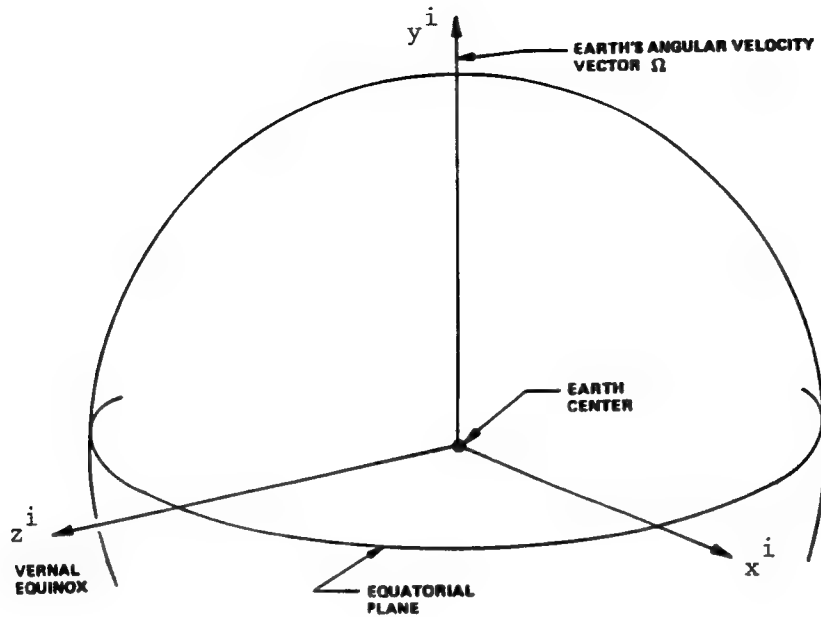


Figure 2 - 3. Inertial Frame

EARTH FRAME (x^e, y^e, z^e)

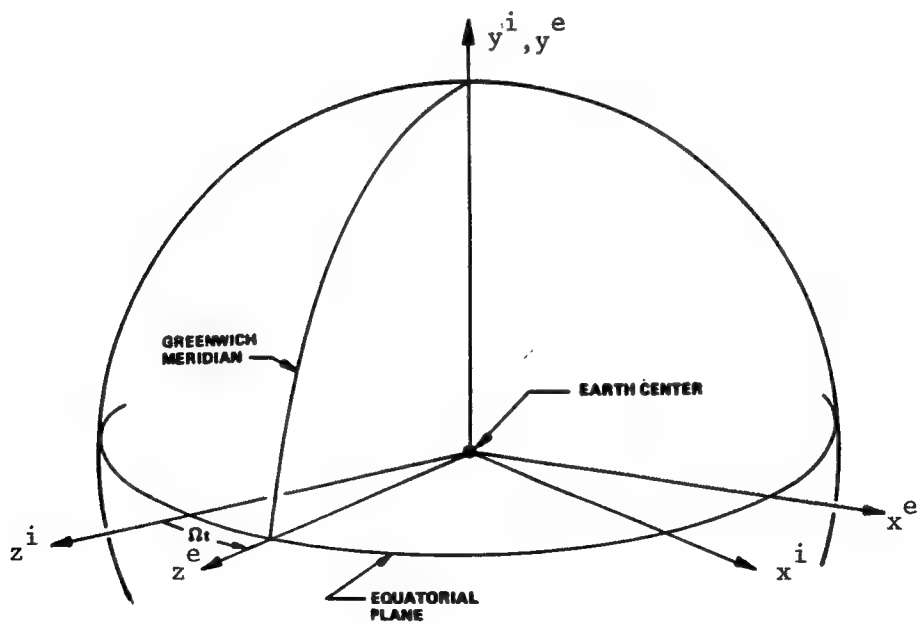


Figure 2 - 4. Earth Frame

GEOGRAPHIC FRAME (x^g , y^g , z^g) = (E, N, U)

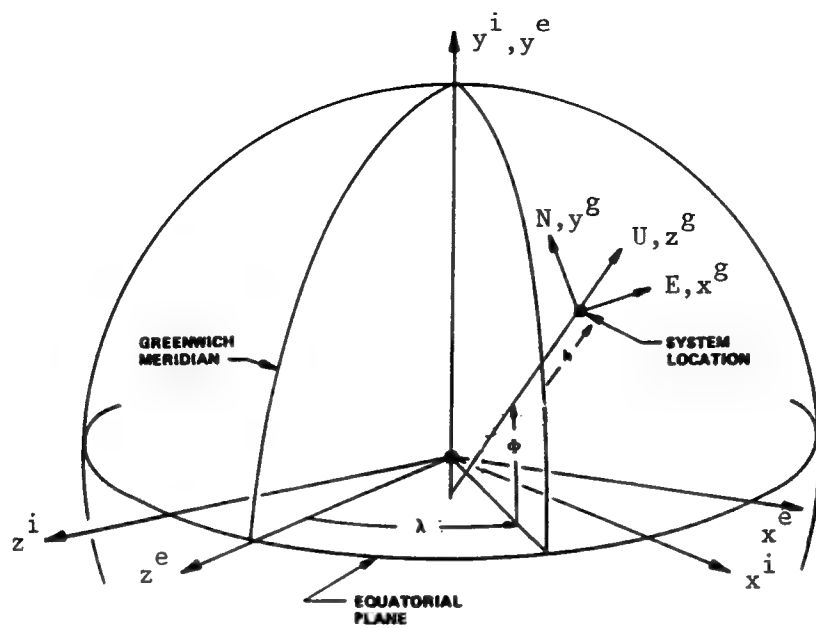


Figure 2 - 5. Geographic Frame

LOCAL LEVEL, WANDER AZIMUTH, NAVIGATION FRAME (x^n , y^n , z^n)

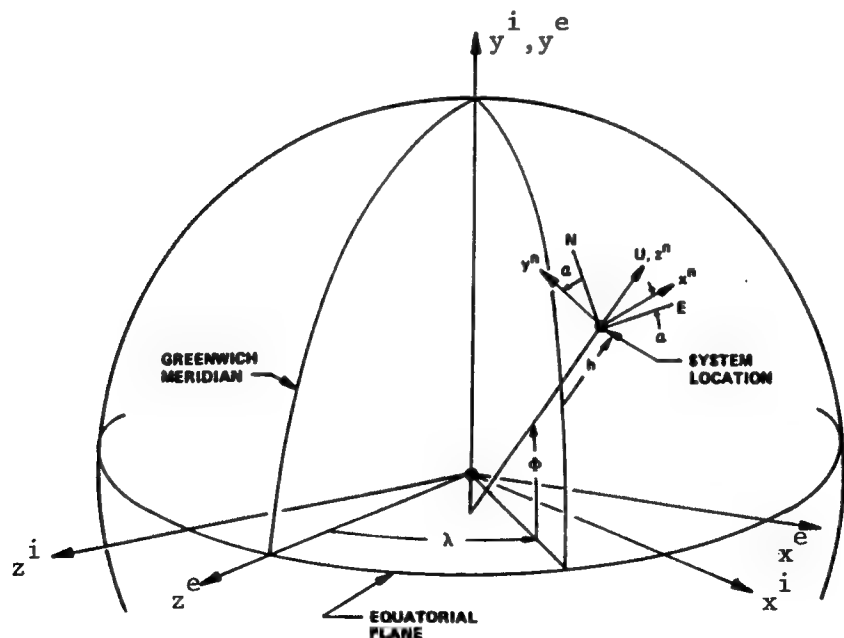


Figure 2 - 6. Navigation Frame

2.7.5 Body Frame (x^b , y^b , z^b)

The body frame is an orthogonal, right-hand frame; its origin is at the vehicle (i.e., aircraft) center-of-mass. Its axes are the vehicle's roll, pitch, and yaw axes [ϕ , θ , ψ]. The x^b axis points in the forward direction, along the roll axis; the y^b axis points to the right (starboard side) of the aircraft, perpendicular to the roll axis, but along the pitch axis; and the z^b axis is positive out the underside of the aircraft. The body frame is denoted as [x^b , y^b , z^b] and is shown in Figure 2 - 7.

2.8 Reference Frame Transformations

The RLG INS modeled in this thesis uses the navigation frame or "local-level-wander-azimuth" frame. It is often necessary to express vectors such as position, attitude, velocity or acceleration in terms of several different reference frames. As an example, the INS modeled in this thesis also outputs position error in terms of an *error-angle* vector, $[\delta\theta_x, \delta\theta_y, \delta\theta_z, \delta h]^T$, where $\delta\theta_x$ is the error angle about the local level x^g (or E) axis, $\delta\theta_y$ is the error angle about the local level y^g (or N) axis, $\delta\theta_z$ is the error about the local level z^g (or U) axis, and δh is the altitude error [3,38]. Even though this definition is clear, if the error-angle vector is to have *physical* meaning, it must be transformed into a vector in *navigation* error terminology, $[\delta\phi, \delta\lambda, \delta\alpha, \delta h]^T$, where $\delta\phi$ is the error in latitude, $\delta\lambda$ is longitude error, $\delta\alpha$ is alpha angle error and δh is again the altitude error.

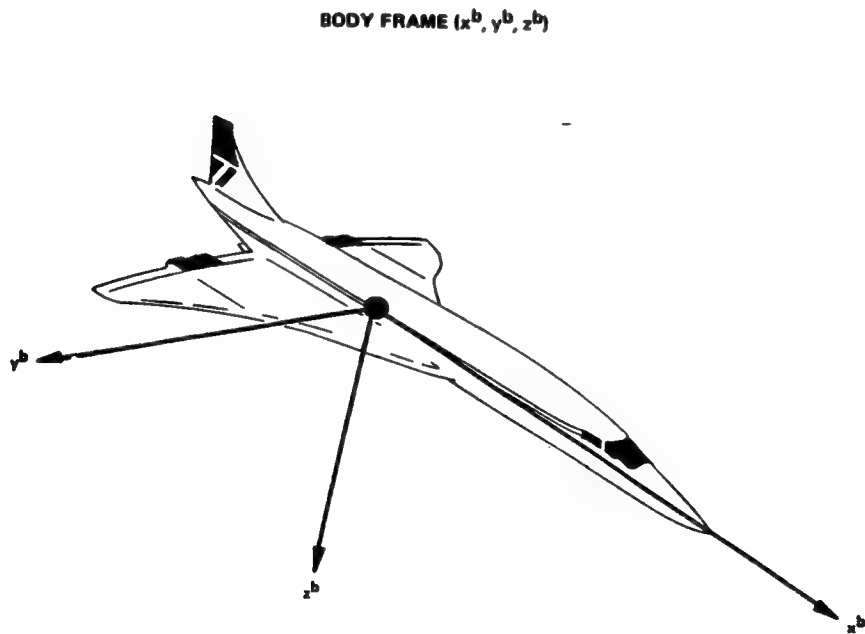


Figure 2 - 7. Body Frame

A transformation matrix, $C_{\text{Error Angle}}^{\text{Navigation Error}}$, permits compact transformation of the error-angle vector into an equivalent expression in navigation error space. The transformation matrix, $C_{\text{Error Angle}}^{\text{Navigation Error}}$ is shown below in Equation (2-1) [3,58]:

$$C_{\text{Error Angle}}^{\text{Navigation Error}} = \begin{bmatrix} -\cos \alpha & \sin \alpha & 0 & 0 \\ \sin \alpha \sec \phi & \cos \alpha \sec \phi & 0 & 0 \\ -\sin \alpha \tan \phi & -\cos \alpha \tan \phi & 1 & 0 \\ 0 & 0 & 0 & 1 \end{bmatrix} \quad (2.2)$$

Other transformations are as follows (from [7]):

2.8.1 Inertial Frame to Earth Frame, C_i^e

$$C_i^e = \begin{bmatrix} \cos \Omega t & 0 & -\sin \Omega t \\ 0 & 1 & 0 \\ \sin \Omega t & 0 & \cos \Omega t \end{bmatrix} \quad (2.3)$$

2.8.2 Earth Frame to Geographic Frame, C_e^g

$$\begin{aligned} C_e^g &= \begin{bmatrix} 1 & 0 & 0 \\ 0 & \cos \phi & -\sin \phi \\ 0 & \sin \phi & \cos \phi \end{bmatrix} \begin{bmatrix} \cos \lambda & 0 & -\sin \lambda \\ 0 & 1 & 0 \\ \sin \lambda & 0 & \cos \lambda \end{bmatrix} \\ &= \begin{bmatrix} \cos \lambda & 0 & -\sin \lambda \\ -\sin \phi \sin \lambda & \cos \phi & -\sin \phi \cos \lambda \\ \cos \phi \sin \lambda & \sin \phi & \cos \phi \cos \lambda \end{bmatrix} \end{aligned} \quad (2.4)$$

where

λ = longitude

ϕ = latitude

α = alpha angle

2.8.3 Earth Frame to Navigation Frame, C_e^n

$$C_e^n = \begin{bmatrix} \cos \alpha & \sin \alpha & 0 \\ -\sin \alpha & \cos \alpha & 0 \\ 0 & 0 & 1 \end{bmatrix} \begin{bmatrix} 1 & 0 & 0 \\ 0 & \cos \phi & -\sin \phi \\ 0 & \sin \phi & \cos \phi \end{bmatrix} \begin{bmatrix} \cos \lambda & 0 & -\sin \lambda \\ 0 & 1 & 0 \\ \sin \lambda & 0 & \cos \lambda \end{bmatrix} \quad (2.5)$$

$$= \begin{bmatrix} \cos \alpha \cos \lambda - \sin \alpha \sin \phi \sin \lambda & \sin \alpha \cos \phi & -\cos \alpha \sin \lambda - \sin \alpha \sin \phi \cos \lambda \\ -\sin \alpha \cos \lambda - \cos \alpha \sin \phi \sin \lambda & \cos \alpha \cos \phi & \sin \alpha \sin \lambda - \cos \alpha \sin \phi \cos \lambda \\ \cos \phi \sin \lambda & \sin \phi & \cos \phi \cos \lambda \end{bmatrix}$$

where

λ = longitude

ϕ = latitude

α = alpha angle

2.8.4 Geographic Frame to Navigation Frame, C_g^n

$$C_g^n = \begin{bmatrix} \cos \alpha & \sin \alpha & 0 \\ -\sin \alpha & \cos \alpha & 0 \\ 0 & 0 & 1 \end{bmatrix} \quad (2.6)$$

where

α = alpha angle

2.8.5 Geographic Frame to Body Frame, C_g^b

$$C_g^b = \begin{bmatrix} 1 & 0 & 0 \\ 0 & \cos \rho & \sin \rho \\ 0 & -\sin \rho & \cos \rho \end{bmatrix} \begin{bmatrix} \cos \theta & 0 & -\sin \theta \\ 0 & 1 & 0 \\ \sin \theta & 0 & \cos \theta \end{bmatrix} \begin{bmatrix} \cos \psi & \sin \psi & 0 \\ -\sin \psi & \cos \psi & 0 \\ 0 & 0 & 1 \end{bmatrix} \begin{bmatrix} 0 & 1 & 0 \\ 1 & 0 & 0 \\ 0 & 0 & -1 \end{bmatrix} \quad (2.7)$$

$$= \begin{bmatrix} \cos \theta \sin \psi & \cos \theta \cos \psi & \sin \theta \\ \sin \rho \sin \theta \sin \psi + \cos \rho \cos \psi & \sin \rho \sin \theta \cos \psi - \cos \rho \sin \psi & -\sin \rho \cos \theta \\ \cos \rho \sin \theta \sin \psi - \sin \rho \cos \psi & \cos \rho \sin \theta \cos \psi + \sin \rho \sin \psi & -\cos \rho \cos \theta \end{bmatrix}$$

where

ρ = roll

θ = pitch

ψ = geographic heading

2.8.6 Navigation Frame to Body Frame, C_n^b

$$\begin{aligned}
 C_n^b &= \begin{bmatrix} 1 & 0 & 0 \\ 0 & \cos\rho & \sin\rho \\ 0 & -\sin\rho & \cos\rho \end{bmatrix} \begin{bmatrix} \cos\theta & 0 & -\sin\theta \\ 0 & 1 & 0 \\ \sin\theta & 0 & \cos\theta \end{bmatrix} \begin{bmatrix} \cos\psi_P & \sin\psi_P & 0 \\ -\sin\psi_P & \cos\psi_P & 0 \\ 0 & 0 & 1 \end{bmatrix} \begin{bmatrix} 0 & 1 & 0 \\ 1 & 0 & 0 \\ 0 & 0 & -1 \end{bmatrix} \\
 &= \begin{bmatrix} \cos\theta\sin\psi_P & \cos\theta\cos\psi_P & \sin\theta \\ \sin\rho\sin\theta\sin\psi_P + \cos\rho\cos\psi_P & \sin\rho\sin\theta\cos\psi_P - \cos\rho\sin\psi_P & -\sin\rho\cos\theta \\ \cos\rho\sin\theta\sin\psi_P - \sin\rho\cos\psi_P & \cos\rho\sin\theta\cos\psi_P + \sin\rho\sin\psi_P & -\cos\rho\cos\theta \end{bmatrix} \quad (2.8)
 \end{aligned}$$

where

$$\begin{aligned}
 \rho &= \text{roll} \\
 \theta &= \text{pitch} \\
 \psi_P &= \text{platform heading}
 \end{aligned}$$

2.9 Kalman Filter Theory

2.9.1 What is a Kalman Filter?

A Kalman filter is simply an optimal recursive data processing algorithm [40] that can be shown to be optimal by essentially any standard, given the appropriateness of several underlying assumptions. These assumptions are that the system in question can be adequately modeled as linear with white, Gaussian system and measurement noises.

One aspect of the word "optimal" is that the Kalman filter can incorporate all information (measurements) provided to it [40]. It processes all available measurements regardless of their precision to "estimate" the current value of the variables of interest with use of (from [40]):

- Knowledge of the system and measurement device dynamics
- The statistical description of the system noises, measurement errors and uncertainty in the dynamics models.
- Any available information about inertial conditions of the variables of interest.

For example, to determine the velocity of an aircraft, one could use a Doppler radar, or the velocity indications from an inertial navigation system, or the pitot and static pressure and relative wind information in the air data system. Rather than ignore any of

these outputs, a Kalman filter could be built to combine all this data and knowledge of the various systems dynamics to generate an overall best estimate of velocity. Another way a Kalman filter is optimal is that it obtains the best estimate of desired quantities from data provided by a noisy environment. Here the word “optimal” means that the Kalman filter minimizes errors in essentially all respects, and it does so recursively. The word *recursive* means that, unlike certain data processing concepts, the Kalman filter doesn't require all previous data to be kept in storage and reprocessed every time new measurements are taken.

To “see” how a Kalman filter works, a simple example taken directly from [39] will be presented. It is included it here because it helped the author understand the concept of a Kalman Filter in his AFIT studies.

2.9.2 Kalman Filter Example

Suppose that you are lost at sea during the night and have no idea at all of your location. So you take a star sighting to establish your position (for the sake of simplicity, consider a one-dimensional location). At some time t_1 you determine your location to be z_1 . However, because of inherent measuring device inaccuracies, human error, and the like, the result of your measurement is somewhat uncertain. Say you decide that the precision is such that the standard deviation (one-sigma value) involved is σ_{z_1} (or

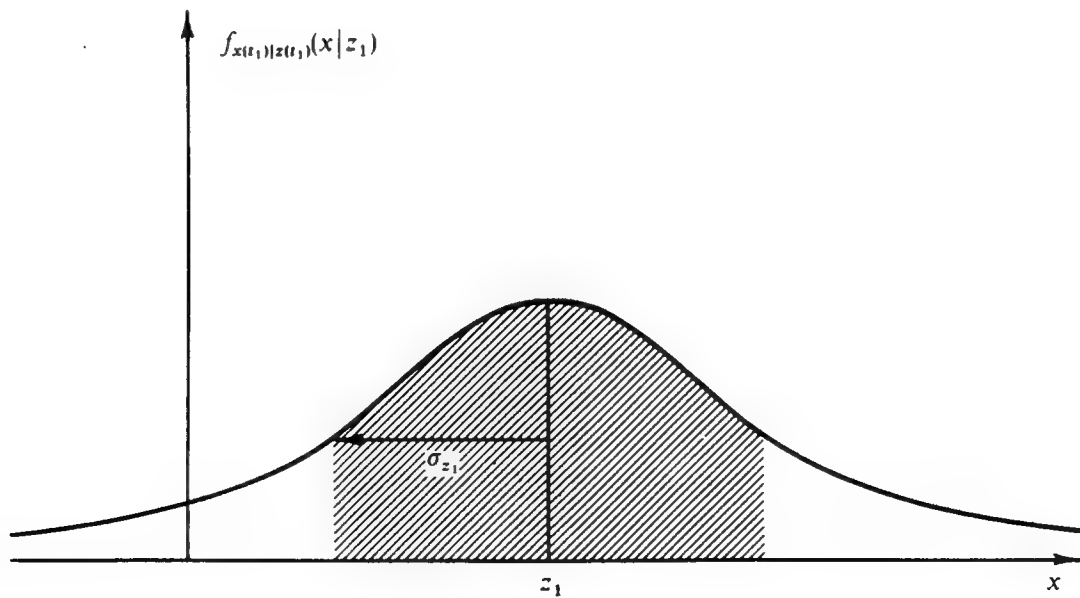


Figure 2 - 8. Conditional Density of Position Based on Measured Value z_1

equivalently, the variance, or second order central statistic, is $\sigma_{z_1}^2$). Thus, you can establish the conditional probability of $x(t_1)$, your position at time t_1 , conditioned on the observed value of the measurement being z_1 , as depicted in Figure 2 - 8. This is a plot of $f_{x(t_1)|z(t_1)}(x|z_1)$ as a function of the location x : it tells you the probability of being in any one location, based upon the measurement you took. Note that σ_{z_1} is a direct measure of the uncertainty: the larger σ_{z_1} is, the broader the probability peak is, spreading the probability "weight" over a larger range of x values. For a Gaussian density, 68.3% of the probability "weight" is contained within the band σ units to each side of the mean, the shaded portion in Figure 2 - 8.

Based this conditional probability density, the best estimate of your position is

$$\hat{x}(t_1) = z_1 \quad (2.9)$$

and the variance of the error in the estimate is

$$\sigma_x^2(t_1) = \sigma_{z_1}^2 \quad (2.10)$$

Note that \hat{x} is both the mode (value that locates the peak) and the median (value with 1/2 of the probability weight to each side), as well as the mean (center-of-mass).

Now say a trained navigator friend takes an independent fix right after you do, at time $t_2 \equiv t_1$ (so that the true position has not changed at all), and obtains a measurement z_2 with a variance $\sigma_{z_2}^2$. Because he has a higher skill, assume the variance in his measurement to be somewhat smaller than in yours. Figure 2 - 9 presents the conditional density of your position at time t_2 , based only on the measured value z_2 . Note the narrower peak due to smaller variance, indicating that you are rather certain of your position based on his measurement.

At this point, you have two measurements available for estimating your position. The question is, how do you combine these data? It can be shown that, based on the assumptions made, the conditional density of your position at $t_2 \equiv t_1$, $x(t_2)$ given *both* z_1 and z_2 , is a Gaussian density with mean μ and variance σ^2 as indicated in Figure 2 - 10 with

$$\mu = \left[\frac{\sigma_{z_2}^2}{\sigma_{z_1}^2 + \sigma_{z_2}^2} \right] z_1 + \left[\frac{\sigma_{z_1}^2}{\sigma_{z_1}^2 + \sigma_{z_2}^2} \right] z_2 \quad (2.11)$$

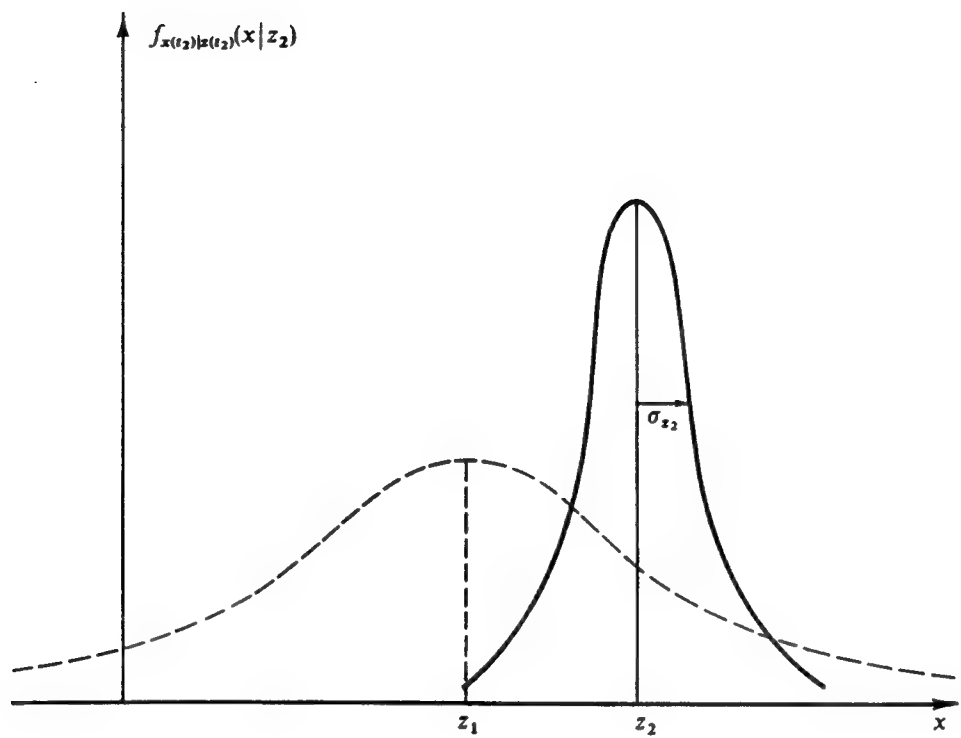


Figure 2 - 9. Conditional Density of Position Based on Measurement z_2 Alone

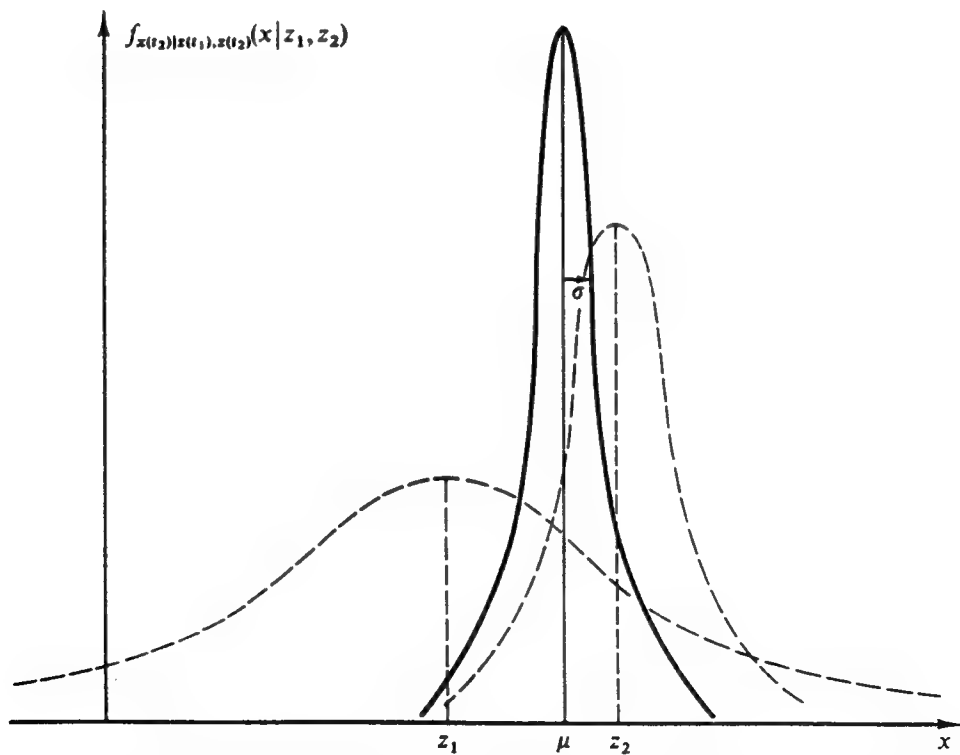


Figure 2 - 10. Conditional density of position based on data z_1 and z_2

$$\frac{1}{\sigma^2} = \frac{1}{\sigma_{z_1}^2} + \frac{1}{\sigma_{z_2}^2} \quad (2.12)$$

Note that, from (2.12), σ is less than either σ_{z_1} or σ_{z_2} , which is to say that the uncertainty in your estimate of position has been decreased by combining the two pieces of information.

Given this density, the best estimate is

$$\hat{x}(t_2) = \mu \quad (2.13)$$

with an associated error variance σ^2 . It is the mode, the median and the mean (or, since it is the mean of a conditional density, it is also termed the conditional mean). Furthermore, it is also the maximum likelihood estimate, the weighted least squares estimate, and the linear unbiased estimate whose variance is less than that of any other linear unbiased estimate. In other words, it is the "best" you can do according to just about any reasonable criterion.

After some study, the form of μ given in (2.11) makes good sense. If σ_{z_1} were equal to σ_{z_2} , which is to say you think the measurements are of equal precision, the equation says the optimal estimate of position is simply the average of the two measurements, as would be expected. On the other hand, if σ_{z_1} were larger than σ_{z_2} , which is to say that the uncertainty involved in the measurement z_1 is greater than that of z_2 , then the equation dictates "weighting" z_2 more heavily than z_1 . Finally, the variances of the estimate is less than σ_{z_1} even if σ_{z_2} is very large: even poor quality data provides some information, and should thus increase the precision of the filter output.

The equation for $\hat{x}(t_2)$ can be rewritten as

$$\hat{x}(t_2) = \left[\frac{\sigma_{z_2}^2}{\sigma_{z_1}^2 + \sigma_{z_2}^2} \right] z_1 + \left[\frac{\sigma_{z_1}^2}{\sigma_{z_1}^2 + \sigma_{z_2}^2} \right] z_2 \quad (2.14)$$

or

$$\hat{x}(t_2) = z_1 + \left[\frac{\sigma_{z_1}^2}{\sigma_{z_1}^2 + \sigma_{z_2}^2} \right] [z_2 - z_1] \quad (2.15)$$

or, in final form that is actually used Kalman filter implementations (noting that $\hat{x}(t_1) = z_1$),

$$\hat{x}(t_2) = \hat{x}(t_1) + K(t_2)[z_2 - \hat{x}(t_1)] \quad (2.16)$$

where

$$K(t_2) = \frac{\sigma_{z_1}^2}{\sigma_{z_1}^2 + \sigma_{z_2}^2} \quad (2.17)$$

These equations say the optimal estimate at t_2 , $\hat{x}(t_2)$, is equal to the best prediction of its value before z_2 is taken, $\hat{x}(t_1)$, plus a correction term of an optimal weighting value times the residual difference between z_2 and the best prediction of its value before it is actually taken, $\hat{x}(t_1)$. It is worthwhile to understand this "predictor-corrector" structure of the filter. Based on all previous information, a prediction of the value that the desired variables and measurement will have at the next measurement time is made. Then, when the next measurement is taken, the difference between it and its predicted value is used to "correct" the prediction of the desired variables.

Using the $K(t_2)$ in Equation (2.17), the variance equation given by (2.12) can be rewritten as

$$\sigma_x^2(t_2) = \sigma_x^2(t_1) - K(t_2)\sigma_x^2(t_1) \quad (2.18)$$

Note that the values of $\hat{x}(t_2)$ and $\sigma_{x_2}^2(t_2)$ embody all the information in $f_{x(t_2)|z(t_1), z(t_2)}(x|z_1, z_2)$. Stated differently, by propagating these two variables, the conditional density of your position at time t_2 , given z_1 and z_2 , is completely specified.

Thus we have solved the (static) estimation problem example from [40]. This will be of vital importance to the practicality of filter implementation. The filter is plain and simple, "just a computer program in a central processor" [40]. If the reader needs a further example detailing dynamics and propagations, see [40].

2.9.3 Linear Kalman Filter:

Whenever possible, a system will be modeled as a set of linear differential equations of the form [40]:

$$\dot{\mathbf{x}}(t) = \mathbf{F}(t)\mathbf{x}(t) + \mathbf{B}(t)\mathbf{u}(t) + \mathbf{G}(t)\mathbf{w}(t) \quad (2.19)$$

where:

\mathbf{x} = "state" vector (n-dimensional)

- F** = homogenous state dynamics matrix ($n \times n$)
- B** = control input matrix ($n \times r$)
- u** = deterministic control input vector (r -dimensional)
- G** = driving noise input matrix ($n \times s$)
- w** = white Gaussian driving noise vector (s -dimensional)

Because the deterministic control term $\mathbf{B}(t)\mathbf{u}(t)$ is zero in this research, it will be ignored hereafter. The expected value (i.e. *mean*), of the white Gaussian driving noise vector, $\mathbf{w}(t)$ is:

$$E\{\mathbf{w}(t)\} = \mathbf{0} \quad (2.20)$$

and the noise strength is $\mathbf{Q}(t)$:

$$E\{\mathbf{w}(t)\mathbf{w}^T(t + \tau)\} = \mathbf{Q}(t)\delta(\tau) \quad (2.21)$$

where $\delta(\cdot)$ is the Dirac delta function.

While Equation (2.19) is written in terms of "whole" value state variables, the models used in the thesis are those of *error* states. This choice of state variable results in simpler dynamics equations [9], and (2.19) may be rewritten as [40]:

$$\dot{\delta\mathbf{x}}(t) = \mathbf{F}(t)\delta\mathbf{x}(t) + \mathbf{B}(t)\mathbf{u}(t) + \mathbf{G}(t)\mathbf{w}(t) \quad (2.22)$$

where $\mathbf{x}(t)$ has been replaced by the error state vector $\delta\mathbf{x}(t)$, and all other quantities retain their previous definitions. The topic of error states is explored more fully in the section on extended Kalman filters.

As previously stated, the Kalman filter incorporates sampled-data measurement information from external measuring devices. Irrespective of the type of measuring device, the equation which is used to describe linear measurements is of the form [3]:

$$\mathbf{z}(t_i) = \mathbf{H}(t_i)\mathbf{x}(t_i) + \mathbf{v}(t_i) \quad (2.23)$$

or, in the case of error-state models:

$$\dot{\mathbf{z}}(t_i) = \mathbf{H}(t_i)\dot{\delta\mathbf{x}}(t_i) + \mathbf{v}(t_i) \quad (2.24)$$

where, in both cases above, \mathbf{H} is the *observation* matrix, and \mathbf{v} is a discrete-time zero-mean white Gaussian measurement noise vector with covariance given by [40]:

$$E\{\mathbf{v}(t_i)\mathbf{v}^T(t_j)\} = \begin{cases} \mathbf{R}(t_i) & \text{for } t_i = t_j \\ \mathbf{0} & \text{for } t_i \neq t_j \end{cases} \quad (2.25)$$

The Kalman filter "propagates" the error state and its covariance from the instant in time immediately following the most recent measurement update, t_i^+ , to the instant in time immediately preceding the next measurement update, t_{i+1}^- , by numerical integration of the following equations [40]:

$$\dot{\hat{\mathbf{x}}}(t / t_i) = \mathbf{F}(t)\hat{\mathbf{x}}(t / t_i) \quad (2.26)$$

$$\dot{\mathbf{P}}(t / t_i) = \mathbf{F}(t)\mathbf{P}(t / t_i) + \mathbf{P}(t / t_i)\mathbf{F}^T(t) + \mathbf{G}(t)\mathbf{Q}(t)\mathbf{G}^T(t) \quad (2.27)$$

The notation for $\hat{\mathbf{x}}(t / t_i)$ and associated error covariance $\mathbf{P}(t / t_i)$ indicate the best estimate of \mathbf{x} and \mathbf{P} at time t , based on measurements through time t_i . Initial conditions are given as

$$\hat{\mathbf{x}}(t_i / t_i) = \hat{\mathbf{x}}(t_i^+) \quad (2.28)$$

$$\mathbf{P}(t_i / t_i) = \mathbf{P}(t_i^+) \quad (2.29)$$

as provided by the measurement update cycle at time t_i . The variables t_i and t_{i+1} indicate the initial and final times for each integration period, respectively.

After propagation, $\hat{\mathbf{x}}(t_{i+1} / t_i) = \hat{\mathbf{x}}(t_{i+1}^-)$ and $\mathbf{P}(t_{i+1} / t_i) = \mathbf{P}(t_{i+1}^-)$ are "updated" (meaning that state estimates are revised, based on new measurement information). The pivotal element in the update equations for sample time t_i shown below is the time-varying Kalman filter gain $\mathbf{K}(t_i)$. The $\mathbf{K}(t_i)$ matrix assigns "weights" to the "measurement residual" (the residual consists of the *difference* between the actual measurement and the filter's prediction of the measurement) based on known measurement noise statistics and filter-computed state error covariance from the previous time step. This process is designed to improve the estimate of each element of the state vector. The update equations are [40]:

$$\mathbf{K}(t_i) = \mathbf{P}(t_i^-)\mathbf{H}^T(t_i)\{\mathbf{H}(t_i)\mathbf{P}(t_i^-)\mathbf{H}^T(t_i) + \mathbf{R}(t_i)\}^{-1} \quad (2.30)$$

$$\hat{\mathbf{x}}(t_i^+) = \hat{\mathbf{x}}(t_i^-) + \mathbf{K}(t_i)\{\mathbf{z}_i - \mathbf{H}(t_i)\hat{\mathbf{x}}(t_i)\} \quad (2.31)$$

$$\mathbf{P}(t_i^+) = \mathbf{P}(t_i^-) - \mathbf{K}(t_i)\mathbf{H}(t_i)\mathbf{P}(t_i^-) \quad (2.32)$$

Although the algorithm shown above is generally applicable to any problem which lends itself to a Kalman filtering solution, it is not necessarily the algorithm which is used in practice. It is often advantageous to use a form of the algorithm known as the *U-D* factorization form [40]. In the *U-D* algorithm, the filter covariance matrix is not propagated as a single square array. The **U** and **D** matrices below representing the pre- and post-measurement filter covariances, respectively, are explicitly computed instead [40]:

$$\mathbf{P}(t_i^-) = \mathbf{U}(t_i^-)\mathbf{D}(t_i^-)\mathbf{U}(t_i^-)^T \quad (2.33)$$

$$\mathbf{P}(t_i^+) = \mathbf{U}(t_i^+)\mathbf{D}(t_i^+)\mathbf{U}(t_i^+)^T \quad (2.34)$$

where the **U** matrices are upper triangular and unitary (and thus contain ones along the main diagonal), and the **D** matrices are simply diagonal [40]. This form offers several advantages including numerical stability, improved precision, and guaranteed non-negativity of the computed covariance's eigenvalues [40]. It is the *U-D* form of the Kalman filter algorithm which is implemented in the MSOFE software [48] that is used in this research.

2.9.4 Linearized and Extended Kalman Filtering

Unfortunately, not all problems are adequately described with linear systems driven by white Gaussian noise. In many cases, the most appropriate model is nonlinear. The navigation problem at hand falls squarely into the nonlinear category. Fortunately, a method exists whereby a nonlinear system may be treated in much the same manner as a linear one for a particular class of problems. Suppose that the nonlinear system may be described by [41]:

$$\dot{\mathbf{x}}(t) = \mathbf{f}[\mathbf{x}(t), \mathbf{u}(t), t] + \mathbf{G}(t)\mathbf{w}(t) \quad (2.35)$$

In this case, the state dynamics vector, $\mathbf{f}[\cdot, \cdot, \cdot]$, is a nonlinear function of the state vector $\mathbf{x}(\cdot)$, time t , and the control input (assumed to be zero in this research). The white Gaussian noise is defined exactly as in (2.20) and (2.21), and it still enters the dynamics model linearly. In addition, the measurement equation may also be a nonlinear function of the state vector and time [41]:

$$\mathbf{z}(t_i) = \mathbf{h}[\mathbf{x}(t_i), t_i] + \mathbf{v}(t_i) \quad (2.36)$$

The noise vector \mathbf{v} is again *zero-mean*, white and Gaussian, entering the measurement equation linearly, and its covariance is described by (2.25).

Recalling that a system must be linear in order to satisfy the assumptions upon which a conventional Kalman filter is based, the nonlinear equations (2.35) and (2.36) must be linearized. The following approach is summarized from [41]:

1. Assume that a nominal state trajectory, $\mathbf{x}_n(t)$, may be generated which satisfies

$$\mathbf{x}_n(t_0) = \mathbf{x}_{n_0} \quad (2.37)$$

and

$$\dot{\mathbf{x}}_n(t) = \mathbf{f}[\mathbf{x}_n(t), \mathbf{u}(t), t] \quad (2.38)$$

where $\mathbf{f}[\cdot, \cdot, \cdot]$ is specified in (2.35), and $\mathbf{u}(t)=\mathbf{0}$.

2. The “nominal” measurements which accompany the nominal trajectory are:

$$\mathbf{z}_n(t_i) = \mathbf{h}[\mathbf{x}_n(t_i), t_i] \quad (2.39)$$

3. The “perturbation” of the state derivative is obtained by subtracting the nominal trajectory from the original nonlinear equation:

$$[\dot{\mathbf{x}}(t) - \dot{\mathbf{x}}_n(t)] = \mathbf{f}[\mathbf{x}(t), \mathbf{u}(t), t] - \mathbf{f}[\mathbf{x}_n(t), \mathbf{u}(t), t] + \mathbf{G}(t)\mathbf{w}(t) \quad (2.40)$$

4. The equation above may be approximated to first order by a Taylor series expansion:

$$\delta\dot{\mathbf{x}}(t) = \mathbf{F}[t; \mathbf{x}_n(t)]\delta\mathbf{x}(t) + \mathbf{G}(t)\mathbf{w}(t) \quad (2.41)$$

where $\delta\mathbf{x}(\cdot)$ represents a first-order approximation of the process $[\mathbf{x}(\cdot) - \mathbf{x}_n(\cdot)]$, and $\mathbf{F}[t; \mathbf{x}_n(t)]$ is a matrix of partial derivatives of \mathbf{f} with respect to its first argument, evaluated along the nominal trajectory [41]:

$$\mathbf{F}[t; \mathbf{x}_n(t)] = \left. \frac{\partial \mathbf{f}[\mathbf{x}, t]}{\partial \mathbf{x}} \right|_{\mathbf{x} = \mathbf{x}_n(t)} \quad (2.42)$$

5. The perturbation measurement equation is derived in like fashion and is expressed as [41]:

$$\delta\mathbf{z}(t_i) = \mathbf{H}[t_i; \mathbf{x}_n(t_i)]\delta\mathbf{x}(t) + \mathbf{v}(t_i) \quad (2.43)$$

where

$$\mathbf{H}[t_i; \mathbf{x}_n(t_i)] = \frac{\partial \mathbf{h}[\mathbf{x}, t_i]}{\partial \mathbf{x}} \Big|_{\mathbf{x} = \mathbf{x}_n(t_i)} \quad (2.44)$$

With the “error-state” model in hand, it is possible to return to the linear filtering theory. An estimate of the whole-valued quantities of interest is obtained from [41]:

$$\hat{\mathbf{x}} = \mathbf{x}_n(t) + \delta \hat{\mathbf{x}}(t) \quad (2.45)$$

The expression above for the linearized Kalman filter is useful, provided that the linearization assumption is not violated. However, if the nominal and “true” trajectories differ by too large an amount, unacceptable errors may result [41]. It is for this reason that extended Kalman filtering is useful in many cases for which perturbation techniques alone do not suffice. Extended Kalman filtering allows for *relinearizing* about newly declared nominals at each sample time, to enhance the adequacy of the linearization process, and thus of the resulting filter performance as well [41].

The extended Kalman filter equations are summarized below. The reader is referred to [41] for details regarding their derivation. The assumed measurement model equation for an extended Kalman filter development is given by Equation (2.36), where $\mathbf{v}(\cdot)$ is once again *zero-mean*, white and Gaussian, with covariance given by (2.25). Measurements are incorporated into the extended Kalman filter via the following set of equations [41]:

$$\mathbf{K}(t_i) = \mathbf{P}(t_i^-) \mathbf{H}^T[t_i; \hat{\mathbf{x}}(t_i^-)] \{ \mathbf{H}[t_i; \hat{\mathbf{x}}(t_i^-)] \mathbf{P}(t_i^-) \mathbf{H}^T[t_i; \hat{\mathbf{x}}(t_i^-)] + \mathbf{R}(t_i) \}^{-1} \quad (2.46)$$

$$\hat{\mathbf{x}}(t_i^+) = \hat{\mathbf{x}}(t_i^-) + \mathbf{K}(t_i) \{ \mathbf{z}_i - \mathbf{h}[\hat{\mathbf{x}}(t_i^-); t_i] \} \quad (2.47)$$

$$\mathbf{P}(t_i^+) = \mathbf{P}(t_i^-) - \mathbf{K}(t_i) \mathbf{H}[t_i; \hat{\mathbf{x}}(t_i^-)] \mathbf{P}(t_i^-) \quad (2.48)$$

where

$$\mathbf{H}[t_i; \hat{\mathbf{x}}(t_i^-)] = \frac{\partial \mathbf{h}[\mathbf{x}, t_i]}{\partial \mathbf{x}} \Big|_{\mathbf{x} = \hat{\mathbf{x}}(t_i^-)} \quad (2.49)$$

The state estimate and covariance are propagated from t_i to t_{i+1} by integrating the following equations [41]:

$$\dot{\hat{\mathbf{x}}}(t / t_i) = \mathbf{f}[\hat{\mathbf{x}}(t / t_i), \mathbf{u}(t), t] \quad (2.50)$$

$$\dot{\mathbf{P}}(t / t_i) = \mathbf{F}[t; \hat{\mathbf{x}}(t / t_i)]\mathbf{P}(t / t_i) + \mathbf{P}(t / t_i)\mathbf{F}^T[t; \hat{\mathbf{x}}(t / t_i)] + \mathbf{G}(t)\mathbf{Q}(t)\mathbf{G}^T(t) \quad (2.51)$$

where

$$\mathbf{F}[t; \hat{\mathbf{x}}(t / t_i)] = \frac{\partial \mathbf{f}[\mathbf{x}(t), t]}{\partial \mathbf{x}} \Big|_{\mathbf{x} = \hat{\mathbf{x}}(t / t_i)} \quad (2.52)$$

and the initial conditions are:

$$\hat{\mathbf{x}}(t_i / t_i) = \hat{\mathbf{x}}(t_i^+) \quad (2.53)$$

$$\mathbf{P}(t_i / t_i) = \mathbf{P}(t_i^+) \quad (2.54)$$

The equations shown above for the extended Kalman filter are programmed into the MSOFE shell [48] for the problem defined by this thesis. It is the fact that the extended Kalman filter is relinearized about each successive estimate of the state $\hat{\mathbf{x}}(t)$ which “enhances the validity of the assumption that deviations from the reference (nominal) trajectory are small enough to allow linear perturbation techniques to be employed” [41].

2.10 Summary

This chapter has presented the basic theory of RLG INS, GPS, and barometric altimeter and radar altimeters. ILS precision approach has also been defined. Reference frames and coordinate transformations used in this thesis have also been defined, as well as describing the Kalman filter by an example from [40] and noting linear, linearized and extended Kalman filter fundamentals. Chapter 3 will describe the design methodology and error models of the RLG INS, GPS, barometric altimeter and radar altimeter avionics used in this thesis for MSOFE simulations.

III. Design Methodology and Error Models

This chapter describes the set-up of the MSOFE computer simulation for the Landing System Model (LSM) error model. This chapter also describes the technique used to determine which “real-world” (*true*) satellite vehicle (SV) ephemeris data was used during MSOFE simulation. A brief description of the use of PROFGEN [47] to generate a transport flight profile will also be discussed.

3.1 Introduction to MSOFE

The name "MSOFE" is an acronym meaning "Multimode Simulation for Optimal Filter Evaluation." MSOFE is a general-purpose, multimode simulation program for designing integrated systems that employ optimal (Kalman) filtering techniques and for evaluating their performance [48]. Its general-purpose construction allows specific user problems to be simulated more quickly and at less cost than without its use. MSOFE has been designed to support a wide variety of system simulation and filter evaluation efforts. It provides two major operating modes:

- 1) Monte Carlo simulation: to generate multiple sample time histories of system truth states, filter states, and filter estimation errors, including nonlinear effects; usable for linear and extended Kalman filters;
- 2) Covariance simulation: to generate time histories of the second-order statistics (covariances) of system truth states, filter states, and filter estimation errors, under the assumption of linear (or linearized) models.

The Monte Carlo and covariance simulation modes of MSOFE are complementary to one another. The covariance mode can generate filter performance statistics via a single run, whereas the Monte Carlo mode requires several sample runs (say, 15 or more) to generate meaningful statistics for a given scenario. However, the covariance mode is limited to linear (or linearized) systems, whereas the Monte Carlo mode can represent nonlinear as well as linear dynamic and measurement processes. In addition, the Monte Carlo mode provides better visibility into the detailed workings of the filter models and computation processes, and can easily be reduced to a deterministic mode (by suppressing noise sampling) when required. Monte Carlo runs (15 runs) were solely performed in this thesis for each case unless otherwise noted.

MSOFE provides a general-purpose simulation environment in which the user embeds a specific problem by supplying up to 14 problem-specific subroutines. The collective set of 14 user routines is named USOFE. The name MSOFE generally references the whole program, that is the union of 63 nonvarying routines in the CSOFE "core part" with the 14 routines in the USOFE "user part". From one problem to the next, the 14 routines of USOFE vary greatly, whereas the 63 routines of CSOFE vary only in the sizes assigned to the vectors and arrays. With MSOFE, users can quickly apply their engineering skills to important filter design issues, rather than to the time-consuming development of support tools [48].

The multimode simulation program MSOFE is part of an existing set of tools developed by [48] to support the design, analysis, and evaluation of a wide variety of integrated systems. Other tools that were used in this thesis were:

- PROFGEN -- a trajectory generator for simulating the translational and rotational dynamics of an aircraft in flight [47].
- MPLOT -- a postprocessor program for satisfying the plotting needs of both MSOFE and PROFGEN, e.g. for computing ensemble statistics from Monte Carlo runs [63].

3.1.1 MSOFE Computer Requirements

MSOFE is written in ANSI standard FORTRAN 77 to provide full portability across a wide variety of computers and compilers. MSOFE was run on a 486 PC and also on a SPARC 10 UNIX machine for this thesis. MSOFE is fully compliant with the ANSI standard except for the way it manages global common blocks. These blocks, which are constructed in the form of individual files, one file per block, are inserted in the code at designated locations. This is called an "INCLUDE" approach, borrowing this name from FORTRAN 90, where this ability is an integral part of that standard. The INCLUDE ability automates common block array sizing and aids program maintenance. It can be easily eliminated or modified for non-supporting computers. This exception to ANSI compliance was permitted because of its usefulness and its wide availability as an extension to most FORTRAN implementations.

The principal system requirements necessary to run MSOFE on a given computer are:

- FORTRAN-77 compiler and linker;
- Ten input/output files open concurrently;

- Program and data memory to load the entire program at one time (it is not overlaid): approximately 200,000 words;
- Output data storage of approximately 40 (Mb) *per hour* in Monte Carlo mode was not uncommon during simulations of this thesis (15 Monte Carlo runs).

MSOFE allows models of any size, limited only by the amount of computer memory available and perhaps by array-size restrictions present in the FORTRAN compiler. There are no size restrictions whatsoever within the core code.

In order for the reader to see the "Big-MSOFE-Picture", Figure 3 - 1 and Figure 3 - 2 (later in Section 3.4) illustrate the overall goal: GPS and radar altimeter measurement information must be fed into an extended Kalman filter to determine the errors, δx , in the INS. As stated earlier, our extended Kalman filter *estimates* the true error, δx , of the INS with an output we note as " $\delta \hat{x}$ ". Once the best estimates, $\delta \hat{x}$, are determined by our extended Kalman filter, we then subtract them (in a feed-forward approach) from the output of the simulated INS blackbox. The feedforward approach is utilized in this thesis due to current Federal Aviation Administration (FAA) restrictions on providing "feedback" to the INS. Without going into a lengthy technical discussion about the differences between feedforward or feedback, feedforward was chosen because it is the most conservative choice, especially if one does not have faith that the extended Kalman filter feedback corrections will always be reliable. The authors belief is that, at the present time, the FAA does not want to "lose" the "pure" INS output during precision approaches. Because of this FAA requirement, a feedforward approach will be utilized in this thesis.

3.2 *Introduction to PROFGEN*

PROFGEN computes position, velocity, acceleration, attitude and attitude rate for an aircraft moving over the earth [47]. Position is given as (geographic) latitude, longitude and altitude. Velocity with respect to earth is coordinatized and presented in a local-vertical frame. Acceleration consists of velocity rates-of-change summed with Coriolis effects and gravity. Attitude consists of roll, pitch and yaw: the Euler angles. [47].

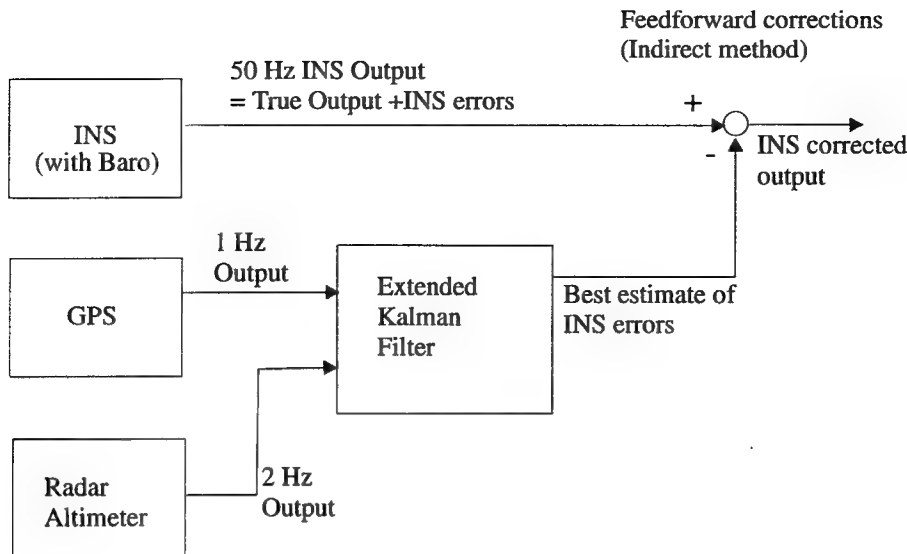


Figure 3 - 1. Overall Landing System Model (LSM) Description

PROFGEN models a point mass responding to maneuver commands specified by the user. These maneuvers are available:

- vertical turns (pitch up or down)
- horizontal turns (yaw left or right)
- sinusoidal "jink" heading changes (oscillates left and right)
- straight flights (great circle or rhumb line path)

PROFGEN is used to create an extended flight profile by concatenating a sequence of maneuvers chosen from the basic four. The user specifies how long each maneuver shall last and thereby divides the flight profile into flight segments [47]. Up to fifty flight segments, may be strung together to produce a varied total profile. The final values of the variables in each segment are passed along as the initial values for the start of the next segment thereby creating uninterrupted time histories for all output variables. The segments for the "Tanker" flight profile used in this thesis are shown in Table 3 - 1. The earth is modeled as a perfect ellipsoid having values for eccentricity, semimajor axis length, spin velocity and gravitational constant equal to those of the DOD World Geodetic System 1972 [47].

A PROF_IN file (PROF_IN is the input file for PROFGEN [47]) was created for a Boeing 707 (KC-135) aircraft based on inputs from [4,59,46]. The actual PROF_IN file used with PROFGEN can be found in Appendix C.

PROFGEN reads in PROF_IN, and outputs a binary flight file called "FLIGHT". FLIGHT contains the flight profile variables shown in Table 3 - 2. Looking at Table 3 - 2 may seem cryptic, but note in the far right column labeled "WRITTEN TO FLIGHT" are the parameters written to the Tanker profile ("FLIGHT") which are followed by the word "YES"; otherwise the parameters are neither computed nor written to the Tanker "FLIGHT" file.

3.3 *The LSM Computer Model*

The LSM computer model was derived directly from the NRS model [45]. Only the LSM will be discussed in detail in this thesis. For more information on the NRS model, see [45]. The computer modeling of the LSM is divided into two portions, the truth model and the filter model. The truth model represents computer-generated simulation of error characteristics of avionics "black-boxes" and environment, that would normally be found in the real world. Because the information and data presented in this thesis was accomplished entirely through computer simulation, the truth model will simulate the errors in true avionics hardware (INS, GPS, Baro, Radar Altimeter) black-boxes. The truth model generates the measurement updates for the LSM filter, the true flight profile of the aircraft and a state variable baseline for evaluating filter performance [45]. The truth model consists of 69 error states about their nominal values. The filter model represents the LSM in its functional form, which is the basis of the filter which could be hosted on-board an aircraft computer. The LSM filter model is a 13-state extended Kalman filter that has been developed through order reduction of the 95-state truth model of [45]. The author's approach was to begin the filter state building using the fewest possible states that would meet precision approach landing requirements. The 13-state LSM was chosen as a first-cut model. An advantage of using only 13 states is that it is not over-burdening to current state-of-the-art aircraft host computers, keeping practicality and dollar affordability in mind. At the completion of this thesis, a determination will be made as to the "usefulness" of the 13-state filter. The tradeoffs involved in using additional error-states to increase performance will be discussed in Chapter 5.

Segment Number	Start Time (sec)	Segment Length (sec)	Nominal Path	Centrifugal Accel (max in g's)	Accel along Velocity vector	ΔRoll (deg)	ΔPitch (deg)	ΔHeading (deg)
1	0	3	STRT	0	0	0	0	0
2	3	30	STRT	0	0.262	0	0	0
3	33	160	VERT	0.21	3.80E-02	0	5	0
4	193	329	STRT	0	1.00E-02	0	0	0
5	522	5	VERT	0.9	-8.75E-02	0	-5	0
6	527	25	HORZ	0.9	1.00E-02	0	0	45
7	552	371	STRT	0	1.00E-02	0	0	0
8	923	35	HORZ	0.9	0	1	0	45
9	958	400	STRT	0	8.00E-03	0	0	0
10	1358	35	HORZ	0.9	0	1	0	45
11	1393	340	STRT	0	0	0	0	0
12	1733	35	HORZ	0.9	0	0	0	45
13	1768	600	JINK	3.41E-02	0	0	200 (sec) for JINK	2
14	2368	35	HORZ	0.9	0	0		45
15	2403	120	VERT	0.311	0	0	-5	0
16	2523	35	VERT	0.9	0	0	5	0
17	2558	372	STRT	0	3.00E-03	0	0	0
18	2930	70	HORZ	0.9	-0.125	0	0	90
19	3000	40	VERT	0.63	-8.50E-02	0	-5	0
20	3040	35	VERT	0.9	0	0	5	0
21	3075	360	VERT	0.9	1.50E-02	0	-1.75	0
22	3435	45	HORZ	0.9	-5.00E-02	1	0	-45
23	3480	104	VERT	0.9	0	0	1.75	0
24	3584	35	HORZ	0.9	-5.00E-02	1	0	45
25	3619	39	VERT	0.24	-0.1882	0	-3	0
26	3658	25	HORZ	0.9	0	0	0	45
27	3683	242	STRT	0	0	0	0	0

Table 3 - 1. PROFGEN Segments for "Tanker" Flight Profile

VARIABLE	DIM	PRINTED NAME(s)	PRINTED TO PROF_OUT	WRITTEN TO FLIGHT
0 time	1	TIME	YES	YES
1 terrestrial longitude	1	TLON	YES	YES
2 geographic latitude	1	GLAT	YES	YES
3 altitude	1	ALT	YES	YES
4 celestial longitude	1	CLON		
5 wander angle	1	ALPHA	YES	YES
6 heading	1	HEAD		
7 roll	1	ROLL	YES	YES
8 pitch	1	PITCH	YES	YES
9 yaw	1	YAW	YES	YES
10 terrestrial longitude rate	1	DTLON		
11 geographic latitude rate	1	DGLAT		
12 altitude rate	1	DALT		
13 celestial longitude rate	1	DCLON		
14 wander angle rate	1	DALPHA	YES	YES
15 heading rate	1	DHEAD		
16 roll rate	1	DROLL	YES	YES
17 pitch rate	1	DPITCH	YES	YES
18 yaw rate	1	DYAW	YES	YES
19 signed earth velocity magnitude	1	VET		
20 signed earth velocity magnitude rate	1	DVET		
21 position in frame i (2) (3)	3	RI		
22 earth velocity in frame i	3	VEI		
23 inertial velocity in frame i (4)	3	VII		
24 gravitation in frame i	3	GNI		
25 specific force in frame i (5)	3	FII		
26 angular rate, b/i in frame i	3	WBII		
27 DCM to inertial from body	3X3	CIB		
28 DCM to inertial from earth (6)	3X3	CIE		
29 angular rate, e/i in frame e	3	WEIE		
30 position in frame e	3	RE		
31 earth velocity in frame e	3	VEE		
32 inertial velocity in frame e	3	VIE		
33 gravity in frame e	3	GYE		
34 specific force in frame e	3	FIE		
35 angular rate, b/e in frame e	3	WBIE		
36 DCM to earth from body	3X3	CEB		
37 DCM to earth from nav	3X3	CEN		
38 angular rate, n/e in frame n	3	WNEN		
39 position in frame n	3	RN		
40 earth velocity in frame n	3	VEN	YES	YES
41 inertial velocity in frame n	3	VIN		
42 gravity in frame n	3	GYN		
43 specific force in frame n	3	FIN	YES	YES
44 angular rate, b/n in frame n	3	WBIN		
45 DCM to nav from body	3X3	CNB		
46 angular rate, b/n in frame b	3	WBNB		
47 position in frame b	3	RB		
48 earth velocity in frame b	3	VEB		
49 inertial velocity in frame b	3	VIB		
50 gravity in frame b	3	GYB		
51 specific force in frame b	3	FIB		
52 angular rate, b/b in frame b	3	WBIB		

Table 3 - 2. PROFGEN Flight Profile Outputs

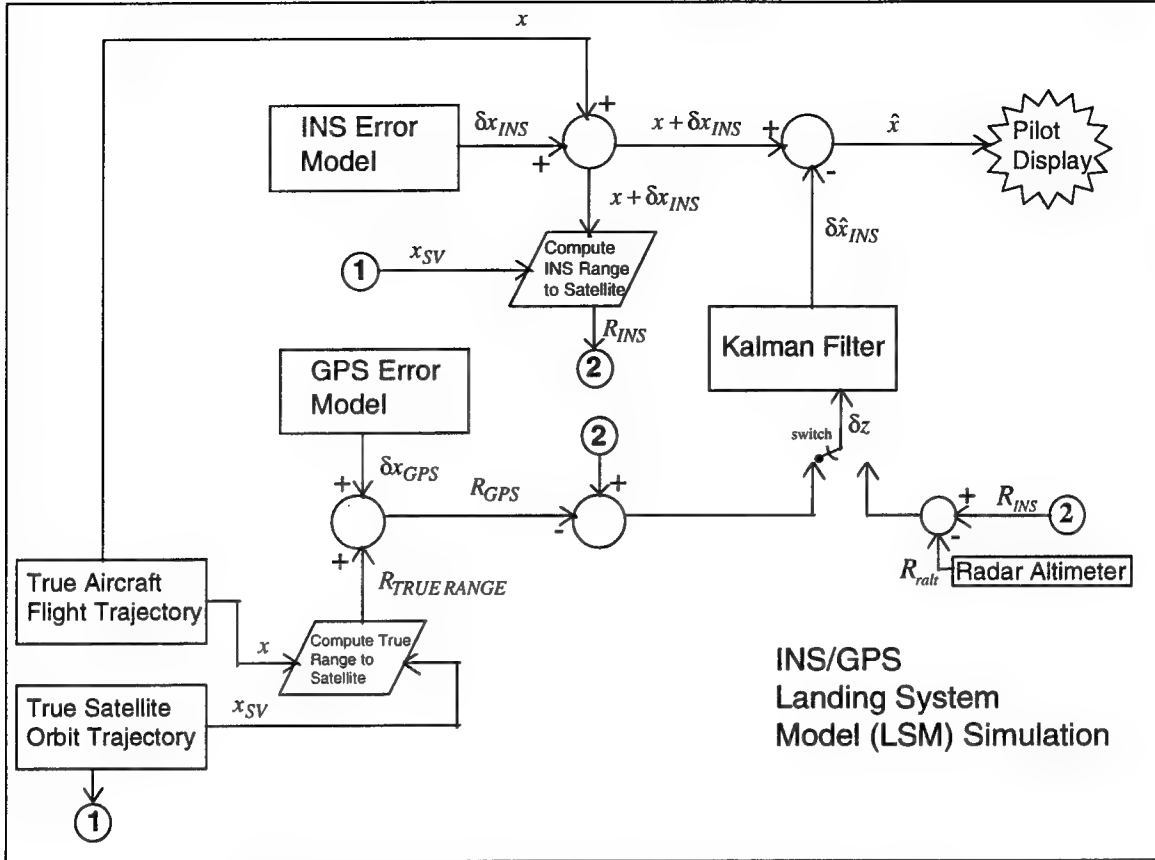


Figure 3 - 2. Truth and Filter Model Block Diagram

The block diagram, Figure 3 - 2 explains how the filter and truth models interact in the MSOFE computer simulation. PROFGEN [47] provides a simulated flight profile and the U.S. Coast Guard GPS Bulletin Board Service (BBS) [24] provides true SV ephemeris data for any SV. Use of the "real-world" ephemeris replaced the prior FORTRAN ORBIT functions used by past researchers at AFIT [45,58,3]. The best four SV were chosen by using System Effectiveness Model (SEM) software [18] and selecting the best (lowest) position dilution of precision (PDOP). With this information, the truth model is able to simulate a real world INS navigation solution, $x + \delta x_{INS}$, and generate the real world GPS and radar altimeter measurements, R_{GPS} and R_{ralt} respectively. The LSM filter in Figure 3 - 2 is represented by the Kalman filter block. The corrections from the LSM filter are subtracted from the INS navigation solution to generate the best possible navigation solution available, $\hat{x} = x + \delta x_{INS} - \delta \hat{x}_{INS}$ [45]. The switch in Figure 3 - 2 does not imply "either/or", instead it implies use of radar altimeter measurements as well as GPS receiver outputs can be used. Now that the MSOFE implementation of the LSM filter has been explained, the truth and filter models for the GPS, radar altimeter and the INS subsystems will be described.

3.4 LSM Model Description

This section presents the truth and filter model propagation and measurement equations, (2.35) and (2.36), respectively. The following presentation will be divided up by navigation subsystems with most parts taken directly from [45]. First the INS portion of the equations will be presented, then the GPS, followed by the radar altimeter.

Before the different navigation subsystems are individually described, the high-level state and measurement equations are provided for the LSM filter, followed by those for the truth model. Equations (3.1) and (3.2) show how the different navigation subsystems models combine to form a single LSM filter model:

$$\delta\dot{x}_f = \begin{bmatrix} F_{INS_f} & 0 \\ 0 & F_{GPS_f} \end{bmatrix} \delta x_f + \begin{bmatrix} w_{INS_f} \\ w_{GPS_f} \end{bmatrix} \quad (3.1)$$

$$\delta z_f = \begin{bmatrix} H_{INS_f} \\ H_{GPS_f} \end{bmatrix} \delta x_f + \begin{bmatrix} v_{INS_f} \\ v_{GPS_f} \end{bmatrix} \quad (3.2)$$

As stated earlier, the overall filter model consists of 13 states; 11 for the INS and 2 for the GPS. Table A.4 in Appendix A provides a description of the 13-state vector, δx_f , implemented in the filter model. References to further descriptions of the sub-matrices in the filter equations can be found in Table 3 - 3. It should be noted that the barometric altimeter aiding measurements are considered to be INS measurements, while the GPS and radar altimeter measurements are the respective updates for the baro/inertial system from the GPS and radar altimeter.

The propagation and measurement equations for the LSM *truth* model is presented in similar fashion below:

$$\delta\dot{x}_t = \begin{bmatrix} F_{Filter} & F_{INS_t1} & 0 \\ 0 & F_{INS_t2} & 0 \\ 0 & 0 & F_{GPS_t} \end{bmatrix} \delta x_t + \begin{bmatrix} w_{Filter} \\ w_{INS_t} \\ w_{GPS_t} \end{bmatrix} \quad (3.3)$$

Filter Model	Location of Description	Truth Model	Location of Description
F_{INS_f}	Section 3.4.1.3	$F_{INS \text{ Filter}}$	Section 3.4.1.3, 3.4.2.1
-	-	$F_{INS_{t1}}$	Section 3.4.1.2
-	-	$F_{INS_{t2}}$	Section 3.4.1.2
F_{GPS_f}	Section 3.4.2.2	F_{GPS_t}	Section 3.4.2.1
w_{INS_f}	Section 3.4.1.3	w_{INS_t}	Section 3.4.1.2
w_{GPS_f}	Section 3.4.2.2	w_{GPS_t}	Section 3.4.2.1
H_{INS_f}	Section 3.4.1.4	H_{INS_t}	Section 3.4.1.4
H_{GPS_f}	Section 3.4.2.3	H_{GPS_t}	Section 3.4.2.3

Table 3 - 3. References for the Sub-Matrices of the LSM Truth and Filter

$$\delta z_t = \begin{bmatrix} H_{INS_t} \\ H_{GPS_t} \end{bmatrix} \delta x_t + \begin{bmatrix} v_{INS_t} \\ v_{GPS_t} \end{bmatrix} \quad (3.4)$$

The LSM truth model consists of the original thirteen states of the filter model (represented by F_{Filter} and w_{Filter}), augmented by additional INS and GPS states (the radar altimeter measurements were modeled as corrupted only by white noise, thus no additional states were necessary). The total number of states for the navigation subsystems is 69; 39 INS states, and 30 GPS states. Tables A.1-A.3, in Appendix A gives a full description of each individual state of the truth model. Also Tables B.1-B.4 and Tables B.6-B.7 in Appendix B have a complete listing of the components of the F and the Q noise strengths associated with the w vector components in Equation (3.3).

While the first thirteen states of the filter model are nearly identical to the first thirteen states of the truth model, there is one crucial difference [45]. The filter model dynamics driving noise and measurement noise do not correlate exactly with those of the first thirteen states of the truth model. The filter model noise statistics values have been altered to achieve good tuning against the truth model [40]. The following sections will provide a detailed presentation into the exact make-up of the truth and filter model propagation and measurement equations for all navigation subsystems used in this thesis.

3.4.1 The Inertial Navigation System (INS) Model.

This section presents the truth and filter models used for the INS. The INS model is a strapped-down wander azimuth system that senses aircraft motion via gyros and accelerometers and is used as the primary source for navigation [45]. The INS model has been derived from a medium accuracy RLG INS 93-state model [1,38]. First, the original 93-state model will be presented, followed by the reduced-ordered 39-state truth and 11-state filter models. After the INS truth and filter state equations have been defined, barometric altimeter measurement equations will be presented.

3.4.1.1 The 93-State LN-93 Error Model.

The 93-state Litton INS MSOFE computer model has been generated by the Wright Laboratories, Avionics Directorate, Avionics System Integration and Research Team (ASIRT). Their development uses both past AFIT research and INS vendor [38] documentation to "fine-tune" past modeling efforts [50,58,65]. The 93-state model generates a high number of documented error sources that are found in the Litton wander-azimuth LN-93 INS [38]. These errors are described using six categories of states [45]:

$$\delta x = [\delta x_1^T \delta x_2^T \delta x_3^T \delta x_4^T \delta x_5^T \delta x_6^T]^T \quad (3.5)$$

where δx is a 93×1 column vector and:

- δx_1 : represents the "general" error vector containing 13 position, velocity, attitude, and vertical channel errors (representative of a Pinson model of INS error characteristics).
- δx_2 : consists of 16 gyro, accelerometer, and baro-altimeter exponentially time-correlated errors, and "trend" states. These states are modeled as first order Markov processes in the truth (system) model.
- δx_3 : represents gyro bias errors. These 18 states are modeled as random constants in the truth model.
- δx_4 : is composed of the accelerometer bias error states. These 22 states are modeled in exactly the same manner as the gyro bias states.
- δx_5 : depicts accelerometer and gyro initial thermal transients. The 6 thermal transient states are first order Markov processes in the system model.

δx_6 : models the gyro compliance errors. These 18 error states are modeled as biases in the system model.

The 93-State Litton model state space differential equation is given by:

$$\begin{Bmatrix} \dot{\delta x}_1 \\ \dot{\delta x}_2 \\ \dot{\delta x}_3 \\ \dot{\delta x}_4 \\ \dot{\delta x}_5 \\ \dot{\delta x}_6 \end{Bmatrix} = \begin{bmatrix} F_{11} & F_{12} & F_{13} & F_{14} & F_{15} & F_{16} \\ 0 & F_{22} & 0 & 0 & 0 & 0 \\ 0 & 0 & 0 & 0 & 0 & 0 \\ 0 & 0 & 0 & 0 & 0 & 0 \\ 0 & 0 & 0 & 0 & 0 & F_{55} \\ 0 & 0 & 0 & 0 & 0 & 0 \end{bmatrix} \begin{Bmatrix} \delta x_1 \\ \delta x_2 \\ \delta x_3 \\ \delta x_4 \\ \delta x_5 \\ \delta x_6 \end{Bmatrix} + \begin{Bmatrix} w_1 \\ w_2 \\ 0 \\ 0 \\ 0 \\ 0 \end{Bmatrix} \quad (3.6)$$

A full description of the sub-matrices for this equation is given in the Litton LN-93 manual [38]. This large state model represents the most accurate model available for the LN-93 navigation errors [45].

3.4.1.2 The 39-State INS Truth Model.

While the 93-state model is a very accurate representation of the INS error characteristics, the high dimensionality of the state equations makes the model very CPU-intensive for “first-look” projects. The intent of this thesis is not to generate a high fidelity model of the Litton LN-93, but rather to evaluate performance characteristics associated with a particular *class* of INS (medium precision or lower precision). Previous AFIT theses have demonstrated that reduced-ordered truth models can be used in place of the 93-state truth model without losing a significant degree of accuracy [45,52,50]. Therefore the INS truth model has been reduced to a 39-state model. The reduced-ordered model retains only the truly essential states from Equation (3.6). The truth model state space equation is defined in Equation (3.7):

$$\begin{Bmatrix} \dot{\delta x}_1 \\ \dot{\delta x}_2 \\ \dot{\delta x}_3 \\ \dot{\delta x}_4 \end{Bmatrix} = \begin{bmatrix} F_{11} & F_{12} & F_{13} & F_{15} \\ 0 & F_{22} & 0 & 0 \\ 0 & 0 & 0 & 0 \\ 0 & 0 & 0 & 0 \end{bmatrix} \begin{Bmatrix} \delta x_1 \\ \delta x_2 \\ \delta x_3 \\ \delta x_4 \end{Bmatrix} + \begin{Bmatrix} w_1 \\ w_2 \\ 0 \\ 0 \end{Bmatrix} \quad (3.7)$$

It should be noted that the INS truth state vector δx , is a 39-state vector. The four components of δx do not directly correlate to the first four components of the 93-state

Litton model [45]. For a complete listing of the 39 states and how they relate to those in [38], see Tables A.1 and A.2 in Appendix A.

3.4.1.3 *The 11-State INS Filter Model.*

The INS filter model retains the essential states from the 39-state truth model. Through past AFIT research, the 11-state INS filter has been shown to perform adequately when given frequent GPS measurement updates [45,50,65]. Table A.4 in Appendix A shows the 11 states used for the INS filter model. The final INS filter dynamics submatrix, \mathbf{F} , as well as process noise strength \mathbf{Q} and measurement noise covariance \mathbf{R} , can be found in Appendix B.

3.4.1.4 *INS Measurement Model.*

The two measurements that are used to update the filter are the barometric altimeter and the radar altimeter. The barometric altimeter signal is used to correct for inherent instabilities of the vertical channel in the filter. The radar altimeter is used during landing approaches when altitudes are below 3000 feet above ground level (AGL). First the barometric altimeter measurement will be presented, followed by the radar altimeter measurement. It should be noted that, since the LSM filter is an error state filter, it is necessary to develop difference measurement update equations for all the measurements. The barometric altimeter measurement equation is based on the difference between the INS-predicted altitude, Alt_{INS} and the barometric altimeter-predicted altitude Alt_{Bar} :

$$\delta z_{Alt} = Alt_{INS} - Alt_{Bar} \quad (3.8)$$

Therefore it is necessary to develop the two separate measurement signals that will be differenced to attain the proper measurement update for the error state filter [45]. The INS-predicted altitude is the sum of the true altitude, h_t , and the INS error in vehicle altitude above the reference ellipsoid, δh . The barometric altimeter reading is modeled as the sum of the true altitude, h_t , the total time-correlated error in the barometric altimeter, δh_B , and a random measurement noise, v . The difference measurement update signal is formed in Equation (3.9) by subtracting the INS-predicted altitude from the barometric altimeter altitude:

$$\begin{aligned}
\delta z_{Alt} &= Alt_{INS} - Alt_{Bar} \\
&= [h_t + \delta h] - [h_t + \delta h_B - v] \\
&= \delta h - \delta h_B + v
\end{aligned} \tag{3.9}$$

Note that, since v is assumed *zero* mean, white gaussian noise, statistically speaking, one can choose v with either a plus "+" or minus "-" coefficient. The author chooses the coefficient carefully so that the end result shows a plus "+ v " sign.

This completes the presentation of the INS truth and filter state equations as well as the INS measurement equations. The next section will develop similar equations for the radar altimeter used in this thesis.

3.4.2 Radar Altimeter Model.

As a "first-cut" model of the radar altimeter, the measurement equation is based on the difference between the INS predicted altitude, Alt_{INS} and the radar altimeter predicted altitude, Alt_{Ralt} :

$$\begin{aligned}
\delta z_{ALT} &= ALT_{INS} - ALT_{Ralt} \\
&= [h_t + \delta h] - [h_t - v] \\
&= \delta h + v
\end{aligned} \tag{3.10}$$

Note that the errors in the radar altimeter are represented totally as white noise, with no time-correlated component at all. Though admittedly only a first-cut model, it should be sufficient to demonstrate important performance trends.

The radar altimeter measurement noise variance, R_{Filter} or R_{True} , is a function of aircraft altitude above ground level (AGL). The filter model noise variance from [28]:

$$R_{Truth} = \left\{ [0.01]^2 * [Radar Altitude_{True(AGL)}]^2 \right\} + 0.25 Bias \tag{3.11}$$

and the truth model noise variance is the same:

$$R_{Truth} = \left\{ [0.01]^2 * [Radar Altitude_{True(AGL)}]^2 \right\} + 0.25 Bias \tag{3.12}$$

Note that R_{Filter} and R_{Truth} are both time-varying rather than constant, due to the altitude dependency.

This completes the presentation of the radar altimeter measurement and noise variance equations. The next section will develop truth, filter and measurement equations for the Global Positioning System (GPS) used in this thesis.

3.4.3 The Global Positioning System (GPS) Model.

The GPS navigation system used is based on electromagnetic signals transmitted from orbiting GPS satellites. This model has been developed throughout research at AFIT, and many of its fundamental concepts are addressed in a variety of sources [39,50,56,58]. GPS generates navigation information by acquiring the range to multiple satellites of known position, called “*pseudoranges*”. The navigation information passed to the LSM filter is the respective range and ephemeris data position to each of four satellites [45,39]. The next three sections will present all the necessary equations to define the GPS truth and filter error models fully.

3.4.3.1 The 30-State GPS Truth Model

There are five types of error sources that are modeled in the GPS truth model state equations. The first two states represent the errors in the user clock and are modeled as follows:

$$\begin{Bmatrix} \delta \dot{R}_{clk_U} \\ \delta \dot{D}_{clk_U} \end{Bmatrix} = \begin{bmatrix} 0 & 1 \\ 0 & 0 \end{bmatrix} \begin{Bmatrix} \delta R_{clk_U} \\ \delta D_{clk_U} \end{Bmatrix} \quad (3.13)$$

where

$$\begin{aligned} \delta R_{clk_U} &= \text{range equivalent of user clock bias} \\ \delta D_{clk_U} &= \text{velocity equivalent of user clock drift} \end{aligned}$$

The initial state estimates and covariances for these states were chosen to be consistent with previous AFIT research, [45,50,56,58] and are:

$$\begin{Bmatrix} \hat{\delta R}_{clk_U}(t_0) \\ \hat{\delta D}_{clk_U}(t_0) \end{Bmatrix} = \begin{bmatrix} 0 \\ 0 \end{bmatrix} \quad (3.14)$$

and

$$P_{\delta R_{clk_U}, \delta D_{clk_U}}(t_0) = \begin{bmatrix} 9.0 \times 10^{14} \text{ ft}^2 & 0 \\ 0 & 9.0 \times 10^{10} \text{ ft}^2 / \text{sec}^2 \end{bmatrix} \quad (3.15)$$

Because these error sources are a function of the user equipment, they are common to all the satellite vehicles. The remaining five sources of errors are unique to each satellite vehicle (SV), based on their individual equipment and their position with respect to the user. The first SV-specific error source is the code loop error, δR_{loop} . Although the code loop is part of the user equipment shared by all the SV's, its error magnitude is relative to each SV. The second and third SV-specific errors are the atmospheric interference with the EM signals, δR_{ion} and δR_{trop} , as related to the ionospheric and tropospheric delay in the signal's propagation. The code loop error, tropospheric delay, and ionospheric delay are all modeled as first order Markov processes with time constants shown in Equation (3.16), consistent with previous AFIT research [58,65,50,45]. All three are driven by zero-mean white Gaussian noise with strengths shown in Equation (3.19). The fourth SV-specific error source is due to inaccuracies in the clocks on board the SV's, δR_{Sclk} and the final error source is based on line-of-sight errors between the SV's and the receiver, δx_{s_i} , δy_{s_i} , δz_{s_i} , respectively. The model for these states shown in Equation (3.16):

$$\begin{Bmatrix} \dot{\delta R}_{loop} \\ \dot{\delta R}_{trop} \\ \dot{\delta R}_{ion} \\ \dot{\delta R}_{Sclk} \\ \dot{\delta x}_{s_i} \\ \dot{\delta y}_{s_i} \\ \dot{\delta z}_{s_i} \end{Bmatrix} = \begin{bmatrix} -1 & 0 & 0 & 0 & 0 & 0 & 0 \\ 0 & -\frac{1}{500} & 0 & 0 & 0 & 0 & 0 \\ 0 & 0 & -\frac{1}{1500} & 0 & 0 & 0 & 0 \\ 0 & 0 & 0 & 0 & 0 & 0 & 0 \\ 0 & 0 & 0 & 0 & 0 & 0 & 0 \\ 0 & 0 & 0 & 0 & 0 & 0 & 0 \\ 0 & 0 & 0 & 0 & 0 & 0 & 0 \end{bmatrix} \begin{Bmatrix} \delta R_{loop} \\ \delta R_{trop} \\ \delta R_{ion} \\ \delta R_{Sclk} \\ \delta x_{s_i} \\ \delta y_{s_i} \\ \delta z_{s_i} \end{Bmatrix} + \begin{Bmatrix} w_{cl} \\ w_{trop} \\ w_{ion} \\ 0 \\ 0 \\ 0 \\ 0 \end{Bmatrix} \quad (3.16)$$

where the initial covariance for the states is given by:

$$P_{GPS} = \begin{bmatrix} 0.25 \text{ ft}^2 & 0 & 0 & 0 & 0 & 0 & 0 \\ 0 & 1.0 \text{ ft}^2 & 0 & 0 & 0 & 0 & 0 \\ 0 & 0 & 1.0 \text{ ft}^2 & 0 & 0 & 0 & 0 \\ 0 & 0 & 0 & 0.25 \text{ ft}^2 & 0 & 0 & 0 \\ 0 & 0 & 0 & 0 & 25 \text{ ft}^2 & 0 & 0 \\ 0 & 0 & 0 & 0 & 0 & 25 \text{ ft}^2 & 0 \\ 0 & 0 & 0 & 0 & 0 & 0 & 25 \text{ ft}^2 \end{bmatrix} \quad (3.17)$$

and mean values and strengths of the dynamics driving noise are given by:

$$E\{w_{GPS}(t)\} = 0 \quad (3.18)$$

$$E\{w_{GPS}(t)w_{GPS}^T(t+\tau)\} = \begin{bmatrix} 0.5 & 0 & 0 & 0 & 0 & 0 & 0 \\ 0 & 0.004 & 0 & 0 & 0 & 0 & 0 \\ 0 & 0 & 0.004 & 0 & 0 & 0 & 0 \\ 0 & 0 & 0 & 0 & 0 & 0 & 0 \\ 0 & 0 & 0 & 0 & 0 & 0 & 0 \\ 0 & 0 & 0 & 0 & 0 & 0 & 0 \\ 0 & 0 & 0 & 0 & 0 & 0 & 0 \end{bmatrix} \frac{ft^2}{sec} \cdot \delta(\tau) \quad (3.19)$$

A quick reference of the truth model non-zero GPS dynamics matrix components is provided in Tables B.4 of Appendix B. This ends the description of the 30-state truth model. Now the filter model will be presented.

3.4.3.2 The 2-State GPS Filter Model

Various research efforts have shown that two states provide a sufficient model for GPS [50,52,45]. The primary argument is that the errors modeled by the other 28 states are small when compared to the two states common to all SV's. By adding dynamics driving noise, of strength Q , and re-tuning the filter, the overall performance of the LSM can be maintained with the significantly reduced-order model of Equation (3.20):

$$\begin{Bmatrix} \dot{\delta R}_{clk_U} \\ \dot{\delta D}_{clk_U} \end{Bmatrix} = \begin{bmatrix} 0 & 1 \\ 0 & 0 \end{bmatrix} \begin{Bmatrix} \delta R_{clk_U} \\ \delta D_{clk_U} \end{Bmatrix} + \begin{Bmatrix} w_{R_{clk}} \\ w_{D_{clk}} \end{Bmatrix} \quad (3.20)$$

The values implemented for the dynamics driving noise strengths can be found in Table B.8 of Appendix B. It should be noted that, in the tuning process, the measurement noise covariance values R (as shown in Appendix B) have also been adjusted to achieve adequate tuning of the filter [40]. This completes the description of the GPS filter model. The next section presents the GPS measurement equations for both the truth and the filter models.

3.4.3.3 GPS Measurement Model

There are four GPS measurement updates, one from each of the satellite range signals received by the LSM filter. These measurement updates are once again *difference* measurements. First the GPS truth model difference measurement will be fully presented, followed by a brief description of the filter measurement. The GPS difference measurement is formed by taking the difference of the INS-calculated pseudorange, R_{INS} and actual pseudorange, R_{GPS} .

$$\delta z_{GPS} = R_{INS} - R_{GPS} \quad (3.21)$$

The real pseudorange, R_{GPS} is the sum of the true range form the user to the satellite plus all the errors in the pseudorange signal propagation.

$$R_{GPS} = R_t + \delta R_{loop} + \delta R_{trop} + \delta R_{ion} + \delta R_{Sclk} + \delta R_{Uclk} - v \quad (3.22)$$

where

R_{GPS}	=	GPS pseudorange measurement, from SV to user
R_t	=	true range, from SV to user
δR_{loop}	=	range error due to code loop error
δR_{trop}	=	range error due to tropospheric delay
δR_{ion}	=	range error due to ionospheric delay
δR_{Sclk}	=	range error due to SV clock error
δR_{Uclk}	=	range error due to use clock error
v	=	zero-mean white Gaussian measurement noise

Note that, since v is assumed *zero* mean, white gaussian noise, statistically speaking, one can choose v with either a plus "+" or minus "-" coefficent . As in equation (3.9), the author chooses the coefficent carefully so that the end result shows a plus "+v" sign in equation (3.25) and equation (3.26).

The second source of a range measurement is the INS itself, R_{INS} [45]. R_{INS} is the difference between the LSM-calculated position, X_U and the satellite position from the ephemeris data X_S . This difference vector is represented below in the ECEF frame:

$$R_{INS} = |X_U - X_S| = \left| \begin{pmatrix} x_U \\ y_U \\ z_U \end{pmatrix}^e - \begin{pmatrix} x_S \\ y_S \\ z_S \end{pmatrix}^e \right| \quad (3.23)$$

An equivalent form for Equation (3.23) is

$$R_{INS} = \sqrt{(x_U - x_S)^2 + (y_U - y_S)^2 + (z_U - z_S)^2} \quad (3.24)$$

Based on Assumption 12 from Chapter 1, Equation (3.24) can be approximated and rewritten in terms of the true range and a truncated first-order Taylor series, with perturbations representing the errors in X_U and X_S :

$$R_{INS} = R_t + \frac{\partial R_{INS}(X_S, X_U)}{\partial X_U} \Big|_{(X_S, X_U)_{nom}} \cdot \delta X_U + \frac{\partial R_{INS}(X_S, X_U)}{\partial X_S} \Big|_{(X_S, X_U)_{nom}} \cdot \delta X_S \quad (3.25)$$

The solution for R_{INS} is found by substituting Equations (3.24) into Equation (3.25) and evaluating the partial derivatives to get [45]:

$$\begin{aligned} R_{INS} = R_t & - \left[\frac{x_S - x_U}{|R_{INS}|} \right] \cdot \delta x_U - \left[\frac{y_S - y_U}{|R_{INS}|} \right] \cdot \delta y_U - \left[\frac{z_S - z_U}{|R_{INS}|} \right] \cdot \delta z_U \\ & + \left[\frac{x_S - x_U}{|R_{INS}|} \right] \cdot \delta x_S + \left[\frac{y_S - y_U}{|R_{INS}|} \right] \cdot \delta y_S + \left[\frac{z_S - z_U}{|R_{INS}|} \right] \cdot \delta z_S \end{aligned} \quad (3.26)$$

Finally, the GPS pseudorange truth model *difference* measurement is given as:

$$\begin{aligned} \delta z_{GPS_i} &= R_{INS} - R_{GPS} \\ &= - \left[\frac{x_S - x_U}{|R_{INS}|} \right] \cdot \delta x_U - \left[\frac{y_S - y_U}{|R_{INS}|} \right] \cdot \delta y_U - \left[\frac{z_S - z_U}{|R_{INS}|} \right] \cdot \delta z_U \\ &+ \left[\frac{x_S - x_U}{|R_{INS}|} \right] \cdot \delta x_S + \left[\frac{y_S - y_U}{|R_{INS}|} \right] \cdot \delta y_S + \left[\frac{z_S - z_U}{|R_{INS}|} \right] \cdot \delta z_S \\ &- [1]\delta R_{loop} - [1]\delta R_{trop} - [1]\delta R_{ion} \\ &- [1]\delta R_{Sclk} - [1]\delta R_{Uclk} + v \end{aligned} \quad (3.27)$$

The user position errors in Equation (3.27) can be derived from the first three states of the filter or truth model using an orthogonal transformation [9,45].

The filter model for the GPS measurement will now be derived. Since the filter model does not contain the states for the errors in the satellite position, these terms are removed from the equation. The filter model measurement equation can therefore be written as:

$$\begin{aligned}\delta z_{GPS_f} &= R_{INS} - R_{GPS} \\ &= -\left[\frac{x_S - x_U}{|R_{INS}|}\right] \cdot \delta x_U - \left[\frac{y_S - y_U}{|R_{INS}|}\right] \cdot \delta y_U - \left[\frac{z_S - z_U}{|R_{INS}|}\right] \cdot \delta z_U \\ &\quad - [1]\delta R_{Uclk} + v\end{aligned}\tag{3.28}$$

The filter measurement noise variance, R , will be tuned to attain adequate performance despite the reduction in order from the truth model and the Taylor series approximation. The measurement noise variances for both the filter and the truth model equations are provided in Table B.9 of Appendix B. This completes the description of the GPS measurement equations and the entire LSM filter and truth model equations.

3.5 Chapter Summary

This chapter presents the modeling set-up of the LSM MSOFE computer simulation. An introduction to MSOFE and PROFGEN is provided. The truth model and filter model propagation and measurement equations are described for the INS/Baro, Radar Altimeter, and GPS subsystems. A "first-cut" model of the radar altimeter model has been presented. The radar altimeter measurements should play a key role in allowing our aircraft to meet precision approach requirements. The INS/Baro and GPS truth model is located in tabular form in Appendix A. The dynamic submatrices F_{Filter} , F_{INS1} , F_{INS2} , and F_{GPS} , and process noise strength and measurement noise covariance matrices for filter and truth models are presented in Appendix B. Results and analysis of the LSM simulation are presented in Chapter 4.

IV. Results and Analysis

This chapter presents results and analysis of the following items:

- 4.1 "Tanker" trajectory (detailed KC-135 flight profile) created using PROFGEN [47].
- 4.2 SV Ephemeris Data, (GDOP, PDOP, HDOP, VDOP SV numbers) using SEM 3.6 [18].
- 4.3 Development of The Three INS's
- 4.4 Filter Tuning Example (using Case I error states,). See Table 4 - 1.
- 4.5 Case I-VI performance results (includes radar altimeter aiding).
- 4.6.1 Case VII-IX performance results (includes single pseudolite aiding).
- 4.6.2 Case X-XII performance results (includes radar altimeter and pseudolite aiding).
- 4.7 Case XIII-XV performance results (includes one GPS time-out for the three INS accuracies: 0.4 nm/hr, 2.0 nm/hr and 4.0 nm/hr).
- 4.8 CASE XVI performance results (includes two GPS time-outs with radar altimeter aiding, during final approach using a low accuracy (4.0 nm/hr) INS.

As a helpful aid, Tables 4-1 and 4-2 show Cases I-IX and Cases X-XVI integration comparisons, respectively.

Case I	Case II	Case III	Case IV	Case V	Case VI	Case VII	Case VIII	Case IX
Barometric Altimeter								
0.4 nm/hr CEP INS	0.4 nm/hr CEP INS	2.0 nm/hr CEP INS	2.0 nm/hr CEP INS	4.0 nm/hr CEP INS	4.0 nm/hr CEP INS	0.4 nm/hr CEP INS	2.0 nm/hr CEP INS	4.0 nm/hr CEP INS
P-Code GPS								
----	Radar Altimeter	----	Radar Altimeter	----	Radar Altimeter	Pseudolite	Pseudolite	Pseudolite

Table 4 - 1. Case I-IX Integration Comparisons

Case X	Case XI	Case XII	Case XIII	Case XIV	Case XV	Case XVI
Barometric Altimeter	Barometric Altimeter	Barometric Altimeter	Barometric Altimeter	Barometric Altimeter	Barometric Altimeter	Barometric Altimeter
0.4 nm/hr CEP INS	2.0 nm/hr CEP INS	4.0 nm/hr CEP INS	0.4 nm/hr CEP INS	2.0 nm/hr CEP INS	4.0 nm/hr CEP INS	4.0 nm/hr CEP INS
P-Code GPS	P-Code GPS	P-Code GPS	P-Code GPS	P-Code GPS	P-Code GPS	P-Code GPS
Radar Altimeter and Pseudolite	Radar Altimeter and Pseudolite	Radar Altimeter and Pseudolite	None	None	None	Radar Altimeter
No GPS Outage	No GPS Outage	No GPS Outage	Single GPS Outage	Single GPS Outage	Single GPS Outage	Double GPS Outages

Table 4 - 2. Case X-XI Integration Comparisons

Tables 4 - 1 and 4 - 2 show a total of sixteen different cases that were completed in this thesis. All cases use the Tanker (KC-135) flight profile of Section 4.1 and the P-Code receiver always uses four SVs overhead. Cases I - VI show how an the additional radar altimeter measurements can aid three different INS's using baro altimeter and a P-Code GPS receiver. Cases VII - IX show how use of a single pseudolite measurement in close proximity to a runway can aid three different INS's using baro altimeter and P-Code GPS aiding. Cases X - XII show the performance enhancements of using a single pseudolite measurement and radar altimeter measurements. The results of Cases X - XII can be compared with Cases (I, III, V) - no radar altimeter or pseudolite, Cases (II, IV, VI) - just radar altimeter, and Cases (VII, VIII, IX) - just pseudolite, to see the additional benefit of each measurement source. Case XIII - XV shows simply a single GPS outage with the 0.4/2/4 nm/hr INSs. Use of the radar altimeter occurs during final approach. Case XVI shows a double GPS outage; where use of radar altimeter occurs during the aircraft landing. Only the 4 nm/hr INS is evaluated for this special case. Also, all results will be compared with Table 4 - 3, illustrating landing performance 1σ requirements at respective decision heights.

Precision Approach Parameters (in feet, all 1-sigma values)			
Category	Decision Height	Azimuth	Elevation
I	200 feet	+/- 28.1	+/- 6.8
II	100 feet	+/- 8.6	+/- 2.8
III	50 feet	+/- 6.8	+/- 1.0

Table 4 - 3 Precision Approach Accuracy Requirements at Decision Heights

4.1 *The Tanker (KC-135) flight profile*

A PROF_IN file (PROF_IN is the input file for PROFGEN [47]) was created for a Boeing 707 (KC-135) aircraft based on inputs from [4,59,46]. The actual PROF_IN file used with PROFGEN can be found in Appendix C. PROFGEN reads in PROF_IN, and outputs a binary flight file called "FLIGHT". FLIGHT contains the flight profile variables shown in Chapter 3, Table 3 - 2.

The Tanker flight profile is simulated to start at WPAFB, OH. with the following initial conditions:

- Runway 23 R (Heading 232°)
- Initial Latitude 39.055° N
- Initial Longitude 84.033° W
- Initial altitude 825 feet
- Aircraft take-off (rotation) speed 150 knots
- Initial wander angle (alpha) 45°

As described in Chapter 3, PROFGEN outputs are concatenated segments. See Table 3-1 in Chapter 3. Using Table C - 1 of Appendix C and Table 3 - 1 of Chapter 3, the Tanker flight profile will now be defined:

- The tanker aircraft rolls down the runway for 30 seconds; during this time its velocity transitions from 0 knots to 150 knots at which time aircraft rotation occurs.
- The tanker climbs at a +5° pitch over the next 494 seconds, obtaining an altitude of 19,996 feet and velocity of 326 knots, at an elapsed time of 527 seconds.
- The tanker makes a +45° (rolled to the right) turn and continues straight, with a gradual acceleration, maintaining an altitude of 19996 feet. Final velocity is 393 knots at an elapsed time of 923 seconds.

- The tanker makes another +45° turn and continues straight with a gradual acceleration, maintaining an altitude of 19,996 feet. Final velocity is 453 knots at an elapsed time 1393 seconds.
- The tanker makes another +45° turn and immediately begins a 600-second segment of mild horizontal jink maneuvers maintaining an altitude of 19,996 feet (the jink maneuver is a sinusoidal heading change of ± 2 degrees, every 200-second period). Final velocity is 454 knots, at an elapsed time 2368 seconds. The jinking maneuver is clearly evident in the Tanker flight profiles of Appendix D: Figure D - 2 (Wander Azimuth Angle), Figure D - 3 (X-Velocity), and Figure D - 4 (Roll and Heading).
- The tanker makes another + 45 degree turn and immediately begins to descend and maintain an altitude of 12255 feet. Final velocity is 453 knots at an elapsed time of 2558 seconds.

Note: It was during this maneuver, that the filter (for all cases) showed a degradation in latitude error and slight degradation in longitude error. Possibly, a more realistic Tanker profile would have decreased velocity, before making such a large altitude descent (though the tanker does not exceed a 1g maneuver at any given time). This profile is meant to be realistic; there was no attempt to put in maneuvers to enhance identifiability of certain states (i.e., no 42-minute "legs", butterfly patterns, etc.).

- Deceleration now begins, with a +90° turn, followed by a -5° pitch (down) to an altitude of 10,678 feet. Final velocity is 244 knots at an elapsed time of 3075 seconds.
- Slight acceleration followed by gradual deceleration begins with a -45° turn and a negative 1.75° pitch (down) to an altitude of 4425 feet. Final velocity is 304 knots at an elapsed time of 3584 seconds.
- Gradual deceleration continues with a +45° turn, followed by a -3° glideslope pitch (down). True altitude mean sea level "MSL" is 3799 feet or 2974 feet above ground level "AGL", velocity is 131 knots at an elapsed time of 3658 sec.
- The tanker makes its final +45° turn to align with the WPAFB runway (23R at 232° heading). The -3 degree glideslope continues, until the tanker aircraft touches down at an altitude of 825 feet (MSL) or 0 feet (AGL). Aircraft velocity while on final approach is 132 knots at all times. Touchdown occurs at an elapsed time of 3912.5 sec.

The aircraft reaches Cat I, II, III decision heights at the following flight profile times indicated in Table 4 - 4.

Category of Precision Approach	Decision Height in feet	Elapsed Time in seconds	Aircraft Altitude (AGL) in feet	Aircraft Altitude (MSL) in feet
I	200	3896	200	1025
II	100	3904	100	925
III	50	3908	50	875

Table 4 - 4. Category I, II and III Decision Height Profile Times

Note: Vertical velocity (Z-velocity) = $-11.6975 \text{ ft/sec} = 6.92465 \text{ knots} \sim 7.9687 \text{ mph}$ during the final approach. As stated earlier in Chapter 3, the PROFGEN output file "FLIGHT" is used as the truth model trajectory in the MSOFE LSM simulation.

4.2 Satellite Vehicle Data Using SEM3.6

When MSOFE [48] begins, one of the many files it reads is the FLIGHT file provided by PROFGEN (See Section 4.1). Another file MSOFE must read for this thesis is the SV ephemeris data (provided by the National Geodetic Office). (This thesis is the first at AFIT to use true SV ephemeris data provided by the National Geodetic Office). The method used to insert the true ephemeris data into MSOFE is by modifying a FORTRAN routine [57] which appends true ephemeris data to the end of the binary FLIGHT file. A copy of this Fortran routine ("ADDSV.for") is found in Appendix E. A sample of the true SV ephemeris data, obtained by the National Geodetic Office is also found in Appendix E.

The SV ephemeris used in the LSM simulation was selected based upon the best four SV available for a random day (i.e., 21 May 94 used in this thesis) by the software SEM3.6 [18]. The task to choose which 4 SVs to use was determined as follows:

- Random day (21 May 94) selected.
(GPS week 749, Day of year 141).
- GPS Almanac data file "051994A.AL3" (See Appendix E) was obtained (downloaded) via the Coast Guard Bulletin Board Services (CGBBS).
- LAT/LONG/ALT along the Tanker flight profile was noted and entered in SEM 3.6.
 - Best 4 SV based on PDOP algorithm
 - 5° mask angle

- Scenario duration: 2 hours [Begin time 04:00 UTC
(Coordinated Universal Time or 08:00 Eastern time)]

SEM 3.6 uses the identical position dilution of precision (PDOP) algorithm that the Collins Receiver 3-A P-Code GPS receiver [13] utilizes. The best four satellite vehicles (SV) are then numerically displayed to the user. The 5° mask angle was chosen based on the author's knowledge as a realistic number utilized by most GPS receivers. "Mask angle" is defined in this thesis as the angle made from the surface of the GPS receiver antenna. Thus all satellites in view above a 5° angle made from the GPS antenna surface, on 21 May 94, between the hours of 04:00 - 06:00 GMT are "fair-game" to use in the selection of "Best-4" SVs based on a PDOP algorithm. "GMT" is defined as Greenwich mean time (same as Zulu or Universal time). Plots obtained from SEM3.6 (GDOP, PDOP, VDOP, TDOP, SV Bearing/Elevation, SV Rise/Set, Number of Visible SVs and Elevation/Time) are shown in Appendix F.

The Dilution of Precisions (DOPs) in Appendix F are defined as:

$$GDOP = (\sigma_x^2 + \sigma_y^2 + \sigma_z^2 + \sigma_t^2)^{1/2} = \text{Geometric Dilution of Precision}$$

$$PDOP = (\sigma_x^2 + \sigma_y^2 + \sigma_z^2)^{1/2} = \text{Position Dilution of Precision}$$

$$HDOP = (\sigma_x^2 + \sigma_y^2)^{1/2} = \text{Horizontal Dilution of Precision}$$

$$VDOP = (\sigma_z^2)^{1/2} = \text{Vertical Dilution of Precision}$$

$$TDOP = (\sigma_t^2)^{1/2} = \text{Time Dilution of Precision}$$

- The SV Bearing/Elevation: Displays the position of SVs that are visible at the selected location during the specified time window for the date and mask angle chosen.
- SV Rise/Set: Shows the rise times, set times, visibility periods, and selection (in use) periods for each SV as functions of time.
- Number of Visible SVs: Shows as a function of time, the total number of SVs visible during the time period under evaluation.
- Elevation/Time: Displays the elevation of visible SVs as a function of time.

For further information on SEM 3.6 software and SEM 3.6 output plot format, see [18].

For further information on DOPs, see [17].

The SVs chosen and entered in the LSM simulation are summarized in Table 4 - 5:

Time (UTC)	Satellite Vehicle Number	PROFGEN elapsed time (seconds)	PDOP
04:15	6,16,17,28	0	2.25
04:55	6,12,17,28	2400	2.29
05:10	1,12,17,28	3300	2.47

Table 4 - 5. Satellite Vehicles Chosen During Simulation

Note that changing of SVs can become quite evident in enhancing or degrading one's overall navigation solution (by increasing or decreasing DOP). Sections 4.5 - 4.8 clearly show evidence of *degradation* when a SV change occurs at T = 2400 seconds.

4.3 Development of The Three INS's

It was an objective in this thesis to compare a medium accuracy INS (0.4 nm/hr) with a lower quality inertial navigation systems in the range of 2 to 4 nm/hr. The NRS model (obtained from [45,50] drifts at an accuracy of approximately 0.4 nm/hr (CEP). This drift rate is considered medium accuracy for this thesis, thus two lower accuracy INS models were created (2.0 nm/hr CEP and 4.0 nm/hr CEP). The choice of error state modification to the existing NRS INS model [45,50] was based in part from personal conversations with [31]. Modifications to the system covariance matrices for each respective INS are shown in Table 4 - 6. Only random constant shaping filter states were changed (not the 1st order Gauss-Markov drift states, etc.). To avoid "CEP" confusion, CEP will be defined next, directly from [10].

In the case of two jointly Gaussian variables x and y , where $\sigma_x = \sigma_y = \sigma$, and $\rho = 0$, the normal distribution

$$f_{x,y}(x,y) = \frac{1}{2\pi\sigma_x\sigma_y\sqrt{1-\rho^2}} e^{\frac{-1}{2(1-\rho^2)} \left[\frac{(x-\bar{x})^2}{\sigma_x^2} + \frac{(y-\bar{y})^2}{\sigma_y^2} - \frac{2\rho(x-\bar{x})(y-\bar{y})}{\sigma_x\sigma_y} \right]} \quad (4.1)$$

is called *circular* [10].

LSM State Number	LSM State Name	0.4 nm/hr Value	2.0 nm/hr Value	4.0 nm/hr Value	SNU 84-1 State	NRS State	Units
23	X-component of gyro drift rate repeatability	1.78E-16	1.61E-14	5.46E-14	30	25	(°/hr)/hr
24	Y-component of gyro drift rate repeatability	2.11E-16	1.96E-14	6.35E-14	31	26	(°/hr)/hr
25	Z-component of gyro drift rate repeatability	2.11E-16	1.96E-14	6.35E-14	32	27	(°/hr)/hr
26	X-component of gyro scale factor error	2.49E-11	9.09E-10	3.00E-9	33	28	%
27	Y-component of gyro scale factor error	2.50E-11	9.00E-10	3.00E-9	34	29	%
28	Z-component of gyro scale factor error	2.49E-11	9.09E-10	3.01E-9	35	30	%
29	X-component of accelerometer bias repeatability	2.31E-7	2.17E-5	7.26E-5	48	31	µg
30	Y-component of accelerometer bias repeatability	2.31E-7	2.17E-5	7.26E-5	49	32	µg
31	Z-component of accelerometer bias repeatability	2.30E-7	2.16E-5	7.25E-9	50	33	µg
32	X-component of accelerometer and velocity quantizer scale factor error	1.44E-8	5.18E-7	1.73E-6	51	34	%
33	Y-component of accelerometer and velocity quantizer scale factor error	1.44E-8	5.14E-7	1.73E-6	52	35	%
34	Z-component of accelerometer and velocity quantizer scale factor error	1.44E-8	5.14E-7	1.73E-6	53	36	%
35	X-component of accelerometer and velocity quantizer scale factor asymmetry	6.25E-10	7.50E-9	2.50E-8	54	37	%
36	Y-component of accelerometer and velocity quantizer scale factor asymmetry	6.25E-10	7.55E-9	2.50E-8	55	38	%
37	Z-component of accelerometer and velocity quantizer scale factor asymmetry	6.25E-10	7.50E-9	2.50E-8	56	39	%
38	X accelerometer misalignment about Z-axis	8.74E-15	3.14E-13	3.17E-12	66	40	arc-sec
39	Y accelerometer misalignment about Z-axis	3.76E-10	9.46E-13	1.40E-7	67	41	arc-sec
40	Z accelerometer misalignment about Y-axis	3.76E-10	9.40E-13	1.40E-7	68	42	arc-sec
41	X accelerometer misalignment about Y-axis	3.76E-10	9.40E-13	1.40E-7	69	43	arc-sec

Table 4 - 6. MSOFE Initial System Covariance Parameters for 0.4/2.0/4.0 nm/hr INS

where

$$\begin{aligned}\bar{x} &= E[x] \\ \bar{y} &= E[y] \\ \sigma_x^2 &= E[(x - \bar{x})^2] \\ \sigma_y^2 &= E[(y - \bar{y})^2] \\ \rho &= E[(x - \bar{x})(y - \bar{y})] / (\sigma_x \sigma_y)\end{aligned}\tag{4.2}$$

(Here: ρ = the correlation coefficient of x and y , σ_x is the standard deviation of x and σ_y is the standard deviation of y). Then the probability density for radial distance r from the point (\bar{x}, \bar{y}) corresponding to $f(x,y)$ is

$$f(r) = (r / \sigma^2) e^{-r^2/2\sigma^2}\tag{4.3}$$

where

$$r^2 = (x - \bar{x})^2 + (y - \bar{y})^2\tag{4.4}$$

r is called the *radial* error [10]. The equal probability ellipses are circles in this case, since $\sigma_x = \sigma_y = \sigma$. The probability p' that a point (x,y) taken at random will fall within a circular ring, whose center is at (\bar{x}, \bar{y}) and whose inner and outer radii are r and $r + \Delta r$, is

$$p' = f(r) \Delta r\tag{4.5}$$

The probability p that a point (x,y) taken at random will fall within the circle

$$(x - \bar{x})^2 + (y - \bar{y})^2 = (c\sigma)^2\tag{4.6}$$

for a particular value of c is

$$p = 1 - e^{-c^2/2}\tag{4.7}$$

When $c = 1.1774$, $p = 0.5$, and the circle of radius 1.1774σ is called the 50 percent probability circle [10]. The radius of this circle is called the circular probable error or CEP and

$$\text{CEP} = 1.1774\sigma \quad (4.8)$$

Approximations are often made for the CEP calculation when the actual error distribution has elliptical rather than circular equal-probability loci. The approximation used in this thesis is:

$$\text{Estimate}(CEP) = 0.588[\sigma_x + \sigma_y] \quad (4.9)$$

The CEP curves for one hour of operation of the three inertial navigation systems created in this thesis are shown in Figure 4 - 1.

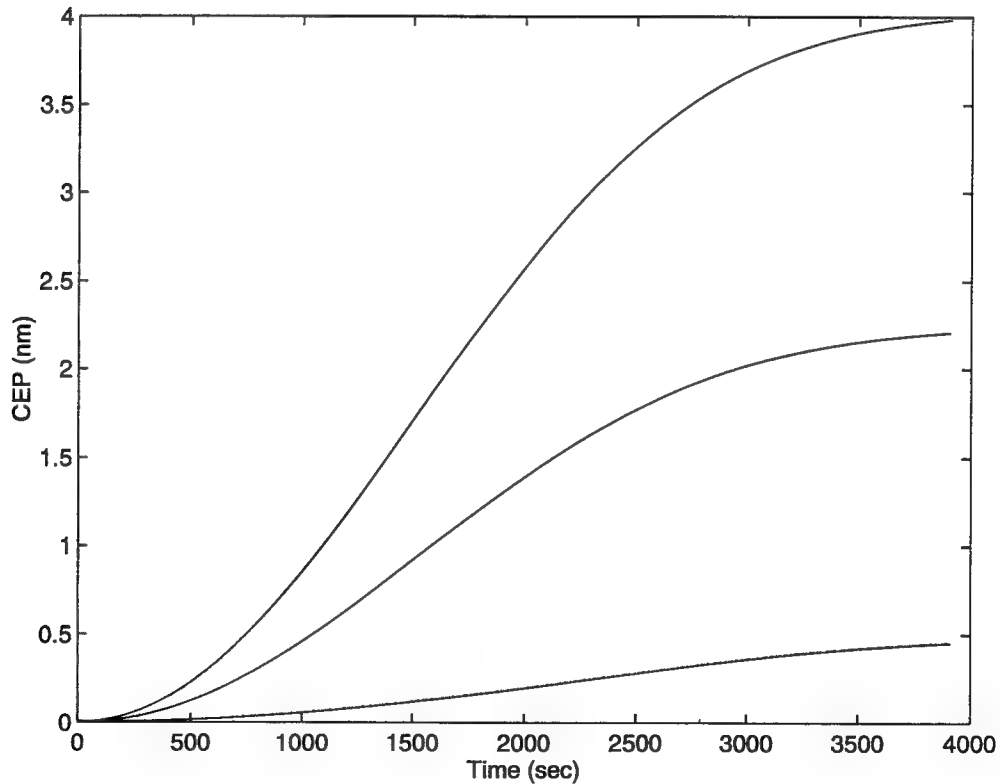


Figure 4 - 1. CEP curves for the 0.4 nm/hr, 2.0 nm/hr and 4.0 nm/hr INS

4.4 Filter Tuning Example

This section describes the author's approach to tuning the filter error states. Obviously, to land an aircraft safely, a 3-dimensional representation of position is of utmost importance, particularly with regard to the vertical axis. Also of importance to the author was to estimate the GPS clock bias error adequately since this is the largest contributor to the P-Code GPS receiver error. Again, looking at the "big-picture", the truth model used in the simulation is composed of 69 error states which attempt to represent the actual error outputs of the real-world avionics on board our simulated aircraft. Theoretically, 69 error states is a minuscule amount when actually an infinite amount of error states would be needed to represent the real-world avionics; nevertheless, the 69 error states are assumed to provide an adequate *truth* source.

Our truth model (numbering 69 error states) requires a large amount of computer processing, and a filter based upon this truth model would not be feasible at the present time to use onboard civil aviation aircraft. Our objective in this thesis is to minimize computer processor time (through number of error states) and costs, thus we try to use a subset of the truth model error states as the filter model error states. If we are successful, we will be able to choose a truth model subset (in this thesis called the filter model, which is composed of 13 states) that adequately models the truth model (remembering that the truth model represents the real world). We will add a specific amount of white noise to the differential equations for our individual filter model error states to compensate for truth model error states we were unable to model specifically and distinctly using our "less-complex" filter model. Performing this procedure is considered tuning the dynamics noise strengths or "Q" values of the filter model. (Another parameter tuned is the "R" value of the measurement equations, i.e., the measurement noise covariance matrix. The "R" tuning is not described in this example, though it follows similar procedures. For more information see [40,41,42]). Recall "Q" and "R" from earlier model equations of Chapter 3.

Let's look at several states of Case I (which utilizes a 0.4 nm/hr INS) that were tuned using the legend in Figure 4 - 2.

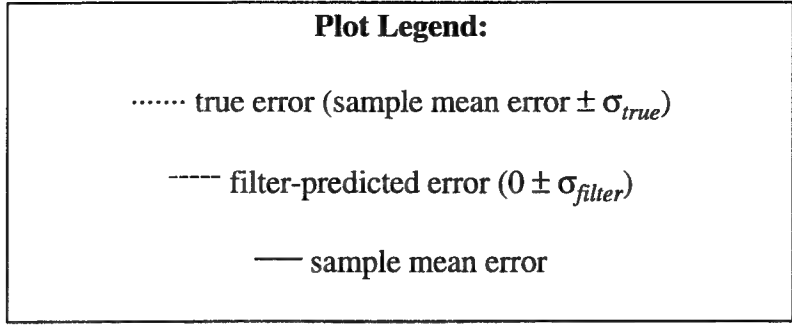


Figure 4 - 2. Plot Legend

The plots contained in Appendix G - Appendix U contain *five* traces. The innermost trace (a solid line —) on each data plot is the **sample mean** error time history for the applicable error state and is defined by [58,40]:

$$\hat{M}_e(t_i) = \frac{1}{N} \sum_{j=1}^N e_j(t_i) = \frac{1}{N} \sum_{j=1}^N \left\{ \hat{x}_j(t_i) - x_{true_j}(t_i) \right\} \quad (4.10)$$

where $\hat{x}_j(t_i)$ is the filter-computed estimate of a given navigation variable and $x_{true_j}(t_i)$ is the *truth* model value of the same variable, at time t_i , for sample run j . N is the number of Monte Carlo runs in the simulation (15 in this thesis) [45].

In addition to the center trace, two more *pairs* of lines are plotted. The first pair (represented by "dots" in the plots) is the *Mean ± Sigma*. The *Mean ± Sigma* is symmetrically displaced about the *mean error*, $\hat{M}_e(t_i)$. The *Mean ± Sigma* is the sum of the previously defined mean, $\hat{M}_e(t_i)$, and the actual filter standard deviation $\pm \sqrt{P_e(t_i)}$, where $P_e(t_i)$ is the *true* error sample variance at time t_i . The true standard deviation is calculated from the following equation [45,40]:

$$\sigma_{true}(t_i) = \sqrt{P_e(t_i)} = \sqrt{\frac{1}{N-1} \sum_{j=1}^N e_j^2(t_i) - \frac{N}{N-1} \hat{M}_e^2(t_i)} \quad (4.11)$$

where N is the number of runs in the Monte Carlo simulation (15 in this thesis), and $\hat{M}_e^2(t_i)$ is the square of the mean of the variable at each time of interest.

The last pair of traces (represented by "dashes" ----) is the filter-computed $\pm \sigma$ filter values for the same variables of interest and are symmetrically displaced about zero because the filter "believes" that it is producing zero mean errors [45]. These quantities

are propagated and updated in the MSOFE [48] software using the covariance propagation equation shown in Chapter 2. Thus, this last pair of traces represents the filter's estimate of the size of its own error.

We first begin this example with tuning the three tilt error states. A fruitful tuning strategy was found to entail tuning the platform (tilts) first, then tuning the accelerometers. Looking at Figure G - 1 in Appendix G, we see conservative tuning for the North, West and Azimuth Tilts when compared with Figure G - 2 in Appendix G (the true error, mean error $\pm \sigma_{true}$, is well within filter-computed, $0 \pm \sigma_{filter}$, error). Figure G - 2 has been tuned by decreasing the Q values as shown in Table 4 - 7.

LSM Filter State Number	LSM State Name	Q-value (Before) (ft ² /s ⁴)	Q-value (After) (ft ² /s ⁴)	SNU-84 State Number	NRS State Number
4	N-Tilt	9.52E-13	8.56E-13	4	4
5	W-Tilt	9.52E-13	8.56E-13	5	5
6	Az-Tilt	1.62E-11	1.52E-11	6	6

Table 4 - 7. Q-Values for N, W and Az Tilts (Before and After Tuning)

The North, West and Vertical velocity error states were tuned conservatively at the start as shown in Figure G - 3. Figure G - 4 shows final tuning of North, West and Vertical velocities. Note that the vertical velocity plot in Figure G - 4 may not be conservative enough: true mean error $\pm \sigma_{true}$ does not *always* stay within $0 \pm \sigma_{filter}$. Table 4 - 8 shows the old and new filter tuning Q values of Figure G - 3 and Figure G - 4.

LSM Filter State Number	LSM State Name	Q-value (Before) (ft ² /s ⁴)	Q-value (After) (ft ² /s ⁴)	SNU-84 State Number	NRS State Number
7	N-Velocity	1.54E-3	5.15E-6	7	7
8	W-Velocity	1.54E-3	5.15E-6	8	8
9	Vertical Velocity	7.20E-3	7.72E-3	9	9

Table 4 - 8. Q-Values for N, W and Vertical Velocity (Before and After Tuning)

Lastly, the remainder of the filter states were tuned. The results of these filters tunings are used for Case I. If the reader is interested, final tuning plots for all filter states of this example can be found by looking in Appendix H, Case I tuning plots.

4.5 Radar Altimeter/Baro/GPS Aiding of the 0.4 nm/hr, 2.0 nm/hr and 4.0 nm/hr INS

This section discusses the results of Cases I-VI. Case I-VI plots are located in Appendix H - Appendix M. Cases I, III and V do not use radar altimeter aiding, whereas, Cases II, IV and VI do.

4.5.1 Case I and Case II - 0.4 nm/hr INS

- Case I (Figures H - 1 - H - 6 in Appendix H)

The Tanker flight profile as described in Section 4.1 was flown with no outages (at all times) of 4 SV GPS coverage. Throughout the flight, the INS errors were bounded by GPS aiding. Filter-predicted error of longitude during the last 11 minutes of flight slightly underestimate the true error (Figure H-1 and Figure H-3 being of particular interest with respect to performance). This slight underestimation (2 feet) can easily be corrected by adjusting the 'Q' value for the respective horizontal error state following the tuning example described in Section 4.4. The primary goal of this thesis was to show filter performance trends; 'Q' value filter tuning as shown for *all cases* is reasonable, though not in an ultimate final form for flight test purposes due to time constraints. Note again that, for all cases, changing of SVs can become quite evident in enhancing or degrading one's overall navigation solution (by increasing or decreasing DOP). Sections 4.5 - 4.8 clearly show evidence of *degradation* when a SV change occurs at T = 2400 seconds.

Note that conservative filter performance of Table 4 - 9 is due to conservative σ_{filter} vs. σ_{true} 'R' tuning of the satellite vehicle measurements. The σ_{filter} and σ_{true} values chosen for satellite vehicle 'R' measurements were 8.66 ft and 1.414 ft, respectively; See Table B - 11 in Appendix B (discussed in Section I for Case II). The choices of σ_{filter} and σ_{true} dictate a "flooring" value seen in the true and filter performance. The 'R' tuning values stated above are used for all cases in Section 4.5 - 4.8; thus in all cases investigated in this thesis, the filter performance will show overly conservative results (evident in Tables 4 - 9, 4 - 11, 4 - 13, and 4 - 21).

- Case II (Figures I - 1 - I - 6 in Appendix I)

This is the same as Case I except at approximately 3000 ft (AGL), the radar altimeter begins to provide measurements to the Kalman filter. The accuracy of the radar

altimeter measurements increases (i.e. "R" value decreases) as altitude above the ground decreases (see Section 3.4.2, radar altimeter description).

The following error states showed improvement using the radar altimeter measurements:

- Aircraft altitude (See Figure I - 2 and I - 3, compared to Figures H - 2 and H - 3)
- Longitude error (See Figure I - 1, compared to H - 1)
- GPS user clock bias (See Figure I - 6, compared to H - 6)

Table 4 - 9 summarizes Case I and Case II landing system performance at respective decision heights.

Position Error State	Decision Height (feet)	Case I True Error (feet)	Case I Filter Error (feet)	Case II True Error (feet)	Case II Filter Error (feet)
δ latitude	200	8.81	9.85	8.72	9.69
δ latitude	100	9.40	9.80	9.13	9.69
δ latitude	50	8.61	9.80	8.35	9.69
δ longitude	200	9.14	10.68	8.83	10.58
δ longitude	100	9.77	10.68	9.65	10.58
δ longitude	50	8.83	10.69	8.70	10.58
δ altitude	200	14.2	15.1	3.76	7.74
δ altitude	100	15.65	15.1	2.43	7.57
δ altitude	50	15.3	15.1	2.64	7.52

Table 4 - 9. Case I and Case II 1σ Latitude, Longitude and Altitude Errors

Clearly, as indicated in the last 3 rows of Table 4 - 9, the radar altimeter reduces the altitude error. A zoomed-in plot of horizontal errors latitude, longitude and vertical errors using the radar altimeter for Case II is found in Figure I - 3 of Appendix I. "Flooring" occurs in the altitude plot of Figure I - 3 as the aircraft gets lower in altitude; the filter becomes more overly conservative. Re-tuning to achieve better tuning for all time, especially near decision points, would be useful to accomplish. Note the increased accuracy when the radar altimeter measurements become available at $T \geq 3641$ seconds. The radar altimeter (Case II) reduced the aircraft altitude error during the final approach by approximately 80% (true) and 49% (filter-predicted).

Table 4 - 10 summarizes the Case I and Case II performance in terms of what Category of Precision Approach is met based on Horizontal and Vertical errors.

Case Number	Horizontal (Based on True Estimated Error)	Horizontal (Based on Filter Predicted Error)	Vertical (Based on True Estimated Error)	Vertical (Based on Filter Predicted Error)
I	Cat I	Cat I	None	None
II	Cat I	Cat I	Cat II	None

Table 4 - 10. Precision Landing Category Predicted To Achieve

The filter-predicted error in the vertical channel with radar altimeter aiding exceeds the Category I landing specification by approximately 1 foot, but the true error shows that the system with the radar altimeter could possibly meet Category II landings vertically, but not Category II horizontally. For Case I (Baro-altimeter and P-Code GPS aiding) a precision approach is impossible due to the large vertical errors. Additional tuning ('R_{filter}') of Case II filter is required to meet a precision approach, but it was not accomplished in this thesis due to time constraints.

4.5.2 Case III and Case IV - 2 nm/hr INS

- Case III (Figures J - 1 - J - 6 in Appendix J)

The Tanker profile as described in Section 4.1 was flown with no outages of 4 SV GPS (coverage at all times). Throughout the flight, the 2.0 nm/hr INS errors were bounded by GPS aiding. Filter-predicted error of longitude for the first 11 minutes of flight underestimates the true error. Adjustment of the 'Q' value for the respective horizontal error state should be implemented as described in Section 4.4, though not done due to time constraints.

- Case IV (Figures K - 1 - K - 6 in Appendix K)

This is the same as Case III except at approximately 3000 ft (AGL), the radar altimeter begins to provide measurements to the Kalman filter. The accuracy of the radar altimeter measurements increases as altitude decreases. Using the radar altimeter (Case IV) reduced the aircraft altitude error during final approach by approximately 84% (true) and 47% (filter-predicted).

Table 4 - 11 summarizes Case III and Case IV landing system performance at respective decision heights. Table 4 - 12 summarizes the Case III and Case IV

performance in terms of what Category of Precision Approach is met based on Horizontal and Vertical errors.

In Case III, only the horizontal components of position will meet Category I requirements. Case IV results show that the current filter overestimates the true error by 244% at Decision Height (DH) of 200, 161% at DH of 100 and 345% at DH of 50. Additional filter tuning specifically during the landing phase of the flight profile is needed to meet a CAT I precision approach. Additional tuning was not performed due to time constraints of this project. Conservative tuning of the filter is discussed in Chapter 5.

Position Error State	Decision Height (feet)	Case III True Error (feet)	Case III Filter Error (feet)	Case IV True Error (feet)	Case IV Filter Error (feet)
δ latitude	200	8.49	9.90	8.47	9.75
δ latitude	100	9.01	9.90	9.46	9.74
δ latitude	50	8.67	9.90	8.95	9.74
δ longitude	200	9.16	10.75	9.08	10.60
δ longitude	100	9.81	10.76	9.64	10.65
δ longitude	50	8.79	10.76	9.39	10.65
δ altitude	200	15.1	15.8	2.43	8.37
δ altitude	100	15.93	15.8	3.14	8.21
δ altitude	50	15.3	15.8	1.83	8.16

Table 4 - 11. Case III and Case IV 1σ Latitude, Longitude and Altitude Errors

Case Number	Horizontal (Based on True Estimated Error)	Horizontal (Based on Filter Predicted Error)	Vertical (Based on True Estimated Error)	Vertical (Based on Filter Predicted Error)
III	Cat I	Cat I	None	None
IV	Cat I	Cat I	Cat I	None

Table 4 -12. Precision Landing Category Predicted To Achieve

4.5.3 Case V and Case VI - 4 nm/hr INS

- Case V (Figures L - 1 - L - 6 in Appendix L)
- Case VI (Figures M - 1 -M - 6 in Appendix M)

The 4.0 nm/hr INS was bounded by GPS for Case V and by the combination of GPS/Radar altimeter measurement for Case VI. Again, filter-predicted error of Longitude

for the last 11 minutes of flight may underestimate the true Longitude error. Adjustment of the Q value for the respective horizontal error state should be implemented as described in Section 4.4. Using the radar altimeter (Case VI) reduced the aircraft altitude error during final approach by approximately 85% (true) and 45% (filter predicted).

Table 4 - 13 summarizes Case V and Case VI landing system performance at respective decision heights.

Position Error State	Decision Height (feet)	Case I True Error (feet)	Case I Filter Error (feet)	Case II True Error (feet)	Case II True Error (feet)
δ latitude	200	8.63	9.95	8.40	9.79
δ latitude	100	9.43	9.95	9.16	9.78
δ latitude	50	8.73	9.95	8.85	9.80
δ longitude	200	9.12	10.8	8.77	10.70
δ longitude	100	9.91	10.8	9.93	10.71
δ longitude	50	8.72	10.8	9.44	10.71
δ altitude	200	14.96	15.75	2.39	8.23
δ altitude	100	16.5	15.75	2.82	8.10
δ altitude	50	15.3	15.75	1.75	8.00

Table 4 - 13. Case V and Case VI 1σ Latitude, Longitude and Altitude Errors

Table 4 - 14 summarizes the Case V and Case VI performance in terms of what Category of Precision Approach is met based on Horizontal and Vertical errors.

Case Number	Horizontal (Based on True Estimated Error)	Horizontal (Based on Filter Predicted Error)	Vertical (Based on True Estimated Error)	Vertical (Based on Filter Predicted Error)
V	Cat I	Cat I	None	None
VI	Cat I	Cat I	Cat I	None

Table 4 -14. Precision Landing Category Predicted To Achieve

Additional filter tuning specifically during the landing phase of the flight profile is needed to meet a CAT I precision approach. Due to time constraints, final filter tuning was not accomplished, but will be discussed as an issue in Chapter 5.

4.6 Radar Altimeter/Baro/GPS Aiding of the 0.4 nm/hr, 2.0 nm/hr and 4.0 nm/hr INS using an Additional Single Pseudolite during the Landing Approach

This section discusses the enhancement when an additional measurement from a single pseudolite is positioned along the final approach path. Averaged results from Cases VII to XII will be compared with the *baseline* Cases I, III and V of Section 4.5. "Averaged" values were permitted to be used based on the fact that no significant performance difference is noted between each respective INS *when there were no GPS measurement outages*. An illustration of the aircraft final approach and pseudolite location is found in Section 4.6.1.

4.6.1 Cases VII, VIII and IX - Pseudolite But No Radar Altimeter

Case VII, Case VIII and Case IX follow the configuration found in Table 4 - 15.

Case VII	Case VIII	Case IX
Barometric Altimeter	Barometric Altimeter	Barometric Altimeter
0.4 nm/hr CEP INS	2.0 nm/hr CEP INS	4.0 nm/hr CEP INS
P-Code GPS	P-Code GPS	P-Code GPS
Pseudolite	Pseudolite	Pseudolite

Table 4 - 15. Case VII, Case VIII and Case IX Configurations

- Case VII (Figures N - 1 - N - 6 in Appendix N)
- Case VIII (Figures O- 1 - O - 6 in Appendix O)
- Case IX (Figures P - 1 -P - 6 in Appendix P)

The pseudolite placement was chosen to minimize VDOP errors during a portion of the aircraft landing. VDOP decreased from 1.7 to 1.3 using the single pseudolite. This decrease in VDOP (23 %) is reflected in the decrease in altitude error (21.3%) seen when comparing the averaged results of Cases I, III, V vs. Cases VII - IX; see Table 4 - 16. It should be noted that the GPS receiver maintains lock on the best four SV overhead, while maintaining lock on the fifth SV (the pseudolite on the ground). The designer must maintain the insight on importance of geometry if it is necessary to replace one of the

existing SVs overhead, with a ground based pseudolite instead. The GPS receiver must simultaneously maintain an adequate (minimal) HDOP and PDOP at all times during the precision approach. Alternate locations of pseudolites and their impact on performance (due to geometry) must be chosen with care.

The aircraft is assumed to be following a precision approach pattern, landing at Wright-Patterson AFB, OH as found in [15]. A pseudolite is placed at the coordinates indicated in Figures 4 - 3 and 4 - 4. At T=3641, the pseudolite measurement is available and being processed once every second. The aircraft has continued its descent from 4028 feet (MSL) to 3799 feet (MSL) (where elapsed time is now, T=3658 seconds) and makes a +45° turn to align itself with the runway (Heading 232°). The aircraft continues its descent at a 3° glideslope, now aligned with the runway (Heading 232°) at a velocity of 133 knots. The aircraft lands at an elapsed time of T=3913 seconds true altitude is 0 ft (AGL), 825 ft (MSL).

Looking at the plots of Cases VII, VIII and IX (in Appendix N, Appendix O and Appendix P), it is clearly evident that the Latitude, Longitude, Altitude and GPS clock bias errors are significantly reduced. Seen at T = 2400 and T = 3300 are large effects of latitude, longitude and clock bias error due to satellite vehicle changes. Table 4 - 16 shows the average true error reduction by using the single pseudolite when compared when no pseudolite is used (Case I, Case III and Case V).. Note again that Cases I, III and V results are averaged due to similar results between INS types with no GPS outages.

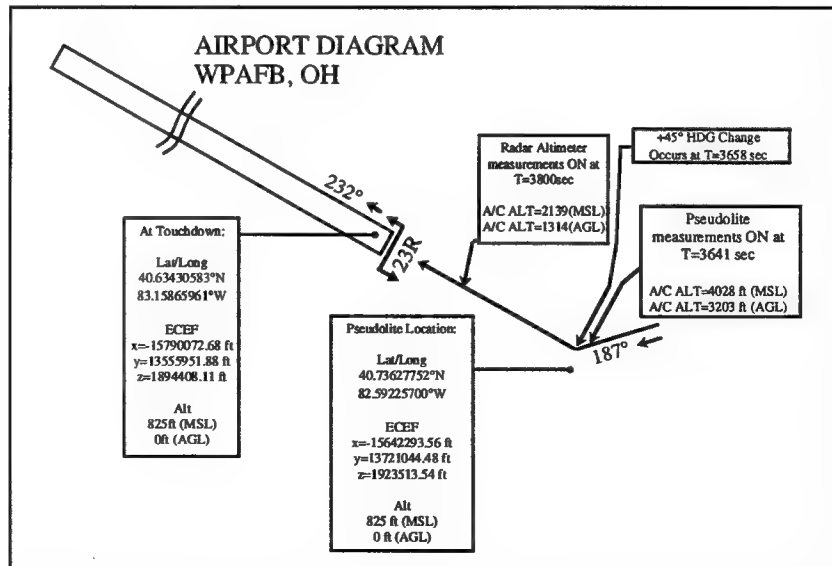


Figure 4 - 3. Top View of Tanker Precision Approach

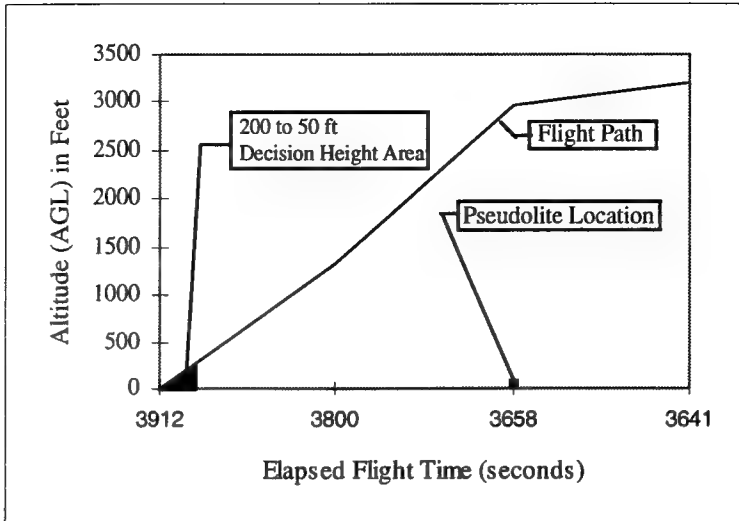


Figure 4 - 4. Side View of Tanker Precision Approach

Error State	Case I, III, V average true error (feet)	Case VII - IX average true error (feet)	% Change in Error
Latitude	8.9	4.6	48.3%
Longitude	9.2	3.9	57.6%
Altitude	15.0	11.8	21.3%
Clock Bias	9.0	4.9	45.6%

Table 4 - 16. Averaged True Error Reduction Using a Single Pseudolite

It should be remembered that by no means is the location of the single pseudolite "optimal". No real criterion was used when selecting the pseudolite location. As can be seen in Figure 4 - 4, by the time the aircraft is near the Category I, 200-foot decision height, the pseudolite location will primarily aid in the horizontal channel. Pseudolite placement nearer to the decision heights may aid the vertical channel by an additional 12% to 23%; the goal is to bring and maintain VDOP from 1.3 to 1.0. Readers may wish to consult [12] for further reference on pseudolites. Also, it was assumed no multipath errors exist at the given location and SV clock bias, SV position errors, tropospheric and ionospheric errors could be ignored. Thus, for an aircraft using a 0.4, 2.0 or 4.0 nm/hr INS, using a P-code receiver (no differential corrections or carrier-phase measurements) and the assumed location (non-optimal) of a single pseudolite, Category I precision approach is met for horizontal errors, but no category of precision approach is possible in the vertical axis (again, based on the non-optimal location of the pseudolite).

Table 4 - 17 summarizes the Case VII, Case VIII and Case XI performance in terms of what category of precision approach could be met based on horizontal and vertical errors.

Case Number	Horizontal (Based on True Estimated Error)	Horizontal (Based on Filter Predicted Error)	Vertical (Based on True Estimated Error)	Vertical (Based on Filter Predicted Error)
VII-IX	Cat I	Cat I	None	None

Table 4 - 17. Precision Landing Category Predicted To Achieve

4.6.2 Cases X, XI and XII - Pseudolite and Radar Altimeter

Cases X, XI and XII follow the configuration found in Table 4 - 18.

- Case X (Figures Q - 1 - Q - 6 in Appendix Q)
- Case XI (Figures R- 1 - R - 6 in Appendix R)
- Case XII (Figures S - 1 -S - 6 in Appendix S)

Cases X, XI and XII are identical to the three cases of the previous section (Section 4.6.1) except at an elapsed flight time of T=3800 (aircraft on final approach at ALT of 2139 MSL or 1314 AGL) the radar altimeter measurements are available. The combination of the pseudolite and radar altimeter give performance enhancements summarized in Table 4 - 19 to Table 4 - 21. A large improvement can clearly be seen in Latitude, Longitude and GPS clock bias when the radar altimeter measurements are available at T \geq 3800 seconds in Appendices Q, R and S.

Case X	Case XI	Case XII
Barometric Altimeter	Barometric Altimeter	Barometric Altimeter
0.4 nm/hr CEP INS	2.0 nm/hr CEP INS	4.0 nm/hr CEP INS
P-Code GPS	P-Code GPS	P-Code GPS
Radar Altimeter and Pseudolite	Radar Altimeter and Pseudolite	Radar Altimeter and Pseudolite
No GPS Outage	No GPS Outage	No GPS Outage

Table 4 - 18. Case X, Case XI and Case XII Configurations

Error State	Case I, III, V average true error (feet)	Case X, XI, XII average true error (feet)	% Change in Error
Latitude	8.9	4.4	50.6%
Longitude	9.2	3.3	64.1%
Altitude	15.0	2.4	84.0%
Clock Bias	9.0	4	55.0%

Table 4 - 19. Averaged True Error Reduction, Case I-II-III vs. Case X-XI-XII

Error State	Case II, IV, VI average true error (feet)	Case X - XII average true error (feet)	% Change in Error
Latitude	8.8	4.4	50.0%
Longitude	9.2	3.3	64.1
Altitude	2.6	2.4	7.7%
Clock Bias	7.5	4	46.7%

Table 4 - 20. Averaged True Error Reduction, Case II-IV-VI vs. Case X-XI-XII

Error State	Case VII, VIII, IX average true error (feet)	Case X - XII average true error (feet)	% Change in Error
Latitude	4.6	4.4	4.4%
Longitude	3.9	3.3	15.4%
Altitude	11.8	2.4	79.7%
Clock Bias	4.9	4	18.4%

Table 4 - 21. Averaged True Error Reduction, Case VII-VIII-IX vs. Case X-XI-XII

Table 4 - 22 summarizes the Case X, Case XI and Case XII performance in terms of what category of precision approach could be met based on horizontal and vertical errors.

Case Number	Horizontal (Based on True Estimated Error)	Horizontal (Based on Filter Predicted Error)	Vertical (Based on True Estimated Error)	Vertical (Based on Filter Predicted Error)
X - XII	Cat II	Cat I	Cat II	None

Table 4 -22. Precision Landing Category Predicted To Achieve

4.7 Example of 0.4 nm/hr, 2.0 nm/hr and 4.0 nm/hr INS Drift during a Loss of GPS Measurement for 1/8 Schuler Period.

- Cases XIII, XIV and XV (Figures T - 1 -T - 13 in Appendix T)

Earlier cases (Cases I-XII, Sections 4.5 and 4.6) showed very little performance differences when comparing say, a 0.4 nm/hr INS and a 4.0 nm/hr INS. Performance differences were noted as slight because *no* degradation to the baro-altimeter, P-code GPS or radar altimeter measurements occurred. This section examines the possibility of loss of GPS for approximately 650 seconds (1/8 Schuler period). This experiment was chosen based upon noting that, in prior Cases I - XII, the three INS's do not seem to yield very different results with continuous GPS aiding. In the real world, loss of GPS measurements will unfortunately be the case and therefore loss of GPS measurements was investigated to view the performance of the true and filter parameters under a short time duration of GPS outage. The 1/8 Schuler period was chosen so it could be possible to multiply the error state degradations by a factor of 8, if one wishes to simulate a full 84-minute Schuler period (also, the flight profile totals only 65 minutes).

Basically, at an elapsed time of T=2000 seconds of the Tanker profile, loss of 4 SV measurements occurs. Loss of 4 SV simulates a possible flight scenario of terrorist jamming, an incapacitated GPS receiver, etc. The true and filter errors are seen to grow larger over time, until the GPS measurements are re-acquired at T=2630 sec. Once GPS measurements are re-acquired, estimation of the INS error occurs. Note the larger true position errors of the 4.0 nm/hr system (Figure T-1, bottom plot) vs. the smaller true position errors of the 0.4 nm/hr system (Figure T - 1, top plot); be aware of the dramatically different scales for the three plots. Also note that the altitude error (Figure T - 3) grows, but becomes bounded by baro altimeter aiding.

The point of this section is to show that, if a low accuracy INS is used in a GPS/INS Kalman filter integration for a landing system implementation, one must realize the consequences if the GPS measurement data is unavailable, especially during final approach. The results of this section are directly comparable to Cases I, III and V. Loss of GPS measurements, but with a system supplemented by a radar altimeter is explored further in Section 4.8.

The plots of Appendix T also show that the 4.0 nm/hr filter tuning overestimates errors grossly, compared with the 0.4 or 2.0 nm/hr filters. Overestimating of the true error by the system filter will be discussed in Chapter 5.

4.8 Performance Example of a 4.0 nm/hr INS during Two Periods of GPS Measurement Loss with Radar Altimeter Aiding during the Final Approach.

- Case XVI (Figures U - 1 -U - 6 in Appendix U)

This is the final performance evaluation researched in this thesis. The following scenario take place using the Tanker profile (See Section 4.1):

- T=1000 seconds: All GPS measurements are lost.
- T=1120 seconds: All GPS measurements have been re-acquired. A 120 second outage was chosen to "deprive" the INS of 120 SV measurements. It was thought this was could simulate a "popped" GPS receiver circuit breaker on the aircraft, allowing the GPS receiver time to re-acquire the *same* SV set as used prior to losing power.
- T=3300 All GPS measurement are lost.
Aircraft altitude is 7524 feet (MSL)
Aircraft altitude is 6699 feet (AGL)
- T=3641 seconds: Radar altimeter measurements are available.
Aircraft altitude is 4028 feet (MSL)
Aircraft altitude is 3203 feet (AGL)
- T=3750 seconds: GPS measurements are available. A 450 second GPS outage was chosen to allow enough time to degrade the INS performance severely.
Aircraft altitude is 2723 feet (MSL)
Aircraft altitude is 1898 feet (AGL)
- T=3915 Aircraft lands safely
Aircraft altitude is 825 feet (MSL)
Aircraft altitude is 0 feet (AGL)

Table 4 - 23 summarizes Case XVI landing system performance at respective decision heights. Table 4 - 24 summarizes the Case XVI performance in terms of what category of precision approach is met based on Horizontal and Vertical errors.

Case XVI was compared with Case VI. Results are shown in Table 4 - 25. Looking at Table 4 - 25, it is evident that a Category I landing is feasible, given the GPS outages listed above, as long as an independent measurement - the radar altimeter, is functioning.

Position Error State	Decision Height (feet)	Case XVI True Error (feet)	Case XVI Filter Error (feet)
δ latitude	200	9.29	9.78
δ latitude	100	8.86	9.78
δ latitude	50	9.47	9.78
δ longitude	200	9.75	10.7
δ longitude	100	9.55	10.7
δ longitude	50	9.71	10.7
δ altitude	200	3.04	11.51
δ altitude	100	3.69	11.4
δ altitude	50	3.98	11.4

Table 4 - 23 Case XVI 1σ Latitude, Longitude and Altitude Errors

Case Number	Horizontal (Based on True Estimated Error)	Horizontal (Based on Filter Predicted Error)	Vertical (Based on True Estimated Error)	Vertical (Based on Filter Predicted Error)
XVI	Cat I	None	Cat I	None

Table 4 - 24. Precision Landing Category Predicted To Achieve

The plots of Appendix U also show that the 4.0 nm/hr filter tuning overestimates errors grossly, compared with the 0.4 or 2.0 nm/hr filters. Overestimating of the true error by the system filter will be discussed in Chapter 5.

Error State	Case VI average true error (feet)	Case XVI average true error (feet)	% Change in Error
Latitude	8.8	9.2	4.5%
Longitude	9.4	9.7	3.2%
Altitude	2.3	3.6	56.5%
Clock Bias	6.0	6.1	1.7%

Table 4 - 25. Averaged True Error % Change, Case VI vs. Case XVI

4.9 Chapter Summary

This ends the analysis of the data collected from Case I to Case XVI scenarios. Tables 4 - 26 and 4 - 27 summarize the results from Case I - XVI, respectively. Note that no Category III precision approach was deemed possible by any Case number in this thesis.

The next chapter summarizes the results of this thesis and presents recommendations for future research.

Precision Approach Category	Case I	Case II	Case III	Case IV	Case V	Case VI	Case VII	Case VIII
I	No	Yes	No	Yes	No	Yes	No	No
II	---	---	---	---	---	---	---	---

Table 4 - 26. Summary of Cases I - VIII: Precision Approach Requirements Met

Precision Approach Category	Case IX	Case X	Case XI	Case XII	Case XIII	Case XIV	Case XV	Case XVI
I	No	---	---	---	No	No	No	Yes
II	---	Yes	Yes	Yes	---	---	---	---

Table 4 - 27. Summary of Cases IX - XVI: Precision Approach Requirements Met

V. Conclusions and Recommendations

Chapter 5 summarizes the research and presents recommendations and conclusions based on results presented in Chapter 4.

5.1 Introduction

In the case of aircraft integration, very few "integrated" GPS/INS studies have been accomplished with respect to implementing precision landing approaches. Instead, the majority of research efforts explored stand-alone GPS receiver technology. Instead of stand-alone GPS techniques, this thesis *integrated* the GPS with an INS/Baro altimeter system and a radar altimeter using an extended Kalman filter to meet FAA Category I and II precision approach *accuracy* requirements.

In order to accomplish thesis goals, this project concentrated on setting up reliable models for three different classes of INS (0.4, 2.0 and 4.0 nm/hr (CEP) INS systems), GPS (4 channel receiver, 5m vertical and 4m horizontal precision, 1σ), Baro Altimeter (50 - 150 ft, 1σ), and Radar altimeter (1% of altitude + "floor" value, 1σ). This thesis also developed a generic precision approach flight profile (using PROFGEN [47]) that encompassed a majority of aircraft types. Lastly, this thesis utilized a single ground-based SV (pseudolite) and available true post-processed ephemeris data [14,24], instead of prior *simulated* ephemeris data used at AFIT [58,3,45,50,27]. Once all the above elements were in place, the Multimode Simulation for Optimal Filter Evaluation (MSOFE) [48] was utilized to perform extended Kalman Filter integration analysis.

5.2 Conclusions

Use of an existing 0.4 nm/hr, 2.0 nm/hr and lower quality 4.0 nm/hr INS, when properly integrated with a 4-channel P-code GPS receiver and radar altimeter, can meet the FAA Category I precision approach. Use of an existing 0.4 nm/hr, 2.0 nm/hr and lower quality 4.0 nm/hr INS, when properly integrated with a 5-channel P-code GPS receiver (one channel using a ground based pseudolite) and radar altimeter, can meet the FAA Category II precision approach. These conclusions are made based on mainly four main factors:

1. Error models used in this simulation are realistic to the respective real-world black box output errors.

2. No radar altimeter measurement outages occur during the landing approach.
3. When radar altimeter measurements are available, the earth's surface will be modeled as flat and referenced approximately to the INS-indicated altitude (referenced to WGS-84 ellipsoid).
4. When use of the single pseudolite information is used, ionospheric, tropospheric, pseudolite position, pseudolite clock and multipath errors are negligible.

The use of real ephemeris data obtained from the National Geodetic Office was a first for use in an AFIT thesis. It is recommended by the author to use real ephemeris data, rather than use existing FORTRAN functions that simulate ephemeris data when possible.

The tanker profile looks to be a realistic flight scenario of a precision ILS approach at Wright-Patterson AFB, OH. PROFGEN [47] was utilized to create a trajectory that would represent a generic transport aircraft from take-off to a precision approach landing. This flight profile was named "Tanker" since its attributes closely resemble those of a KC-135 tanker (Boeing 707) aircraft.

The two additional INS models (2.0 nm/hr and 4.0 nm/hr) were created based on the NRS model of [45]. All models represent a set of "generic" INS's. All performance evaluations conducted in this research showed the 0.4, 2.0 and 4.0 nm/hr INS performed equally well *until* loss of GPS measurements occurred. If loss of GPS measurements occurred, the lower quality INS's navigation performance degraded rapidly. Lastly, due to the high " R_{filter} " radar altimeter measurement noise value and pseudolite measurement noise value, performance of the filter was overly conservative (achieving 1σ errors of 5 - 7 feet) during the final landing approach. Proper tuning of the R_{filter} measurement noise values would allow the filter's estimate of true errors to be less conservative (and more realistic). Time permitting, additional tuning of the filter model would have been accomplished in this thesis.

5.3 *Recommendations*

This thesis has pushed the performance capabilities of the hardware stated in Section 5.2 to meet a Category I and II specifications for landing. In order to meet a Category III approach, more precise measurements must be made available. Recommendations are as follows:

1. Make use of the centimeter accuracy of *carrier-phase* GPS signals, now readily available in commercial receivers. The carrier-phase information can be used for positional information as well as heading information (using multiple antennas) [64]. Decide whether one's algorithm will also handle "integer ambiguity" techniques, or assume no cycle slips. See Section 1.3.2 or [27,6] for more information regarding carrier-phase integer ambiguity and cycle slips.
2. Use Differential GPS measurements at all times for North America (assume Wide-area differential will be available). The models for filter design and for performance evaluation must make the distinction of representing a C/A or P-code receiver using differential corrections.
3. Maintain use of at least one pseudolite along the flight path. In fact, current flight testing is showing that use of two pseudolites optimally placed along the approach path is recommended [11].
4. Use, as a minimum, six (6) independent SV measurements (though, preferably, for any given time, use of all in-view SVs is preferred) rather than the current (archaic) military standard of four SVs (to minimize geometric dilution of precision (GDOP errors). (This thesis only used cases where 4 SV or 5 SV were used at one time).
5. Obtain and use published geographic data of Wright-Patterson AFB, and vicinity, so as to reference the radar altimeter outputs to WGS-84 ellipsoid (to match the INS positional outputs).
6. Use single filter (then continue analysis with small, non-computer-burdening multiple filters) and perform residual monitoring for use as a fault detection and isolation algorithm for GPS Space Segment system errors, to compensate for deliberate and non-deliberate jamming and spoofing of the SV signals. Fault detection must notify the pilot of a possible degraded navigation solution in less than 2 seconds, while minimizing false alarms.
7. Explore utilizing dynamic filter tuning procedures along the approach path when using pseudolites (i.e., at a given runway, multipath errors may be excessive; "R" tuning of the respective measurement may be necessary).

8. All analysis should show a detailed window of performance based on realistic SV geometries. SV geometries used in the analysis should be a function of the predicted number of SVs available within + 5 years time (based on SV launch schedules).

Appendix A. Error State Definitions for the LSM Truth and Filter Models

Tabular listings of the truth and filter models are presented. Tables A - 1 and A - 2 show the 39 INS states for the truth model, with the SNU 84-1 [litton] and NRS [mosle] state numbers given for cross-reference. Table A.3 list the GPS states respectively, and Table A - 4 lists the states in the reduced-ordered LSM filter model.

Note: In Table A - 1, the LSM states 12 and 13 are not included; these are found in Table A - 3.

LSM State	State Symbol	Definition	SNU 84-1 State	NRS State
1	$\delta\theta_x$	X-component of vector angle from true to computer frame	1	1
2	$\delta\theta_y$	Y-component of vector angle from true to computer frame	2	2
3	$\delta\theta_z$	Z-component of vector angle from true to computer frame	3	3
4	ϕ_x	X- component of vector angle from true to platform frame	4	4
5	ϕ_y	Y- component of vector angle from true to platform frame	5	5
6	ϕ_z	Z- component of vector angle from true to platform frame	6	6
7	δV_x	X-component of error in computed velocity	7	7
8	δV_y	Y-component of error in computed velocity	8	8
9	δV_z	Z-component of error in computed velocity	9	9
10	δh	Error in vehicle altitude above reference ellipsoid	10	10
11	δh_B	Total baro-altimeter correlated error	23	11
14	δh_L	Error in lagged inertial	11	16
15	δS_3	Error in vertical channel aiding state	12	17
16	δS_4	Error in vertical channel aiding state	13	18
17	Δx_c	X-component of accelerometer and velocity quantizer correlated noise	17	19
18	Δy_c	Y-component of accelerometer and velocity quantizer correlated noise	18	20
19	Δz_c	Z-component of accelerometer and velocity quantizer correlated noise	19	21
20	δg_x	X-component of gravity vector errors	20	22
21	δg_y	Y-component of gravity vector errors	21	23
22	δg_z	Z-component of gravity vector errors	22	24

Table A - 1. 39-State INS System Model: First 20 States

Note: LSM state 12 and state 13 are located in Table A - 3

State Number	State Symbol	Definition	SNU 84-1 State	NRS State
23	b_x	X-component of gyro drift rate repeatability	30	25
24	b_y	Y-component of gyro drift rate repeatability	31	26
25	b_z	Z-component of gyro drift rate repeatability	32	27
26	S_{gx}	X-component of gyro scale factor error	33	28
27	S_{gy}	Y-component of gyro scale factor error	34	29
28	S_{gz}	Z-component of gyro scale factor error	35	30
29	∇b_x	X-component of accelerometer bias repeatability	48	31
30	∇b_y	Y-component of accelerometer bias repeatability	49	32
31	∇b_z	Z-component of accelerometer bias repeatability	50	33
32	S_{Ax}	X-component of accelerometer and velocity quantizer scale factor error	51	34
33	S_{Av}	Y-component of accelerometer and velocity quantizer scale factor error	52	35
34	S_{Az}	Z-component of accelerometer and velocity quantizer scale factor error	53	36
35	S_{OAx}	X-component of accelerometer and velocity quantizer scale factor asymmetry	54	37
36	S_{OAv}	Y-component of accelerometer and velocity quantizer scale factor asymmetry	55	38
37	S_{OAz}	Z-component of accelerometer and velocity quantizer scale factor asymmetry	56	39
38	μ_1	X accelerometer misalignment about Z-axis	66	40
39	μ_2	Y accelerometer misalignment about Z-axis	67	41
40	μ_3	Z accelerometer misalignment about Y-axis	68	42
41	σ_1	X accelerometer misalignment about Y-axis	69	43

Table A - 2. 39-state INS System Model: Second 19 States

State Number	State Symbol	Definition	NRS State
12	δR_{clku}	User clock bias	14
13	δD_{clku}	User clock drift	15
42	δR_{cloop1}	SV 1 code loop error	68
43	δR_{trop1}	SV 1 tropospheric error	69
44	δR_{ion1}	SV 1 ionospheric error	70
45	δR_{clksv1}	SV 1 clock error	71
46	δx_{sv1}	SV 1 x-component of position error	72
47	δy_{sv1}	SV 1 y-component of position error	73
48	δz_{sv1}	SV 1 z-component of position error	74
49	δR_{cloop2}	SV 2 code loop error	75
50	δR_{trop2}	SV 2 tropospheric error	76
51	δR_{ion2}	SV 2 ionospheric error	77
52	δR_{clksv2}	SV 2 clock error	78
53	δx_{sv2}	SV 2 x-component of position error	79
54	δy_{sv2}	SV 2 y-component of position error	80
55	δz_{sv2}	SV 2 z-component of position error	81
56	δR_{cloop3}	SV 3 code loop error	82
57	δR_{trop3}	SV 3 tropospheric error	83
58	δR_{ion3}	SV 3 ionospheric error	84
59	δR_{clksv3}	SV 3 clock error	85
60	δx_{sv3}	SV 3 x-component of position error	86
61	δy_{sv3}	SV 3 y-component of position error	87
62	δz_{sv3}	SV 3 z-component of position error	88
63	δR_{cloop4}	SV 4 code loop error	89
64	δR_{trop4}	SV 4 tropospheric error	90
65	δR_{ion4}	SV 4 ionospheric error	91
66	δR_{clksv4}	SV 4 clock error	92
67	δx_{sv4}	SV 4 x-component of position error	93
68	δy_{sv4}	SV 4 y-component of position error	94
69	δz_{sv4}	SV 4 z-component of position error	95

Table A - 3. 30-State GPS System Model

State Number	State Symbol	Definition	NRS State
1	$\delta\theta_x$	X-component of vector angle from true to computer frame	1
2	$\delta\theta_y$	Y-component of vector angle from true to computer frame	2
3	$\delta\theta_z$	Z-component of vector angle from true to computer frame	3
4	ϕ_x	X- component of vector angle from true to platform frame	4
5	ϕ_y	Y- component of vector angle from true to platform frame	5
6	ϕ_z	Z- component of vector angle from true to platform frame	6
7	δV_x	X-component of error in computed velocity	7
8	δV_y	Y-component of error in computed velocity	8
9	δV_z	Z-component of error in computed velocity	9
10	δh	Error in vehicle altitude above reference ellipsoid	10
11	δh_B	Total baro-altimeter correlated error	11
12	δclk_b	User clock bias	14
13	δclk_{dr}	User clock drift	15

Table A - 4. 13-State Reduced-Order Filter Model

Appendix B. Dynamics Matrices and Noise Values

B.1 Definition of Dynamics Matrices

In Chapter 3, the truth and filter model dynamics are defined by the submatrices, F_{Filter} , $F_{INS_{t1}}$, $F_{INS_{t2}}$ and F_{GPS_t} of Equation (3.3). The F_{Filter} represents the filter dynamics matrix, which is also a submatrix of the larger truth model dynamics matrix [mosle]. The other three matrices represent the additional truth model non-zero portions of the \mathbf{F} matrix that simulate the real world [mosle]. Tables B.2, B.3, B.4 and B.5 contain the non-zero elements of the dynamics submatrices F_{Filter} , $F_{INS_{t1}}$, $F_{INS_{t2}}$ and F_{GPS_t} , respectively. All undeclared variables shown in the following tables are defined in the LN-93 technical report, along with their units [litton,mosle]. The structure of the dynamics matrices in this chapter correspond to the truth model state definitions in Appendix A and to the AFIT thesis (NRS model) by [mosle]. The notation used in Tables B.2 - B.4 in this Appendix is defined in Table B.1.

ρ_x, ρ_y, ρ_z	Components of angular rate of navigation frame with respect to the earth (craft rate), coordinatized in Litton True frame
$\Omega_x, \Omega_y, \Omega_z$	Components of earth sideral rate vector (earth rate), coordinatized in Litton ECEF, with respect to inertial space
a	Equatorial radius of the earth (6378388 meters)
g_0	Equatorial gravity magnitude ($32.08744 \text{ ft/sec}^2$)
$\omega_{itx}, \omega_{ity}, \omega_{itz}$	Components of angular rate of navigation frame with respect to inertial space (spatial rate), coordinatized in Litton True frame
V_x, V_y, V_z	Components of vehicle velocity vector with respect to earth-fixed coordinates
A_x, A_y, A_z	Components of specific force, coordinatized in Litton True frame
C_{RX}, C_{RY}	Components of earth spheroid inverse radii of curvature
$\omega_{ibx}, \omega_{iby}, \omega_{ibz}$	Components of angular rate of navigation frame with respect to inertial space (spatial rate), coordinatized in Litton Body frame
$C_{i,j}$	Elements of the transformation matrix C_{body}^{nav}
$\beta\delta_{hc}$	Barometer inverse correlation time (600 seconds)
$\beta\nabla_{xc}, \beta\nabla_{yc}, \beta\nabla_{zc}$	Gyro inverse correlation time constants (5 minutes)
$\beta\delta_{gx}, \beta\delta_{gy}, \beta\delta_{gz}$	Gravity vector error inverse correlation time constants (Velocity/correlation distance)
$\sigma_{\delta hc}^2$	Variance of barometer correlated noise
$\sigma_{\nabla xc}^2, \sigma_{\nabla yc}^2, \sigma_{\nabla zc}^2$	Variances of accelerometer correlated noise
$\sigma_{\delta gx}^2, \sigma_{\delta gy}^2, \sigma_{\delta gz}^2$	Variances of gravity vector correlated noise
$\sigma_{\eta bx}^2, \sigma_{\eta by}^2, \sigma_{\eta bz}^2$	Power spectral density value of gyro drift rate white noise
$\sigma_{\eta Ax}^2, \sigma_{\eta Ay}^2, \sigma_{\eta Az}^2$	Power spectral density value of accelerometer white noise
k_1, k_2, k_3, k_4	Vertical channel gains of vertical channel error model (see figure 2 of [litton])

Table B - 1. Notation of Variables used in Tables B - 2 to B - 4

Element	Variable	Element	Variable
(1,3)	$-\rho_y$	(1,8)	$-C_{RY}$
(2,3)	ρ_x	(2,7)	C_{RX}
(3,1)	ρ_y	(3,2)	$-\rho_z$
(4,2)	$-\Omega_z$	(4,3)	Ω_y
(4,5)	ω_{itz}	(4,6)	$-\omega_{ity}$
(4,8)	$-C_{RY}$	(5,1)	Ω_z
(5,3)	$-\Omega_x$	(5,4)	$-\omega_{itz}$
(5,6)	ω_{itx}	(5,7)	C_{RX}
(6,1)	$-\Omega_y$	(6,2)	Ω_x
(6,4)	ω_{ity}	(6,5)	$-\omega_{itx}$
(7,1)	$-2V_y\Omega_y - 2V_z\Omega_z$	(7,2)	$2V_y\Omega_x$
(7,3)	$2V_z\Omega_y$	(7,5)	$-A_z$
(7,6)	A_y	(7,7)	$-V_z C_{RX}$
(7,8)	$2\Omega_z$	(7,9)	$-\rho_y - 2\Omega_y$
(8,1)	$2V_x\Omega_y$	(8,2)	$2V_x\Omega_x - 2V_z\Omega_z$
(8,3)	$2V_z\Omega_y$	(8,4)	A_z
(8,6)	$-A_x$	(8,7)	$-2\Omega_z$
(8,8)	$-V_z C_{RY}$	(8,9)	$\rho_x + 2\Omega_x$
(9,1)	$2V_x\Omega_z$	(9,2)	$2V_y\Omega_z$
(9,3)	$-2V_y\Omega_y - 2V_x\Omega_x$	(9,4)	$-A_y$
(9,5)	A_x	(9,7)	$\rho_y - 2\Omega_y + V_x C_{RX}$
(9,8)	$-\rho_x - 2\Omega_x + V_y C_{RY}$	(9,10)	$2g_o/a$
(11,11)	$-\beta_{dhc}$	(14,15)	$1 \text{ ft}^2/\text{sec}$

Table B-2. Elements of the Dynamics Submatrix F_{Filter}

Element	Variable	Element	Variable	Element	Variable
(9,16)	$-k_2$	(9,17)	-1	(9,18)	k_2
(10,9)	1	(10,16)	$-k_1$	(10,18)	k_1-1
(16,10)	1	(16,16)	-1	(17,16)	k_3
(17,18)	$-k_3$	(18,10)	k_4	(18,16)	$-k_4$
(7,19)	C_{11}	(7,20)	C_{12}	(7,21)	C_{13}
(7,22)	1	(8,19)	C_{21}	(8,20)	C_{22}
(8,21)	C_{23}	(8,23)	1	(9,19)	C_{31}
(9,20)	C_{32}	(9,21)	C_{33}	(9,24)	1
(9,11)	k_2	(10,11)	k_1	(17,11)	$-k_3$
(18,11)	$k_4/600$	(18,18)	k_4-1	(9,43)	$C_{33}A_x^B$
(4,25)	C_{11}	(4,26)	C_{12}	(4,27)	C_{13}
(4,28)	$C_{11}\omega_{ibx}$	(4,29)	$C_{12}\omega_{iby}$	(4,30)	$C_{13}\omega_{ibz}$
(5,25)	C_{21}	(5,26)	C_{22}	(5,27)	C_{23}
(5,28)	$C_{21}\omega_{ibx}$	(5,29)	$C_{22}\omega_{iby}$	(5,30)	$C_{23}\omega_{ibz}$
(6,25)	C_{31}	(6,26)	C_{32}	(6,27)	C_{33}
(6,28)	$C_{31}\omega_{ibx}$	(6,29)	$C_{32}\omega_{iby}$	(6,30)	$C_{33}\omega_{ibz}$
(7,31)	C_{11}	(7,32)	C_{12}	(7,33)	C_{13}
(7,34)	$C_{11}A_x^B$	(7,35)	$C_{12}A_y^B$	(7,36)	$C_{13}A_z^{B'}$
(7,37)	$C_{11} A_x^B $	(7,38)	$C_{12} A_y^B $	(7,39)	$C_{13} A_z^{B'} $
(7,40)	$C_{11}A_y^B$	(7,41)	$-C_{12}A_x^B$	(7,42)	$C_{13}A_y^B$
(7,43)	$C_{13}A_x^B$	(8,31)	C_{21}	(8,32)	C_{22}
(8,33)	C_{23}	(8,34)	$C_{21}A_x^B$	(8,35)	$C_{22}A_y^B$
(8,36)	$C_{23}A_z^{B'}$	(8,37)	$C_{21} A_x^B $	(8,38)	$C_{22} A_y^B $
(8,39)	$C_{23} A_z^{B'} $	(8,40)	$C_{21}A_y^B$	(8,41)	$-C_{22}A_x^B$
(8,42)	$C_{23}A_y^B$	(8,43)	$C_{23}A_x^B$	(9,31)	C_{31}
(9,32)	C_{32}	(9,33)	C_{33}	(9,34)	$C_{31}A_x^B$
(9,35)	$C_{32}A_y^B$	(9,36)	$C_{33}A_z^{B'}$	(9,37)	$C_{31} A_x^B $
(9,38)	$C_{32} A_y^B $	(9,39)	$C_{33} A_z^{B'} $	(9,40)	$C_{31}A_x^B$
(9,41)	$-C_{32}A_x^B$	(9,42)	$C_{33}A_y^B$	---	---

Table B-3. Elements of the Dynamics Submatrix F_{INS_n}

Element	Variable
(19,19)	$-\beta \nabla_{xc} = -3.33E-3 \text{ sec}^{-1}$
(20,20)	$-\beta \nabla_{yc} = -3.33E-3 \text{ sec}^{-1}$
(21,21)	$-\beta \nabla_{zc} = -3.33E-3 \text{ sec}^{-1}$
(22,22)	$-\beta \delta g_x = -8.22E-6 * \sqrt{V_x^2 + V_y^2 + V_z^2} \text{ ft}^{-1}$
(23,23)	$-\beta \delta g_y = -8.22E-6 * \sqrt{V_x^2 + V_y^2 + V_z^2} \text{ ft}^{-1}$
(24,24)	$-\beta \delta g_z = -8.22E-6 * \sqrt{V_x^2 + V_y^2 + V_z^2} \text{ ft}^{-1}$

Table B-4. Elements of the Dynamics Submatrix $F_{INS_{12}}$

Element	Variable	Element	Variable	Element	Variable
(42,42)	$-1 \text{ ft}^2 / \text{sec}$	(43,43)	$-1/500 \text{ ft}^2 / \text{sec}$	(44,44)	$-1/1500 \text{ ft}^2 / \text{sec}$
(49,49)	$-1 \text{ ft}^2 / \text{sec}$	(50,50)	$-1/500 \text{ ft}^2 / \text{sec}$	(51,51)	$-1/1500 \text{ ft}^2 / \text{sec}$
(56,56)	$-1 \text{ ft}^2 / \text{sec}$	(57,57)	$-1/500 \text{ ft}^2 / \text{sec}$	(58,58)	$-1/1500 \text{ ft}^2 / \text{sec}$
(63,63)	$-1 \text{ ft}^2 / \text{sec}$	(64,64)	$-1/500 \text{ ft}^2 / \text{sec}$	(65,65)	$-1/1500 \text{ ft}^2 / \text{sec}$

Table B-5. Elements of the Dynamics Submatrix F_{GPS_i}

B.2 Elements of the Process Noise and Measurement Noise Matrices

This section defines the dynamic noise strengths and measurement noise variances for the truth and filter models. The truth model non-zero dynamics noise strengths are defined in Tables B.6 and B.7. These noise strengths correspond to the driving noises w_{Filter} , w_{INS_i} and w_{GPS_i} in Equation (3.3). Note that the σ^2 terms in Table B.6 are variable names as defined in the Litton technical report [litton] and do not represent variance terms typically associated with the notation σ^2 [mosle]. The filter dynamics driving noise terms implemented after filter tuning for each respective INS integration (0.4 nm/hr, 2.0 nm/hr and 4.0 nm/hr) are listed in Tables B.8, B.9 and B.10. Finally, the measurement noise variances used in the truth and filter models are presented in Table B.11.

Element	Variable	Element	Variable	Element	Variable
(4,4)	$\sigma_{\eta_{bx}}^2 = 190.4E-15$ [ft ³ / sec ⁵]	(5,5)	$\sigma_{\eta_{by}}^2 = 190.4E-15$ [ft ² / sec ⁴]	(6,6)	$\sigma_{\eta_{bz}}^2 = 190.4E-15$ [ft ² / sec ⁴]
(7,7)	$\sigma_{\eta_{Ax}}^2 = 102.9E-9$ [ft ² / sec ⁴]	(8,8)	$\sigma_{\eta_{Ay}}^2 = 102.9E-9$ [ft ² / sec ⁴]	(9,9)	$\sigma_{\eta_{Az}}^2 = 102.9E-9$ [ft ² / sec ⁴]
(11,11)	$2\beta_{\delta hc}\sigma_{\delta hc}^2 =$ 33.34 [ft ² / sec]	(19,19)	$2\beta_{\nabla xc}\sigma_{\nabla xc}^2 =$ 2.75E-11 [ft ² / sec ⁵]	(20,20)	$2\beta_{\nabla yc}\sigma_{\nabla yc}^2 =$ 2.75E-11 [ft ² / sec ⁵]
(21,21)	$2\beta_{\nabla zc}\sigma_{\nabla zc}^2 =$ 2.75E-11 [ft ² / sec ⁵]	(22,22)	$2\beta_{\delta gx}\sigma_{\delta gx}^2 =$ 3.10E-13 [ft ³ / sec ⁵]	(23,23)	$2\beta_{\delta gy}\sigma_{\delta gy}^2 =$ 3.10E-13 [ft ³ / sec ⁵]
(24,24)	$2\beta_{\delta gz}\sigma_{\delta gz}^2 =$ 3.10E-13 [ft ³ / sec ⁵]				

Table B-6. Elements of Truth Model Process Noise Submatrix for the INS Truth Model

Element	Variable	Element	Variable	Element	Variable
(42,42)	0.5 ft ² / sec	(43,43)	0.004 ft ² / sec	(44,44)	0.004 ft ² / sec
(49,49)	0.5 ft ² / sec	(50,50)	0.004 ft ² / sec	(51,51)	0.004 ft ² / sec
(56,56)	0.5 ft ² / sec	(57,57)	0.004 ft ² / sec	(58,58)	0.004 ft ² / sec
(63,63)	0.5 ft ² / sec	(64,64)	0.004 ft ² / sec	(65,65)	0.004 ft ² / sec

Table B-7. Elements of Truth Model Process Noise for GPS States

Element	Variable	Element	Variable
(1,1)	1.2E-13 rad ² /sec	(2,2)	1.5E-13 rad ² /sec
(3,3)	0.0 rad ² /sec	(4,4)	9.5E-13 rad ² /sec
(5,5)	9.5E-13 rad ² /sec	(6,6)	1.6E-11 rad ² /sec
(7,7)	5.1E-6 ft ² /sec ³	(8,8)	5.1E-6 ft ² /sec ³
(9,9)	7.7E-3 ft ² /sec ³	(10,10)	110 ft ² /sec
(11,11)	3E3 ft ² /sec	(12,12)	60 ft ² /sec
(13,13)	5E-15 ft ² /sec ³		

Table B-8. Filter Process Noise Q Values for Case 1 (using 0.4 nm/hr INS)

Element	Variable	Element	Variable
(1,1)	1.2E-13 rad ² /sec	(2,2)	1.5E-13 rad ² /sec
(3,3)	0.0 rad ² /sec	(4,4)	2.9E-11 rad ² /sec
(5,5)	2.9E-11 rad ² /sec	(6,6)	3.4E-11 rad ² /sec
(7,7)	3.1E-3 ft ² /sec ³	(8,8)	3.1E-3 ft ² /sec ³
(9,9)	9.8E-3 ft ² /sec ³	(10,10)	130 ft ² /sec
(11,11)	3E3 ft ² /sec	(12,12)	55 ft ² /sec
(13,13)	5E-15 ft ² /sec ³		

Table B-9. Filter Process Noise Q Values for Case 2 (using 2.0 nm/hr INS)

Element	Variable	Element	Variable
(1,1)	1.2E-13 rad ² /sec	(2,2)	1.5E-15 rad ² /sec
(3,3)	0.0 rad ² /sec	(4,4)	5.7E-10 rad ² /sec
(5,5)	5.7E-10 rad ² /sec	(6,6)	8.0E-11 rad ² /sec
(7,7)	1.7E-3 ft ² /sec ³	(8,8)	1.7E-3 ft ² /sec ³
(9,9)	12.9E-3 ft ² /sec ³	(10,10)	125 ft ² /sec
(11,11)	4.7E3 ft ² /sec	(12,12)	65 ft ² /sec
(13,13)	5E-13 ft ² /sec ³		

Table B-10. Filter Process Noise Q Values for Case 3 (using 4.0 nm/hr INS)

Measurement	Truth Noise	Filter Noise
Baro Altimeter	2500 ft^2	3500 ft^2
Satellite Vehicles	2 ft^2	75 ft^2
Radar Altimeter	(See function, Chapter 3)	(See function, Chapter 3)

Table B-11. Truth and Filter Measurement Noise R Values for Cases 1-3

Appendix C PROF_IN Input File

The PROF_IN input file for PROFGEN representing the Tanker (Boeing 707) Flight Profile is found in this section.

```
'                               PROF_IN
=====
Group 1, General Information
-----
This is a PROFGEN input file and these are general instructions for understanding its organization so it can be used as a template for building similar files.

PROF_IN is the parameter control file for PROFGEN. This file is self-documenting and consists of text and data entered in list directed form. PROF_IN is divided into three Groups with contents as follows:

Group 1: General Information;
Group 2: Problem Control Parameters;
Group 3: Segment Control Parameters.

Each Group is required and each is constructed in two parts. The first part is a "REMINDER" (such as this) that is placed at the head of the Group to identify that Group and convey information about it. The second part is a series of entries for the parameters in that Group. Each parameter is defined by a leading "NOTE" that conveys this set of five characteristics:
  NAME      TYPE      DESCRIPTION      UNITS      DEFAULT      VALUE.
The parameter value is entered following its NOTE. All data in file PROF_IN are entered in list directed form. You must include both the Group REMINDERS and the parameter NOTES (or simple substitutes such as '') in your own PROF_IN file to place-hold this material. The PROFGEN problem title and the compiler choice are the only parameters in Group 1.
=====

'PTITLE CH*80  PROFGEN run title           -      ''
'Tanker3 Profile ( all outputs set to support INS/GPS problem in MSOFE )
'FOR_77 CH*8   Compiler. Controls calls to date, time and CPU timer
          routines. Choices: DEC, LAHEY, UNIX.           -      ''UNIX'
         

=====
Group 2, Problem Control Parameters
-----
Note that each entry in this Group is echoed in Table 1 of PROF_OUT, converted to internal computational units of radians/feet/seconds, placed in Namelist PRDATA, and echoed again in converted form as Namelist output in Table 4. See Table 3 of PROF_OUT for help in specifying IPRSET and IRTSET.

NAME      TYPE      DESCRIPTION      UNITS      DEFAULT
=====
'Problem specs
-----
NSEG     IN      number of flight segments      -      0      ' 27
'TSTART   DP      initial time of trajectory      sec      0.D0      ' 0
'LLMECH   IN      local level mechanization index:
                  1 alpha wander; 2 constant alpha;
                  3 unipolar;    4 free azimuth      -      2      ' 1
'RTOL     DP      relative tolerance for integration      -      0.D0      ' 0.1D-11
'ATOL     DP      absolute tolerance for integration      -      0.D0      ' 0.1D-11

'Earth parameters
-----
ESQ      DP      earth eccentricity squared      - 6.69437999013D-3' /
REQ      DP      earth semimajor axis            m 6.378137D6      ' /
```

Figure C - 1. PROF_IN Input File for PROFGEN

```

'WEI    DP   earth sidereal rate           r/s   7.292115D-5   ' /
'GM     DP   earth gravitational constant m3/s2 3.986005D14   ' /
'GEE    DP   converts PACC/TACC to accel units m/s2   9.8      ' 32.D0
'RHOGL  DP   air density at sea level     kg/m3   1.225     ' 0.002377D0
'ZETA   DP   exponent in air density function,
            rho = RHOSL * exp(-ZETA * alt)  1/m    1.1385D-4   ' 3.47015D-20

'Vehicle specs
-----
ROLRAT DP   maximum roll rate             d/s    1.D0   ' 45.D0
'ROLTC  DP   roll-axis time constant      sec    1.D0   ' 1.D0
'VMASS  DP   vehicle mass                kg     1.D0   ' 15.D0
'RAREA   DP   reference area for drag     m2    1.D0   ' 1.D0
'CDRAG   DP   coefficient of drag         -     1.D0   ' 0.0D0

'State initial conditions
-----
VETO   DP   initial earth velocity magnitude m/s   0.D0   ' /
'ROLLO  DP   initial aircraft roll angle    deg    0.D0   ' /
'PITCHO DP   initial aircraft pitch angle   deg    0.D0   ' /
'HEADO  DP   initial ground path heading   deg    0.D0   ' 232.D0
'ALPHAO DP   initial alpha angle            deg    0.D0   ' 45.D0
'GLATO   DP   initial geographic latitude   deg    0.D0   ' 39.833D0
'TLONO   DP   initial terrestrial longitude deg    0.D0   ' -84.033D0
'CLONO   DP   initial celestial longitude  deg    0.D0   ' /
'ALTO    DP   initial altitude              m     0.D0   ' 825.D0

'I/O controls
-----
JPRNT  IN   print (PROF_OUT file) control   -     1      ' 1
'JRITE  IN   write (FLIGHT file) control    -     0      ' 1
'JPLOT  IN   plot (META file) control       -     0      ' /
'SIUNIT LG   I/O in SI units (else English) -     .T.    ' .F.
'XVU    RL   x viewpoint for 3-D plot      inches -7.5   ' /
'YVU    RL   y viewpoint for 3-D plot      inches -7.5   ' /
'ZVU    RL   z viewpoint for 3-D plot      inches 18.    ' /
'DELR   DP   spread in roll angle outputs deg    0.D0   ' /
'DELP   DP   spread in pitch angle outputs deg    0.D0   ' /
'DELY   DP   spread in yaw angle outputs  deg    0.D0   ' /
'PSEP   DP   min separation in printed outputs sec    0.D0   ' /
'WSEP   DP   min separation in written outputs sec    0.D0   ' /
'IPRSET IN() indices of printed variables nd    52*-1   ' 1,2,3,40,43,5,7,8,9,14,16,17,18 /
'IRTSET IN() indices of written variables  nd    52*-1   ' 1,2,3,40,43,5,7,8,9,14,16,17,18 /

=====
Group 3, Segment Control Parameters
-----
Note that each entry in this Group is echoed in Table 2 of PROF_OUT, converted to internal computational units of radians/feet/seconds, placed in Namelist SGDATA, and echoed again in converted form as Namelist output in Table 5.

NAME   TYPE  DESCRIPTION                      UNITS  DEFAULT
-----
'SEGLNT DP() time interval of each segment
            3.D0 30.D0   160.D0 329.D0   5.D0   25.D0   sec   0.D0'
            371.D0 35.D0   400.D0 35.D0   340.D0
            35.D0 600.D0   35.D0 120.D0 35.D0
            372.D0 70.D0   40.D0 35.D0   360.D0
            45.D0 104.D0   35.D0 39.D0   25.D0
            242.D0   /      /      /      /

```

Figure C - 1 (Continued). PROF_IN Input File for PROFGEN

```

'KTURN  IN() maneuver index: 1 vertical; 2 horizontal;
      3 jink; 4 straight; 5 roll; 6 free fall           -     4
      4 4 1 4 1 2
      4 2 4 2 4
      2 3 2 1 1
      4 2 1 1 1
      2 1 2 1 2
      4 /
'NPATH  IN() path index: 1 great circle; 2 rhumb line           -     2
      /
'TACC   DP() maximum centrifugal acceleration during turn      gees    0.D0'
      0.D0 0.D0    0.21D0  0.D0    0.9D0  0.9D0
      0.D0    0.9D0    0.D0    0.9D0    0.D0
      0.9D0    0.D0    0.9D0    0.311D0  0.9D0
      0.D0    0.9D0    0.63D0  0.9D0    0.9D0
      0.9D0    0.9D0    0.9D0    0.24D0  0.9D0
      0.D0    /
'PACC   DP() signed value of accel along velocity vector      gees    0.D0'
      0.D0 0.262D0  0.038D0  0.01D0 -0.0875D0  0.01D0
      0.01D0 -0.00D0   0.008D0 -0.0D0   0.D0
      -0.0D0   0.D0    -0.00D0 -0.0D0   0.D0
      0.003D0   -0.125D0 -0.085D0   0.D0    0.015D0
      -0.05D0   0.D0    -0.05D0 -0.1882D0 -0.0D0
      -0.0D0    /
'DELHED  DP() for horizontal turns, desired change in heading
      angle; for jinking maneuvers, maximum variation
      of heading angle                                deg    0.D0'
      0.D0 0.D0    0.D0    0.D0    0.D0    45.D0
      0.D0    45.D0    0.D0    45.D0    0.D0
      45.D0    2.D0    45.D0    0.D0    0.D0
      0.D0    90.D0    0.D0    0.D0    0.D0
      -45.D0   0.D0    45.D0    0.D0    45.D0
      0.D0    /
'DELPIT  DP() for vertical turns, desired change in pitch;
      for jinking maneuvers, period of maneuver      deg or sec  0.D0'
      0.D0 0.D0    5.D0    0.D0    -5.D0    0.D0
      0.D0    0.D0    0.D0    0.D0    0.D0
      0.D0    200.D0   0.D0    -5.D0    5.D0
      0.D0    0.D0    -5.0D0   5.0D0  -1.75D0
      0.D0    1.75D0   0.D0    -3.D0    0.D0
      0.D0    /
'DELROL  DP() desired change in roll angle for roll maneuver   deg    0.D0'
      0.D0 0.D0    0.D0    0.D0    0.D0    0.D0
      0.D0    1.D0    0.D0    1.D0    0.D0
      0.D0    0.D0    0.D0    0.D0    0.D0
      0.D0    0.D0    0.D0    0.D0    0.D0
      1.D0    0.D0    1.D0    0.D0    0.D0
      0.D0    /
'DTPRNT DP() time interval for formatted printing on PROF_OUT  sec    1.D8'
      27*1.D0/
'DTRITE DP() time interval for unformatted writes on FLIGHT   sec    1.D8'
      27*1.D0/
'DTPLOT DP() time interval for plotted output on file META   sec    1.D8'
      27*4.D0/
'ICREDO LG() reset kinematic state to its TSTART value        -     .F.
      /

```

Figure C - 1 (Continued). PROF_IN Input File for PROFGEN

Appendix D

The Tanker Flight Profile Plots are found in this section.

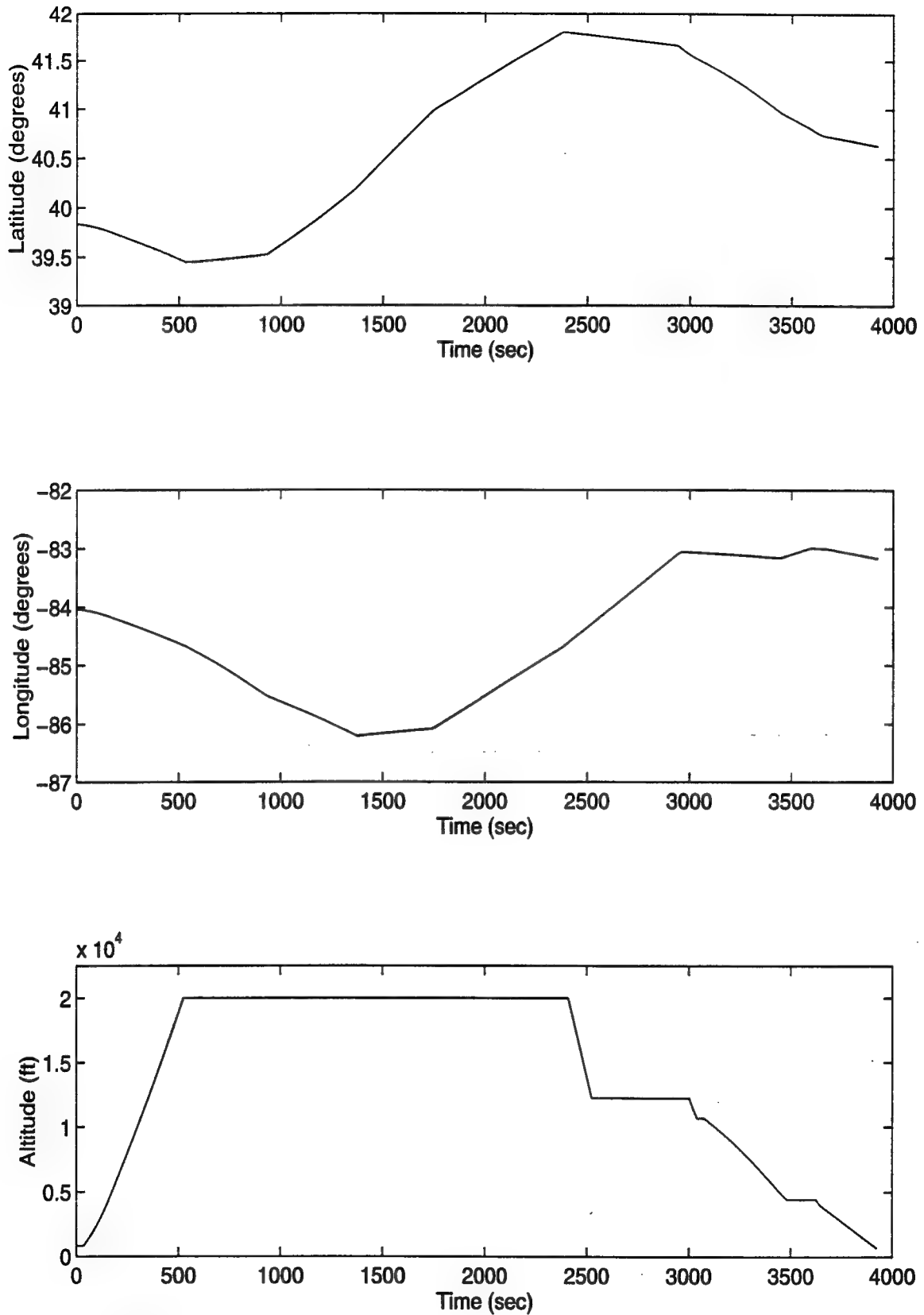


Figure D - 1. Lattitude, Longitiude and Altitude of the Tanker Profile

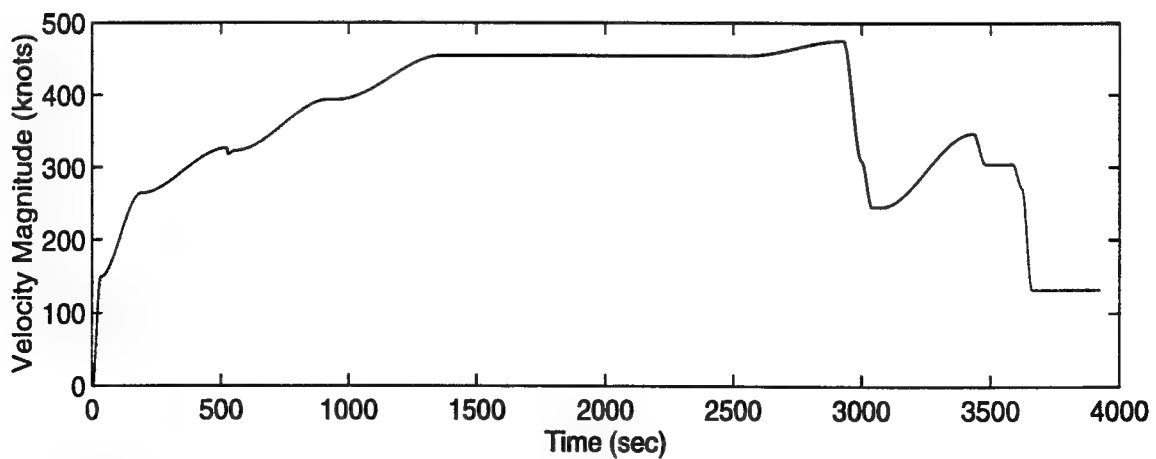
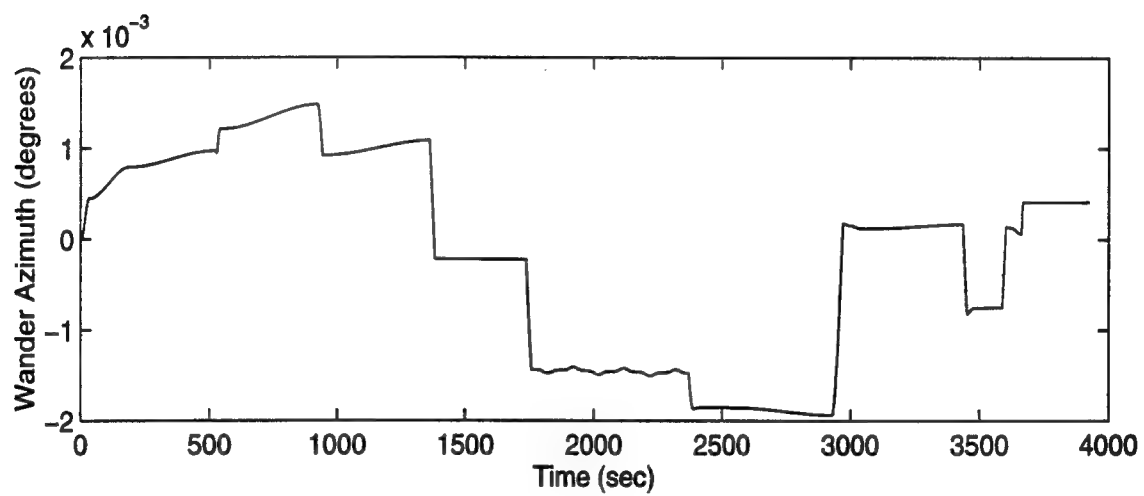
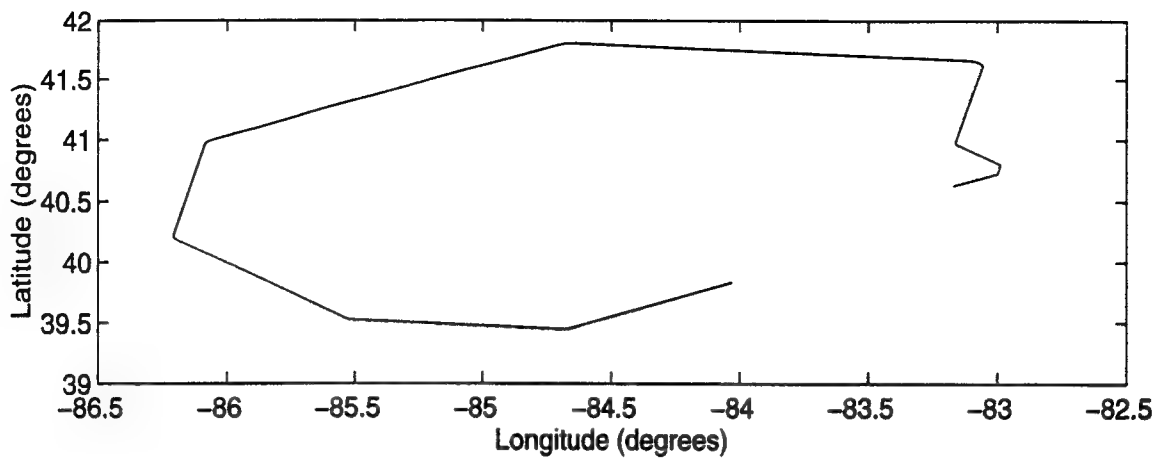


Figure D - 2. 3-D Position, Wander Azimuth and Velocity of the Tanker Profile

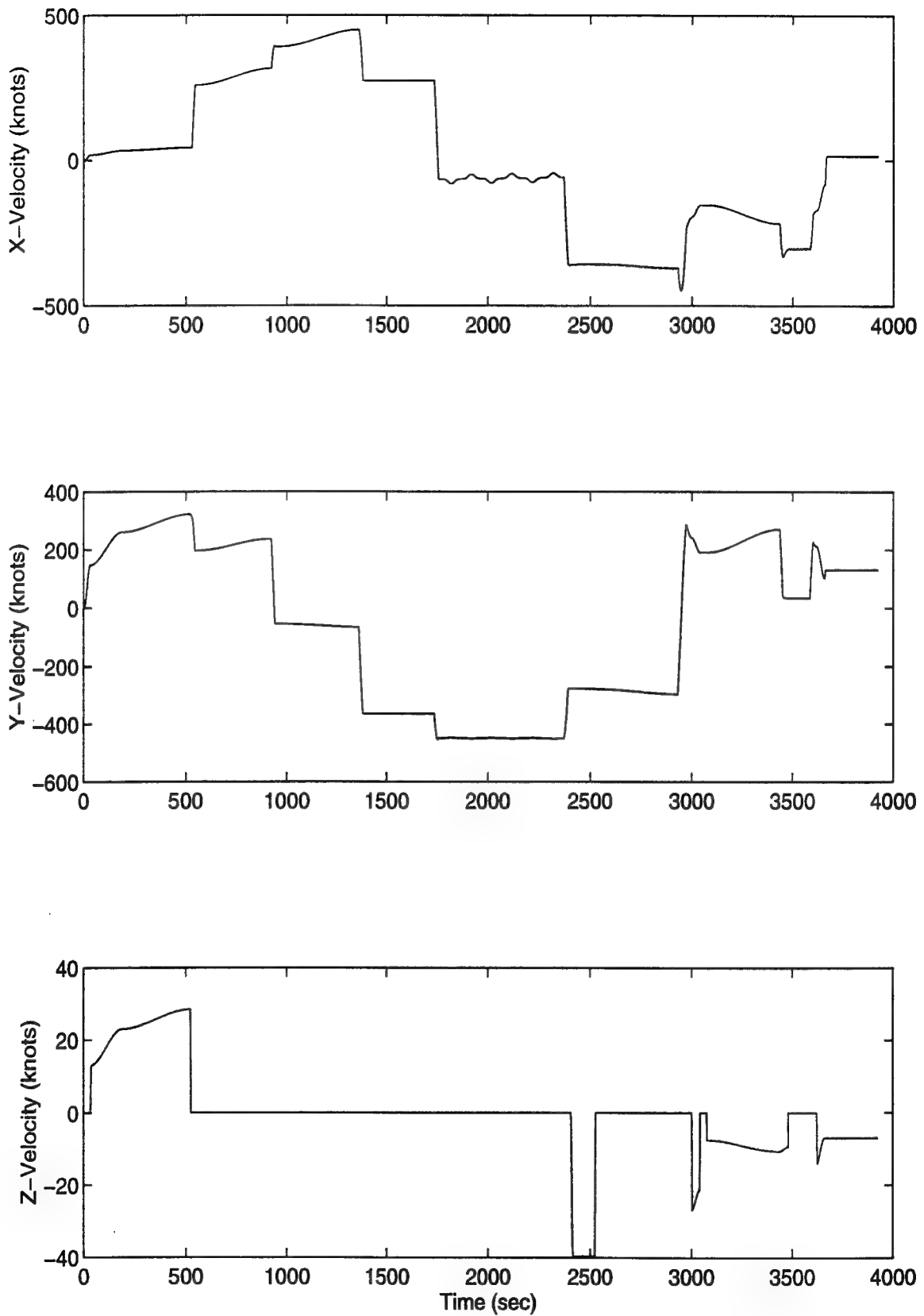


Figure D - 3. X,Y and Z Velocity of the Tanker Profile

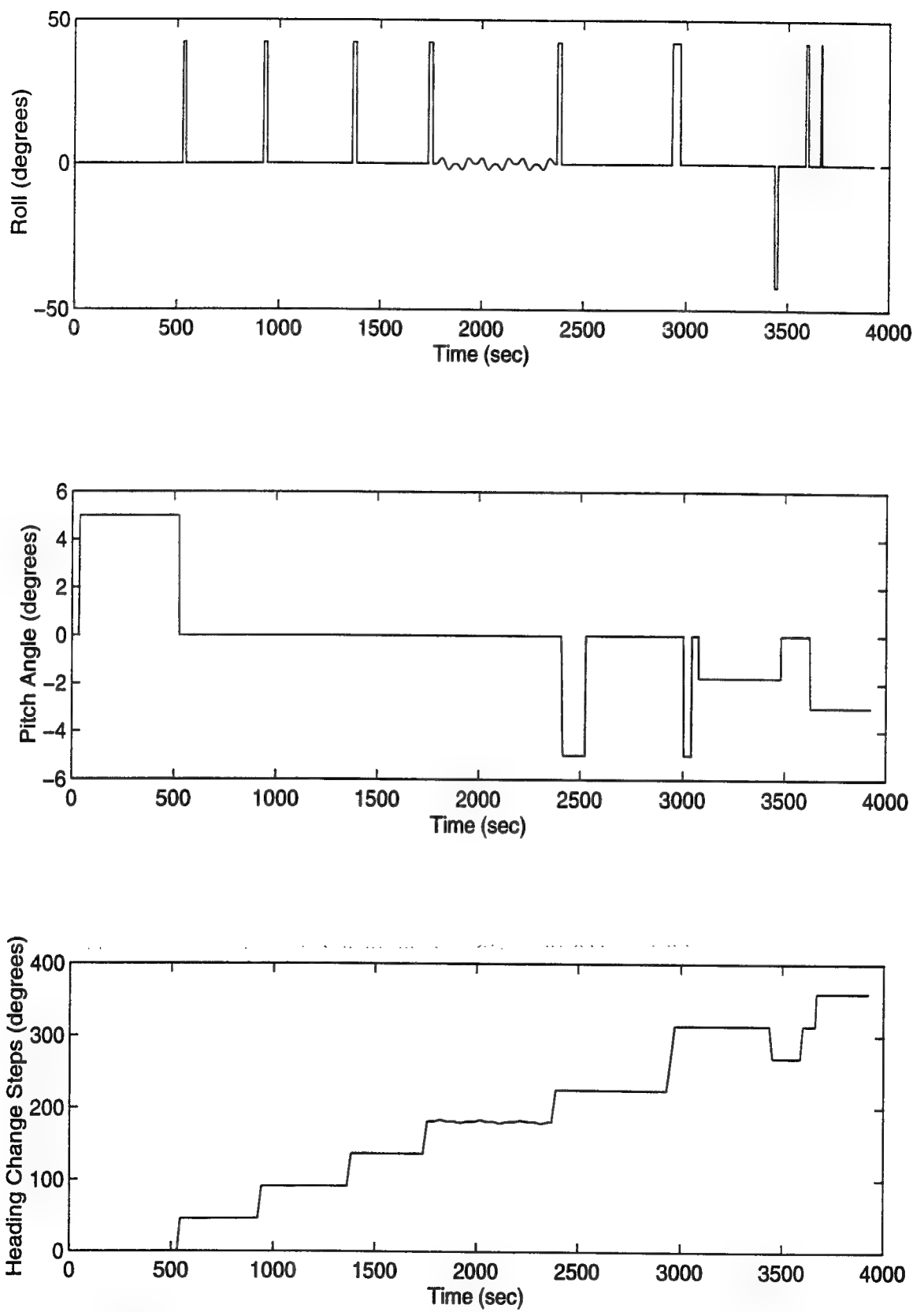


Figure D - 4. Roll, Pitch and Heading Changes of the Tanker Profile

Appendix E

FORTRAN source code ADDSV.for, Sample True ephemeris data and Almanac file "051994A.AL3" are contained in this section. In order to interpret Figure E -2, use the following template shown in Table E - 1. See SEM3.6 User Manual for the template of Figure E - 3.

*	1994	5	21	4	15	0.00000000
P		6	-3808.264821	-26030.699349	-2199.205556	179.659571
<hr/>						
*	YEAR	MONTH	DAY	SV_HOURS	SV_MINUTES	SV_SECONDS
POSITION_INFO	SV#	ECEF_X(in km)	ECEF_Y(in km)	ECEF_Z(in km)	SV Clock Offset (in microsec)	
<hr/>						
	1994	=	YEAR			
	5	=	MONTH			
	21	=	DAY			
	4	=	SV_HOURS			
	15	=	SV_MINUTES			
	0.00000000	=	SV_SECONDS			
	P	=	POSITION_INFO			
	6	=	SV#			
	-3808.264821	=	ECEF_X(in km)			
	-26030.699349	=	ECEF_Y(in km)			
	-2199.205556	=	ECEF_Z(in km)			
	179.659571	=	SV Clock Offset (in microsec)			

Table E - 1. Template for Understanding Figure E - 2.

```

*DECK ADDSV
  PROGRAM ADDSV
C
C This program will read in TANKER3 FLIGHT profile, and merge
C the information with real SV ephemeris data obtained from the
C Coast Guard BBS (National Geodetic Survey Ephemeris)
C
C The output file created will be called "FLIGHT_TANKER3_21my94p4"
C This file will need to be re-named "FLIGHT" so MSOFE will
C read it in properly. Put the "FLIGHT" file in the "runs"
C directory with your MSOFE_IN file.
C
C Adopted from J Solomon add.for code: 9 Sep 94 R.A. Gray
C
C
C
      INTEGER I,J,K
      REAL EPHPOS(10000,12)
      CHARACTER PDATE *10 ,      PTIME *10
      CHARACTER PTITLE *80, TEMP *80
      INTEGER*4 NRT, NYT
      INTEGER*4 IDFLT(17), IDCHEK(29)
C
      DOUBLE PRECISION TKNOT(10000), UKNOT(10000,29)
C
      DATA IDCHEK / 1, 2, 3, 40, 40, 40, 43, 43, 43, 5, 7, 8, 9, 14,
      &           16, 17, 18, 60, 61, 62, 60, 61, 62, 60,
      &           61, 62, 60, 61, 62 /
      DATA NYT / 29 /
C
C-----
C #OPEN FILES
C-----
C
C
      OPEN ( UNIT = 20,
      &   FILE = 'FLIGHT',
      &   FORM = 'UNFORMATTED',
      &   STATUS = 'OLD')
      OPEN ( UNIT = 21,
      &   FILE = '21my94p4',
      &   FORM = 'FORMATTED',
      &   STATUS = 'OLD')
      OPEN ( UNIT = 22,
      &   FILE = 'FLIGHT_TANKER3_21my94p4',
      &   FORM = 'UNFORMATTED', &   STATUS = 'UNKNOWN')
C
C-----
C #READ FLIGHT HEADER
C-----
C
C
      READ (20) PDATE, PTIME, PTITLE
      READ (20) NRT, (IDFLT(I),I=1,NRT)
C
C
C #READ FLIGHT DATA
C-----
C
      DO 100 K = 1, 3920
      READ (20) TKNOT(K), (UKNOT(K, J), J = 1,NRT)

```

Figure E - 1. FORTRAN source code "ADDSV.for"

```

100  CONTINUE
C
C-----
C  #READ GPS DATA
C-----
C
DO 200 I = 1,3920
  READ(21,*) TEMP
  READ(21,201) EPHPOS(I,1),EPHPOS(I,2),EPHPOS(I,3)
  READ(21,201) EPHPOS(I,4),EPHPOS(I,5),EPHPOS(I,6)
  READ(21,201) EPHPOS(I,7),EPHPOS(I,8),EPHPOS(I,9)
  READ(21,201) EPHPOS(I,10),EPHPOS(I,11),
&               EPHPOS(I,12)
C
C  CONVERT FROM KM TO FEET...
C
      EPHPOS(I,1)= EPHPOS(I,1) * 3.2801 * 1000
      EPHPOS(I,2)= EPHPOS(I,2) * 3.2801 * 1000
      EPHPOS(I,3)= EPHPOS(I,3) * 3.2801 * 1000
      EPHPOS(I,4)= EPHPOS(I,4) * 3.2801 * 1000
      EPHPOS(I,5)= EPHPOS(I,5) * 3.2801 * 1000
      EPHPOS(I,6)= EPHPOS(I,6) * 3.2801 * 1000
      EPHPOS(I,7)= EPHPOS(I,7) * 3.2801 * 1000
      EPHPOS(I,8)= EPHPOS(I,8) * 3.2801 * 1000
      EPHPOS(I,9)= EPHPOS(I,9) * 3.2801 * 1000
      EPHPOS(I,10)= EPHPOS(I,10) * 3.2801 * 1000
      EPHPOS(I,11)= EPHPOS(I,11) * 3.2801 * 1000
      EPHPOS(I,12)= EPHPOS(I,12) * 3.2801 * 1000

200  CONTINUE

C
201  FORMAT(5X,F13.6,1X,F13.6,1X,F13.6)
C
C-----
C  #ADD GPS DATA TO FLIGHT DATA
C-----
C
DO 300 I = 1,3920
  DO 300 J = 1,12
    UKNOT(I,J+17) = DBLE( EPHPOS(I,J) )
300  CONTINUE
C
C
C-----
C  #OUTPUT GPS / FLIGHT DATA
C-----
C
      WRITE (22) PDATE, PTIME, PTITLE
      WRITE (22) NYT, (IDCHEK(I),I=1,NYT)
C
      DO 400 K = 1, 3920
        WRITE(22) TKNOT(K), (UKNOT(K, J), J = 1,NYT)
400  CONTINUE
C
      CLOSE(20), CLOSE(21), CLOSE(22)
      STOP  ' ADD DONE.'
C
      END

```

Figure E - 1 (Continued). FORTRAN source code "ADDSV.for"

* 1994 5 21 4 15 0.00000000
 P 6 -3808.264821 -26030.699349 -2199.205556 179.659571
 P 16 22228.030253 -2914.054829 14269.400710 -72.472353
 P 17 -1978.539062 -16483.210409 20480.389383 -51.084448
 P 28 -14135.480147 5206.630899 21842.559082 14.685241
 * 1994 5 21 4 15 1.0000000
 P 6 -3807.902060 -26030.482798 -2202.379803 179.659588
 P 16 22229.666889 -2913.256477 14267.009251 -72.472371
 P 17 -1976.416118 -16484.803199 20479.313405 -51.084449
 P 28 -14136.128577 5203.928088 21842.759458 14.685243
 * 1994 5 21 4 15 2.00000000
 P 6 -3807.539205 -26030.265875 -2205.554003 179.659604
 P 16 22231.303287 -2912.458317 14264.617490 -72.472389
 P 17 -1974.293373 -16486.396028 20478.236982 -51.084450
 P 28 -14136.777174 5201.225288 21842.959367 14.685245
 * 1994 5 21 4 15 3.00000000
 P 6 -3807.176256 -26030.048580 -2208.728154 179.659621
 P 16 22232.939448 -2911.660349 14262.225425 -72.472406
 P 17 -1972.170829 -16487.988896 20477.160114 -51.084451
 P 28 -14137.425939 5198.522499 21843.158810 14.685247
 * 1994 5 21 4 15 4.00000000
 P 6 -3806.813214 -26029.830911 -2211.902258 179.659638
 P 16 22234.575372 -2910.862573 14259.833058 -72.472424
 P 17 -1970.048484 -16489.581803 20476.082800 -51.084452
 P 28 -14138.074872 5195.819722 21843.357787 14.685249
 * 1994 5 21 4 15 5.00000000
 P 6 -3806.450077 -26029.612871 -2215.076314 179.659654
 P 16 22236.211057 -2910.064990 14257.440387 -72.472442
 P 17 -1967.926339 -16491.174748 20475.005041 -51.084453
 P 28 -14138.723973 5193.116956 21843.556298 14.685251
 * 1994 5 21 4 15 6.00000000
 P 6 -3806.086847 -26029.394457 -2218.250322 179.659671
 P 16 22237.846505 -2909.267599 14255.047414 -72.472460
 P 17 -1965.804394 -16492.767731 20473.926836 -51.084454
 P 28 -14139.373241 5190.414202 21843.754343 14.685253

Figure E - 2. Sample from National Geodetic Office True Ephemeris Data

25 051994.A.AL3
 750 32768
 1
 32
 7
 3.61871719360000E-0003 4.03787490677082E-0003 -2.47382546733128E-0009
 5.15368505900000E+0003 -2.18499073561888E-0001 -3.81680029160470E-0001
 9.34495603829844E-0001 -2.47955322270000E-0005 0.00000000000000E+0000
 0
 1
 2
 13
 7
 1.28645896910000E-0002 3.63542500182467E-0003 -2.64844865770802E-0009
 5.15360546900000E+0003 4.34110874460587E-0001 -8.51847509087840E-0001
 -2.11397536351559E-0001 -9.05990600590000E-0005 -3.63797880710000E-0012
 0
 1
 4
 34
 7
 3.16715240480000E-0003 6.62805331970454E-0003 -2.54658524778148E-0009
 5.15349951200000E+0003 -8.88224868033215E-0001 -3.98996607241964E-0001
 5.56436181933807E-0001 2.76565551760000E-0005 0.00000000000000E+0000
 0
 1
 5
 35
 7
 2.04277038570000E-0003 4.40408688739476E-0003 -2.64844865770802E-0009
 5.15354834000000E+0003 4.38525794771209E-0001 -7.47885202727681E-0001
 -8.79619968280586E-0001 4.1961699220000E-0005 3.63797880710000E-0012
 0
 1
 6
 36
 7
 6.08873367310000E-0003 5.28146260959343E-0003 -2.48837742344679E-0009
 5.15367529300000E+0003 7.84484770392502E-0001 -9.51250588590547E-0001
 8.06142540736748E-0001 1.81198120120000E-0004 1.81898940350000E-0011
 0
 1
 7
 37
 7
 6.20937347410000E-0003 6.33813079470329E-0003 -2.47746345635220E-0009
 5.15368798800000E+0003 7.72793384134664E-0001 -8.6423155235642E-0001
 -5.47001490125076E-0001 6.96182250980000E-0004 0.00000000000000E+0000
 0
 1
 9
 39
 7
 2.60972976680000E-0003 3.08419082134277E-0003 -2.61934474550884E-0009
 5.15371142600000E+0003 1.10435722418997E-0001 -2.02198618779358E-0001
 9.39667574686501E-0001 -1.81198120120000E-0005 0.00000000000000E+0000
 0
 1
 12
 10
 3
 1.45077705380000E-0002 4.65393139879435E-0002 -2.19006317174084E-0009

Figure E - 3. SEM3.6 Almanac Data File (051994.al3) Used For: 21 May 94.

```

5.15351025400000E+0003 2.20944414025568E-0001 -5.63353322948398E-0002
6.88273665924971E-0001 3.24249267580000E-0005 0.000000000000000E+0000
0
0

14
14
7
3.12614440920000E-0003 5.97191881407934E-0003 -2.55022323680240E-0009
5.15373291000000E+0003 -5.47894613209864E-0001 9.78019389301773E-0001
-6.49707535115492E-0001 4.76837158200000E-0006 0.000000000000000E+0000
0
1

15
15
7
6.81734085080000E-0003 8.10052823333991E-0003 -2.52111932463505E-0009
5.15363085900000E+0003 -8.77898912451352E-0001 5.72649608752327E-0001
1.15476012945291E-0001 8.48770141600000E-0005 3.63797880710000E-0012
0
1

16
16
7
8.64505767820000E-0004 4.97436971769650E-0003 -2.56841289921599E-0009
5.15353662100000E+0003 -5.44454702377718E-0001 -5.09196621865252E-0001
1.04387400349130E-0001 -7.24792480470000E-0005 0.000000000000000E+0000
0
1

17
17
7
7.39622116090000E-0003 8.47055372544914E-0003 -2.51748133561413E-0009
5.15364502000000E+0003 -8.66931905668387E-0001 6.00263000159655E-0001
8.30542480168520E-0001 -5.14984130860000E-0005 0.000000000000000E+0000
0
1

18
18
7
5.53703308110000E-0003 3.05195604672514E-0004 -2.51384334659322E-0009
5.15374414100000E+0003 -2.32049219860062E-0001 4.18790684681791E-0001
-5.89919703533139E-0001 -7.62939453120000E-0006 0.000000000000000E+0000
0
1

19
19
7
1.25408172610000E-0004 -2.17437168560882E-0003 -2.66300061379169E-0009
5.15359960900000E+0003 1.02508064366804E-0001 -8.89521010320165E-0001
3.50051511019709E-0001 2.86102294920000E-0005 3.63797880710000E-0012
0
1

20
20
7
4.76932525630000E-0003 5.53512823900381E-0003 -2.63389670162434E-0009
5.15353125000000E+0003 4.36904307926814E-0001 4.58547696903478E-0001
-2.63615848922248E-0001 5.34057617190000E-0005 0.000000000000000E+0000
0
1

```

Figure E - 3 (Cont'd). SEM3.6 Almanac Data File (051994.al3) Used For: 21 May 94.

```

21
21
7
  1.10397338870000E-0002  3.97873687860613E-0003 -2.57568887725782E-0009
  5.15362597700000E+0003 -5.57345393927682E-0001  8.95620672682456E-0001
  9.14788257969335E-0003 -2.57492065430000E-0005  0.000000000000000E+0000
0
1

22
22
7
  7.18355178830000E-0003  3.68310352426479E-0003 -2.65936262477077E-0009
  5.15354003900000E+0003  4.38924791650606E-0001 -7.99311402531010E-0002
 -2.24944476253860E-0001  1.23977661130000E-0004  3.63797880710000E-0012
0
1

23
23
7
  8.32128524780000E-0003  5.13651081681166E-0003 -2.55749921484423E-0009
  5.15359179700000E+0003 -5.46834947341484E-0001 -7.51196023020909E-0001
 -1.65312885266793E-0001  5.72204589840000E-0006  0.000000000000000E+0000
0
1

24
24
7
  5.48076629640000E-0003  9.78280379726186E-0003 -2.51020535757230E-0009
  5.15362744100000E+0003 -8.91399160413578E-0001 -6.87911362216682E-0001
  6.78474166136823E-0001  6.27517700200000E-0004  3.27418092640000E-0011
0
1

25
25
7
  5.81312179570000E-0003  8.94565027331417E-0004 -2.63753469064526E-0009
  5.15355957000000E+0003  1.02575664265170E-0001  9.12953036069076E-0001
 -7.64856704540744E-0001 -7.62939453120000E-0006  0.000000000000000E+0000
0
1

26
26
7
  8.31842422490000E-0003  4.95530209660800E-0003 -2.45563580494953E-0009
  5.15363476600000E+0003 -2.25428584871805E-0001 -3.30814701228596E-0001
 -4.97203227333835E-0001 -6.48498535160000E-0005 -3.63797880710000E-0012
0
1

27
27
7
  1.09333992000000E-0002  2.11908510906553E-0003 -2.61934474550884E-0009
  5.15369824200000E+0003  1.06457355526676E-0001  7.64407505673693E-0001
  5.49562924837777E-0001  2.95639038090000E-0005  0.000000000000000E+0000
0
1

28
28
7

```

Figure E - 3 (Cont'd). SEM3.6 Almanac Data File (051994.al3) Used For: 21 May 94.

```

5.21230697630000E-0003 8.88444419668218E-0003 -2.45199781592861E-0009
5.15362744100000E+0003 7.75170821127847E-0001 9.17673683276588E-0001
3.86364096897161E-0001 1.52587890620000E-0005 3.63797880710000E-0012
0
1

29
29
7
5.16462326050000E-0003 3.66022239169097E-0003 -2.47382546733128E-0009
5.15363330100000E+0003 -2.32212423429801E-0001 -5.82052691976437E-0001
5.61828388466135E-0001 1.33514404300000E-0005 0.000000000000000E+0000
0
1

31
31
7
5.00249862670000E-0003 6.14358422218893E-0003 -2.48110144537312E-0009
5.15360058600000E+0003 7.73816318762073E-0001 2.03706971195042E-0001
9.34471242810989E-0001 1.52587890620000E-0005 3.63797880710000E-0012
0
1

```

Figure E - 3 (Cont'd). SEM3.6 Almanac Data File (051994.al3) Used For: 21 May 94.

Appendix F

Plots obtained from SEM 3.6 (GDOP, PDOP, VDOP, TDOP, SV Bearing/Elevation, SV Rise/Set, Number of Visible SVs and Elevation/Time) are shown in this section (Figures F - 1 to F - 5). The best four SV selected for use in this thesis are shown in Section 4.2. Notes: In Figure F - 3, SV Bearing/Elevation Plot, the trajectory *starts* at the respective SV number. In Figure F - 4 , SV Rise/Set, the solid line shows the best 4 SV for a given instant in time. In Figure F - 5, Elevation/Time, the SV number lies *directly under* the start of its elevation line. For more information, Use reference [18].

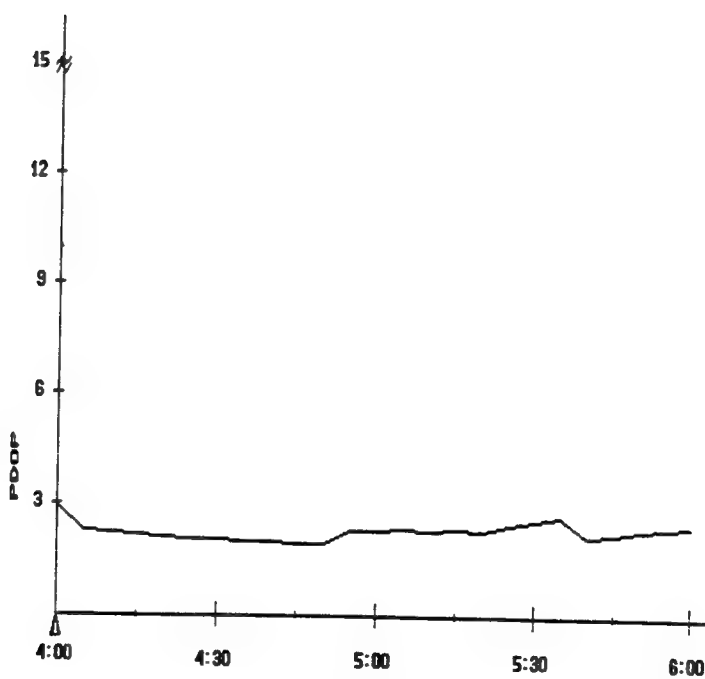
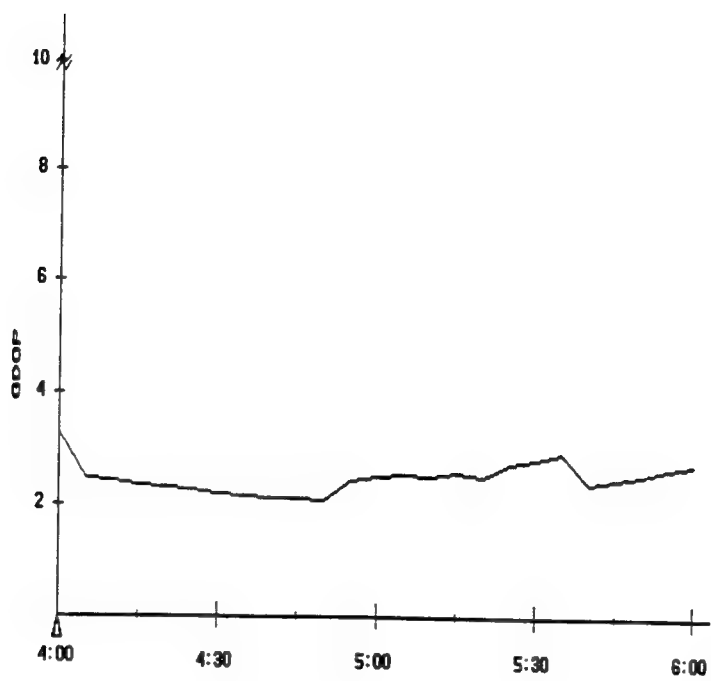


Figure F - 1. GDOP and PDOP

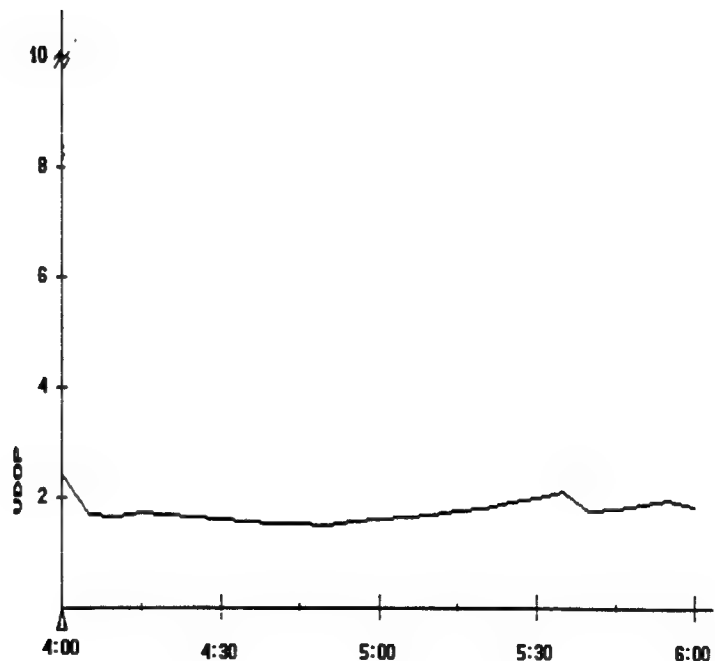
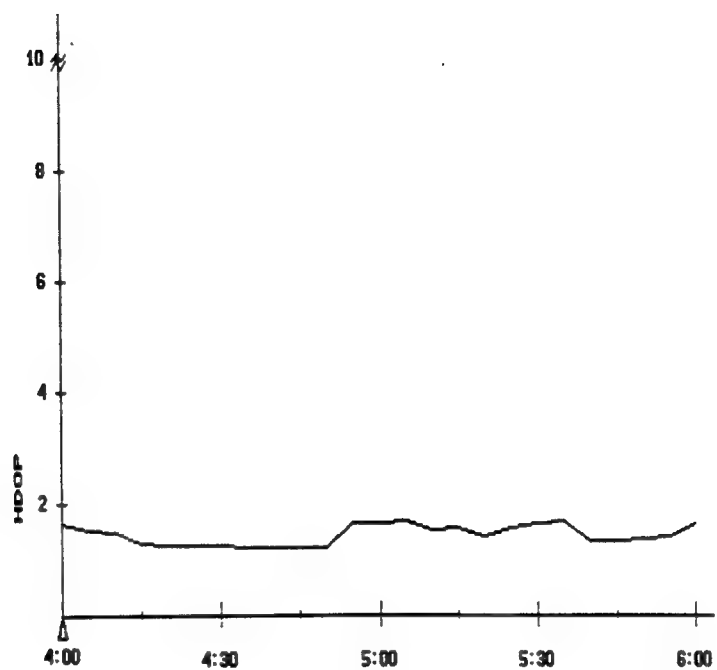


Figure F - 2. HDOP and VDOP

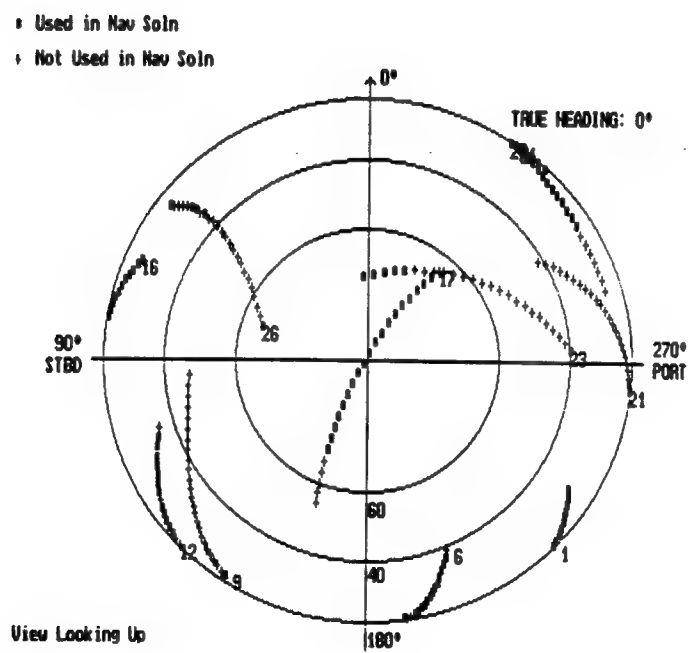
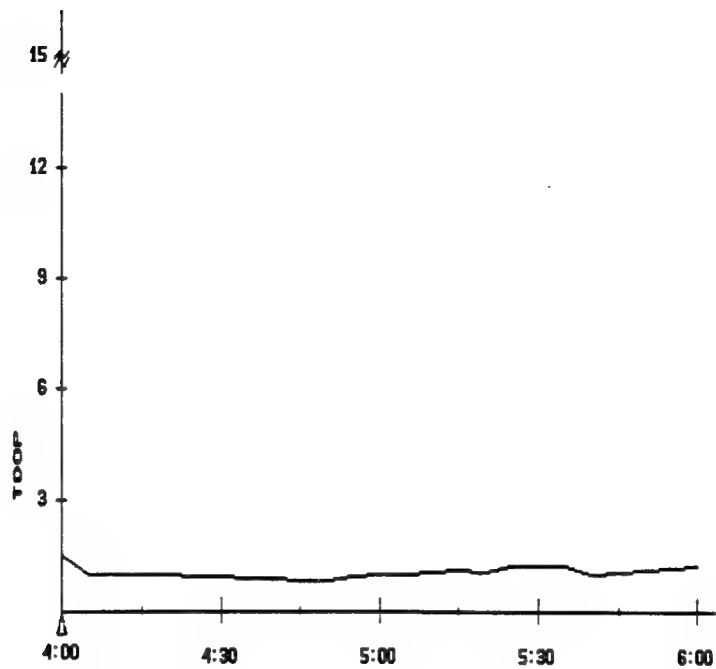


Figure F - 3. TDOP and SV Bearing/Elevation

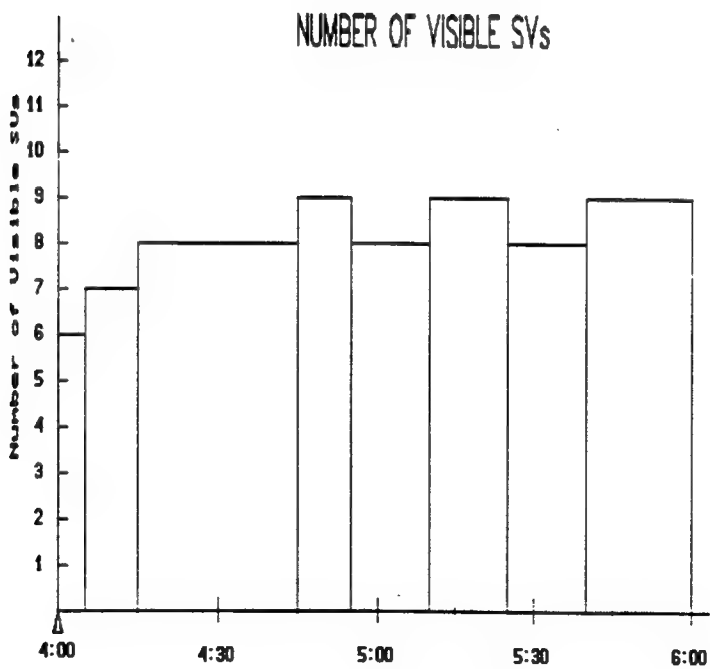
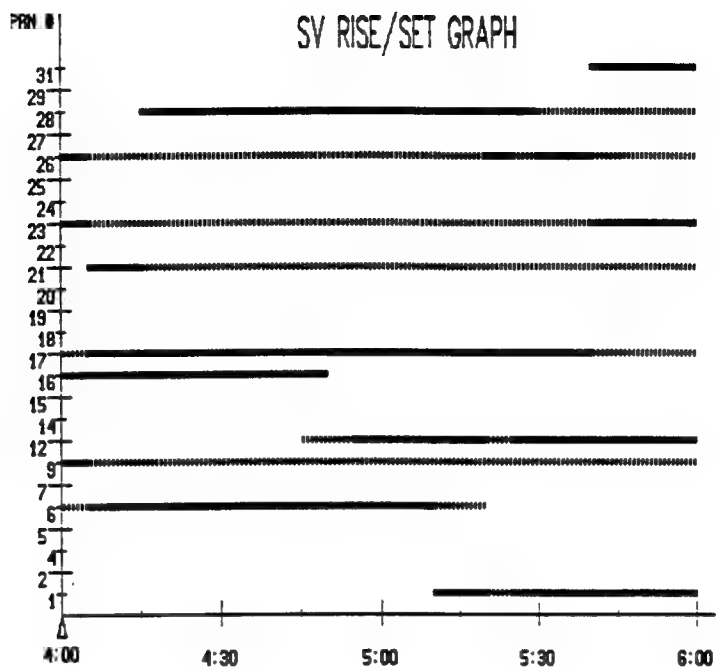


Figure F - 4. SV Rise/Set and Number of Visible SVs

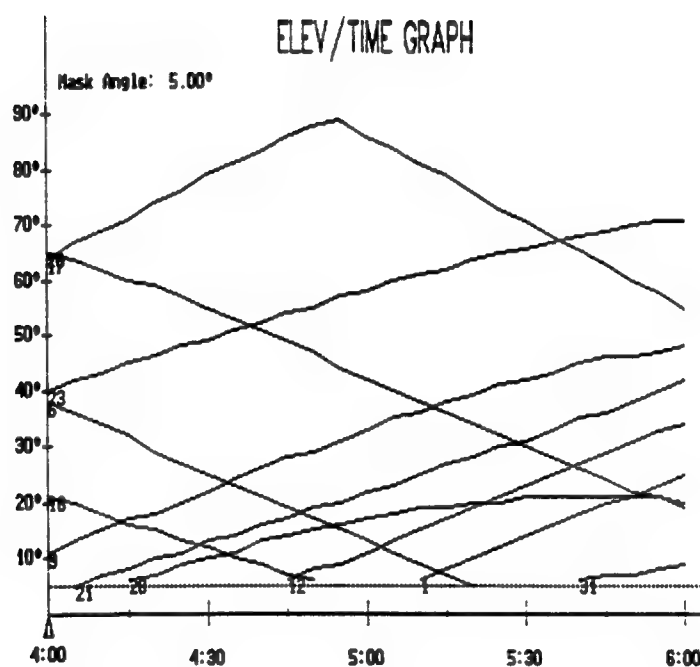
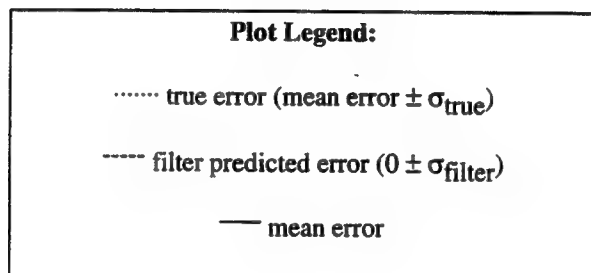


Figure F - 5. Elevation/Time

Appendix G

Plots of North, West and Azimuth Tilts (Figure G - 1 shows conservative Q-tuning, Figure G - 2 shows non-conservative Q-tuning); Plots of North, West and Vertical Velocity (Figure G - 3 shows conservative Q-tuning, Figure G - 4 shows non-conservative Q-tuning).



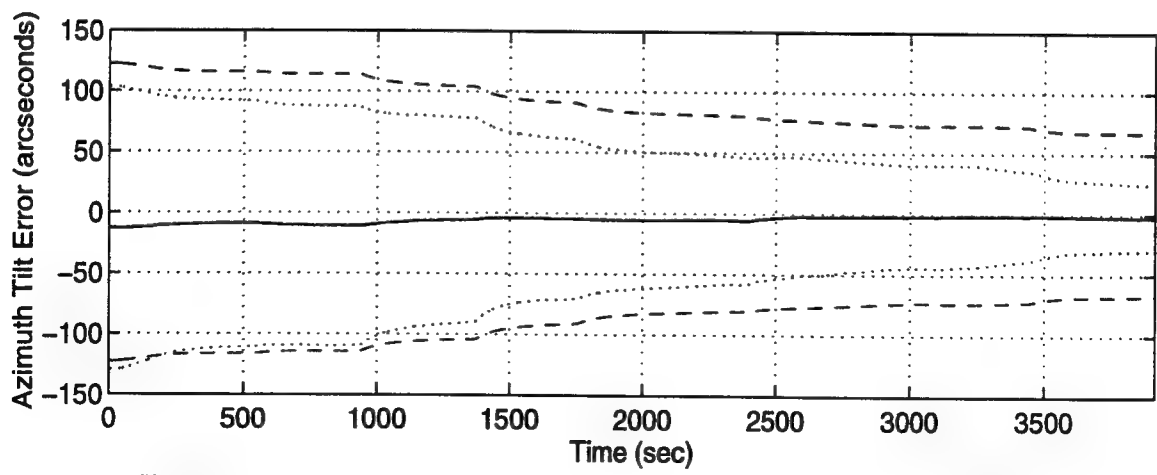
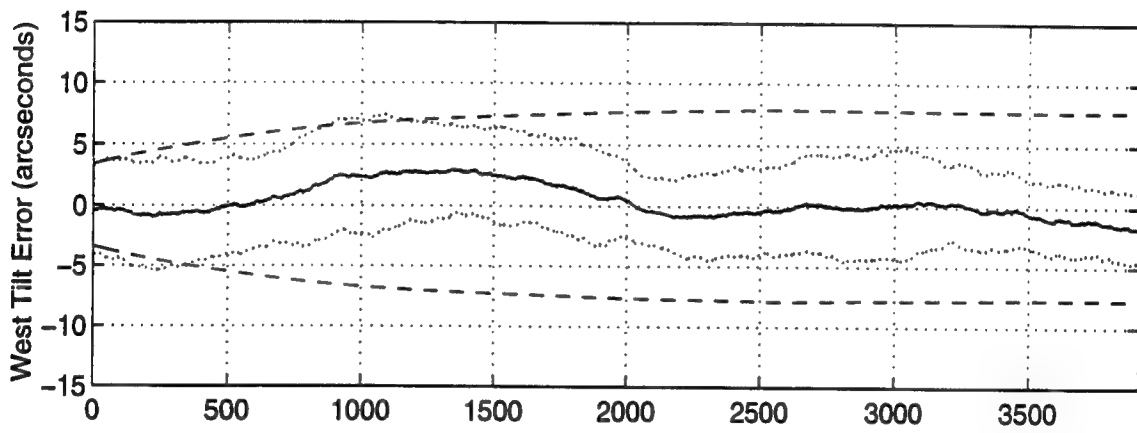
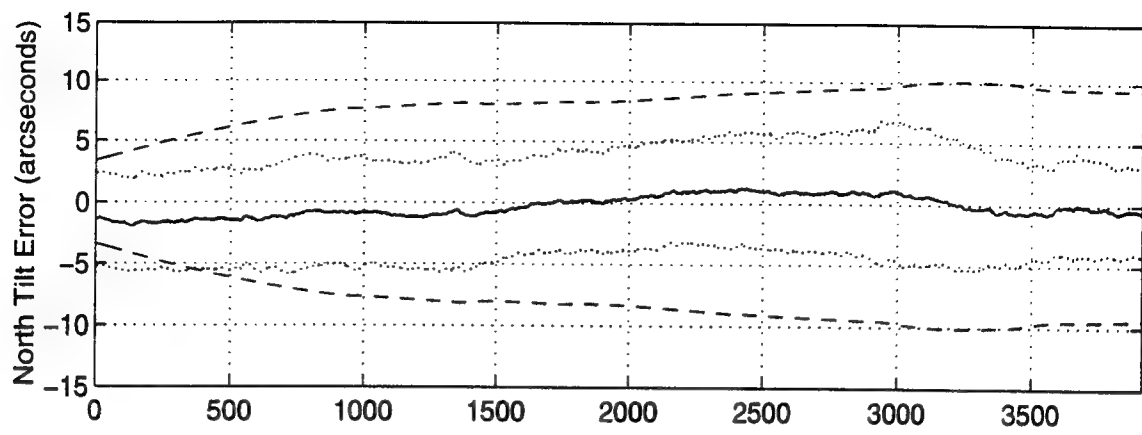


Figure G - 1. North, West and Azimuth Tilts (Conservative Q-tuning)

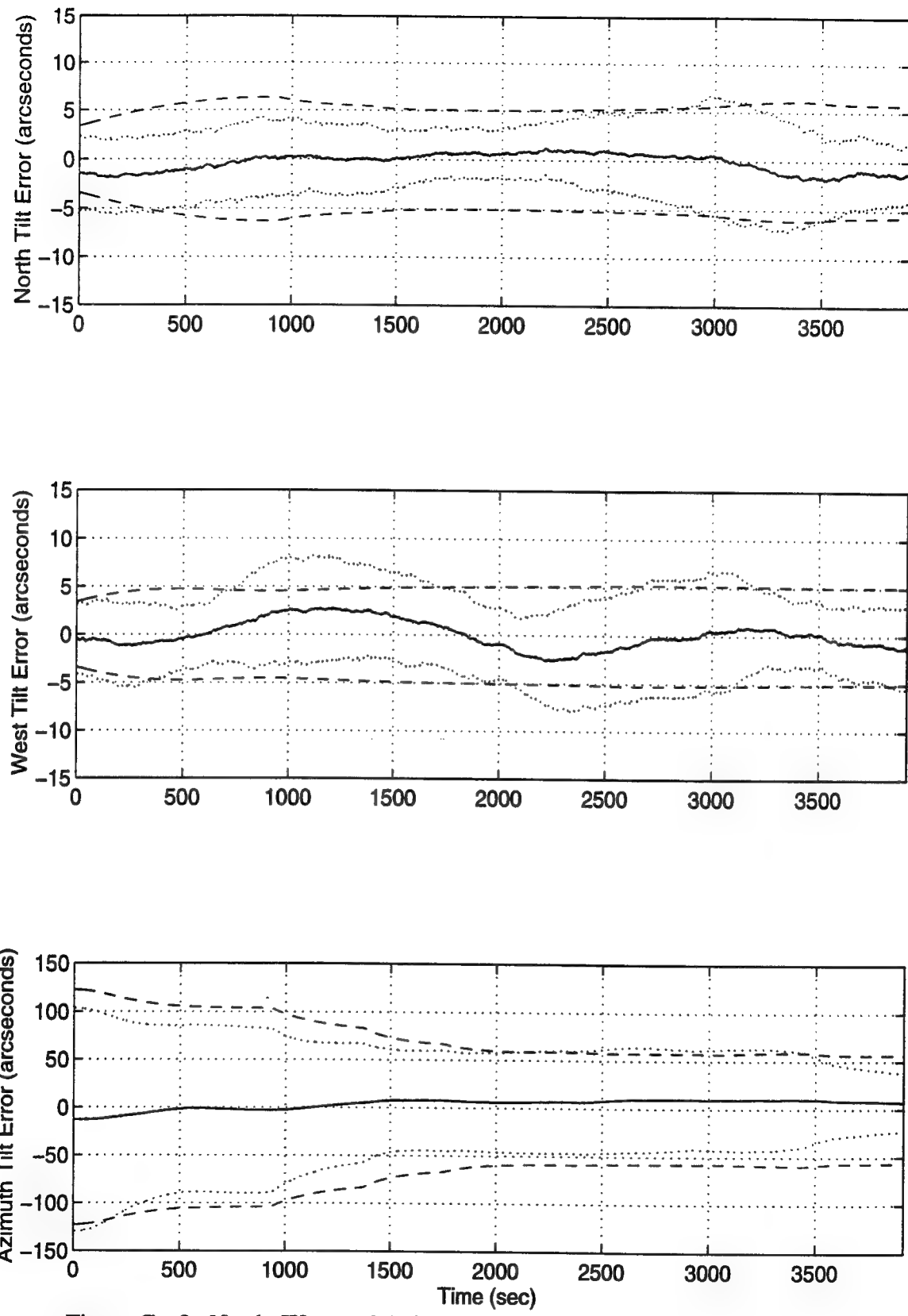


Figure G - 2. North, West and Azimuth Tilts (Non-Conservative Q-tuning)

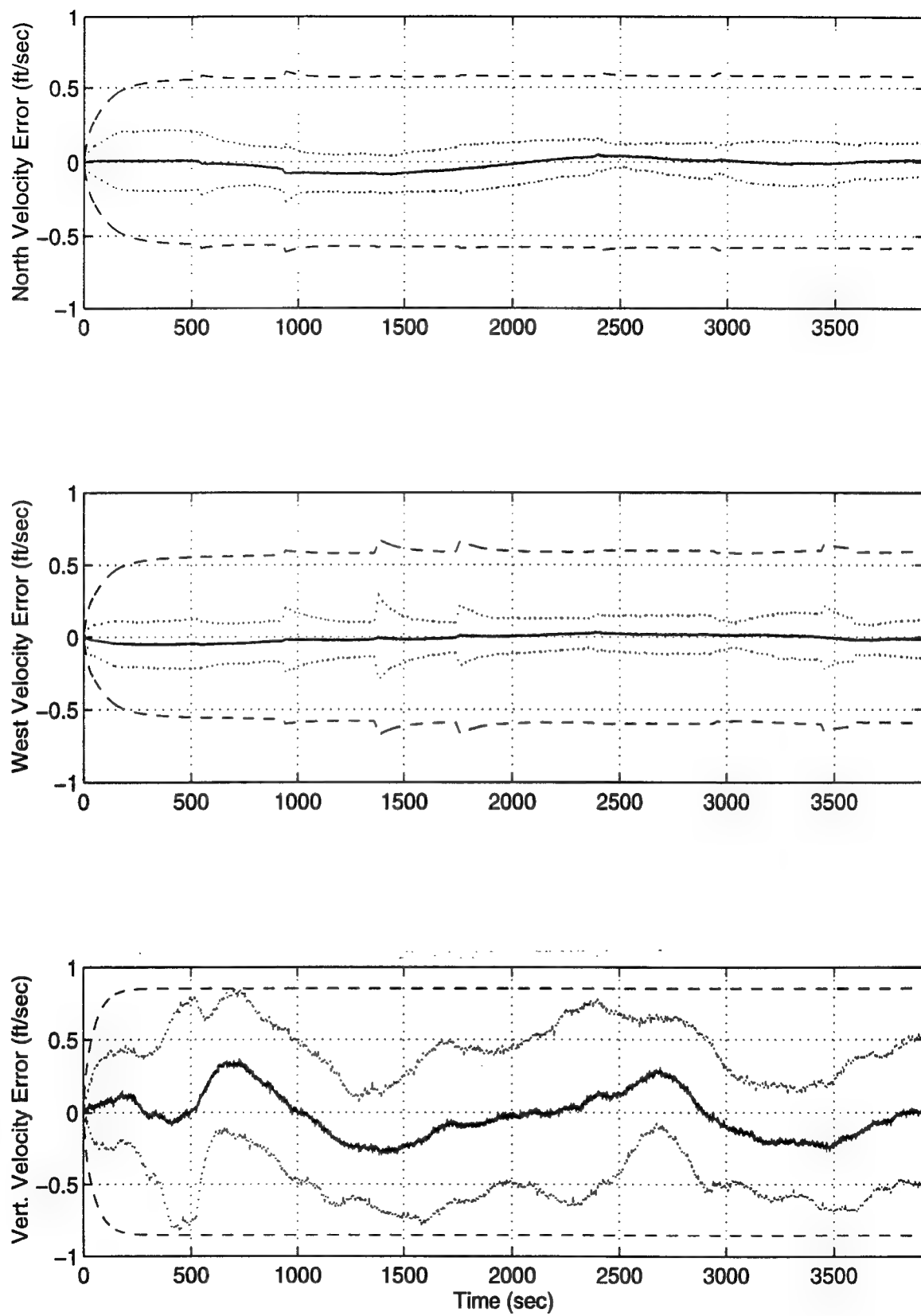


Figure G - 3 North, West and Vertical Velocity (Conservative Q-tuning)

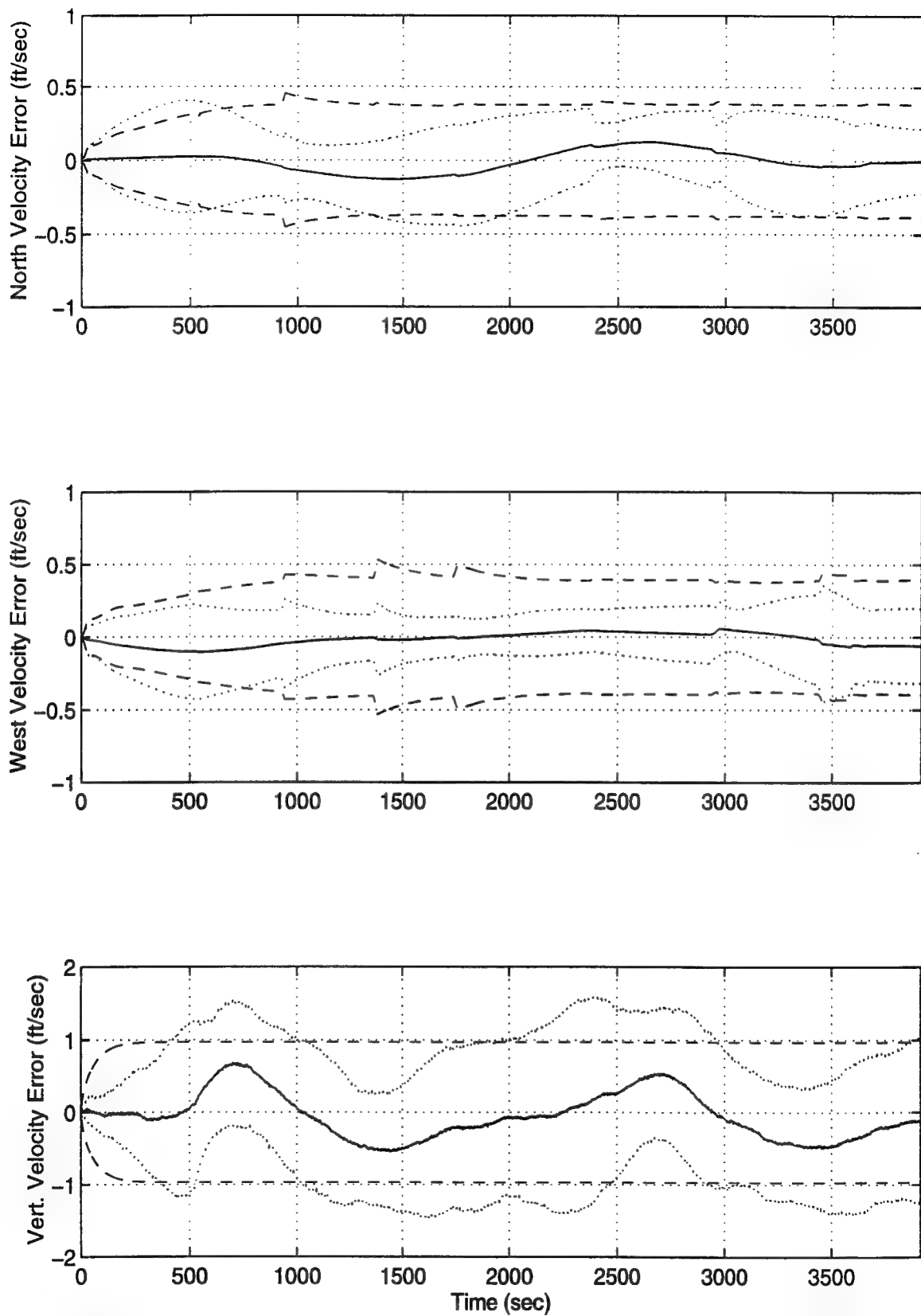
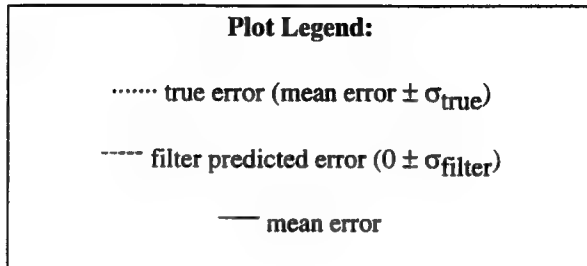


Figure G - 4 North, West and Vertical Velocity (Non-Conservative Q-tuning)

Appendix H

Plots of Case I: Barometric Altimeter, 0.4 nm/hr INS, P-Code GPS Using the Tanker Flight Profile.



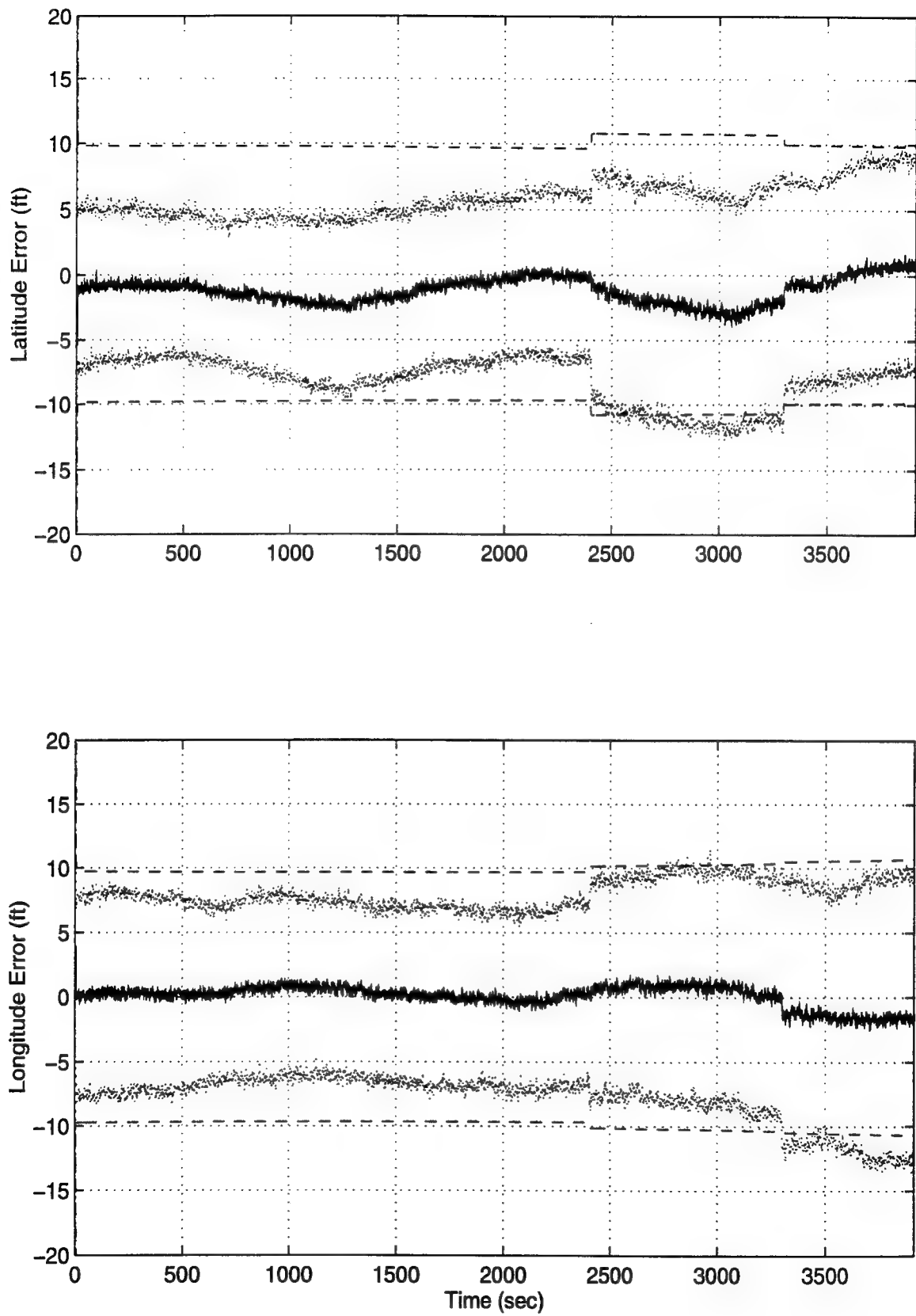


Figure H - 1. Latitude and Longitude Error

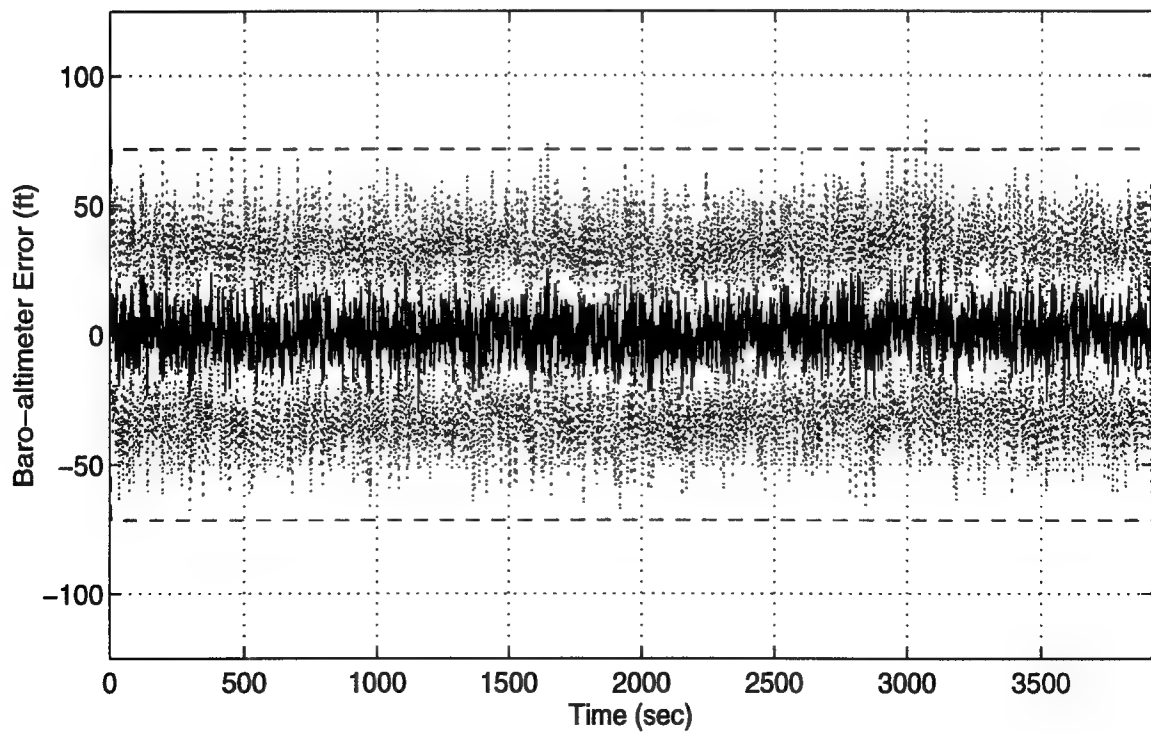
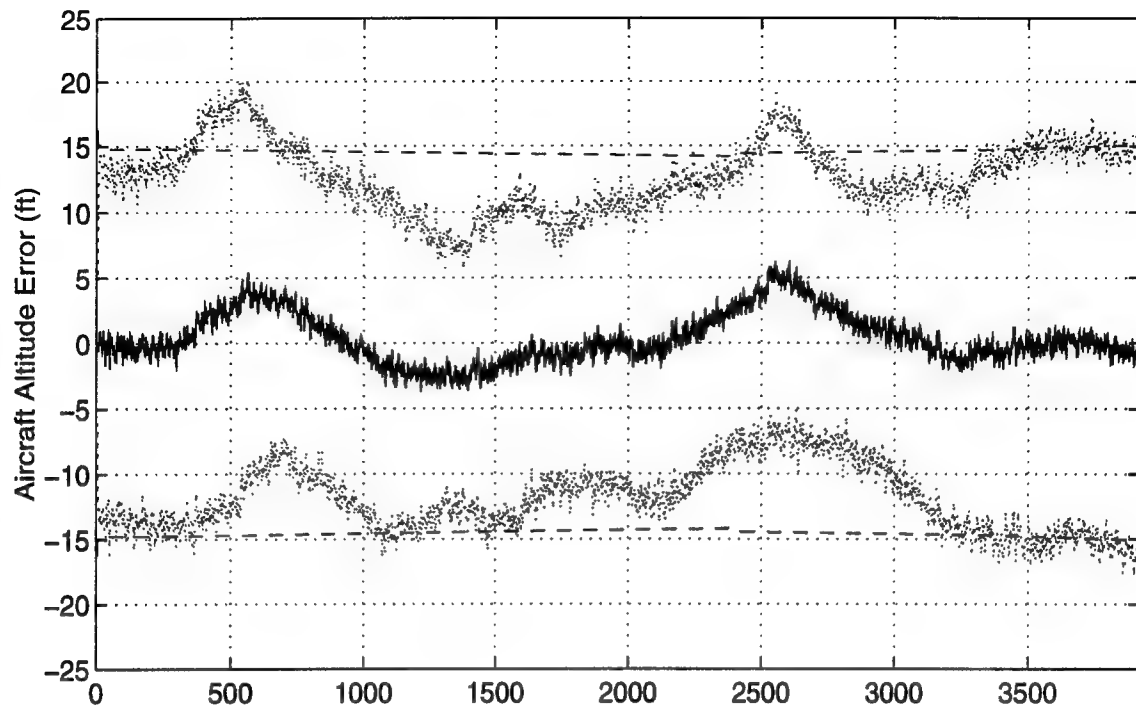


Figure H - 2. Aircraft Altitude and Baro-Altimeter Error

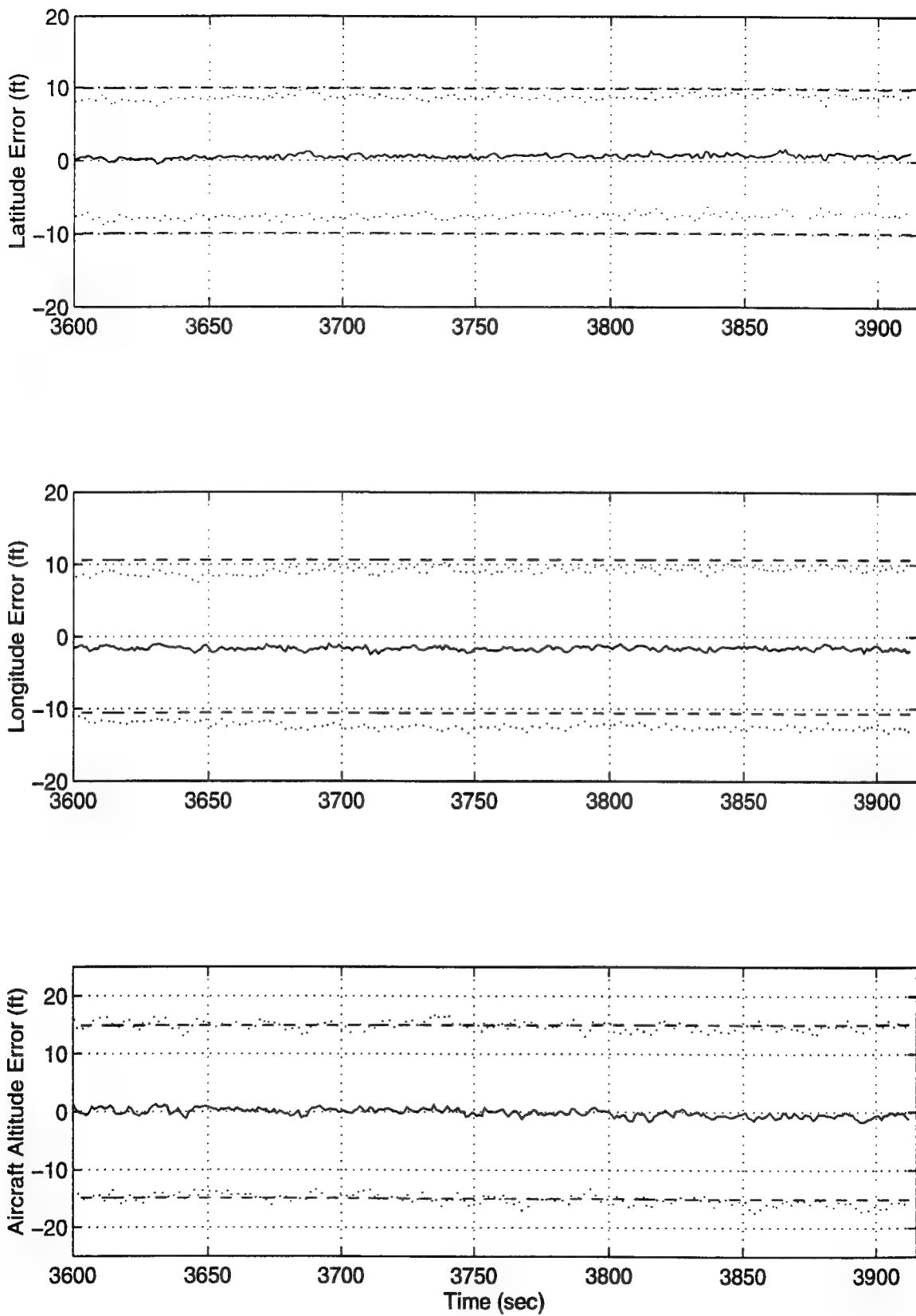


Figure H - 3 Latitude, Longitude and Aircraft Altitude Error

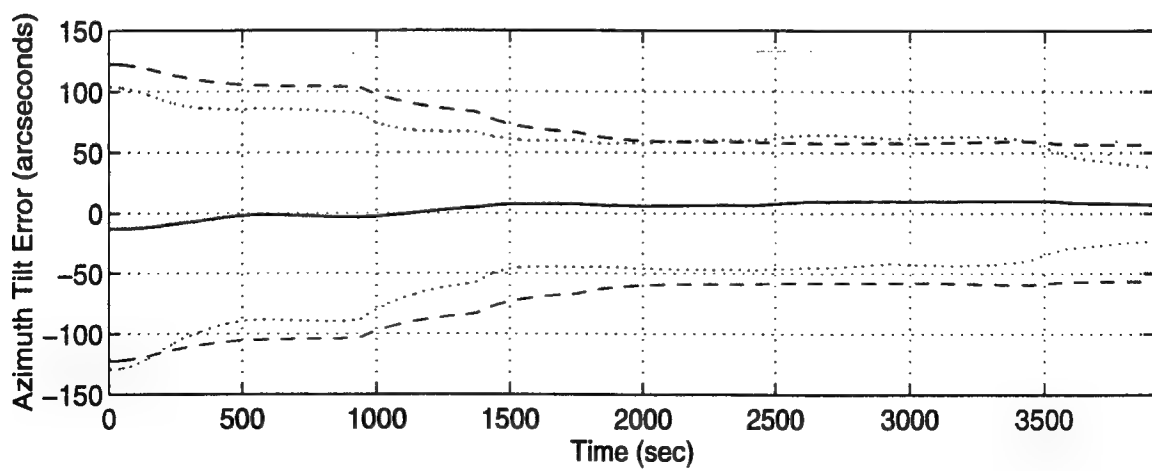
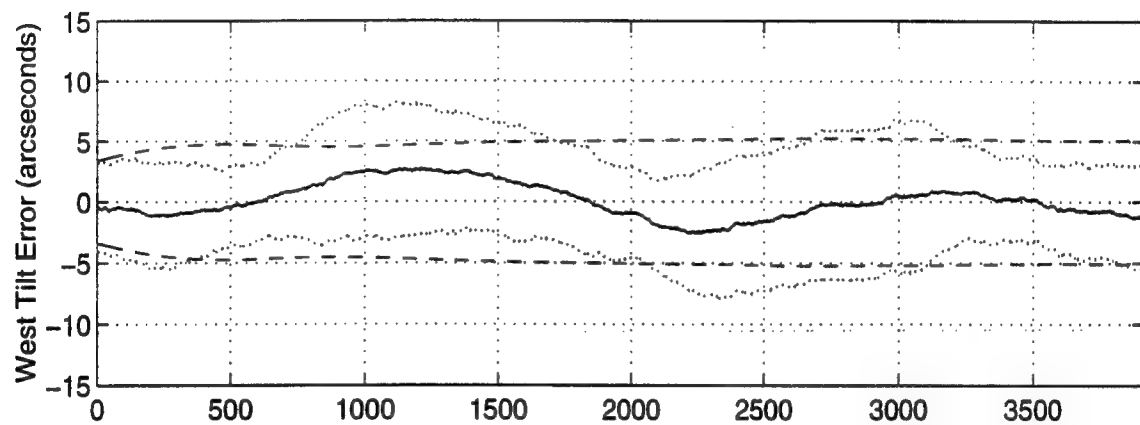
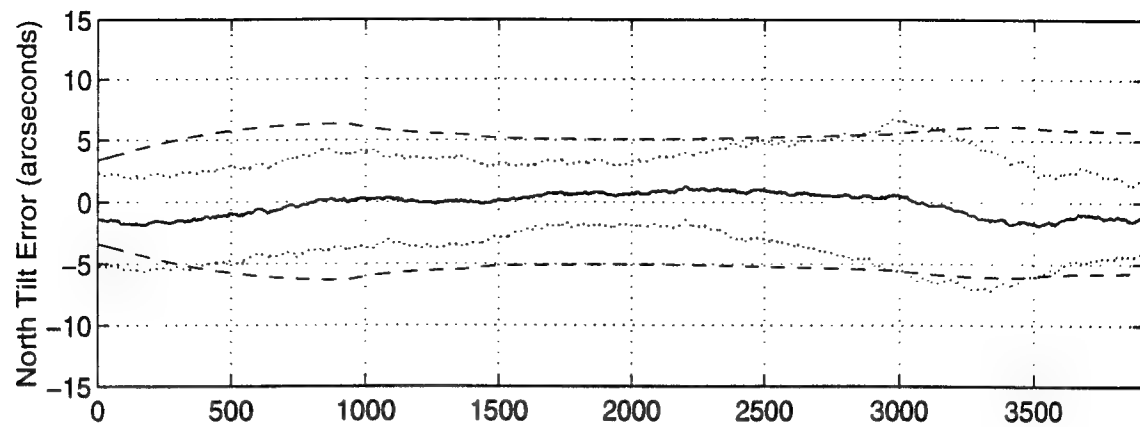


Figure H - 4 North, West and Azimuth Tilt Errors

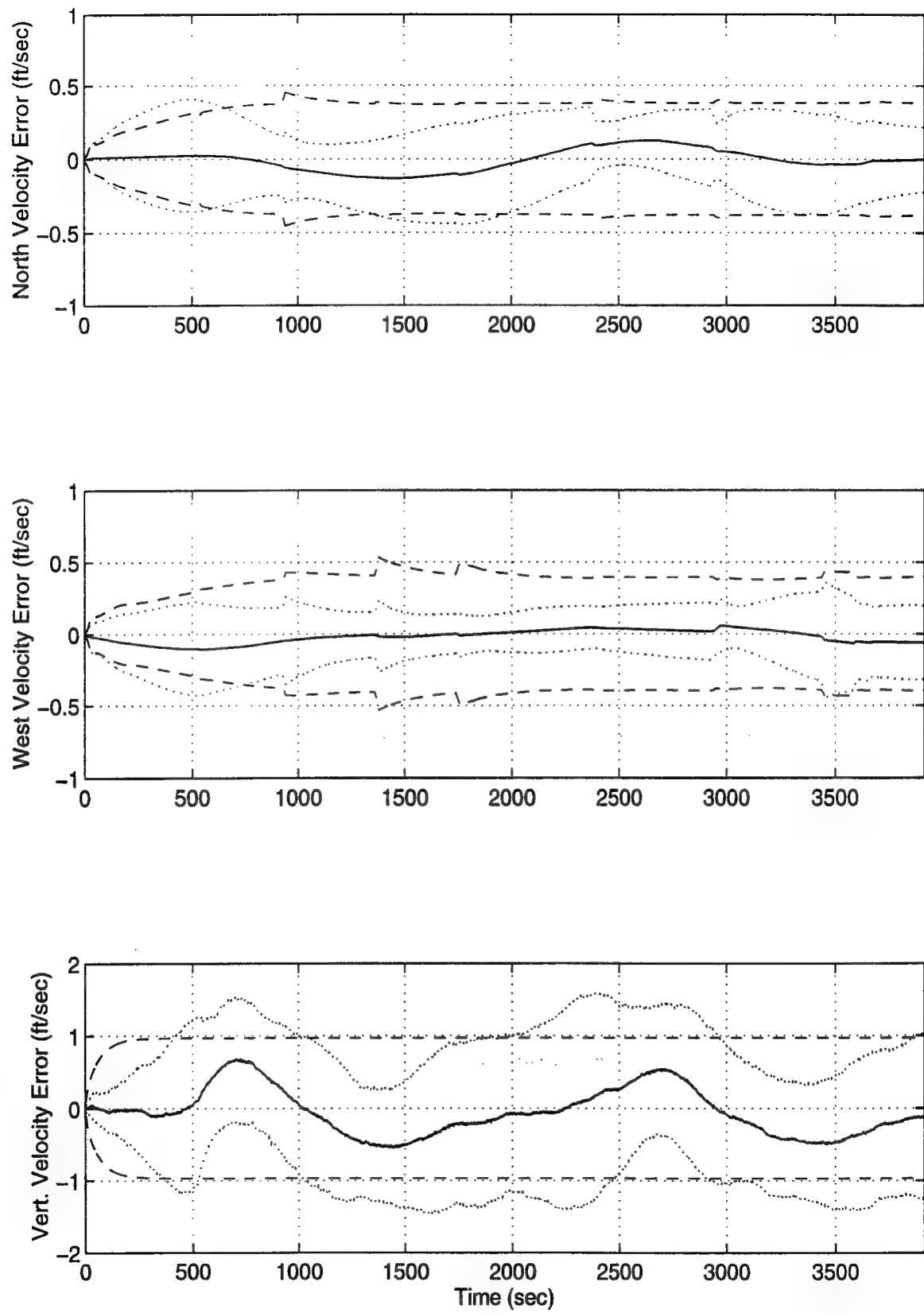


Figure H - 5 North, West and Vertical Velocity Errors

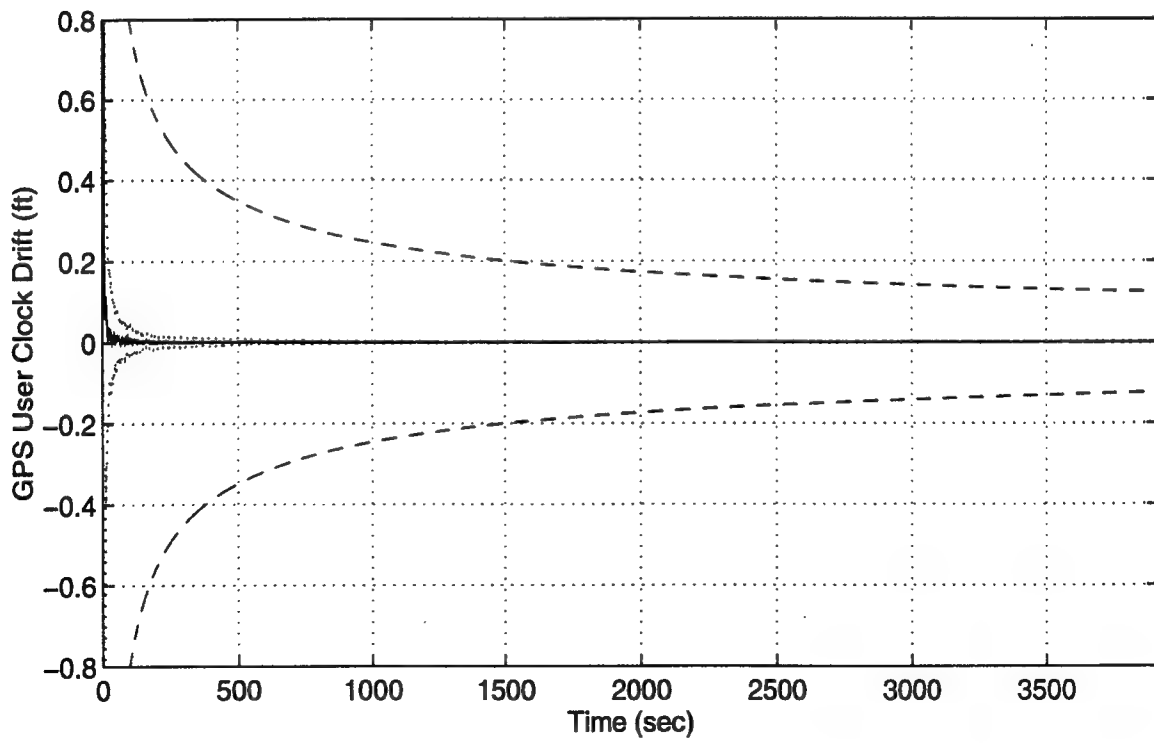
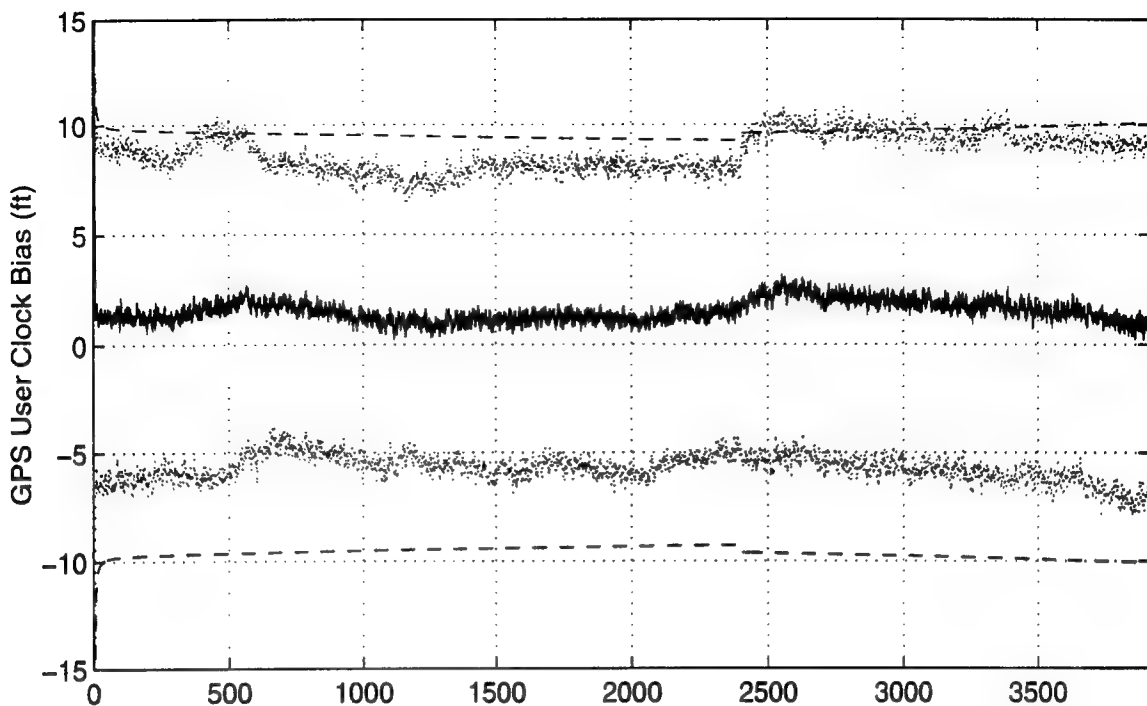
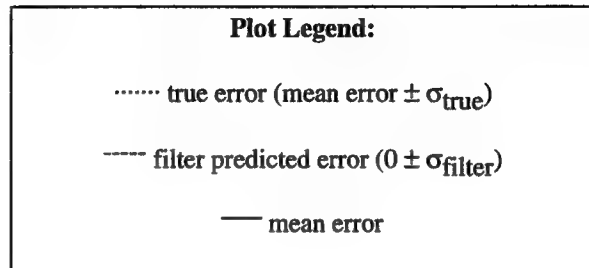


Figure H - 6 GPS User Clock Bias and GPS User Clock Drift

Appendix I

Plots of Case II: Barometric Altimeter, 0.4 nm/hr INS, P-Code GPS and Radar Altimeter Using the Tanker Flight Profile.



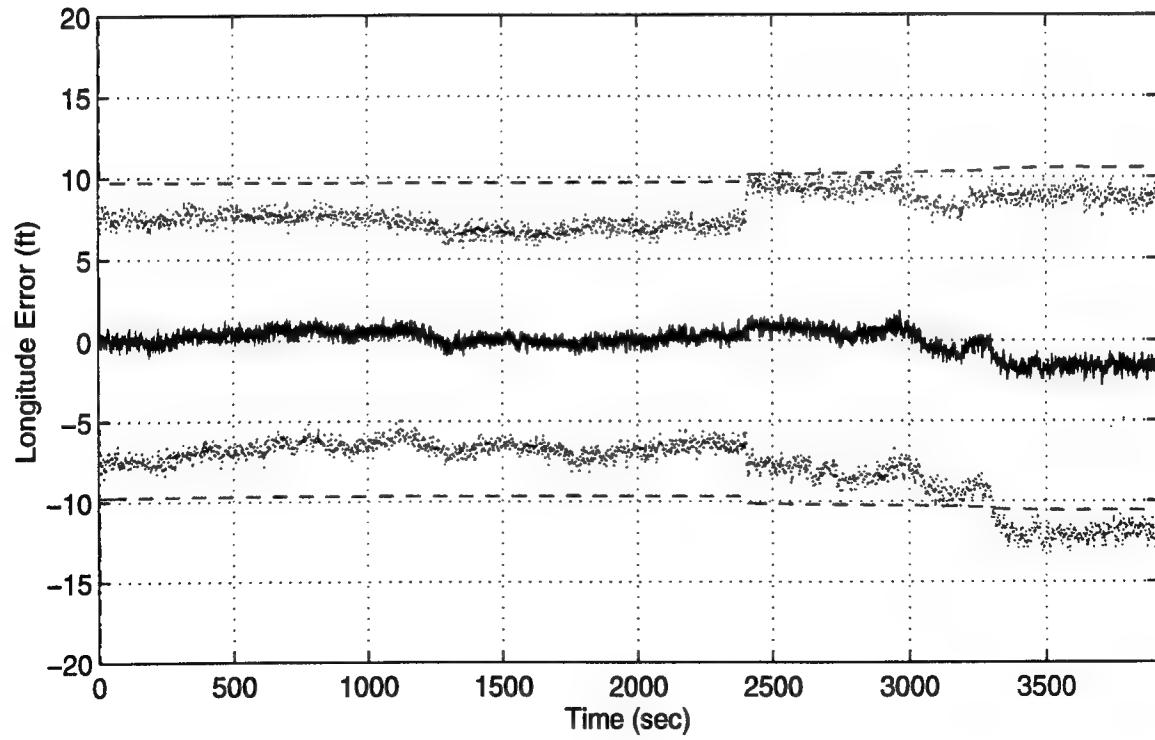
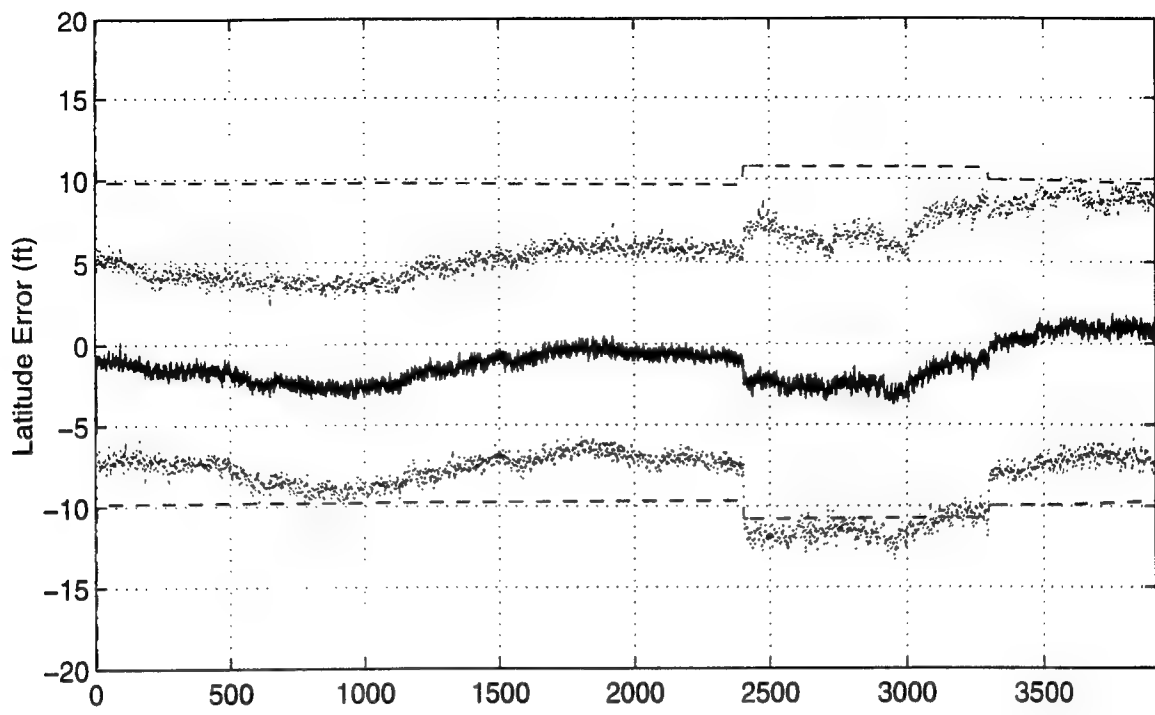


Figure I - 1. Latitude and Longitude Error

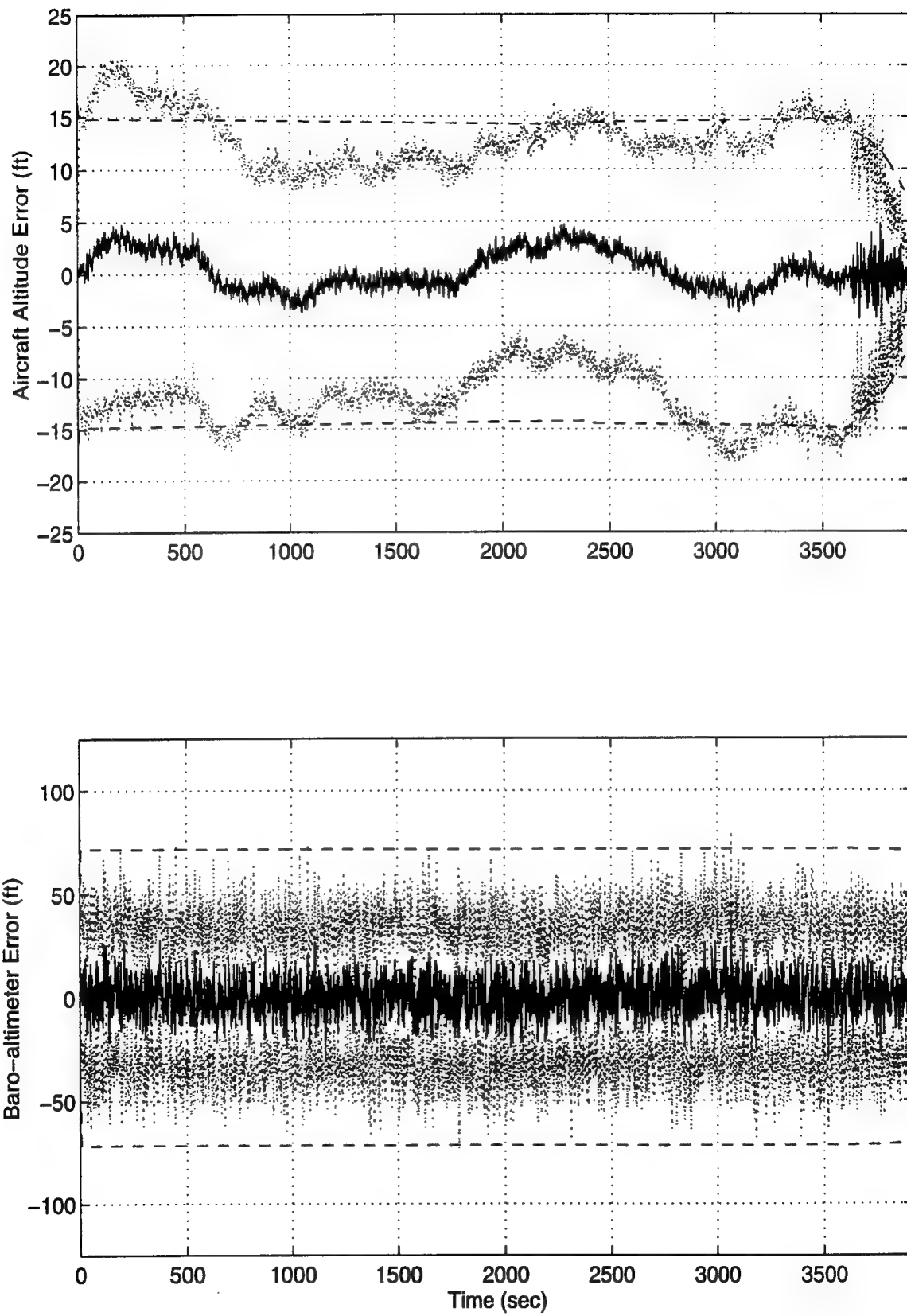


Figure I - 2. Aircraft Altitude and Baro-Altimeter Error

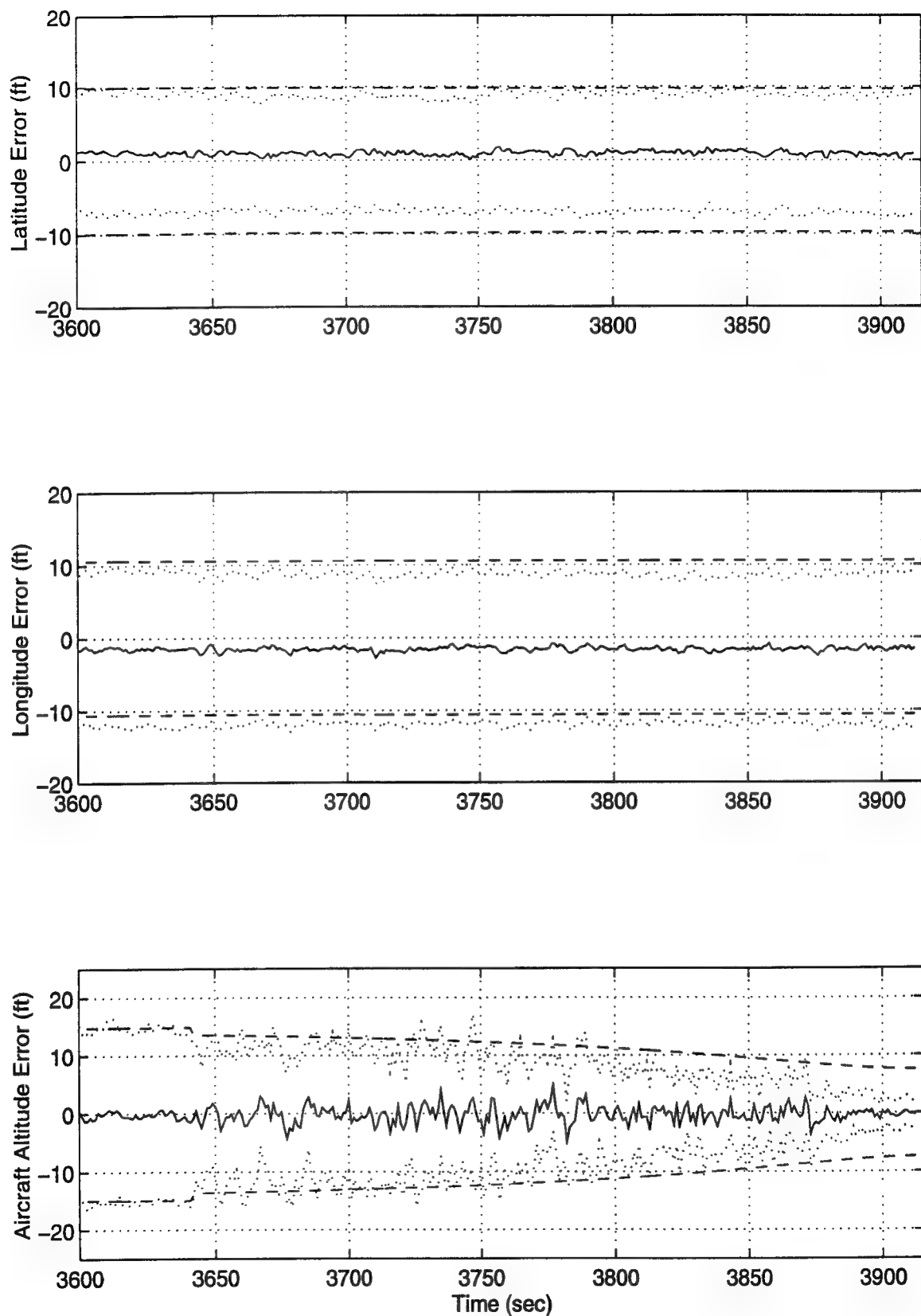


Figure I - 3 Latitude, Longitude and Aircraft Altitude Error

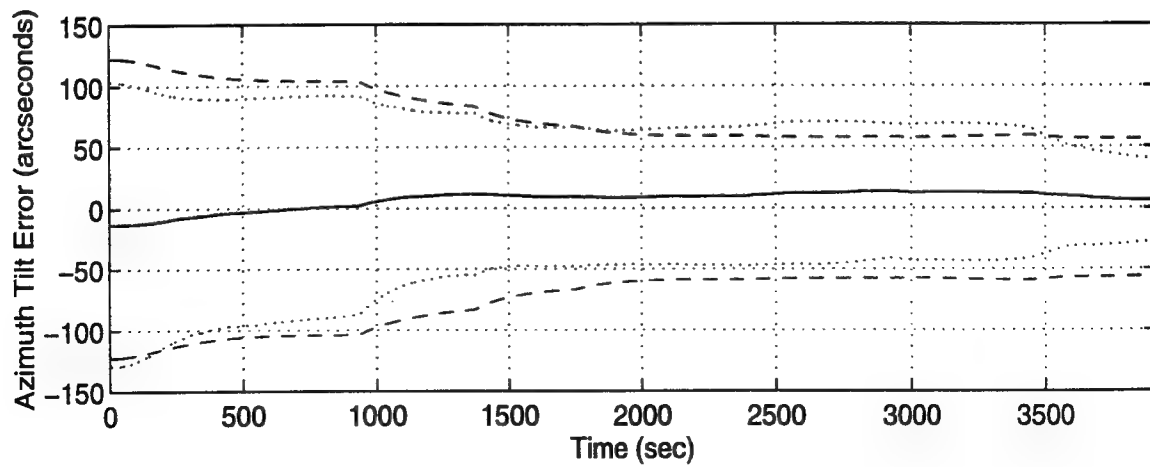
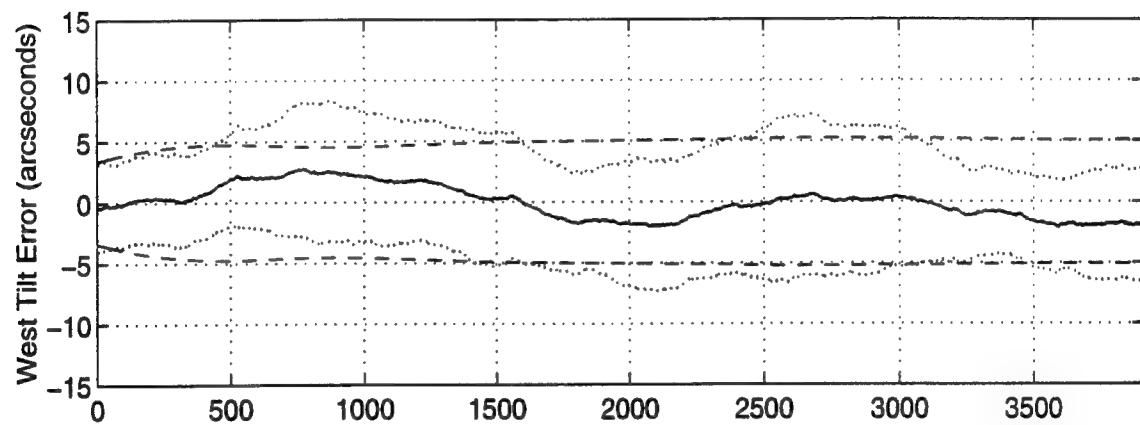
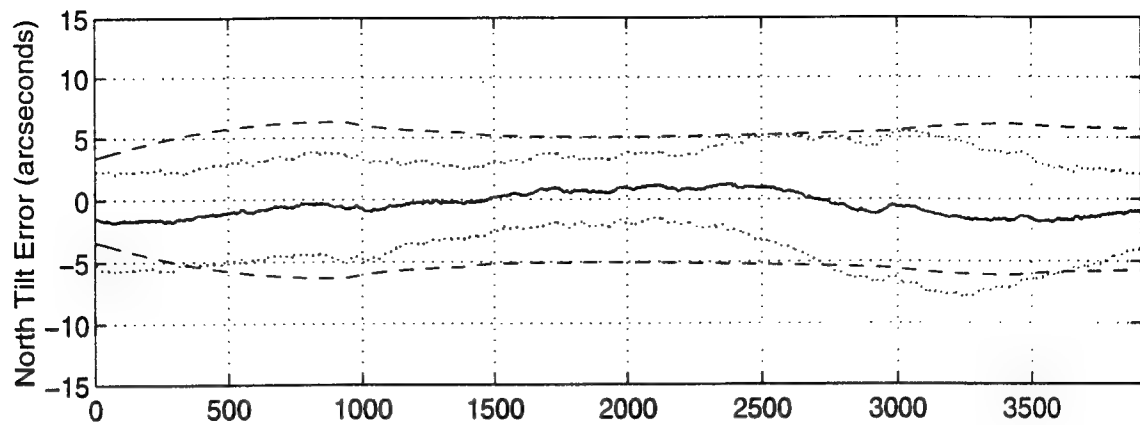


Figure I - 4 North, West and Azimuth Tilt Errors

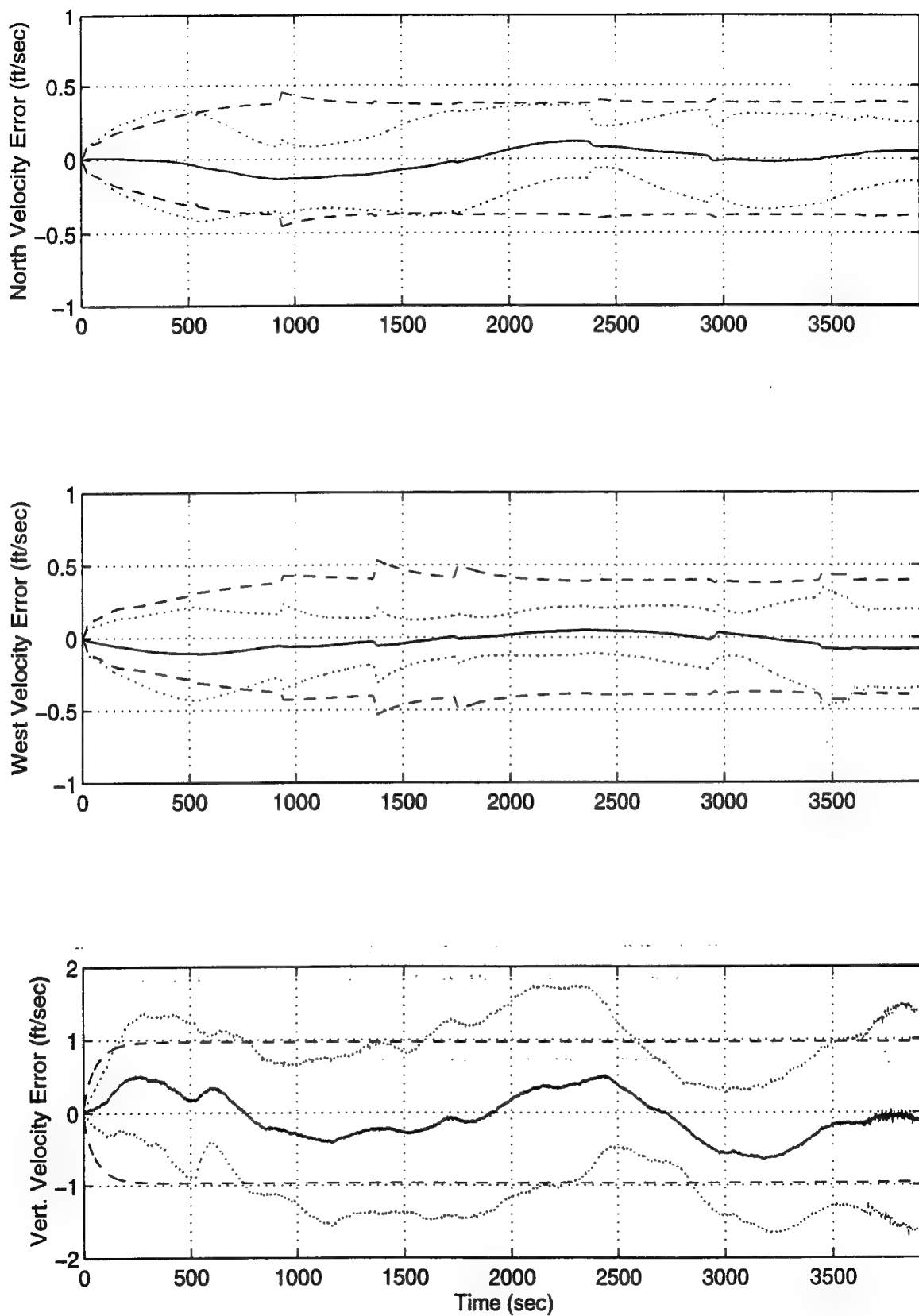


Figure I - 5 North, West and Vertical Velocity Errors

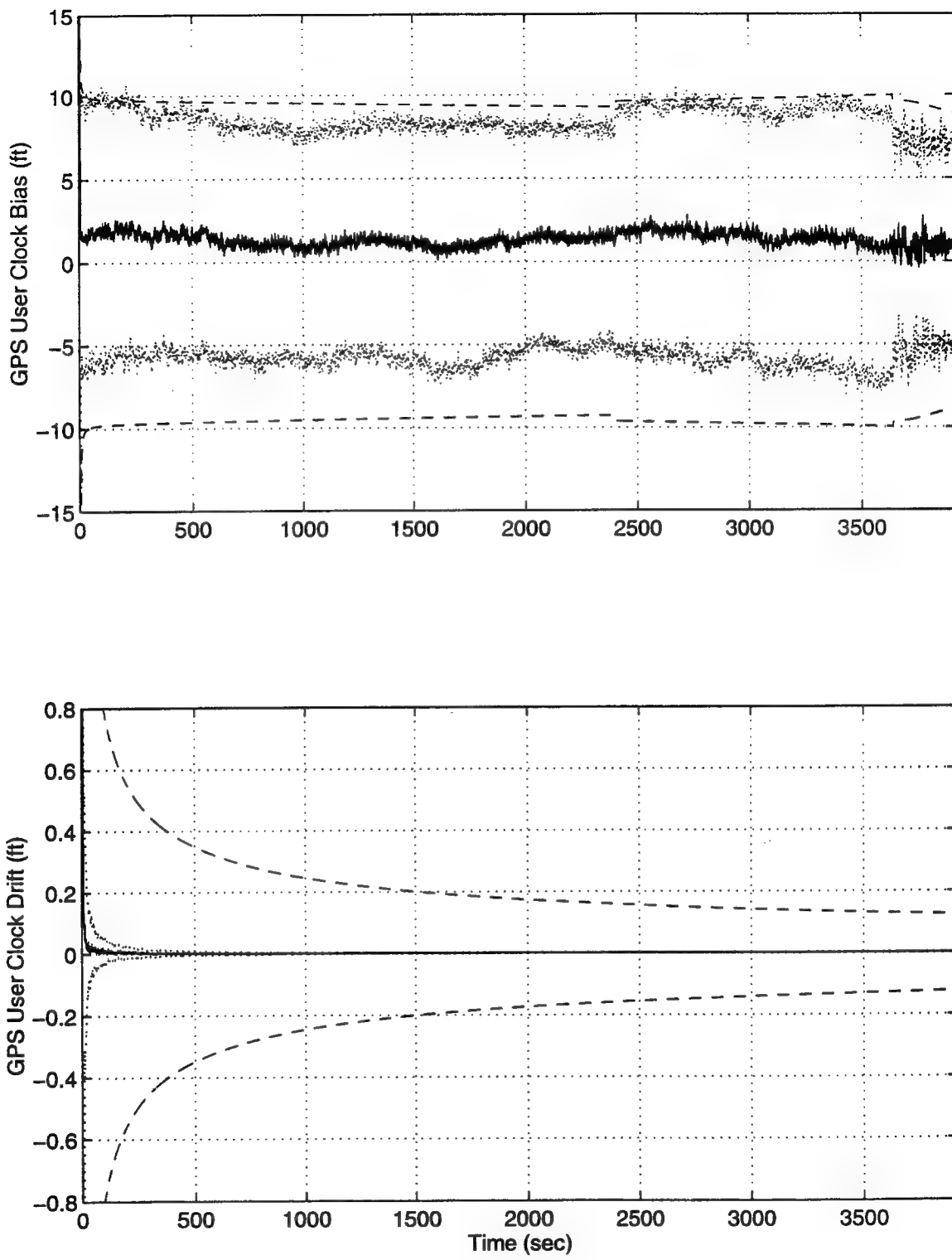
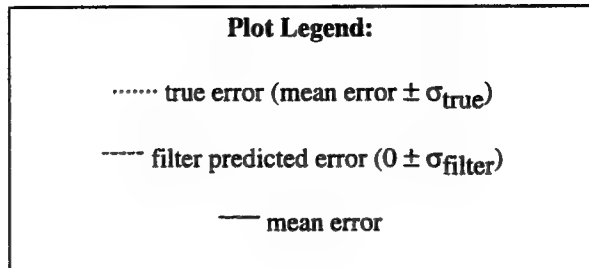


Figure I - 6 GPS User Clock Bias and GPS User Clock Drift

Appendix J

Plots of Case III: Barometric Altimeter, 2.0 nm/hr INS, P-Code GPS Using the Tanker Flight Profile.



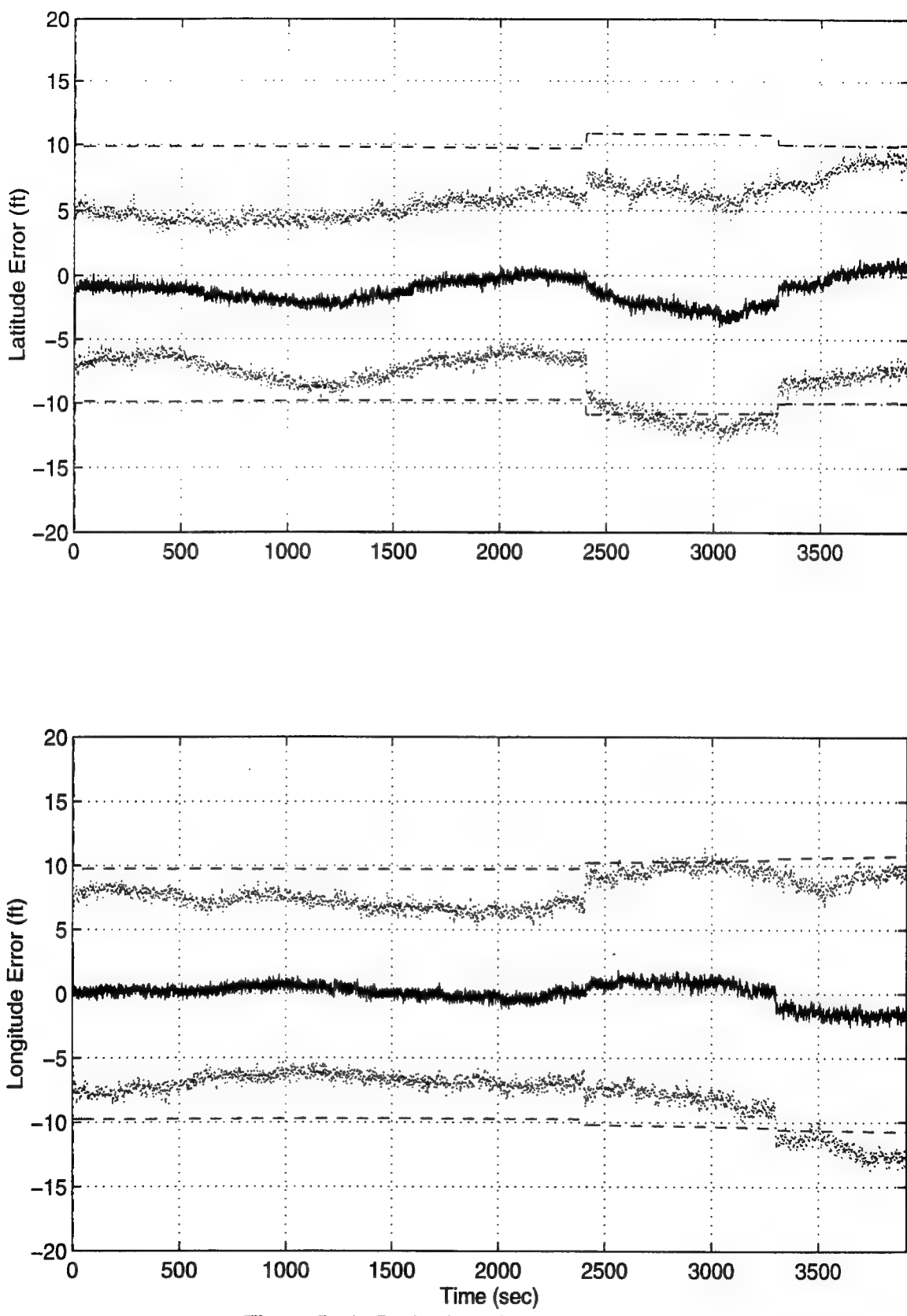


Figure J - 1. Latitude and Longitude Error

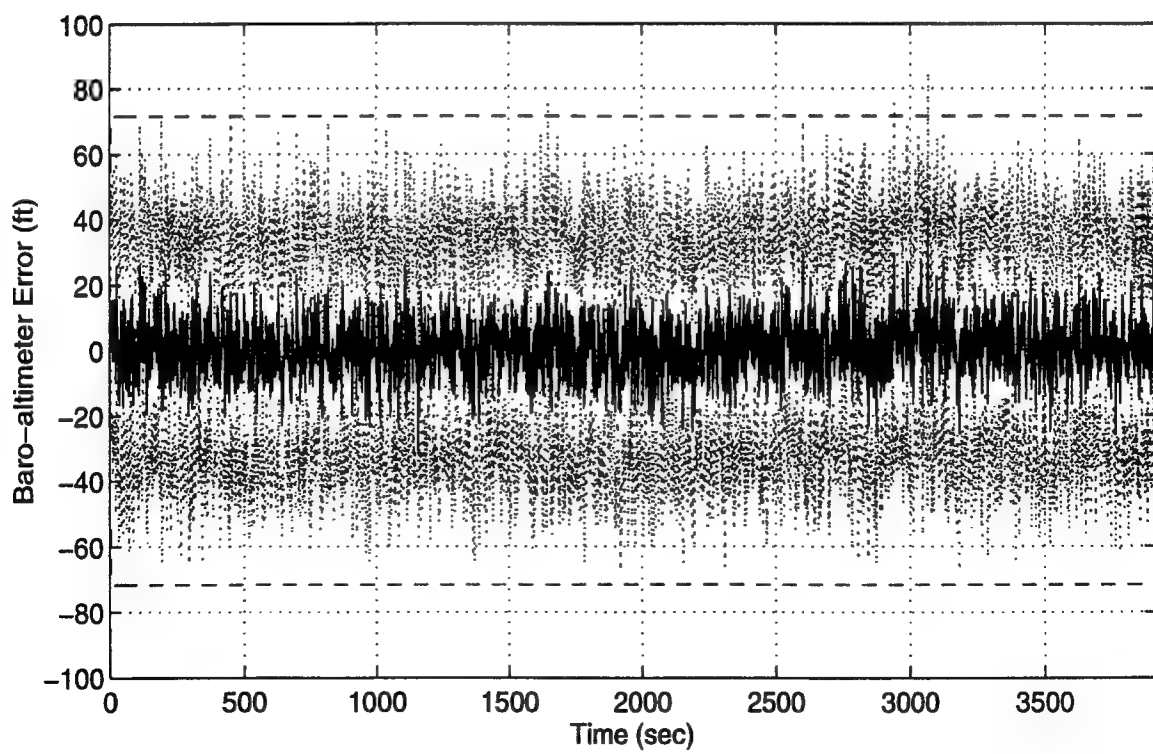
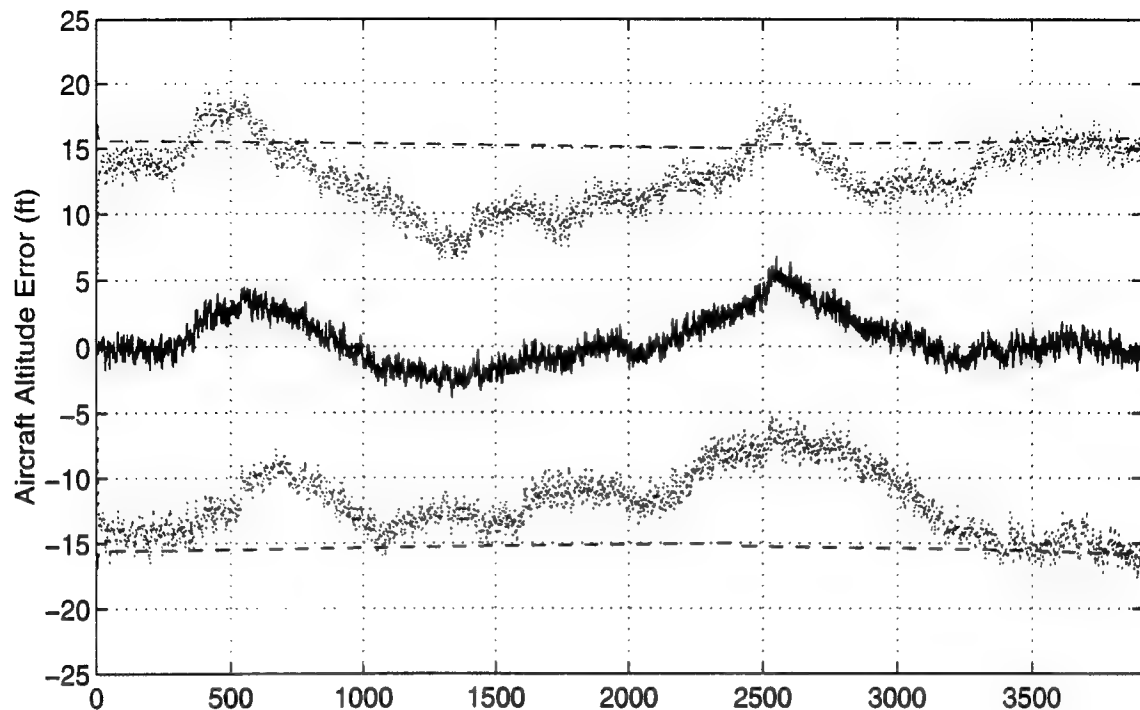


Figure J - 2. Aircraft Altitude and Baro-Altimeter Error

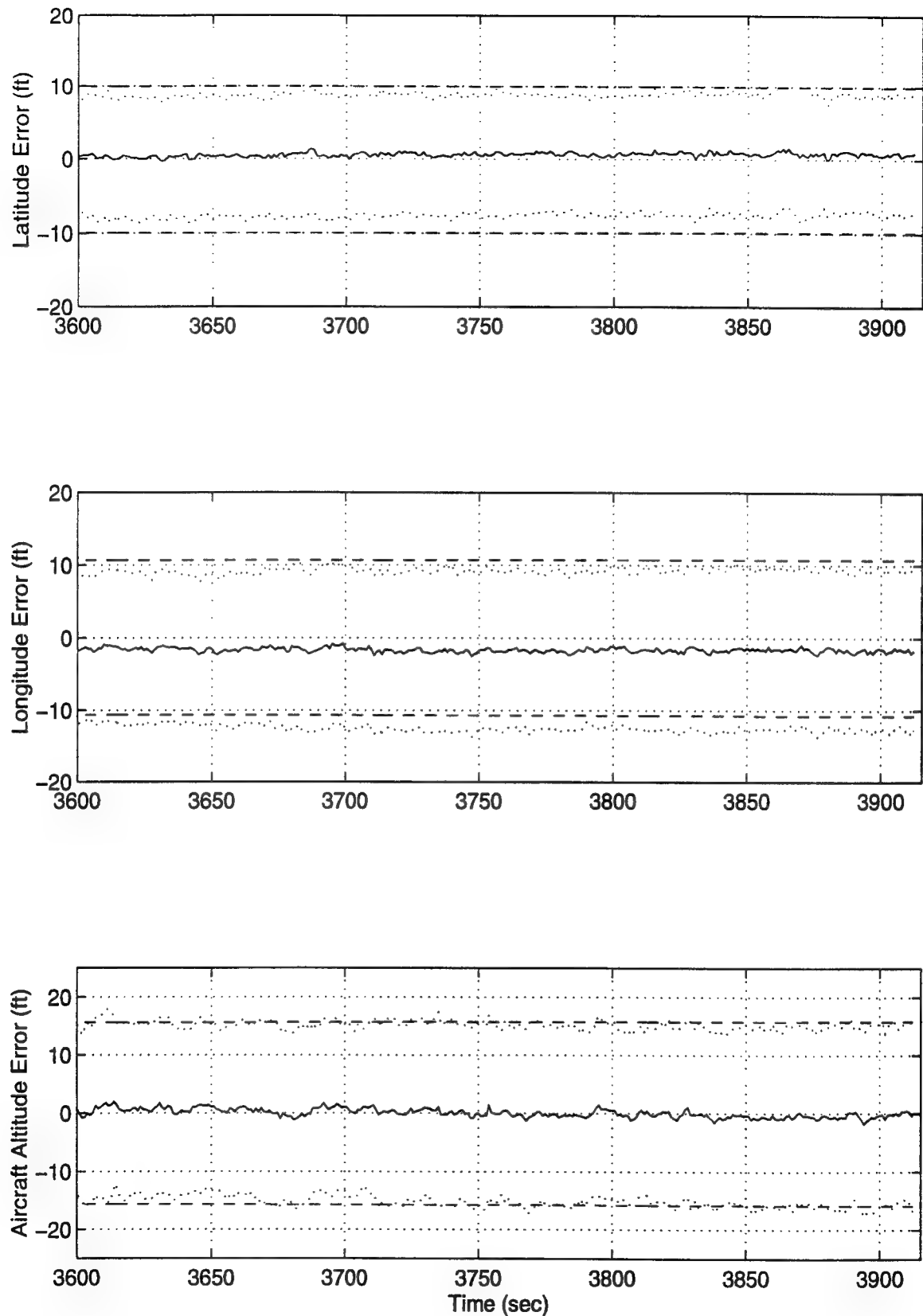


Figure J - 3 Latitude, Longitude and Aircraft Altitude Error

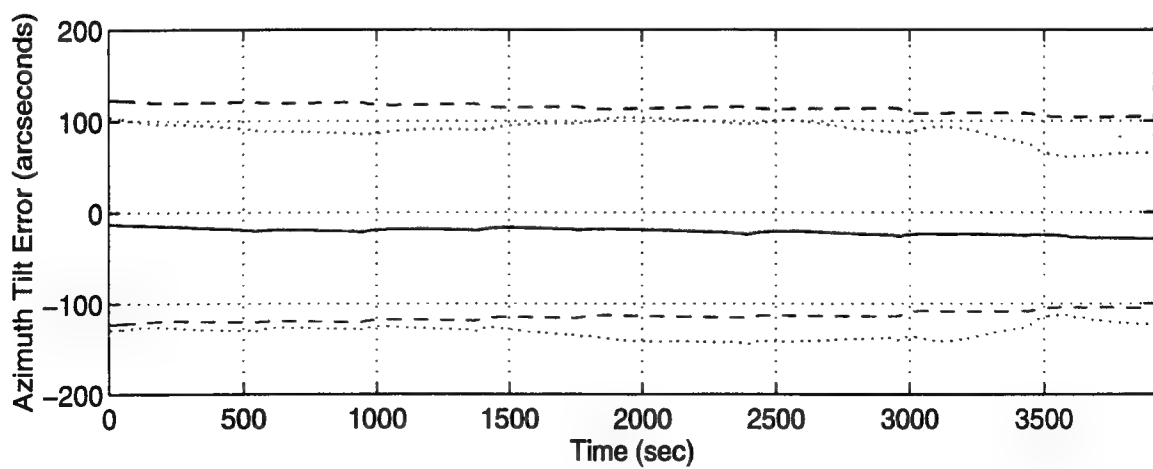
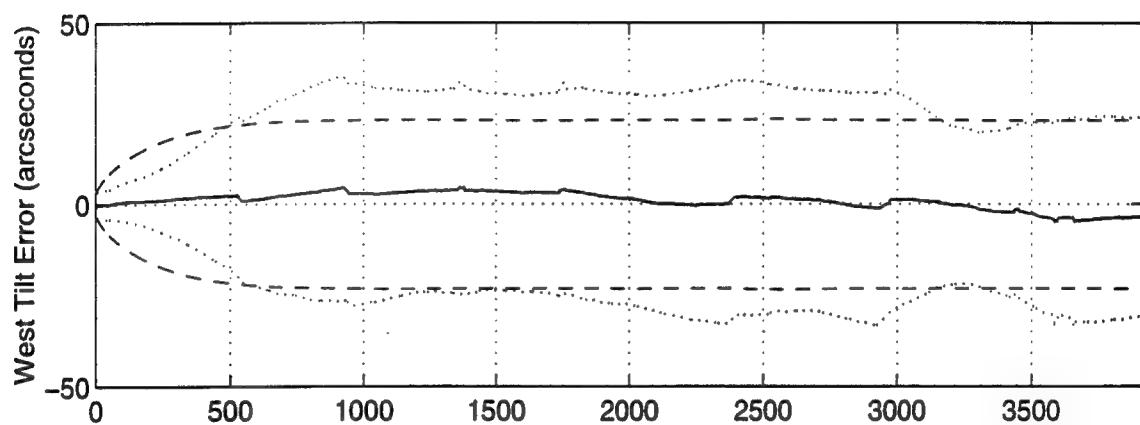
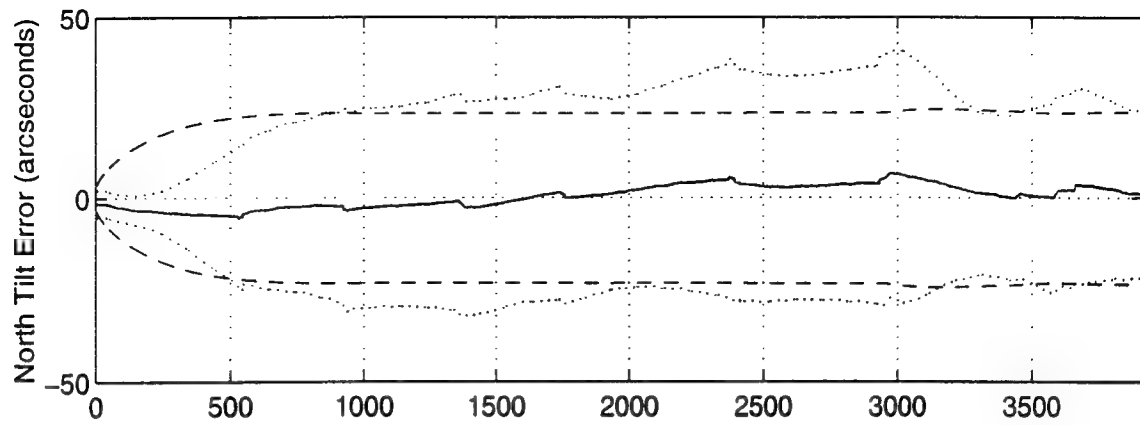


Figure J - 4 North, West and Azimuth Tilt Errors

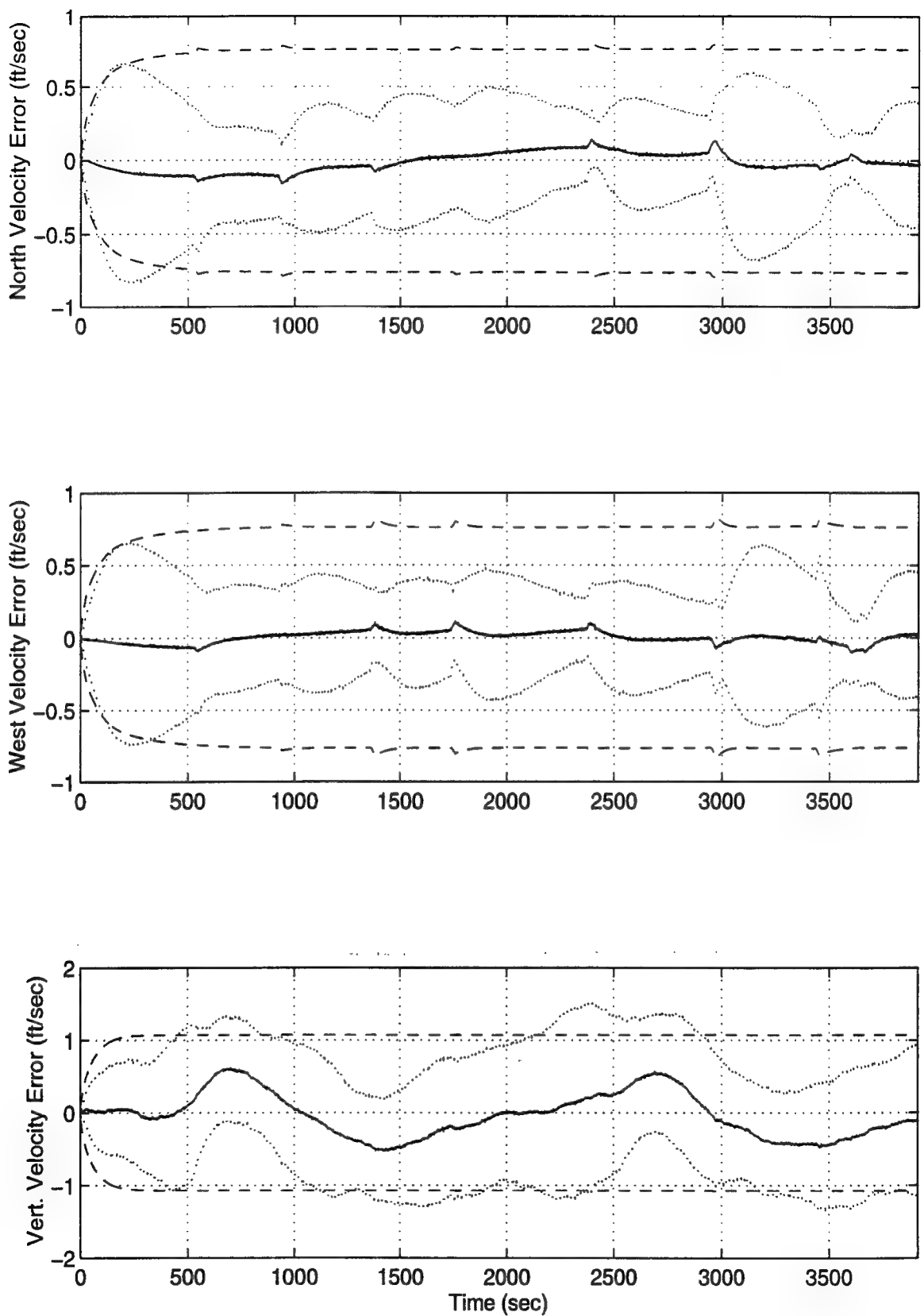


Figure J - 5 North, West and Vertical Velocity Errors

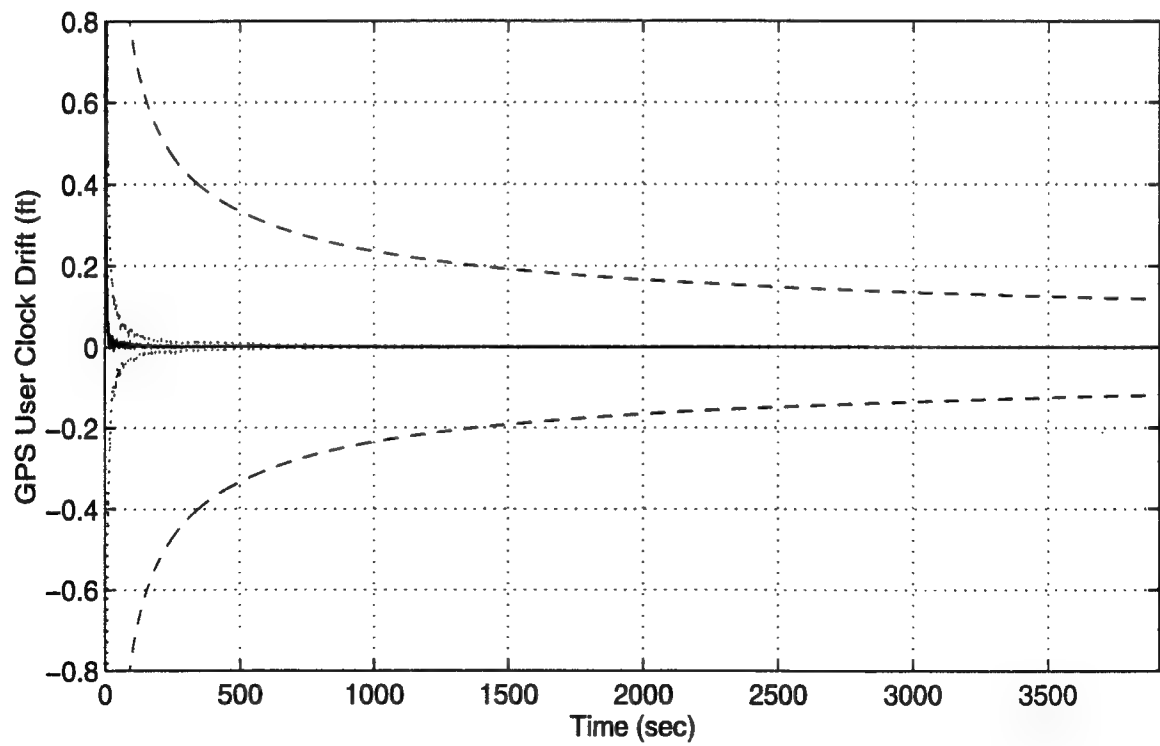
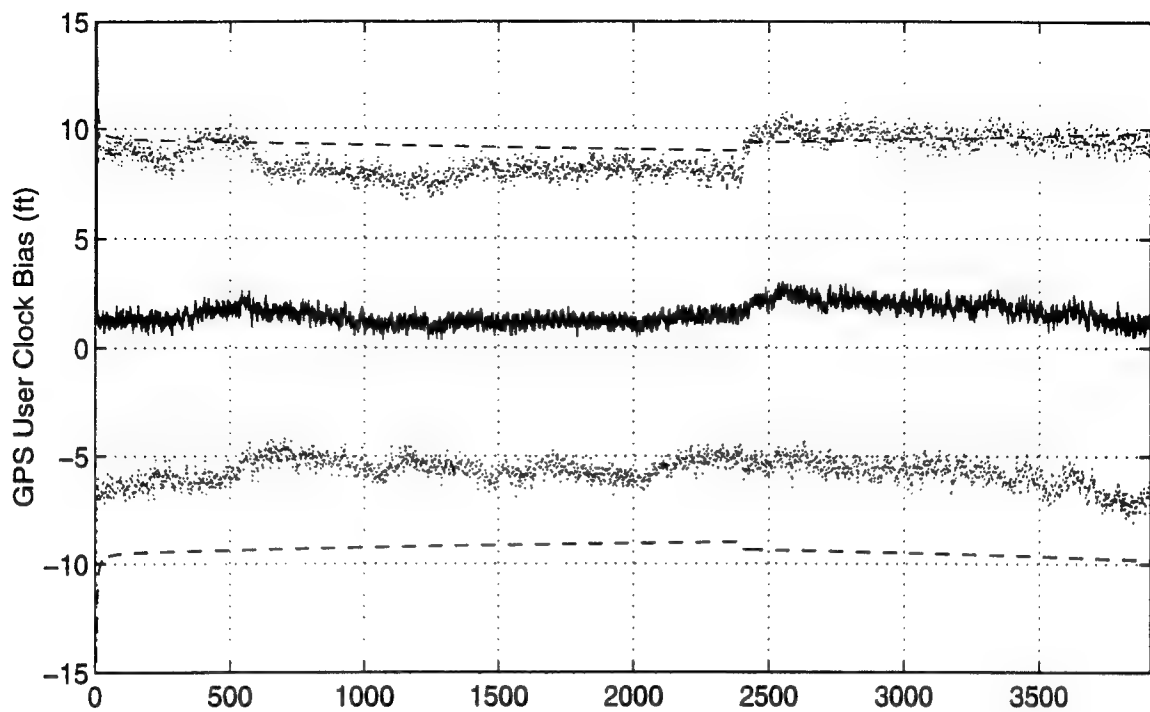
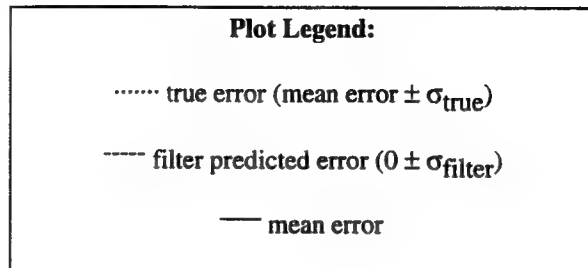


Figure J - 6 GPS User Clock Bias and GPS User Clock Drift

Appendix K

Plots of Case IV: Barometric Altimeter, 2.0 nm/hr INS, P-Code GPS and Radar Altimeter Using the Tanker Flight Profile.



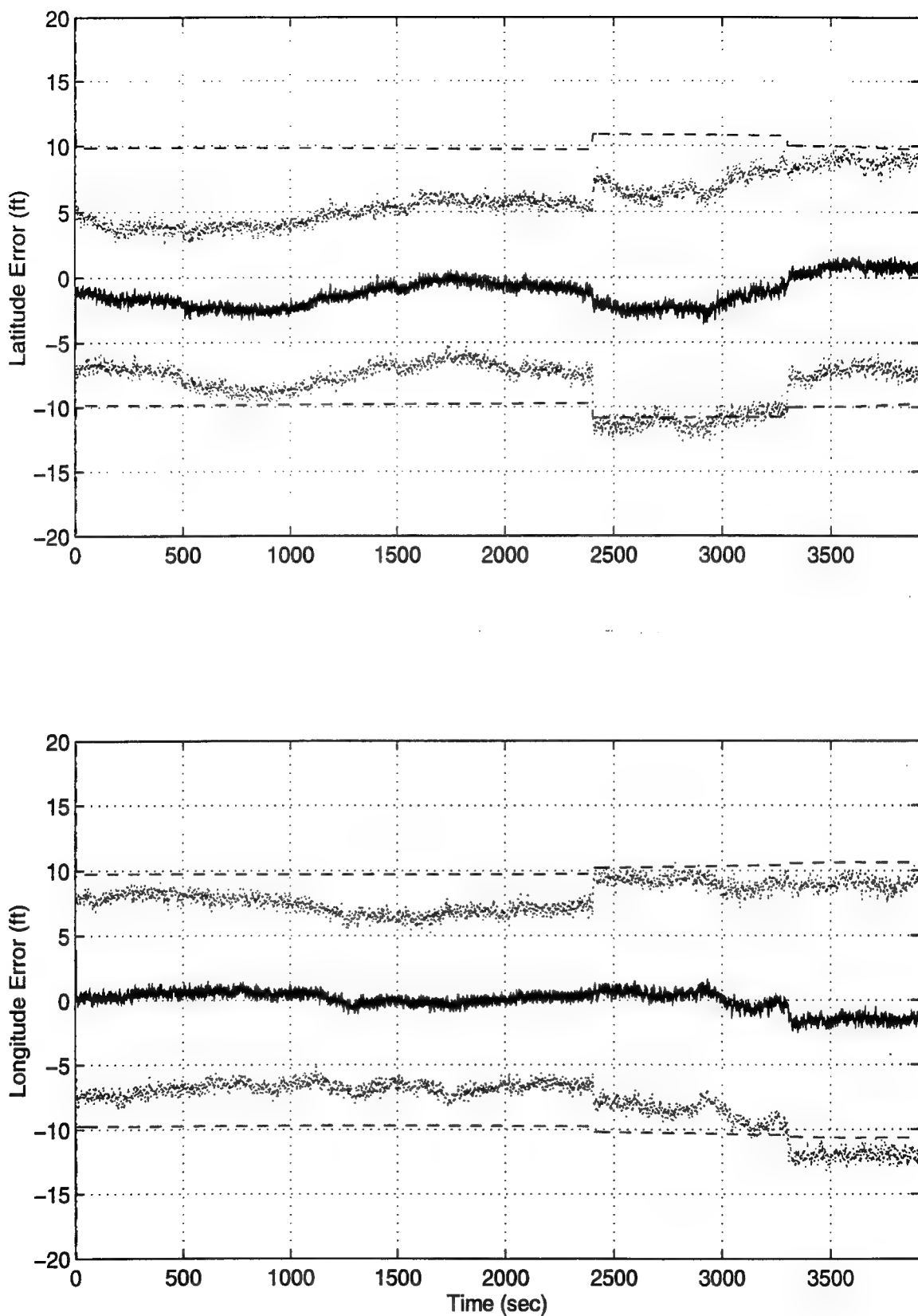


Figure K - 1. Latitude and Longitude Error

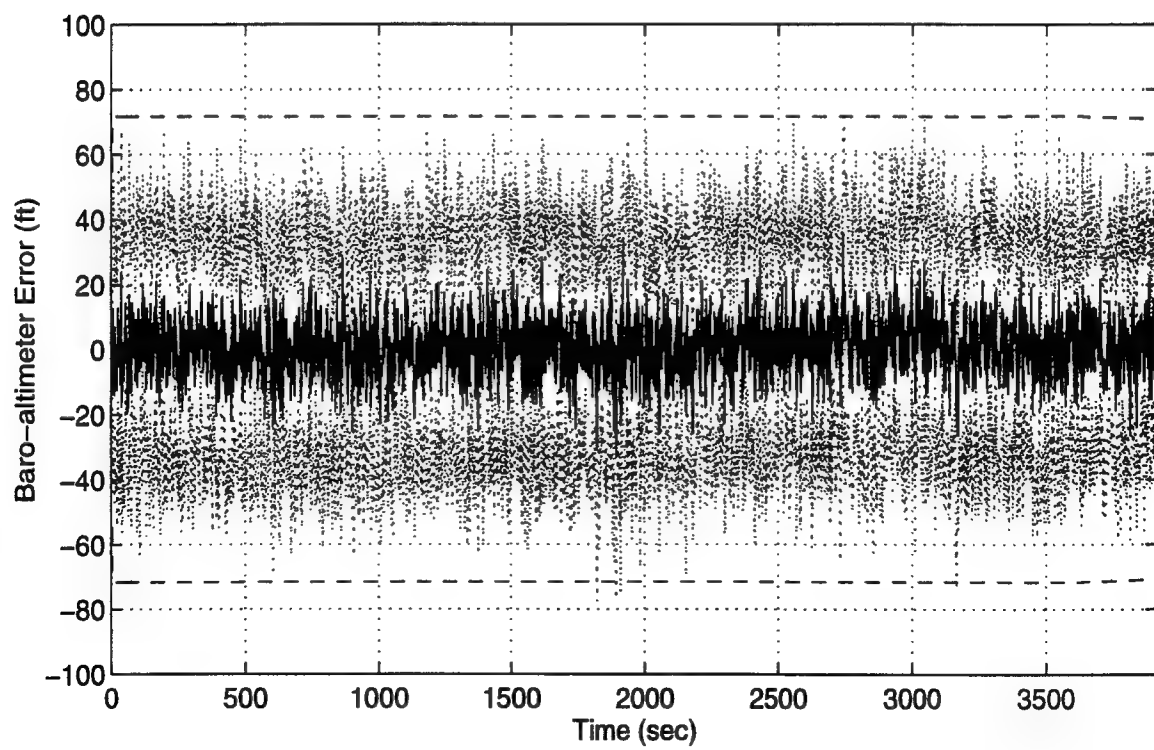
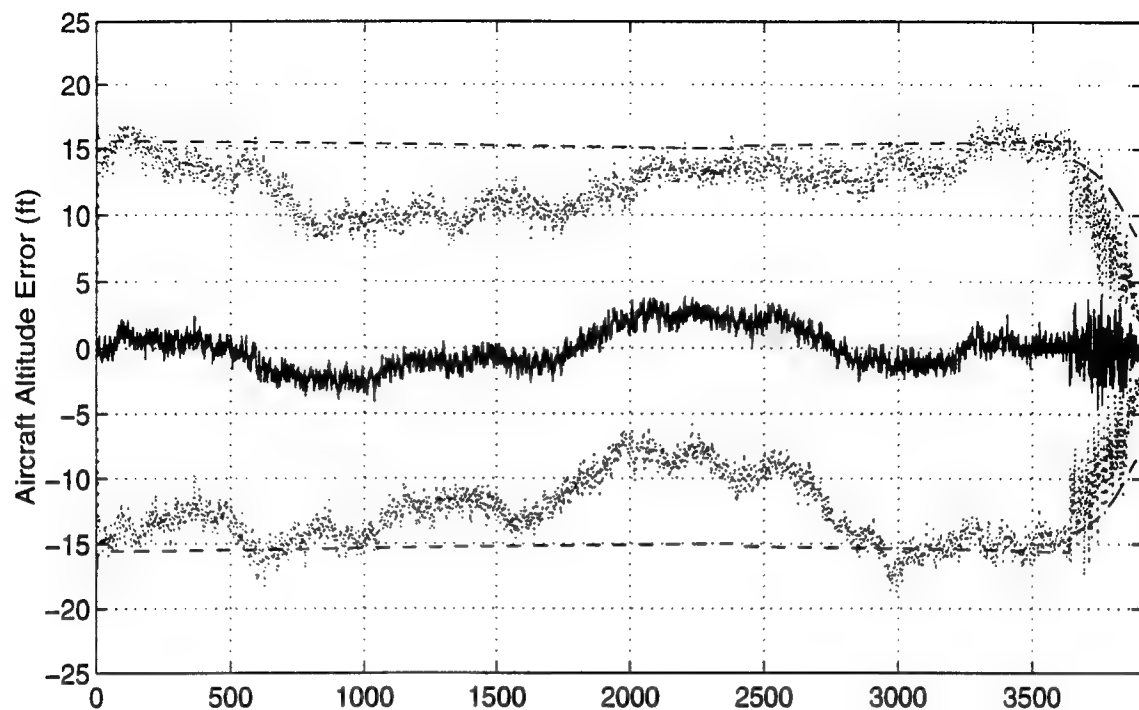


Figure K - 2. Aircraft Altitude and Baro-Altimeter Error

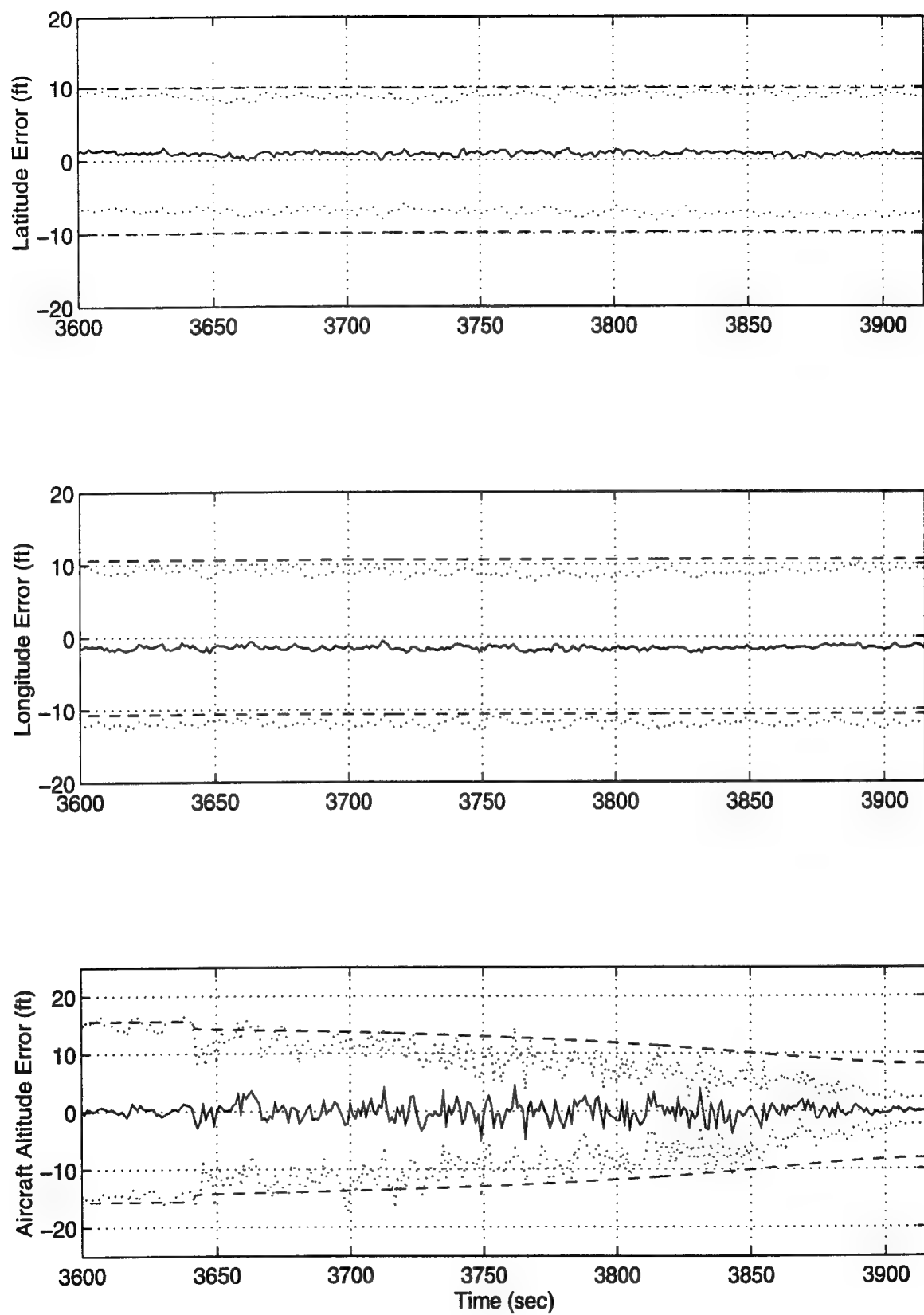


Figure K - 3 Latitude, Longitude and Aircraft Altitude Error

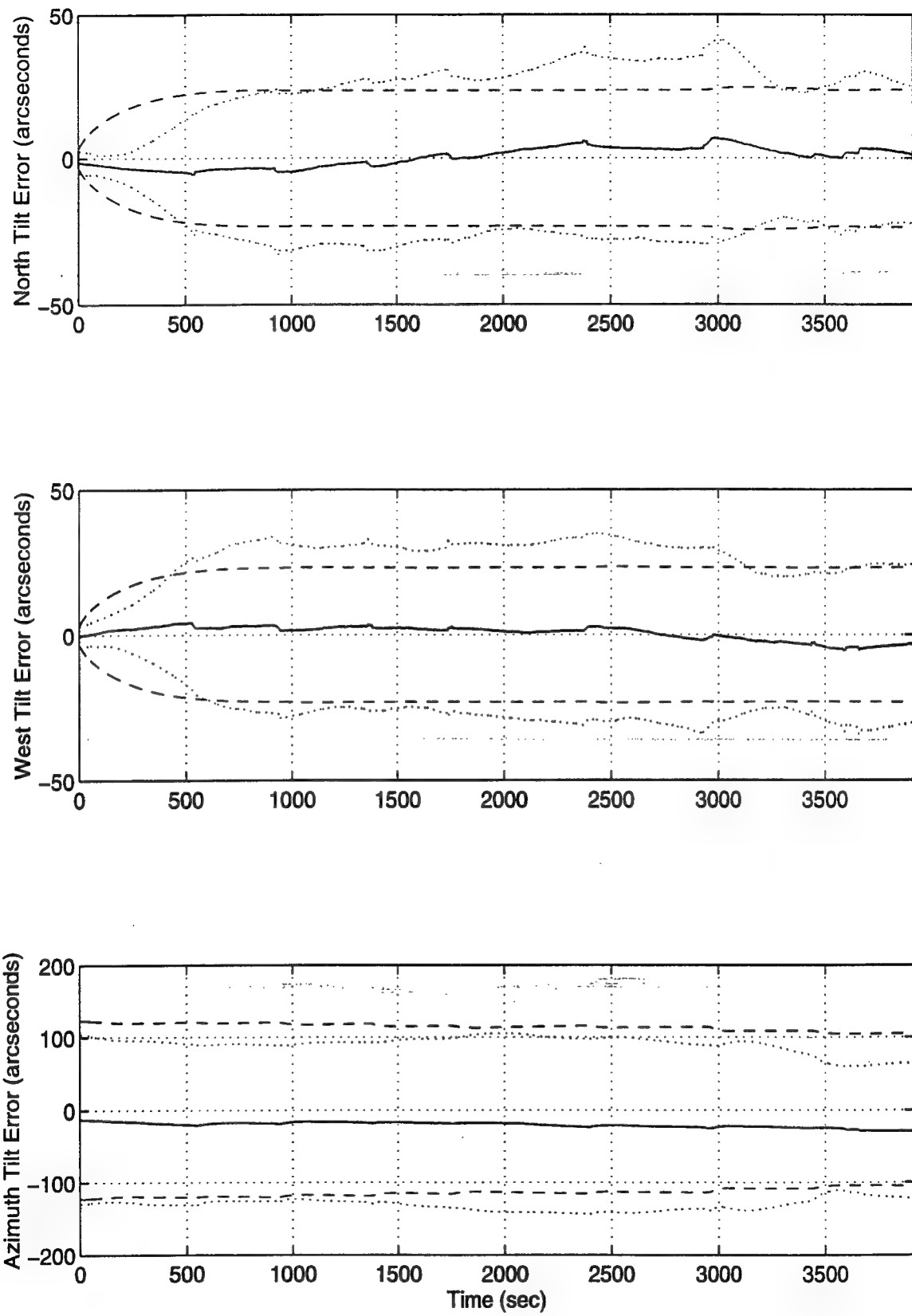


Figure K - 4 North, West and Azimuth Tilt Errors

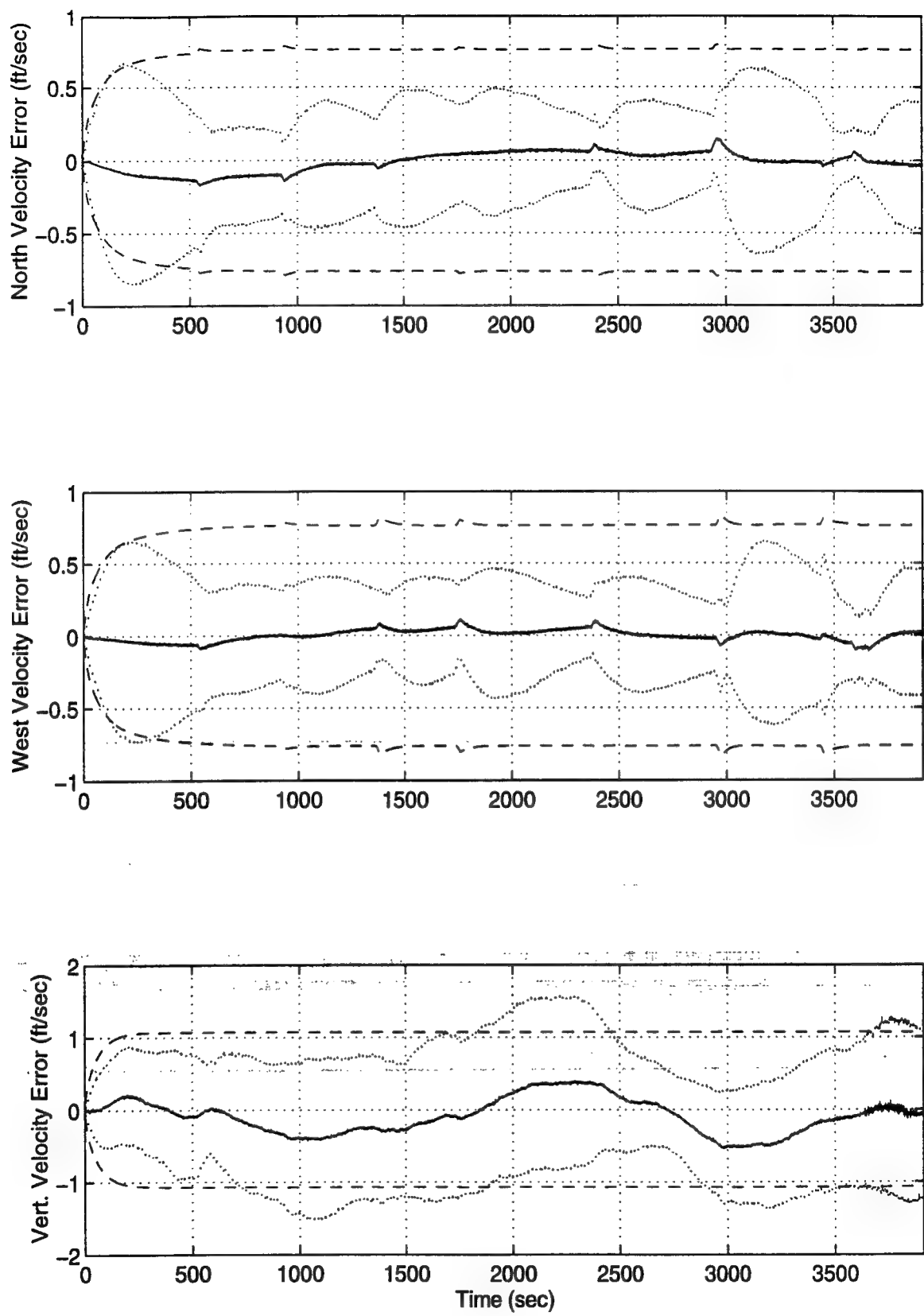


Figure K - 5 North, West and Vertical Velocity Errors

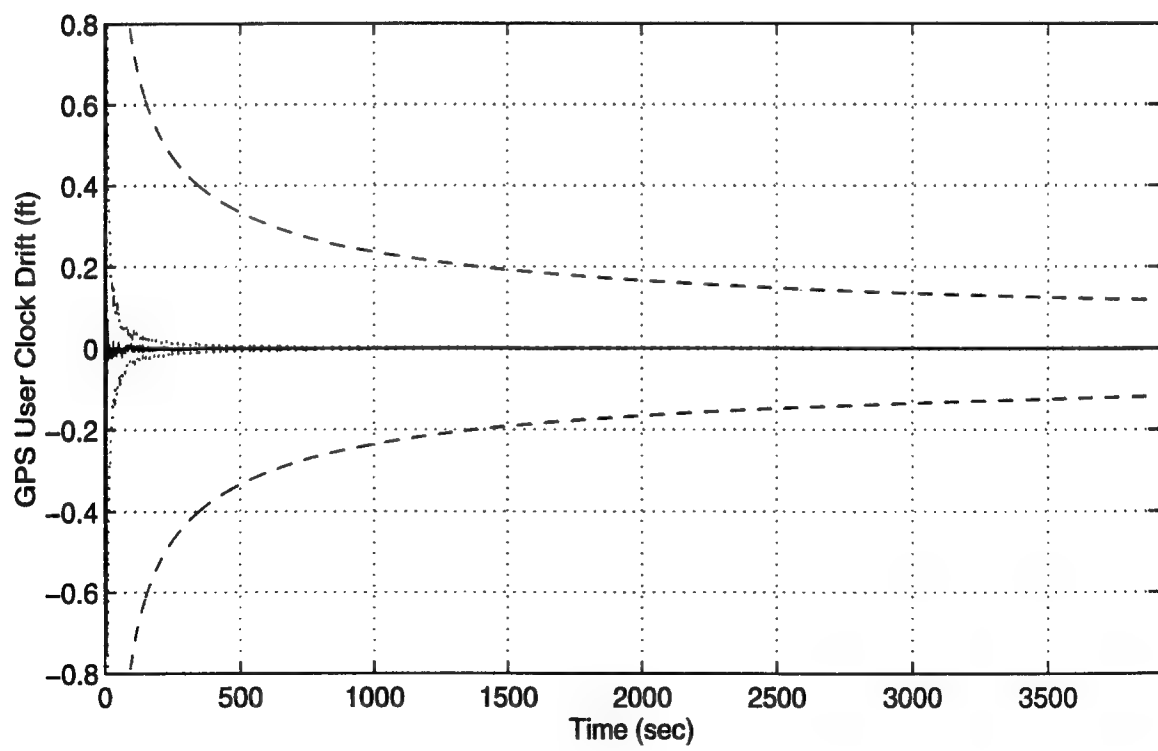
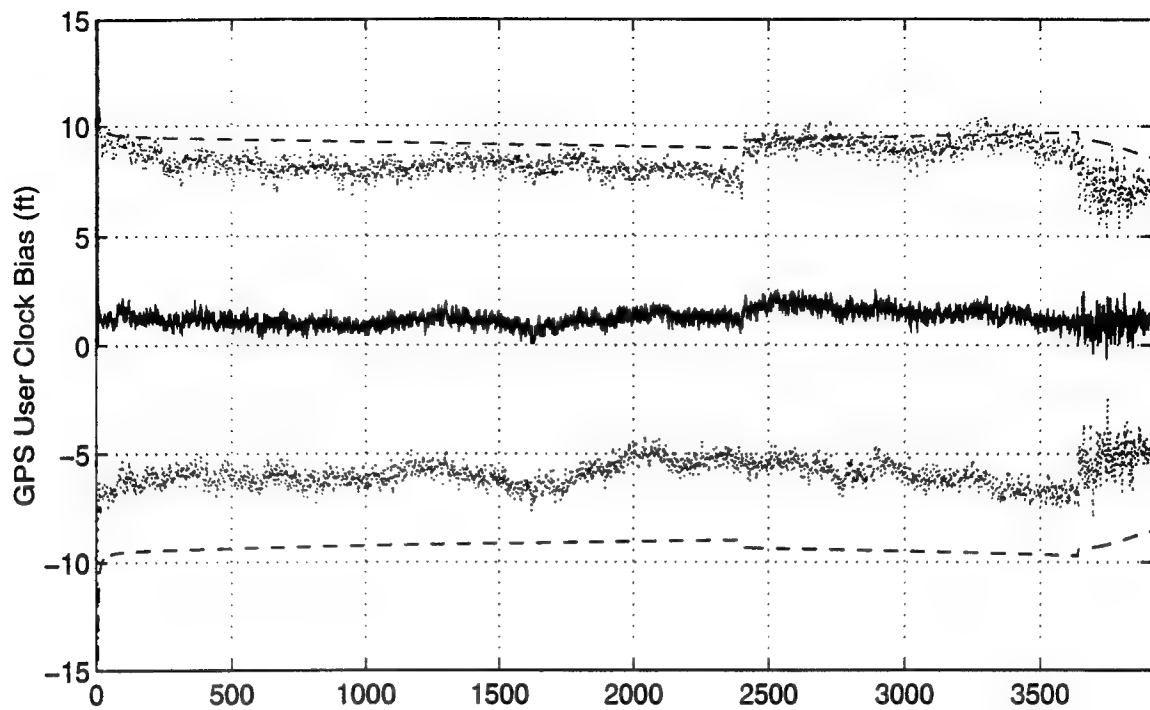
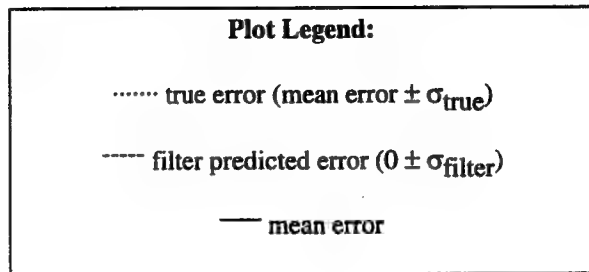


Figure K - 6 GPS User Clock Bias and GPS User Clock Drift

Appendix L

Plots of Case V: Barometric Altimeter, 4.0 nm/hr INS, P-Code GPS Using the Tanker Flight Profile.



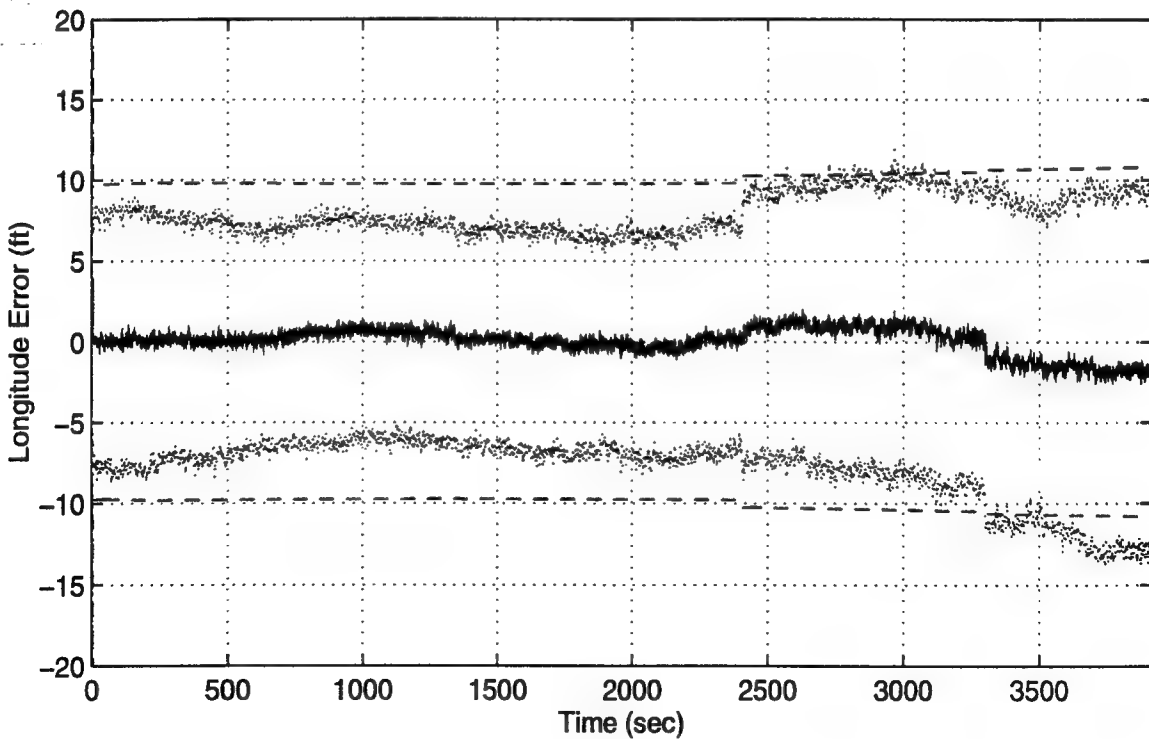
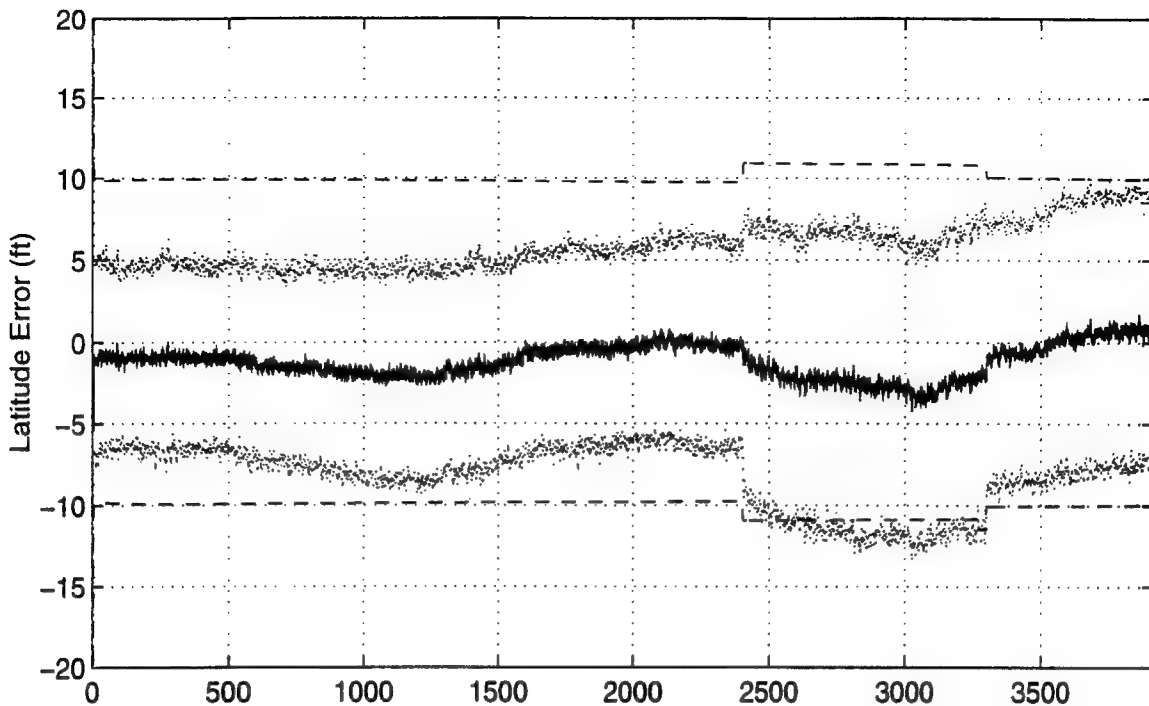


Figure L - 1. Latitude and Longitude Error

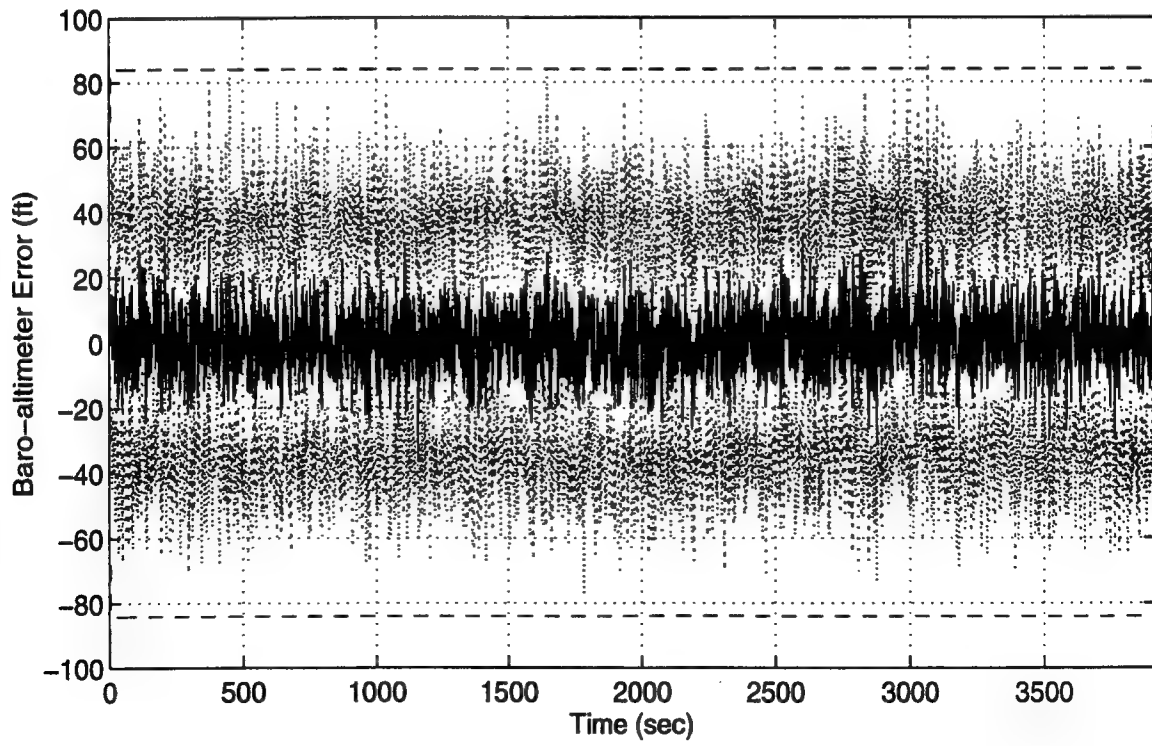
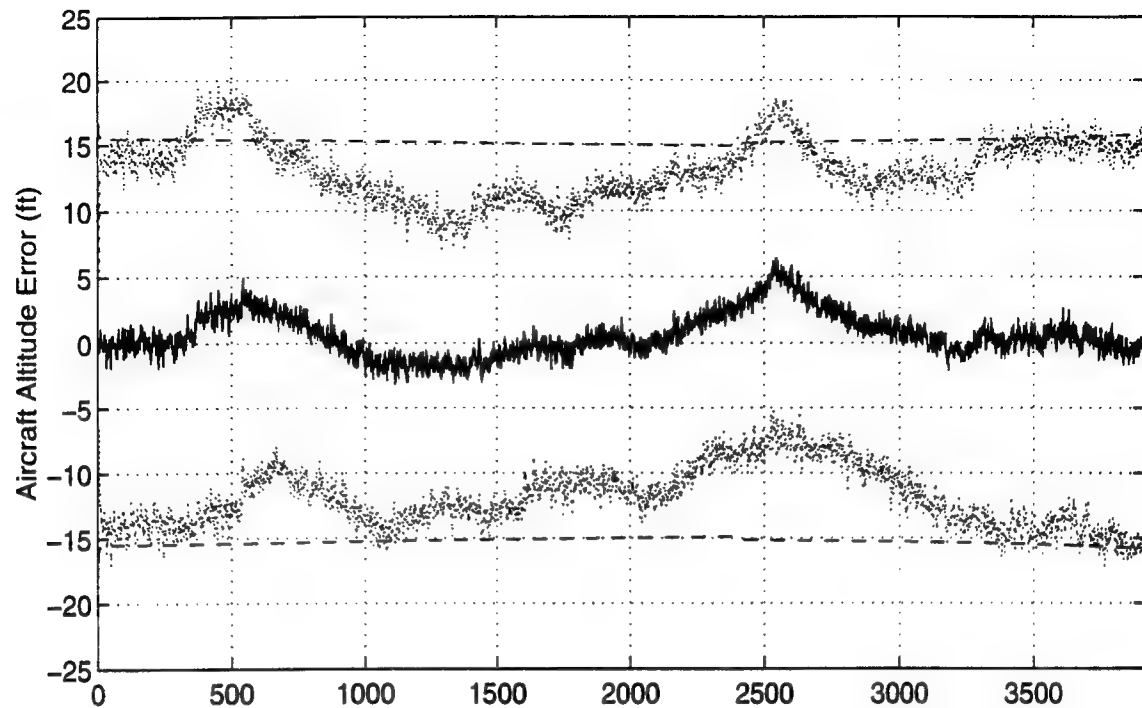


Figure L - 2. Aircraft Altitude and Baro-Altimeter Error

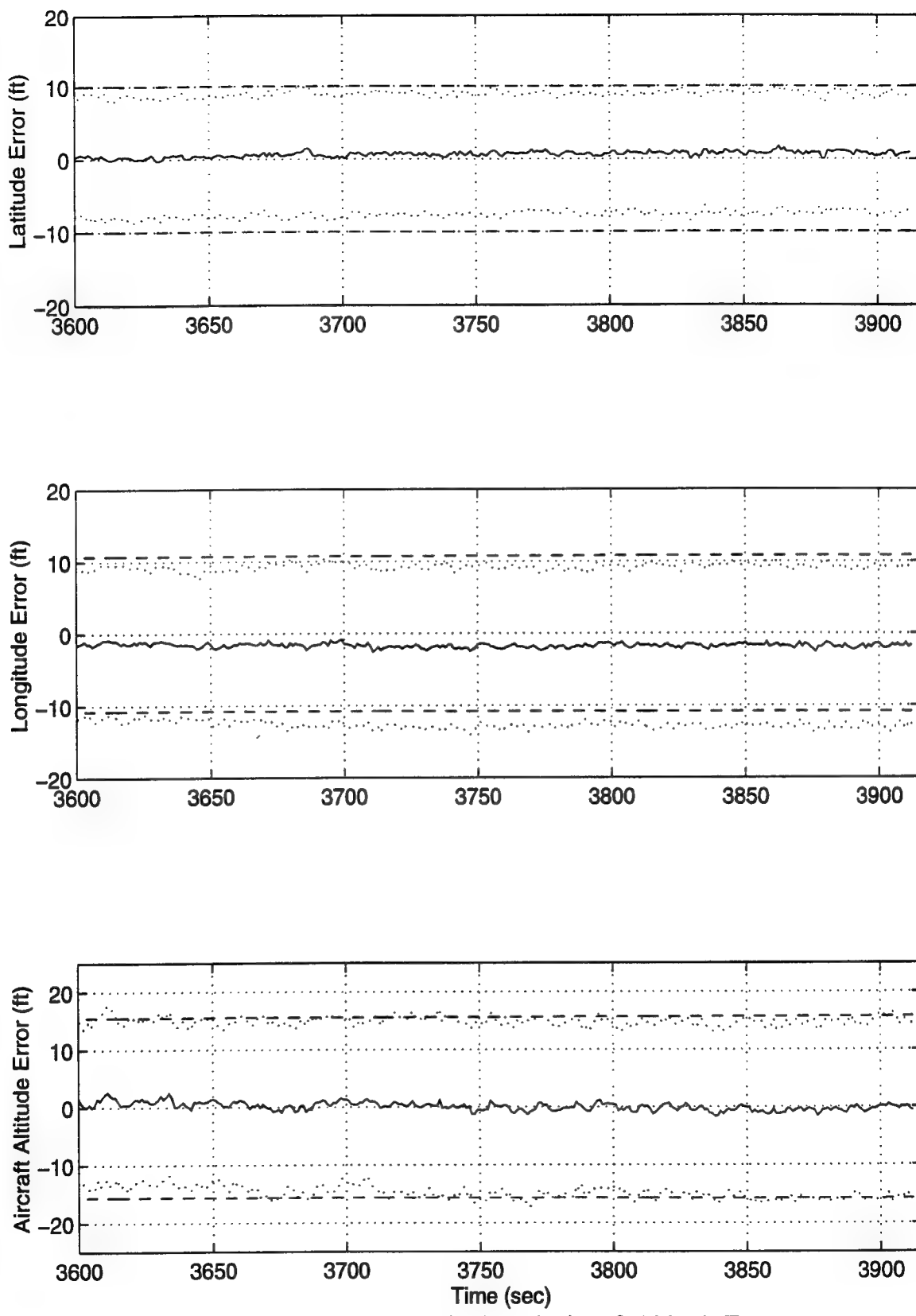


Figure L - 3 Latitude, Longitude and Aircraft Altitude Error

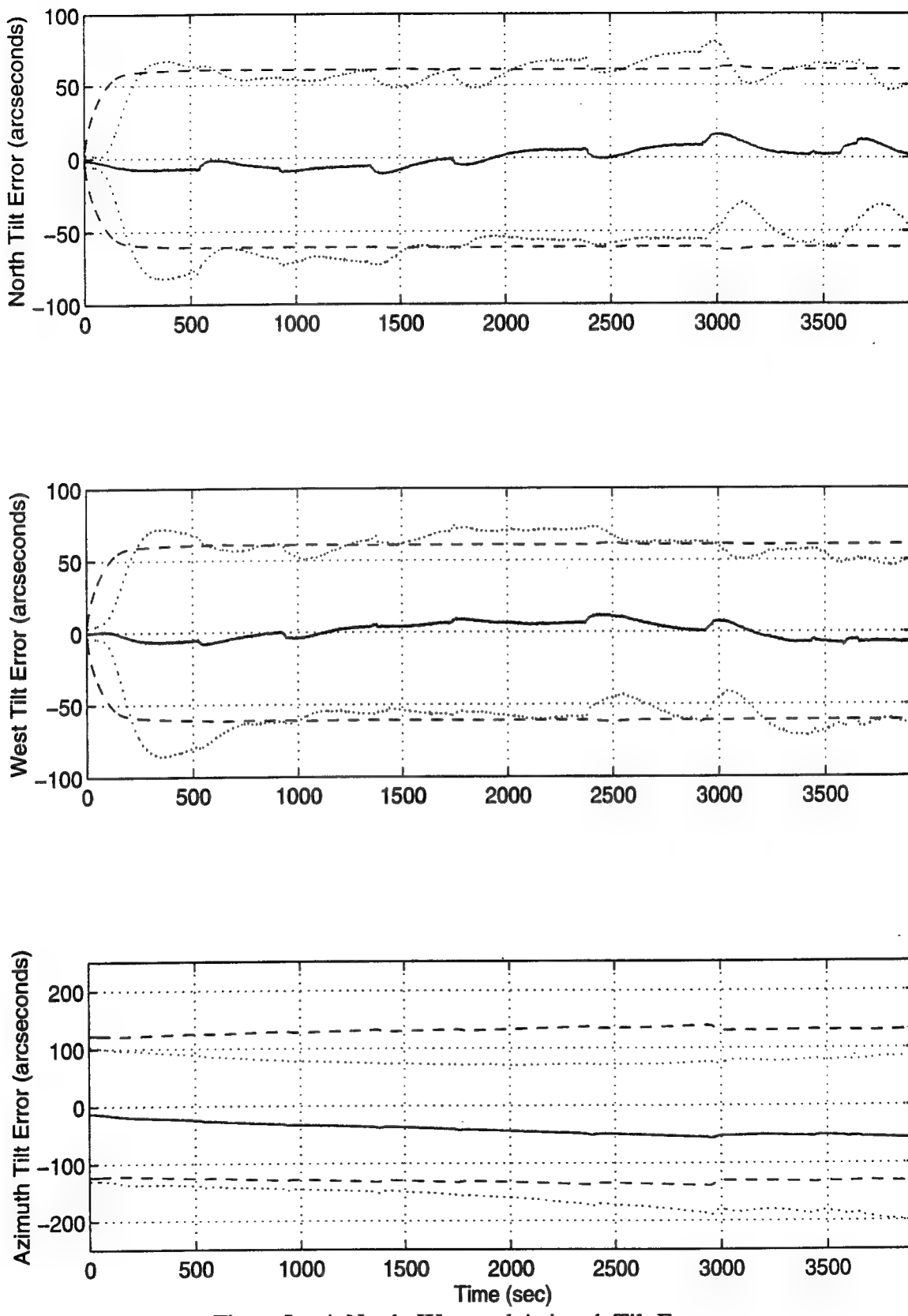


Figure L - 4 North, West and Azimuth Tilt Errors

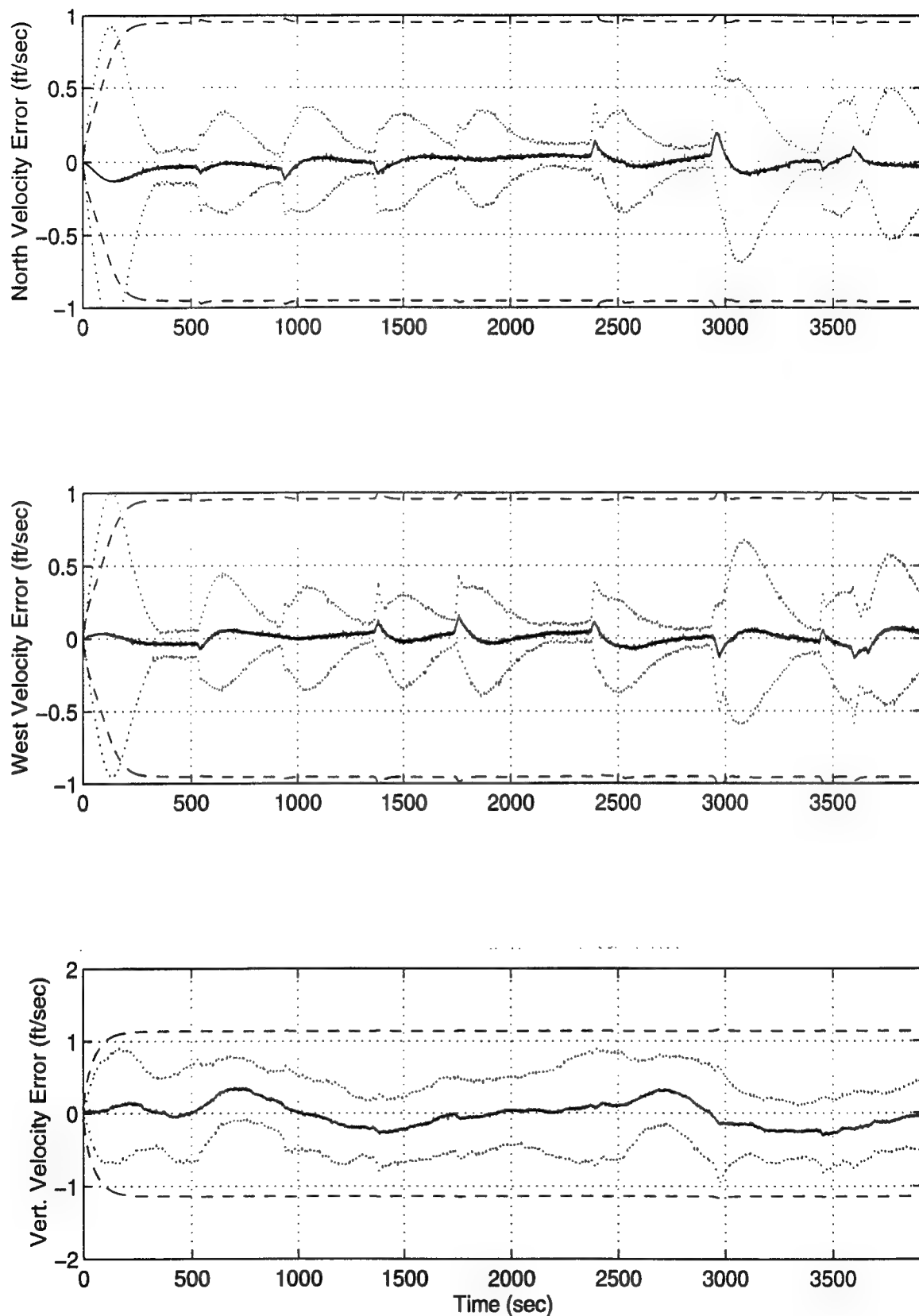


Figure L - 5 North, West and Vertical Velocity Errors

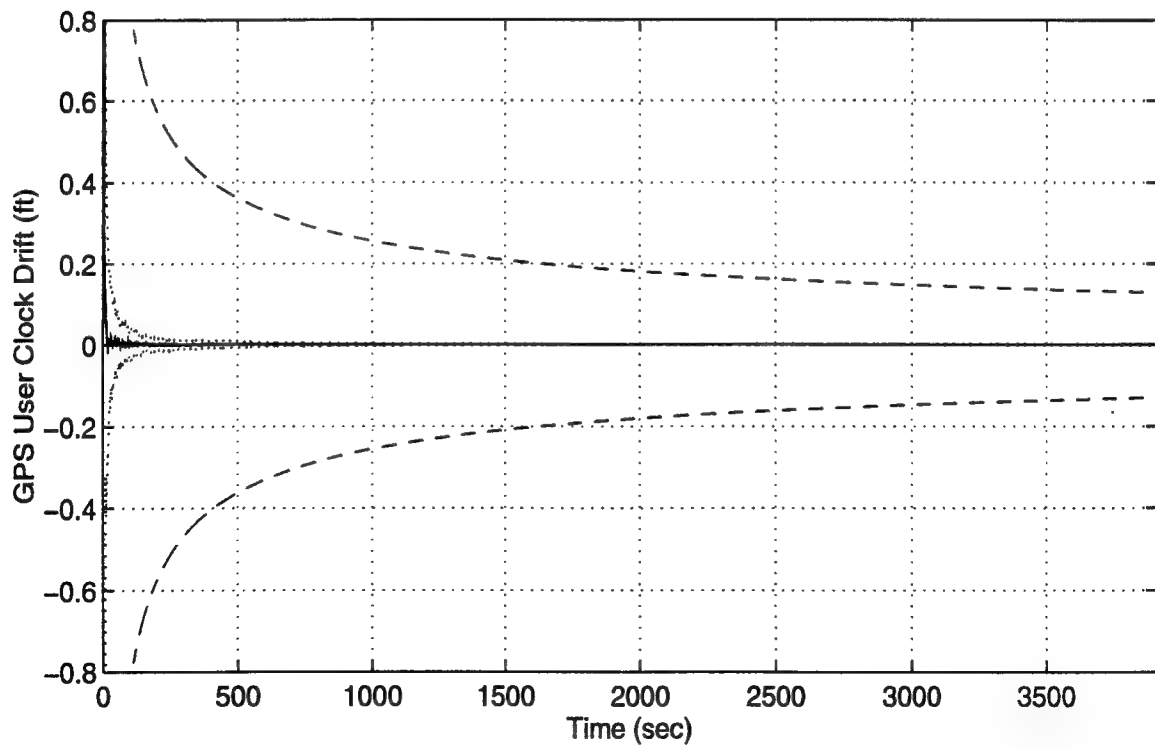
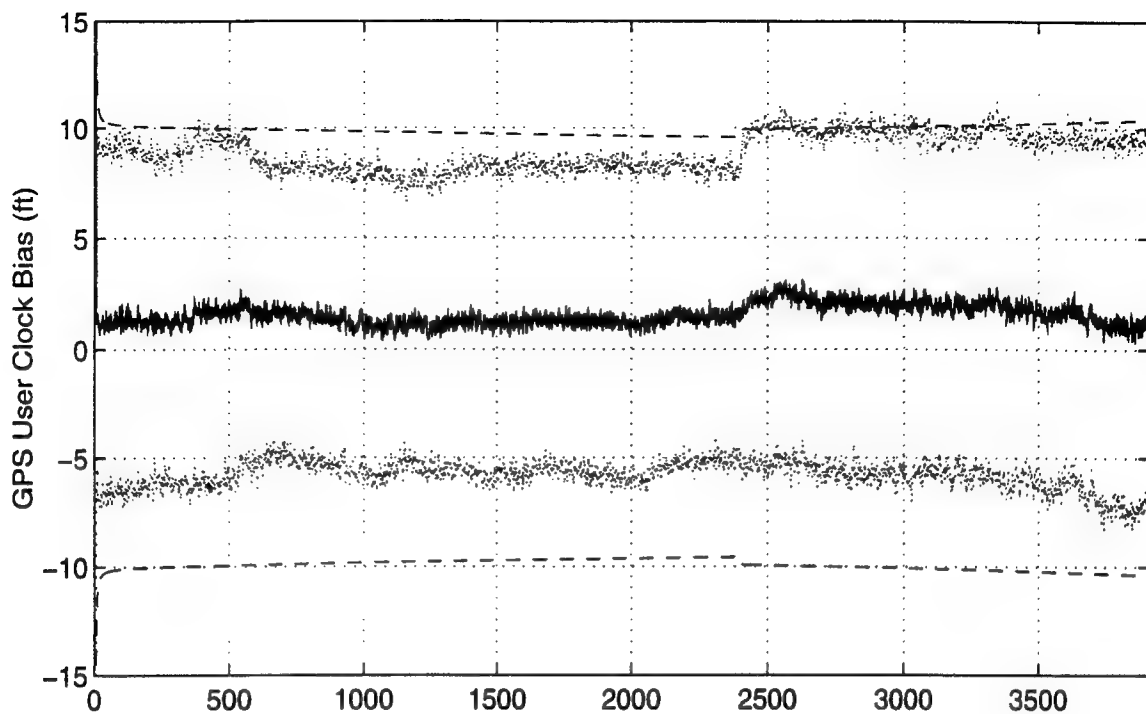
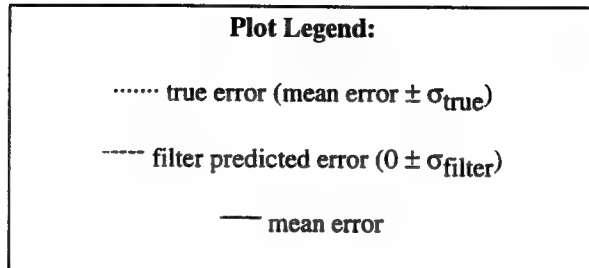


Figure L - 6 GPS User Clock Bias and GPS User Clock Drift

Appendix M

Plots of Case VI: Barometric Altimeter, 4.0 nm/hr INS, P-Code GPS and Radar Altimeter Using the Tanker Flight Profile.



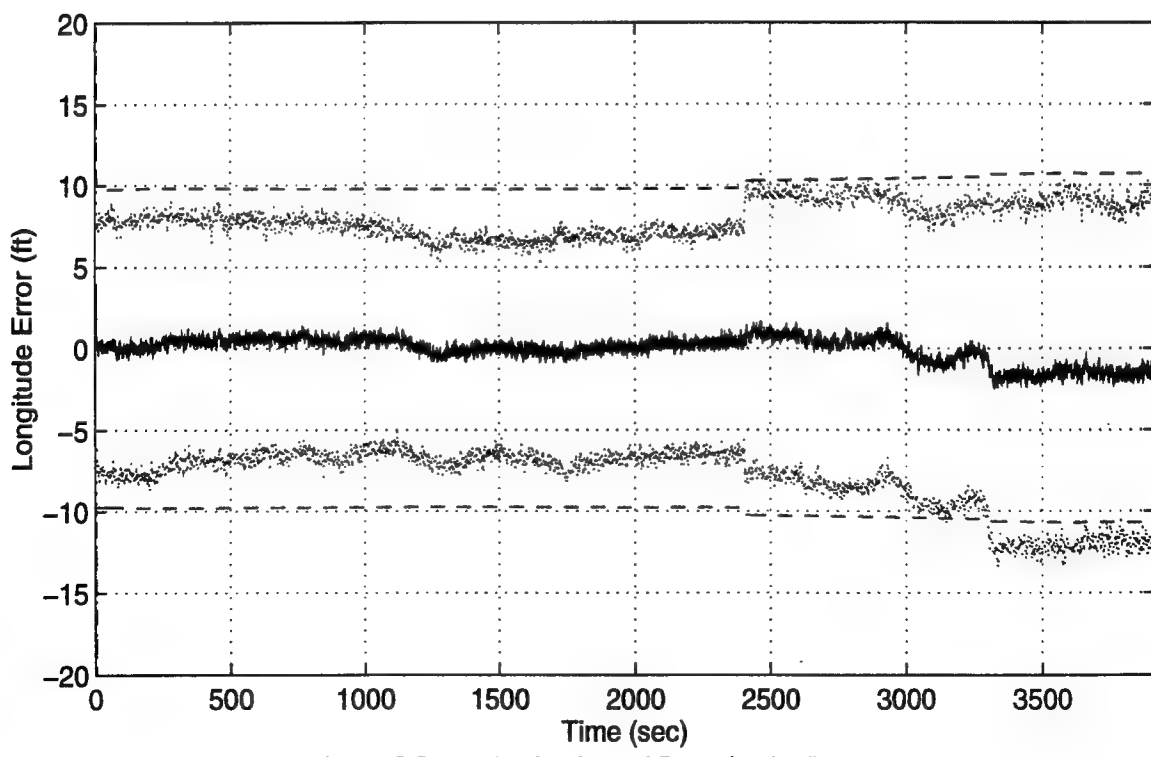
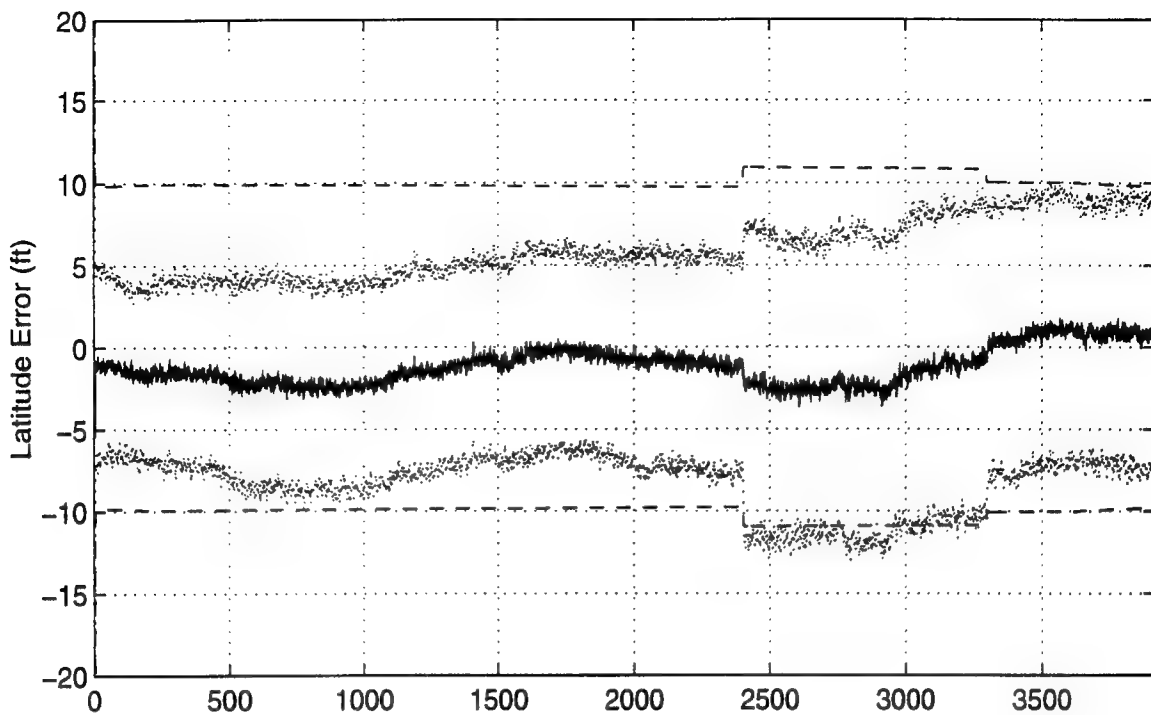


Figure M - 1. Latitude and Longitude Error

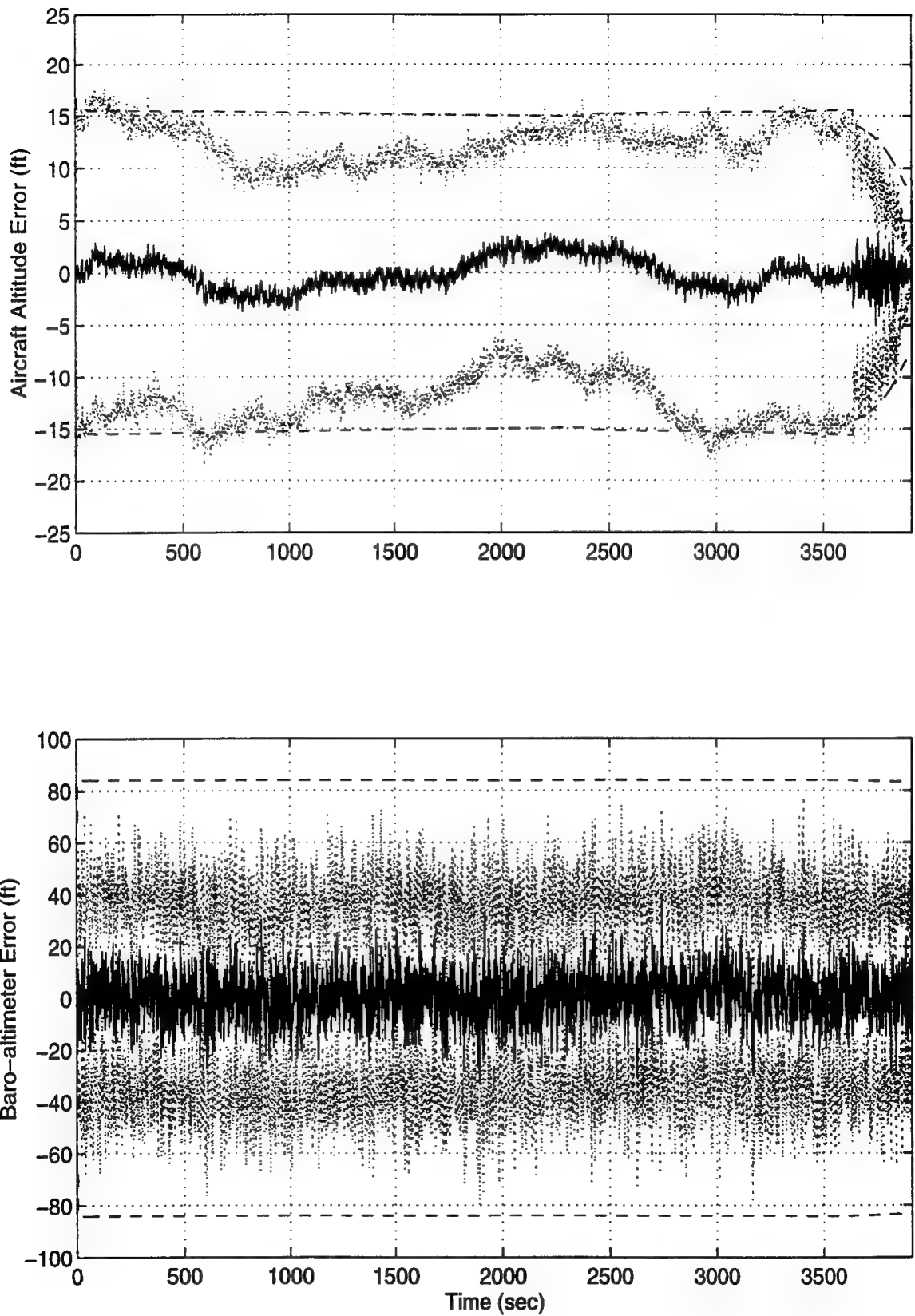


Figure M - 2. Aircraft Altitude and Baro-Altimeter Error

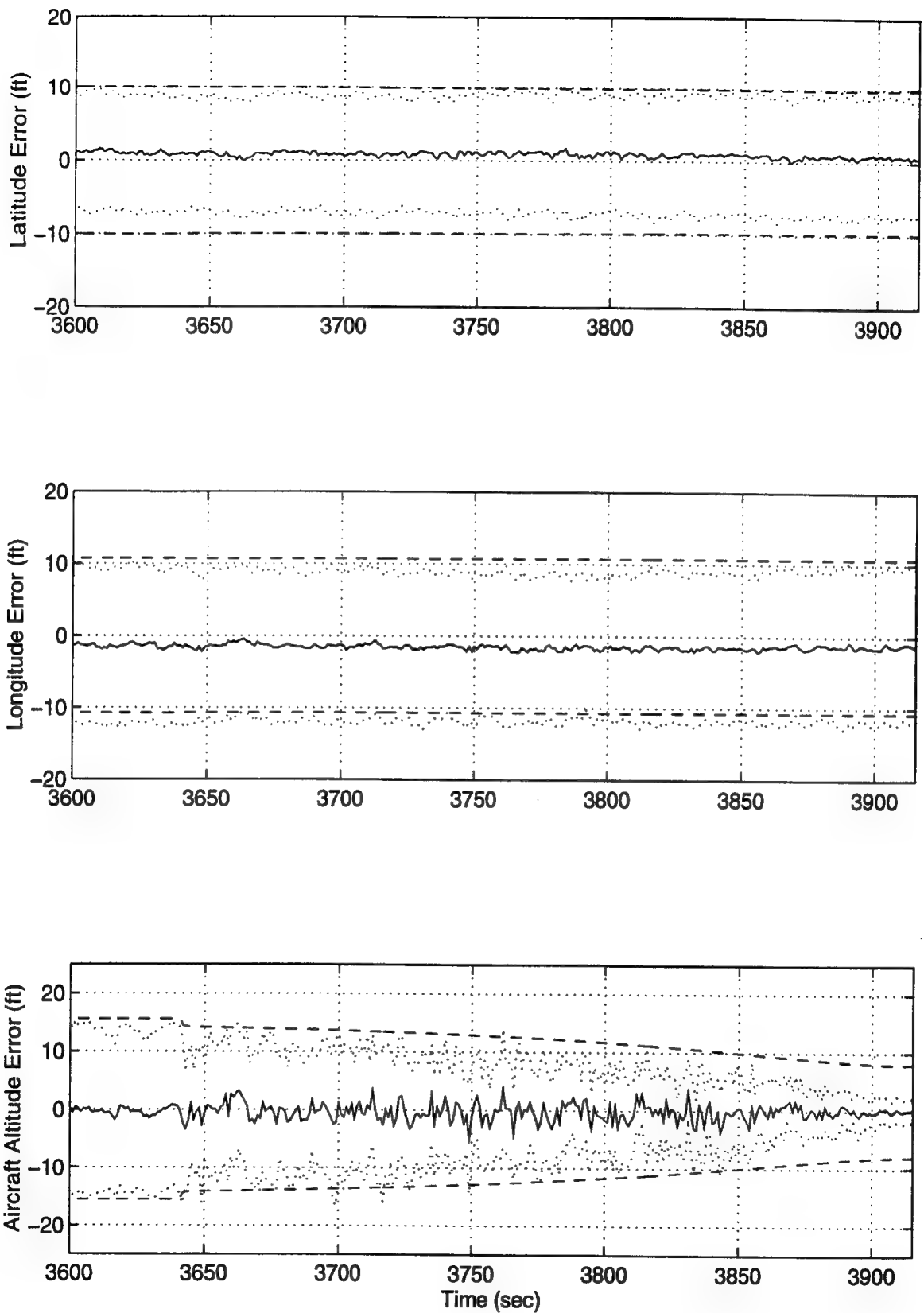


Figure M - 3 Latitude, Longitude and Aircraft Altitude Error

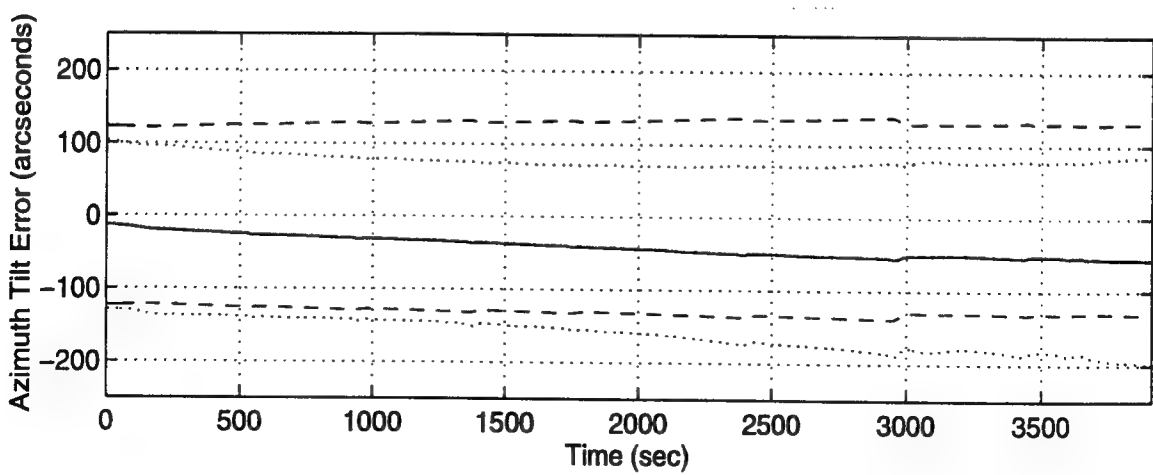
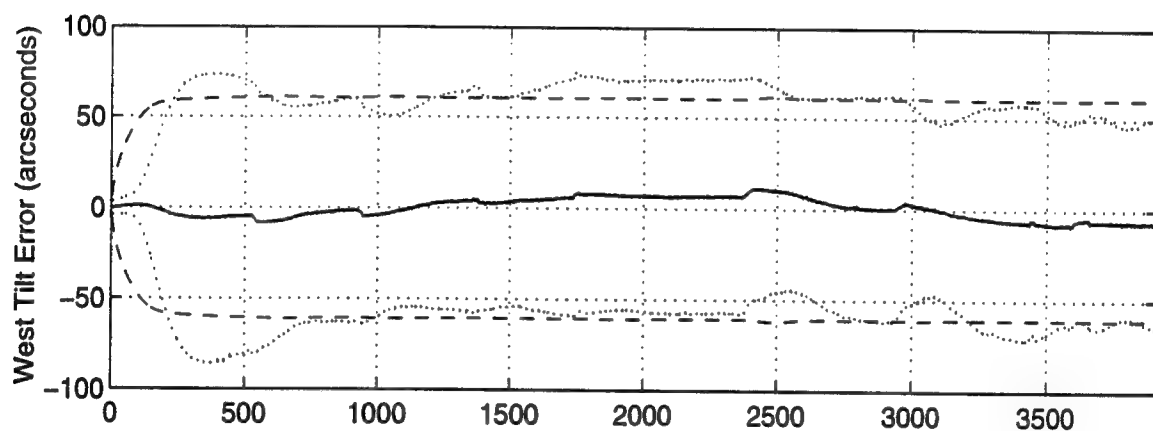
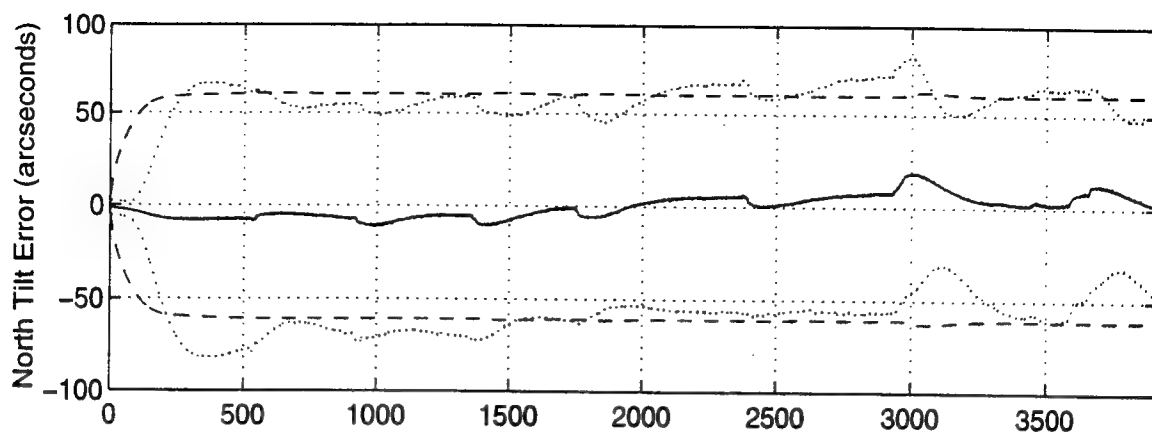


Figure M - 4 North, West and Azimuth Tilt Errors

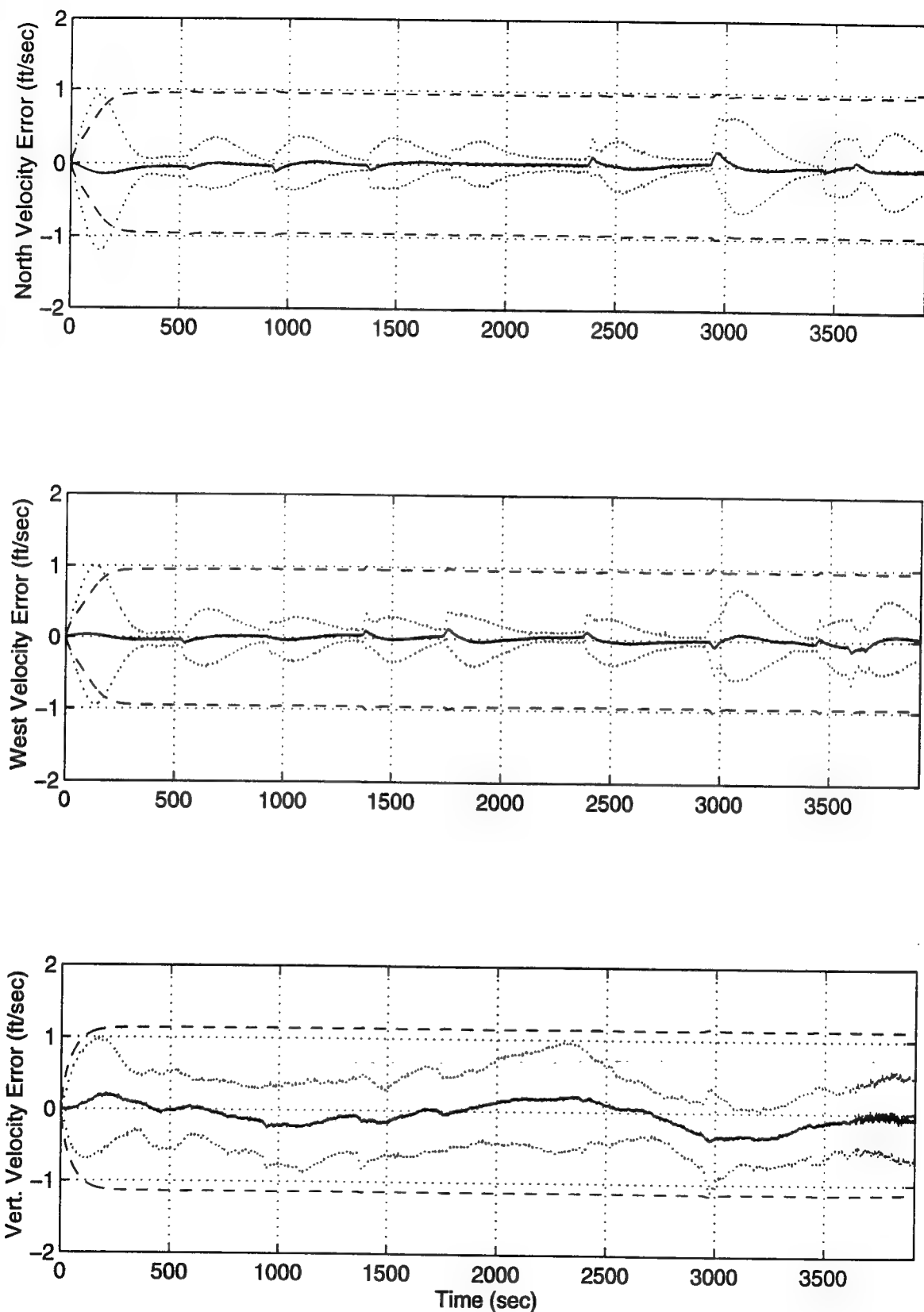


Figure M - 5 North, West and Vertical Velocity Errors

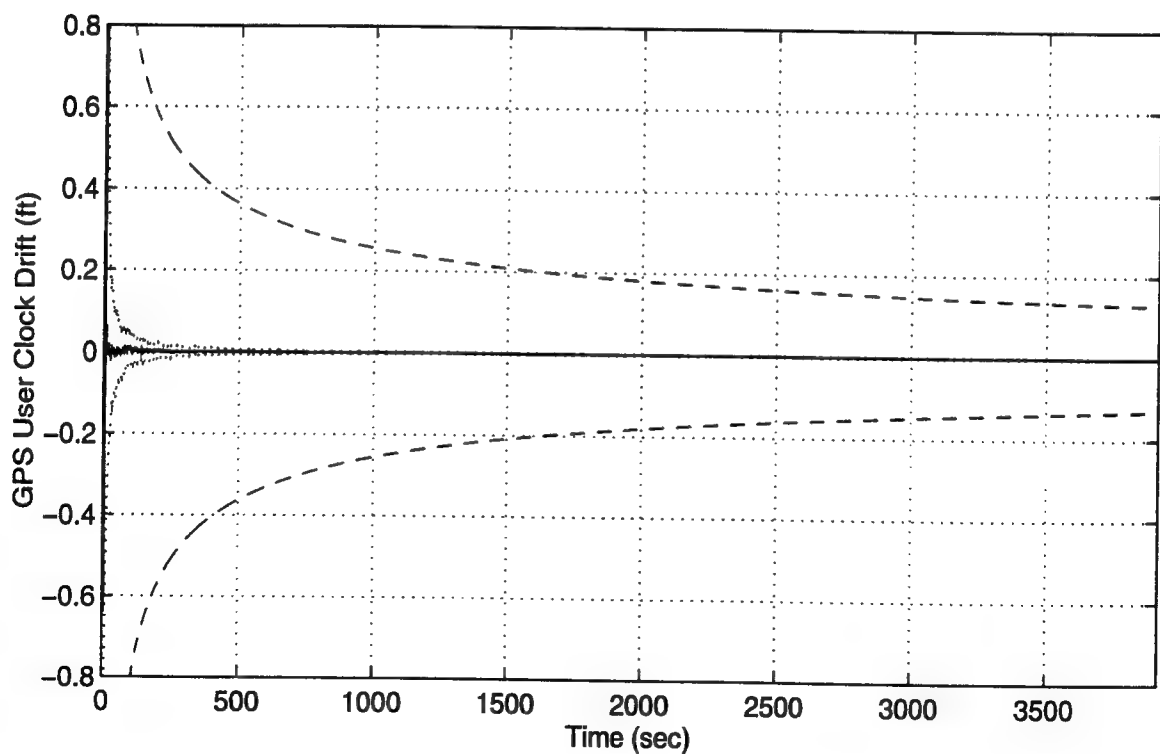
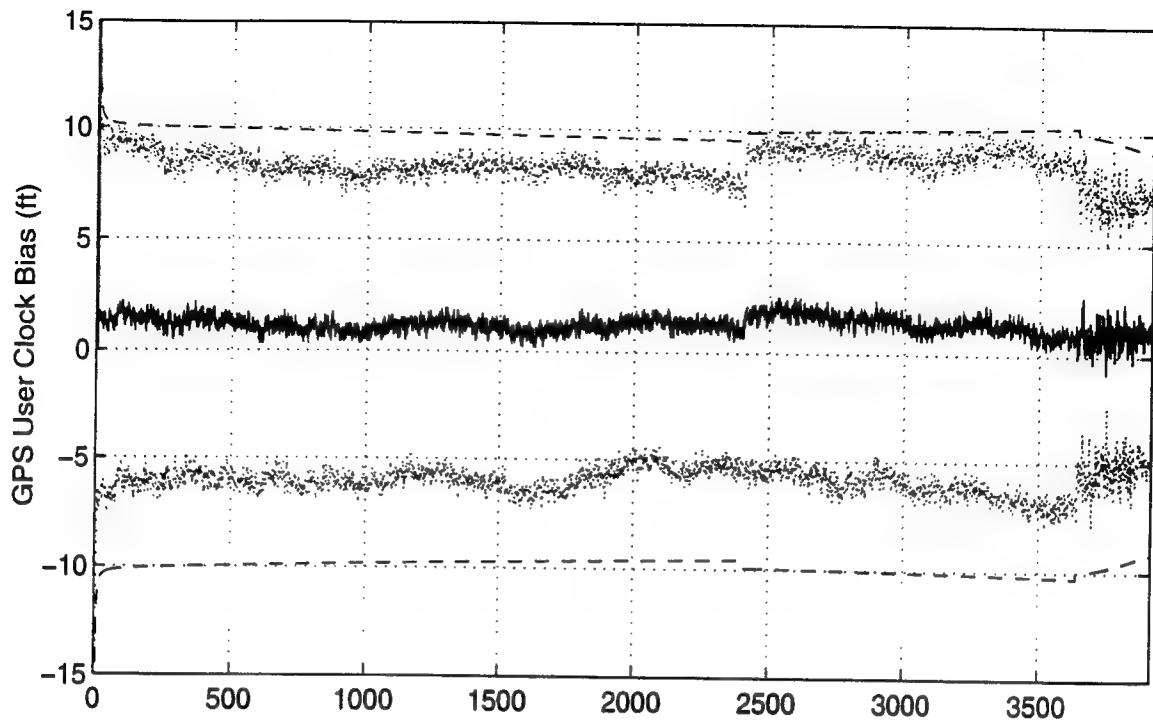
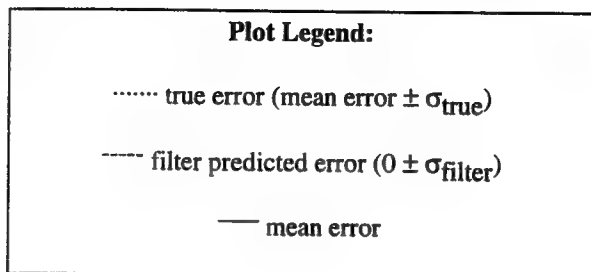


Figure M - 6 GPS User Clock Bias and GPS User Clock Drift

Appendix N

Plots of Case VII: Barometric Altimeter, 0.4 nm/hr INS, P-Code GPS and Single Pseudolite Using the Tanker Flight Profile.



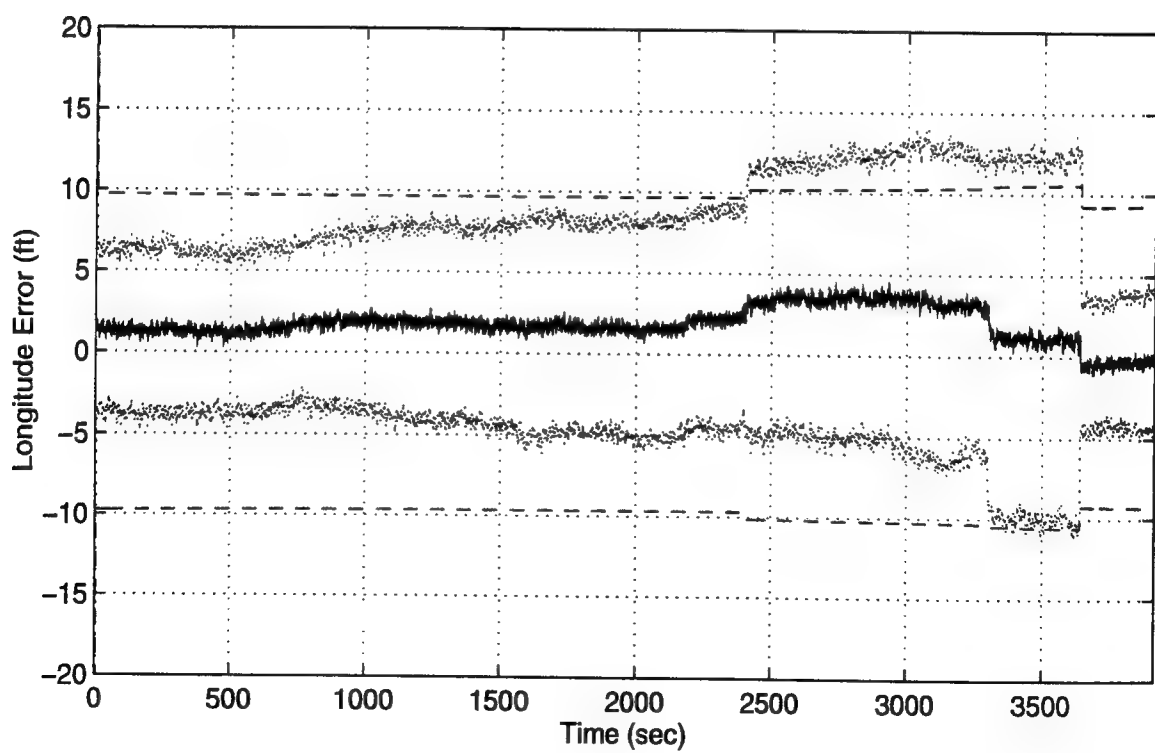
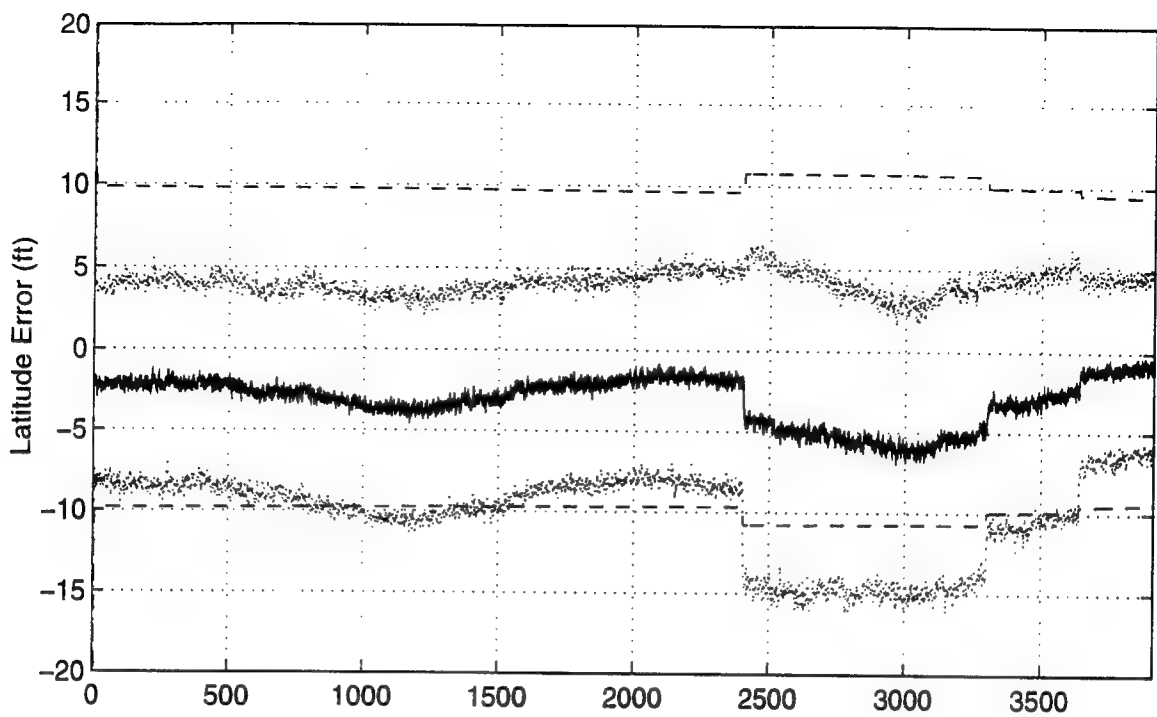


Figure N - 1. Latitude and Longitude Error

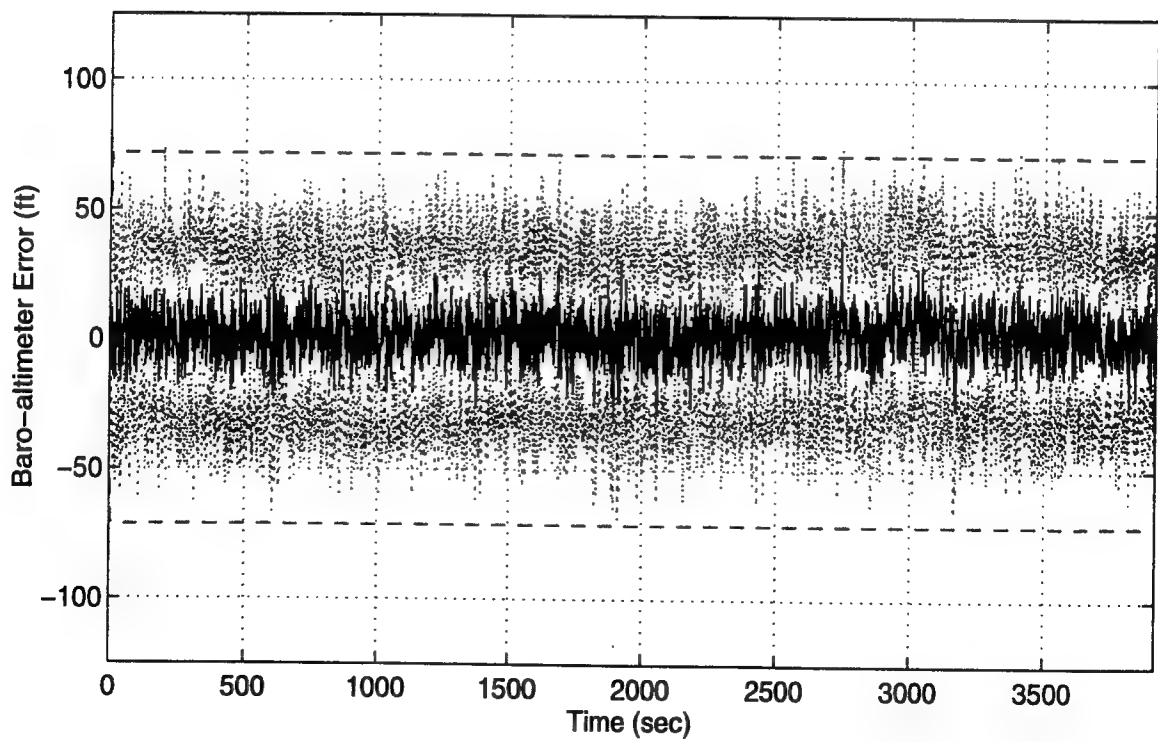
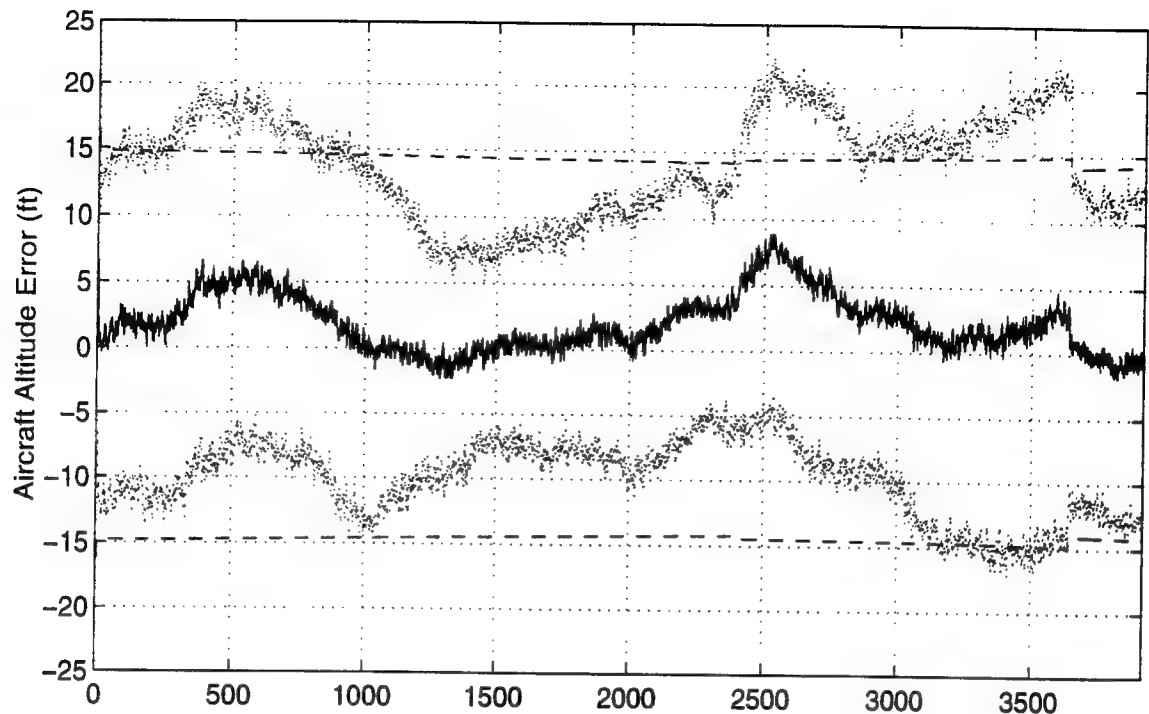


Figure N - 2. Aircraft Altitude and Baro-Altimeter Error

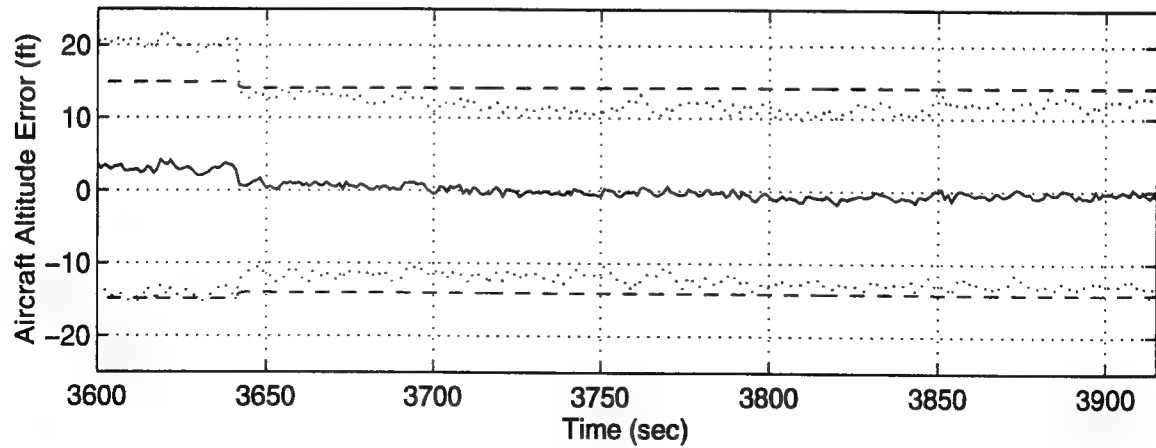
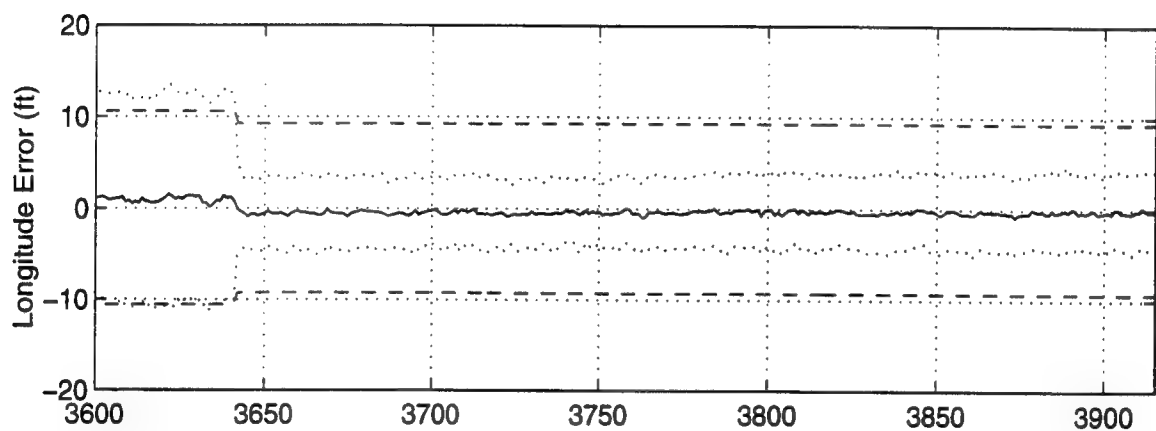
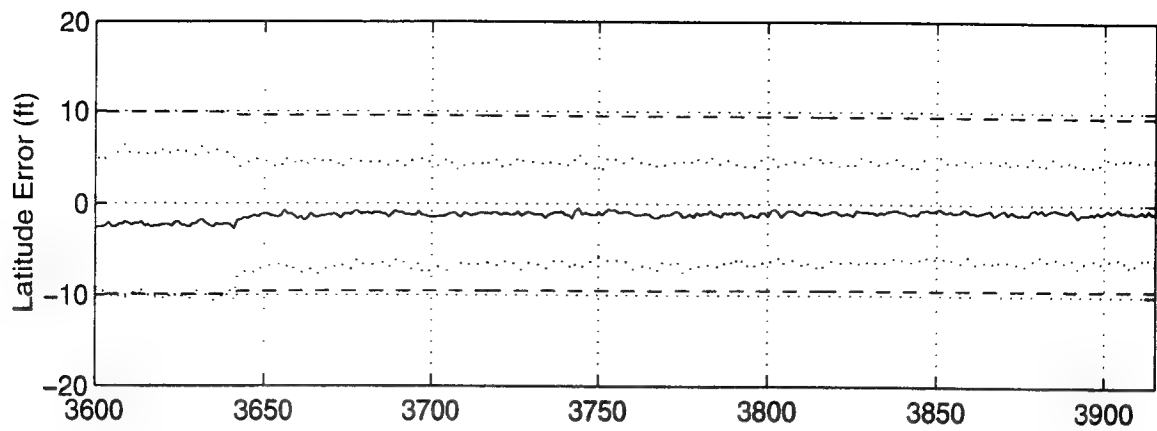


Figure N - 3 Latitude, Longitude and Aircraft Altitude Error

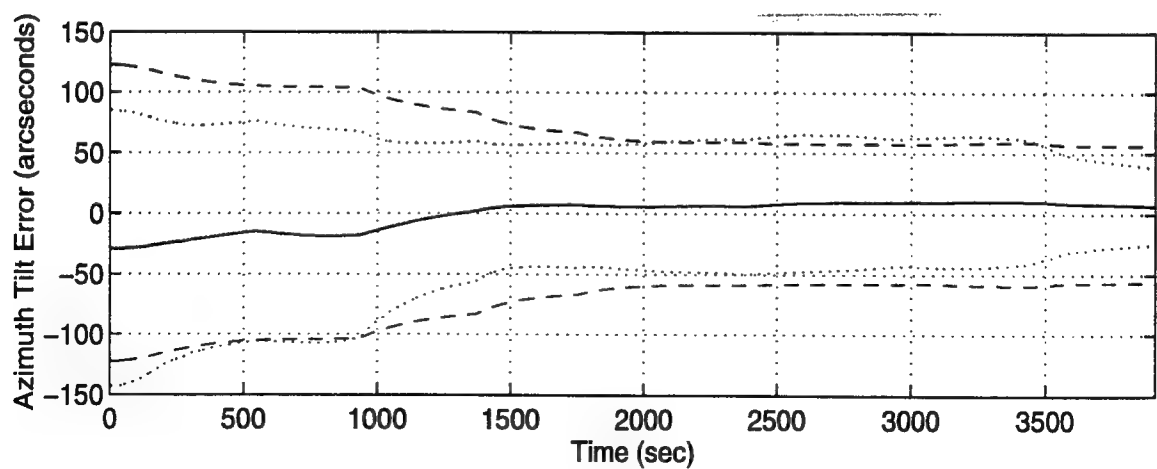
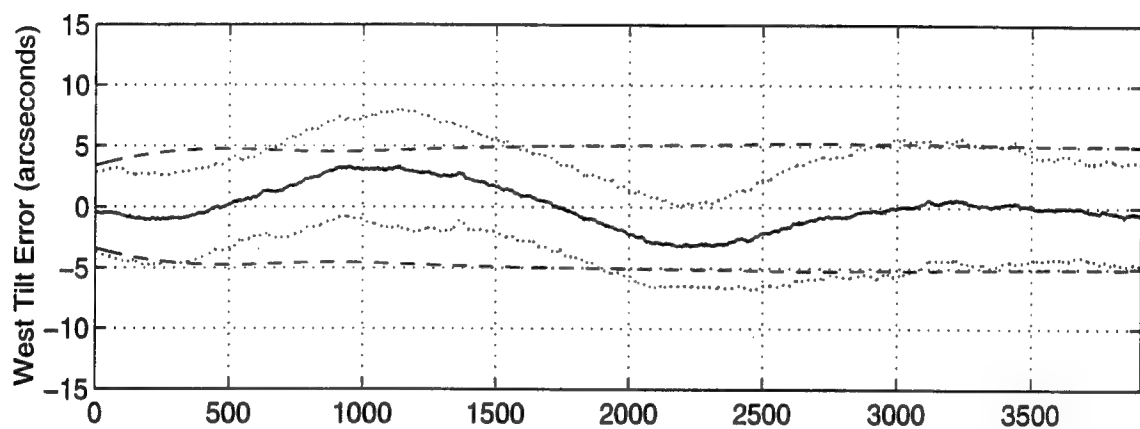
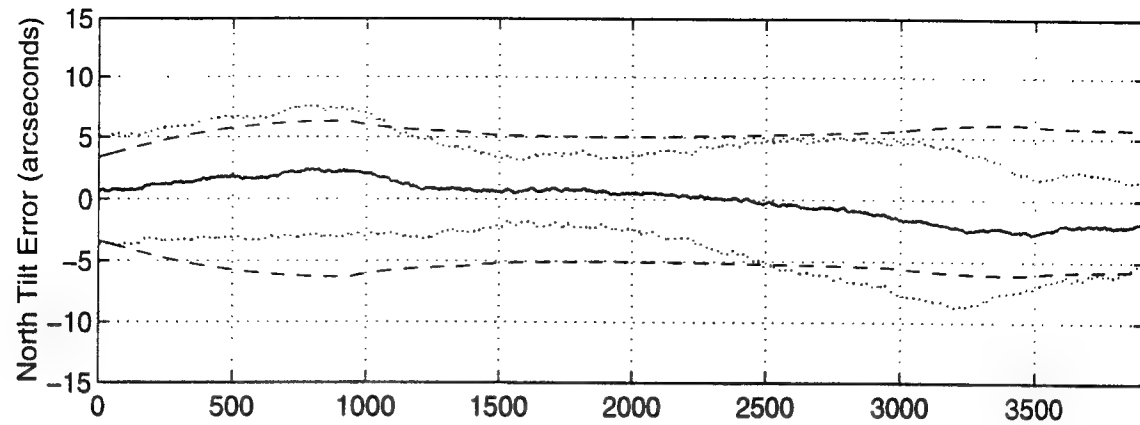


Figure N - 4 North, West and Azimuth Tilt Errors

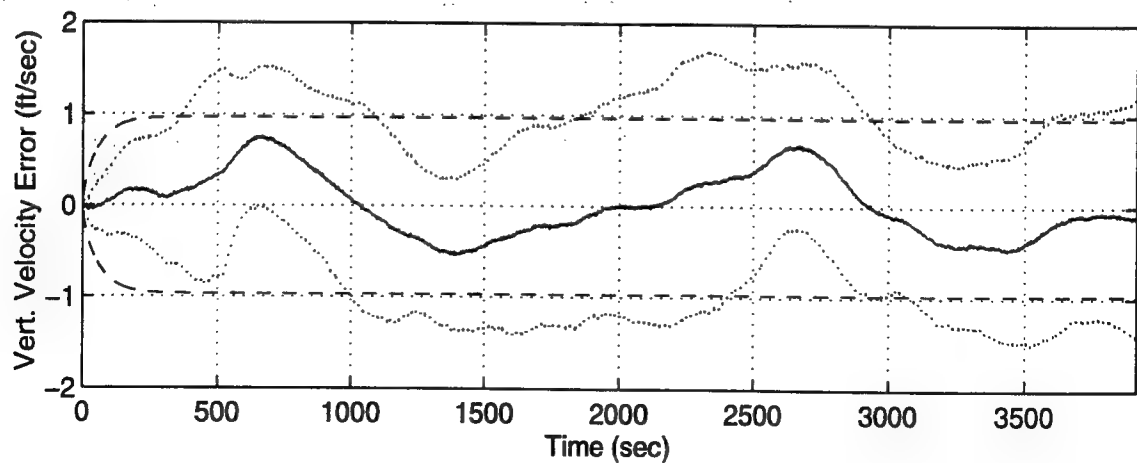
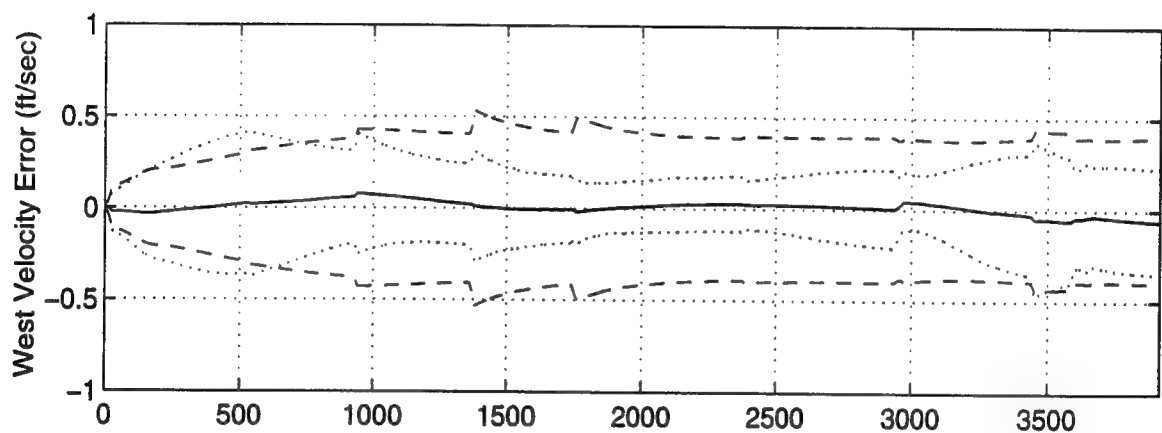
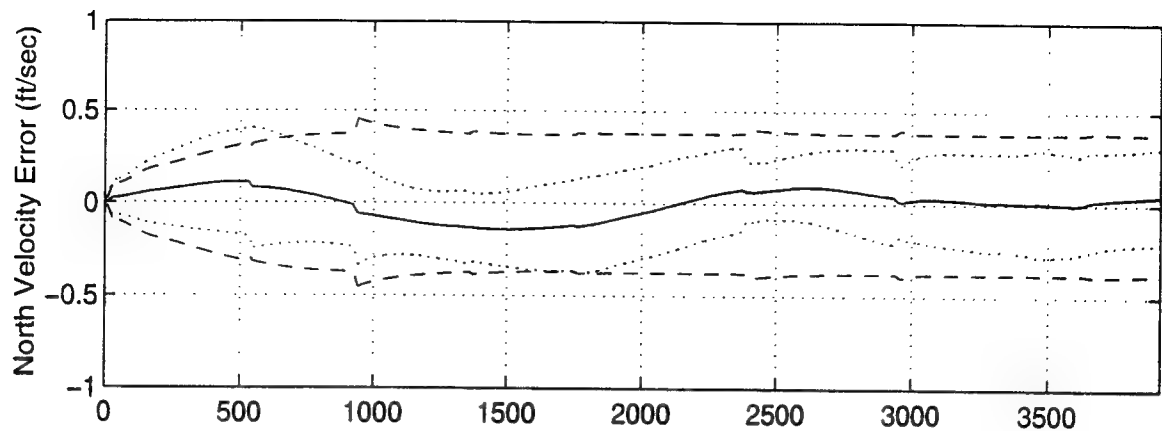


Figure N - 5 North, West and Vertical Velocity Errors

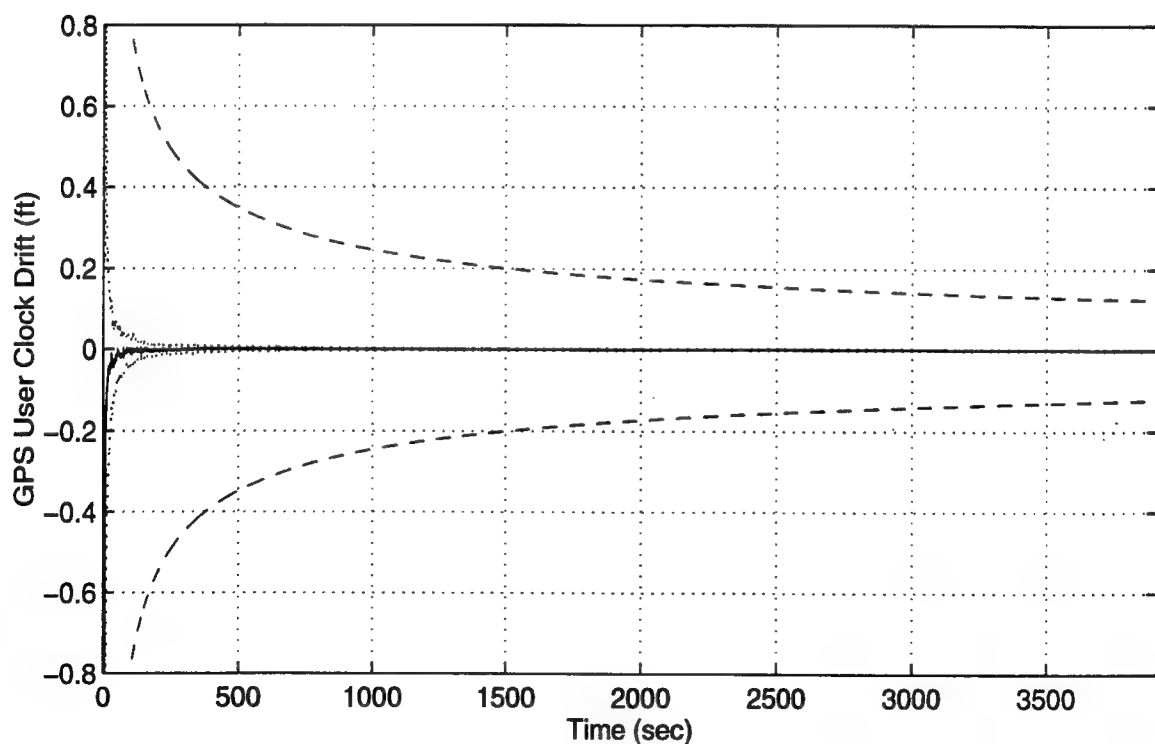
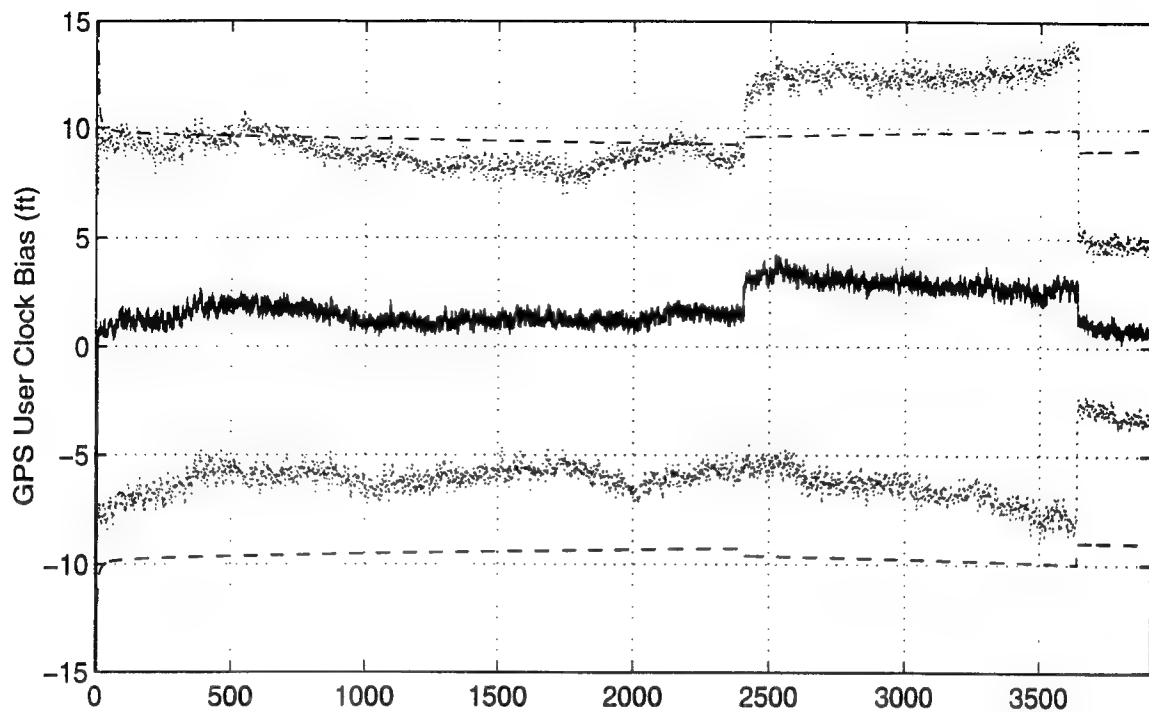
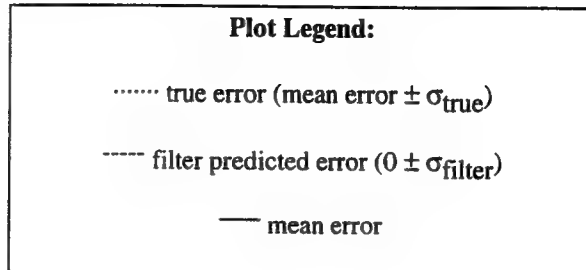


Figure N - 6 GPS User Clock Bias and GPS User Clock Drift

Appendix O

Plots of Case VIII: Barometric Altimeter, 2.0 nm/hr INS, P-Code GPS and Single Pseudolite Using the Tanker Flight Profile.



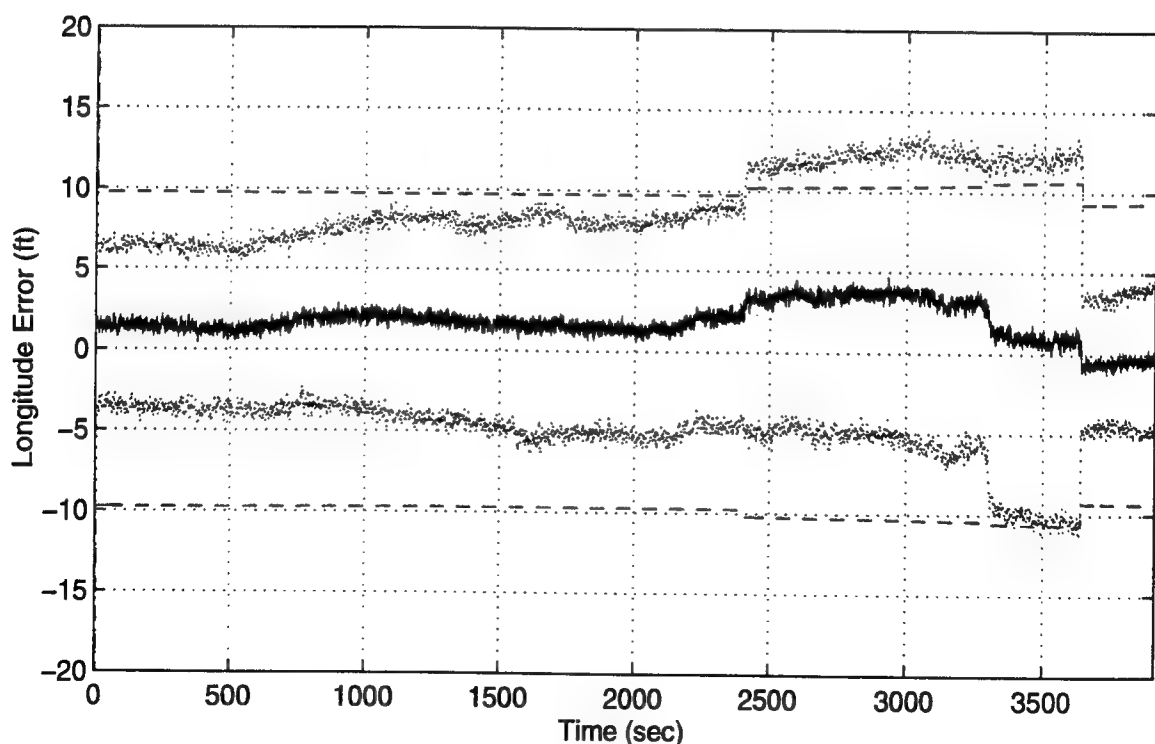
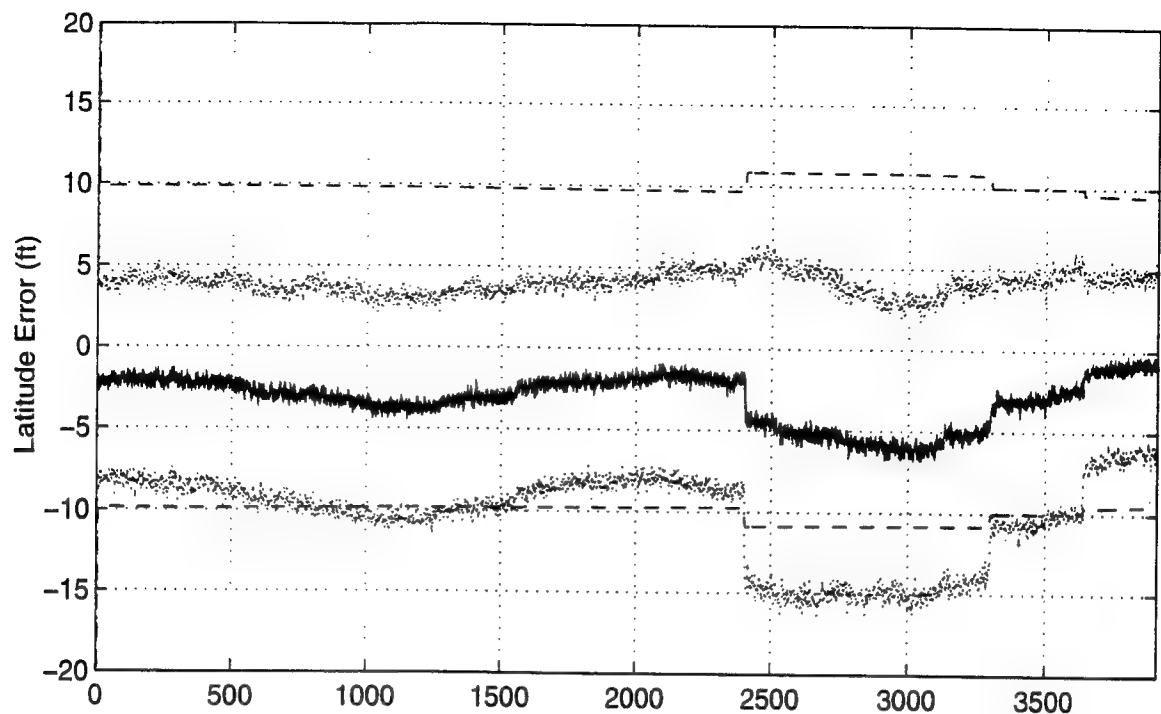


Figure O - 1. Latitude and Longitude Error

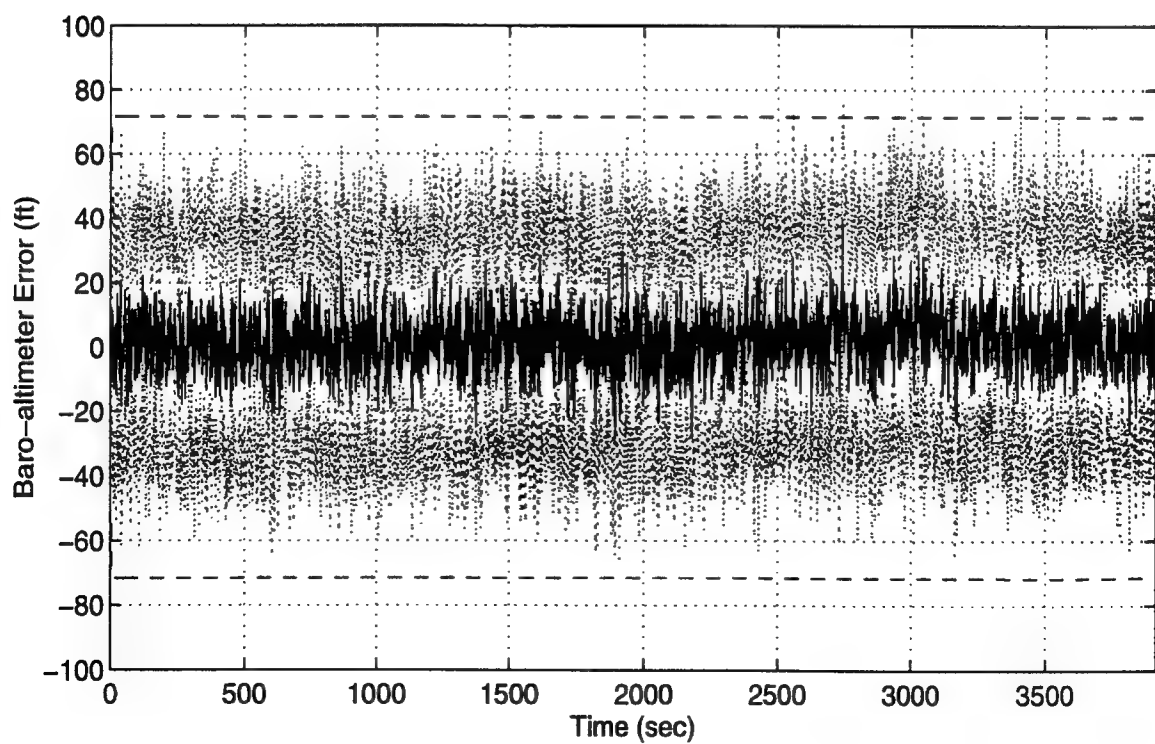
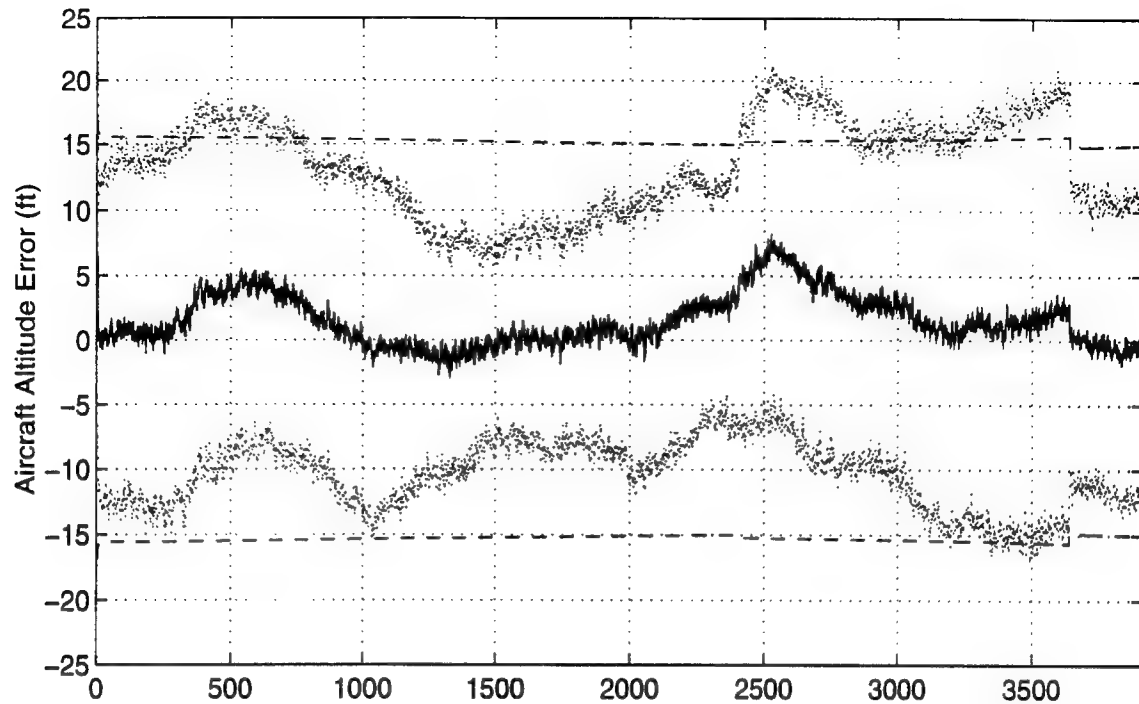


Figure O - 2. Aircraft Altitude and Baro-Altimeter Error

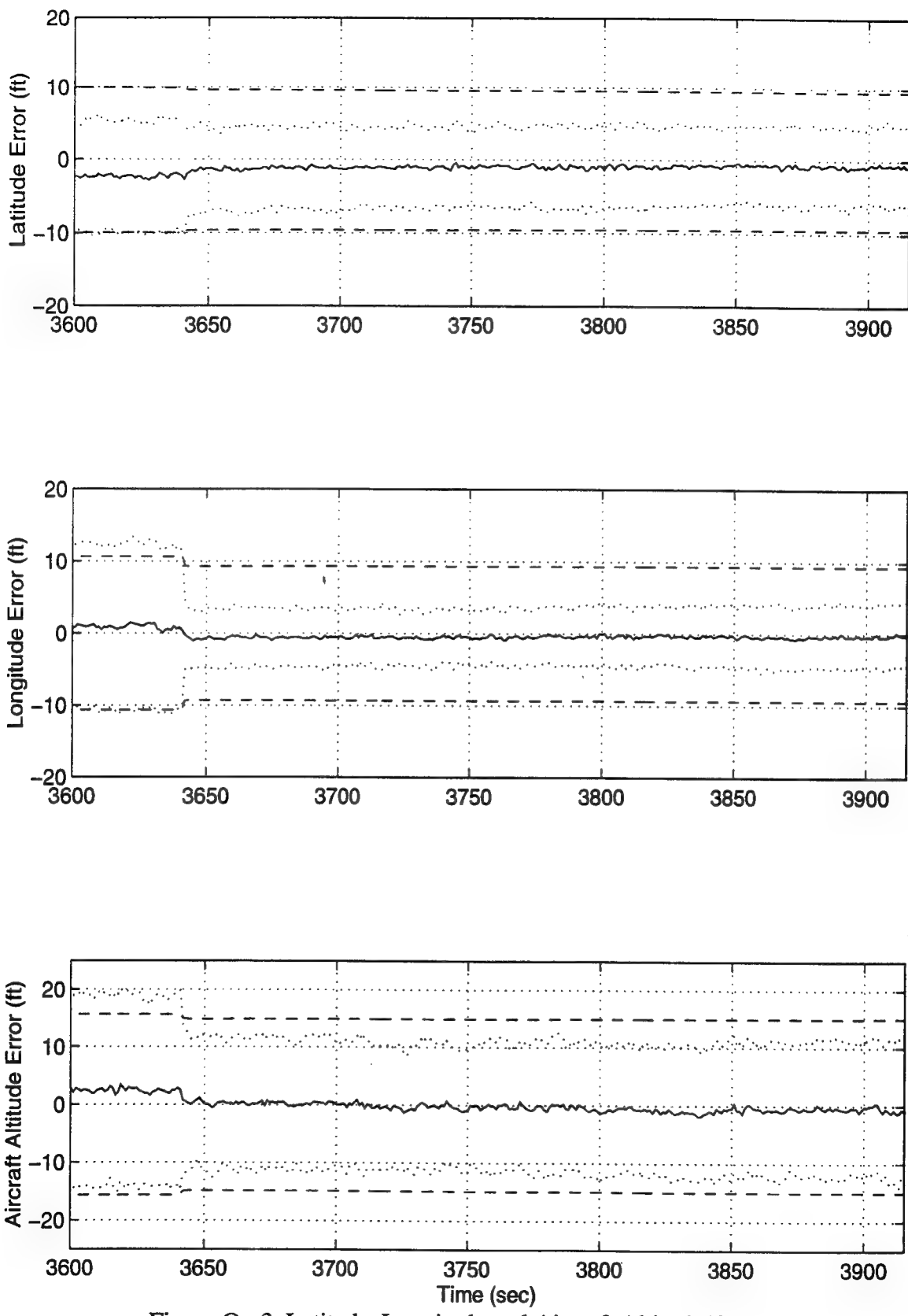


Figure O - 3 Latitude, Longitude and Aircraft Altitude Error

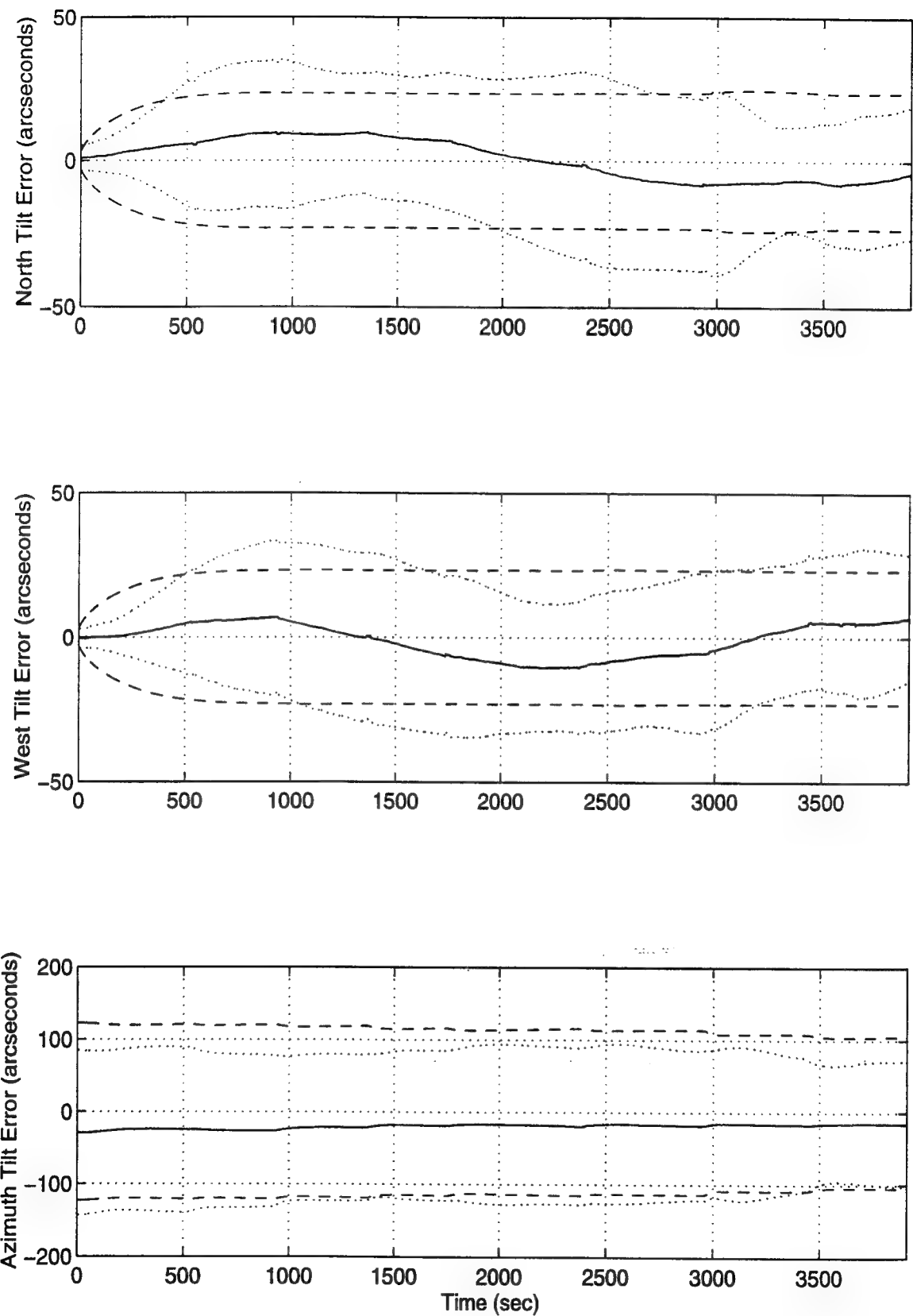


Figure O - 4 North, West and Azimuth Tilt Errors

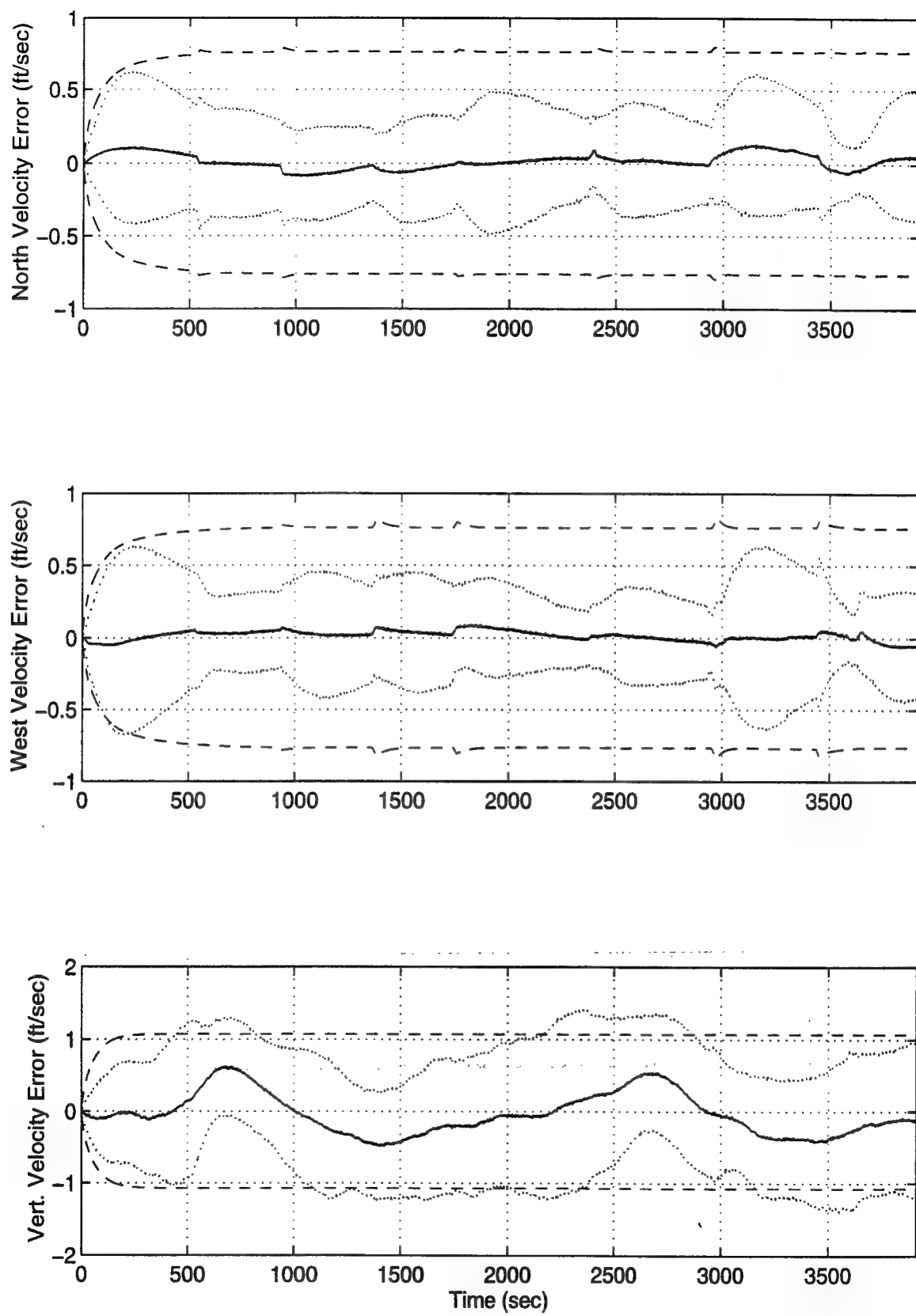


Figure O - 5 North, West and Vertical Velocity Errors

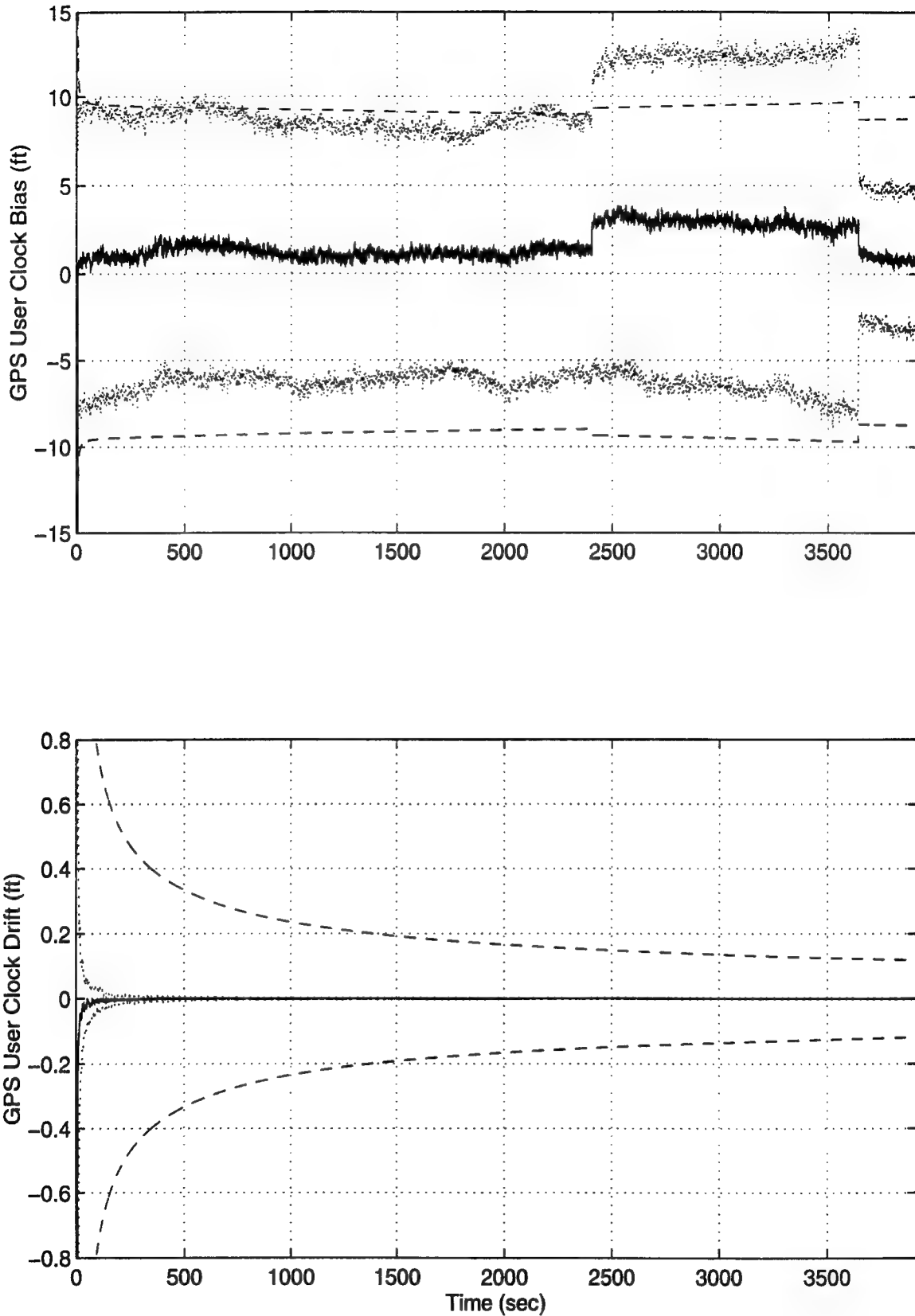
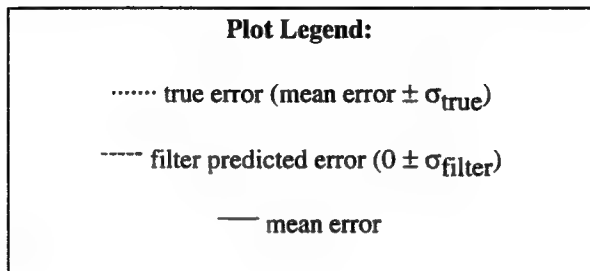


Figure O - 6 GPS User Clock Bias and GPS User Clock Drift

Appendix P

Plots of Case XI: Barometric Altimeter, 4.0 nm/hr INS, P-Code GPS and Single Pseudolite Using the Tanker Flight Profile.



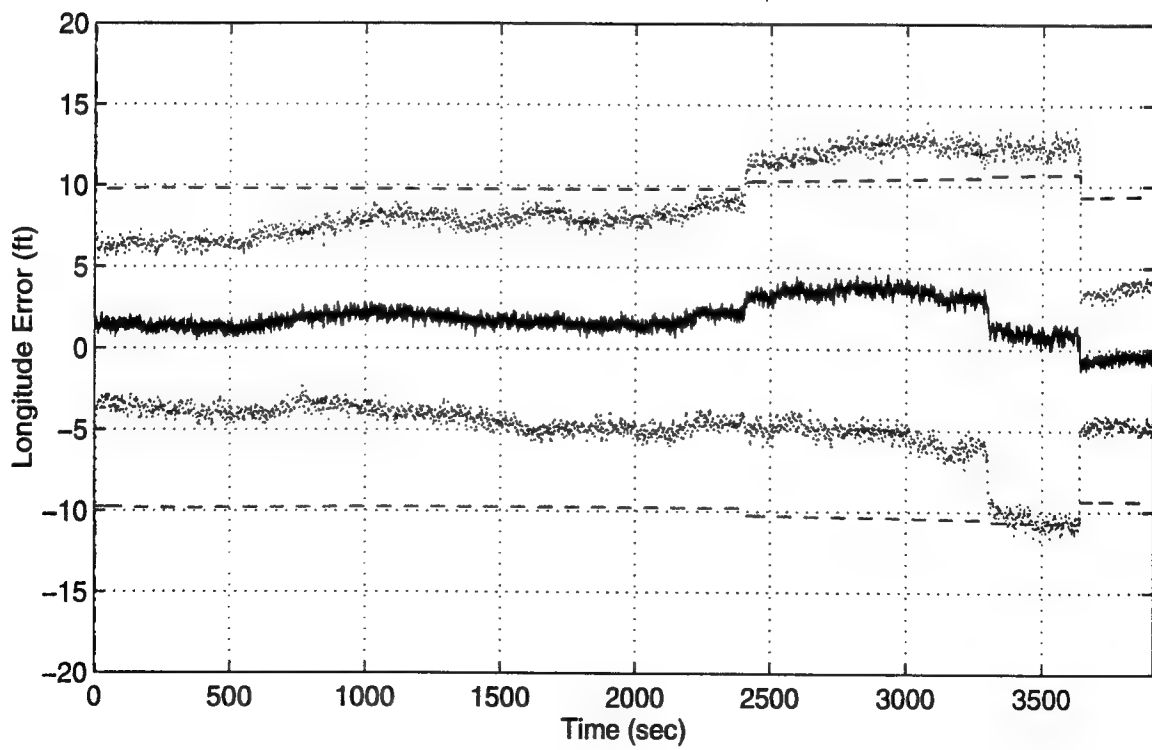
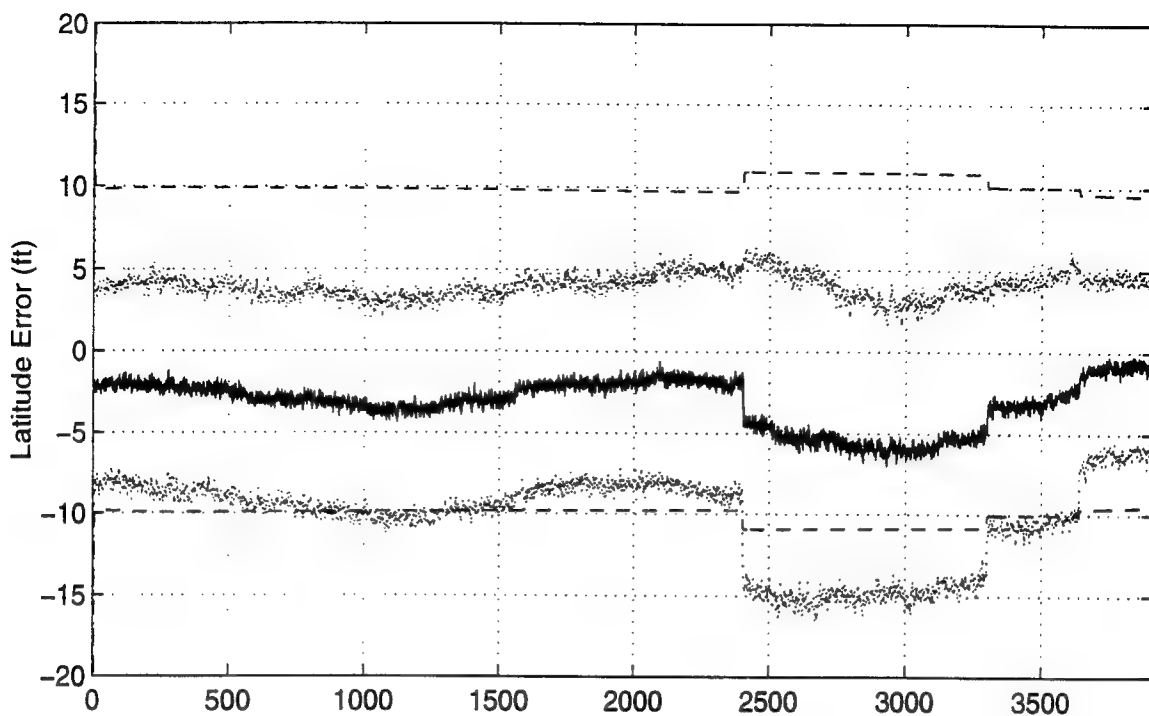


Figure P - 1. Latitude and Longitude Error

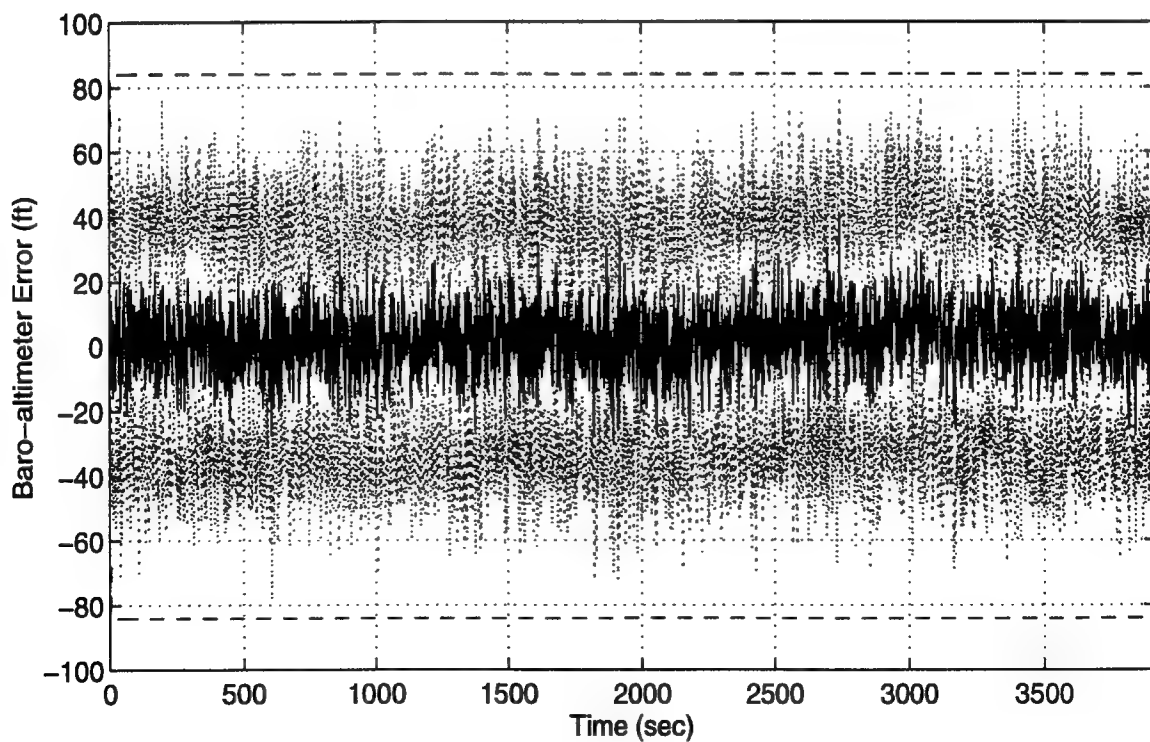
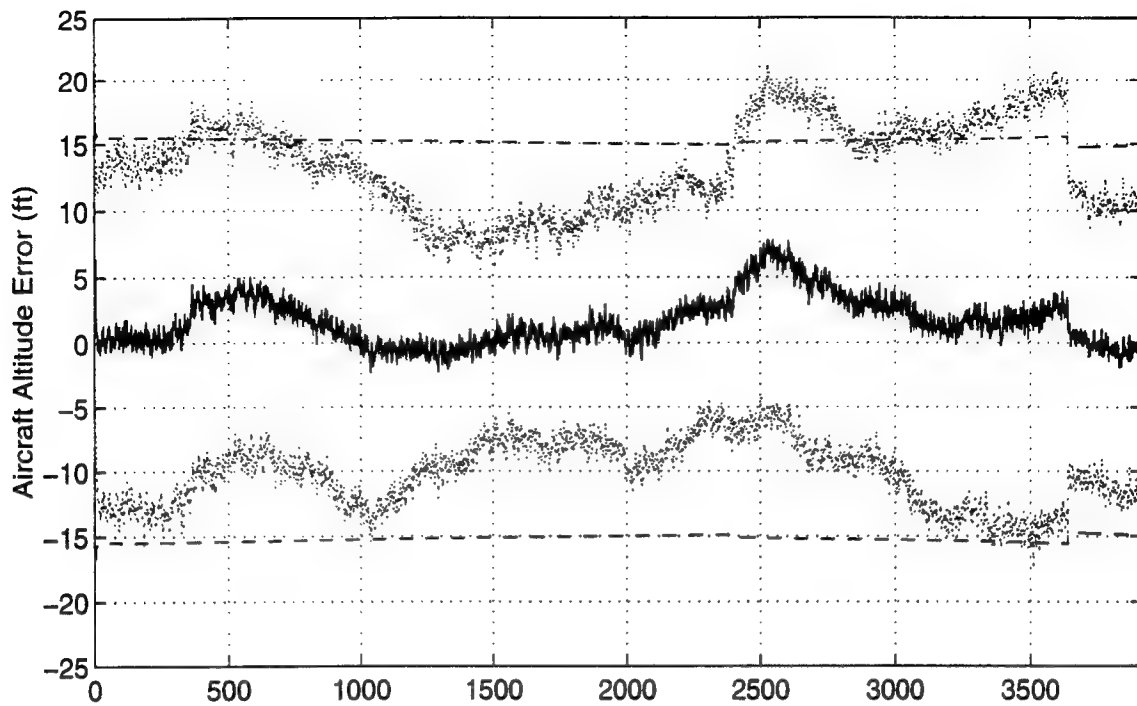


Figure P - 2. Aircraft Altitude and Baro-Altimeter Error

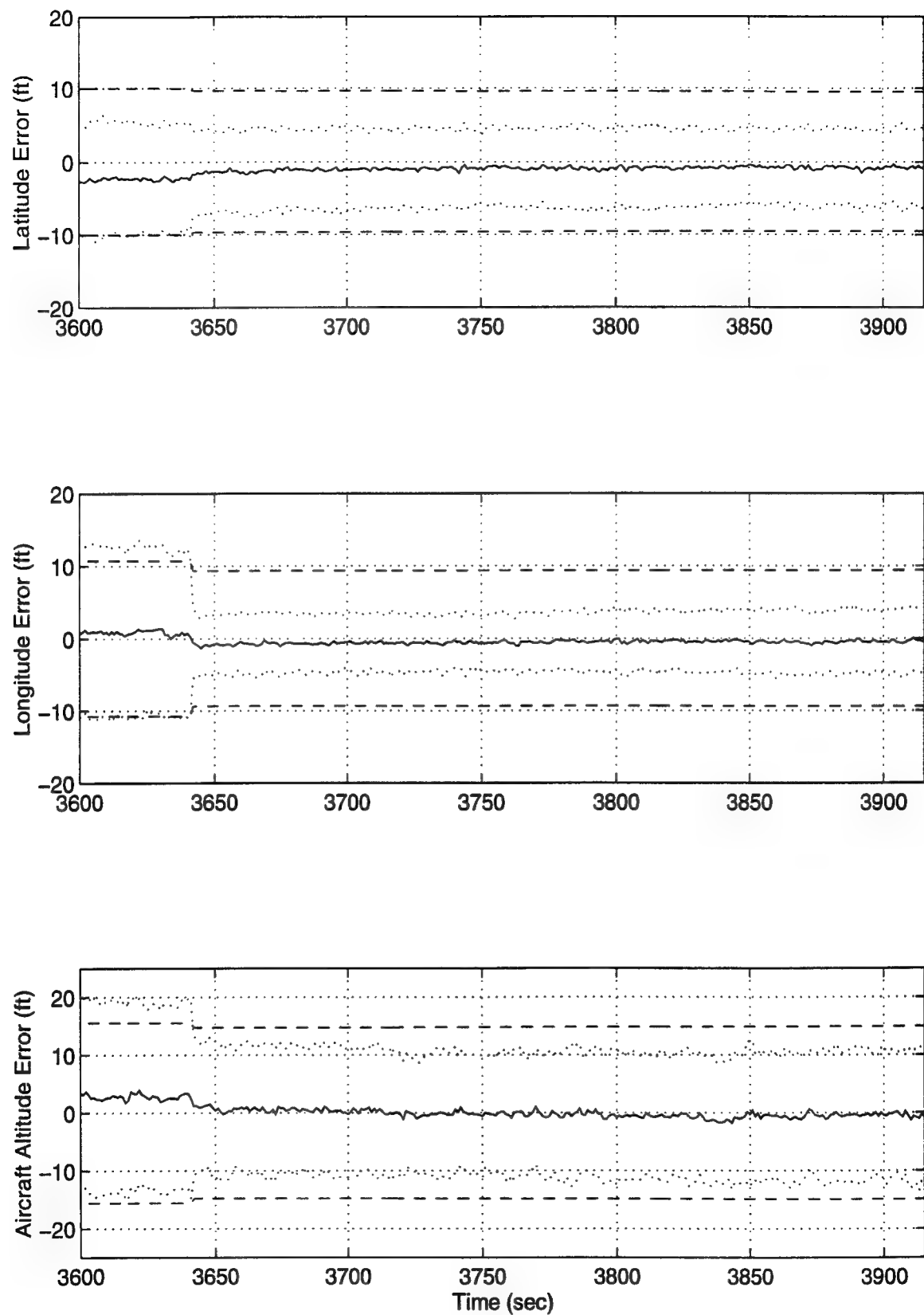


Figure P - 3 Latitude, Longitude and Aircraft Altitude Error

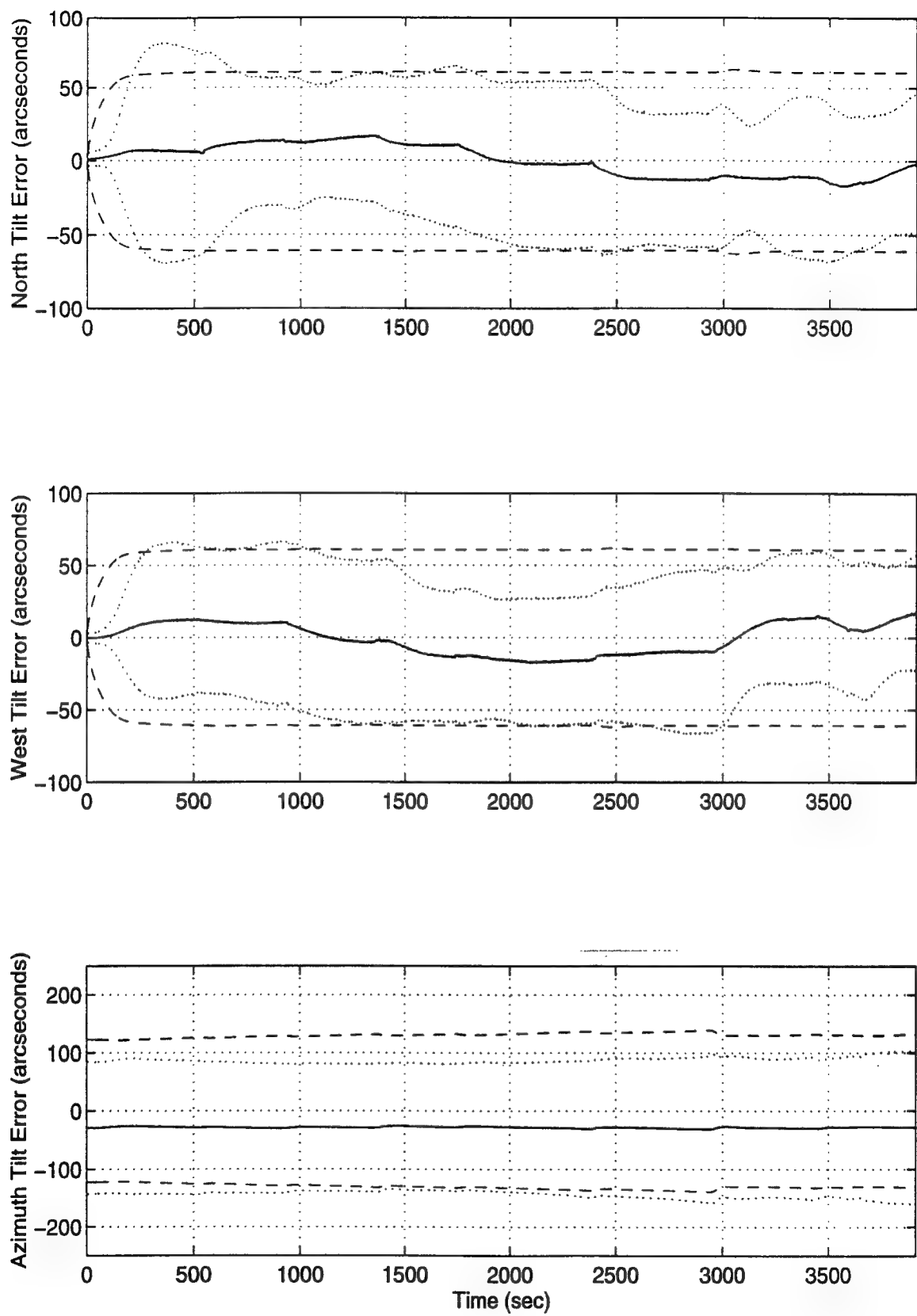


Figure P - 4 North, West and Azimuth Tilt Errors

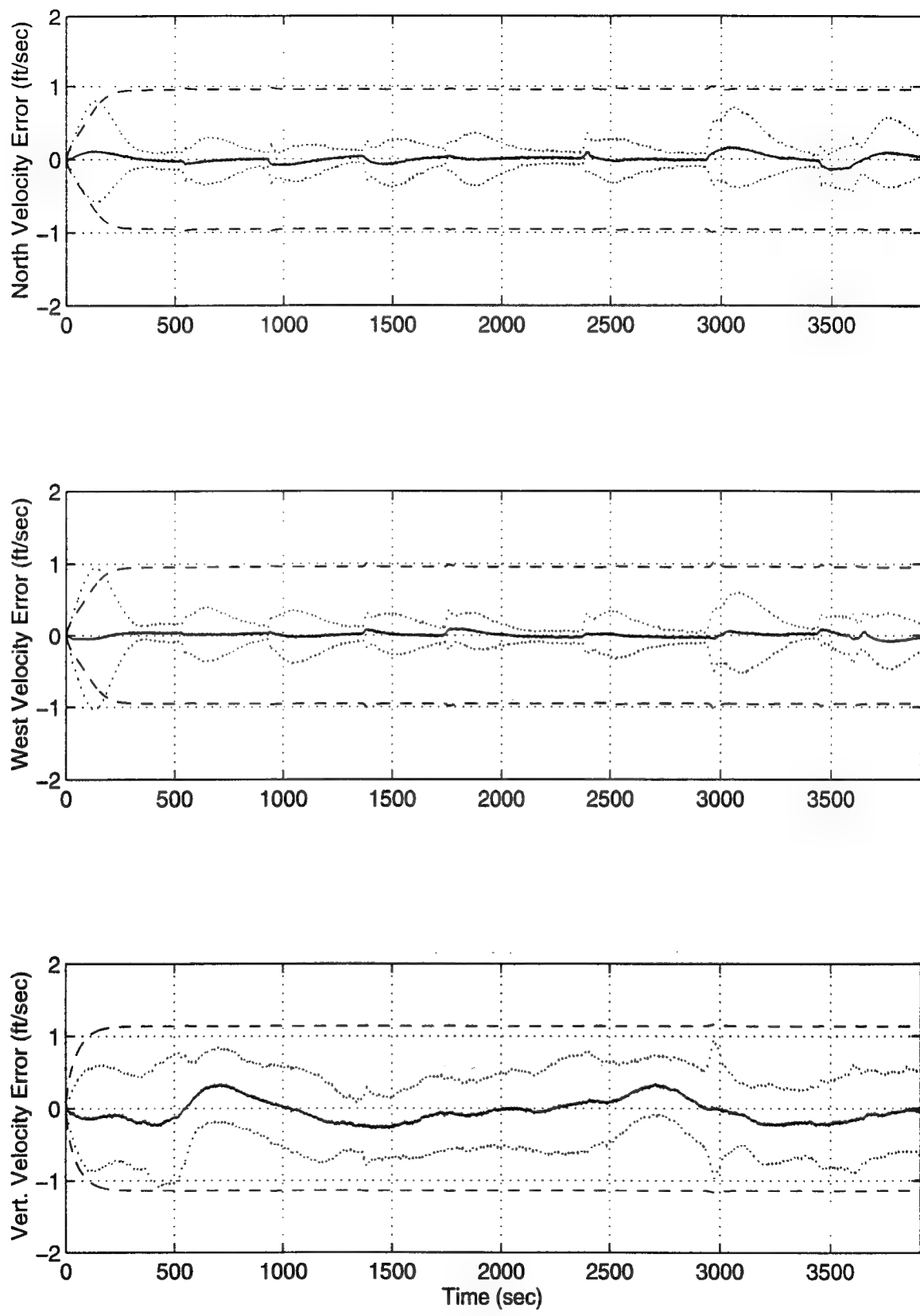


Figure P - 5 North, West and Vertical Velocity Errors

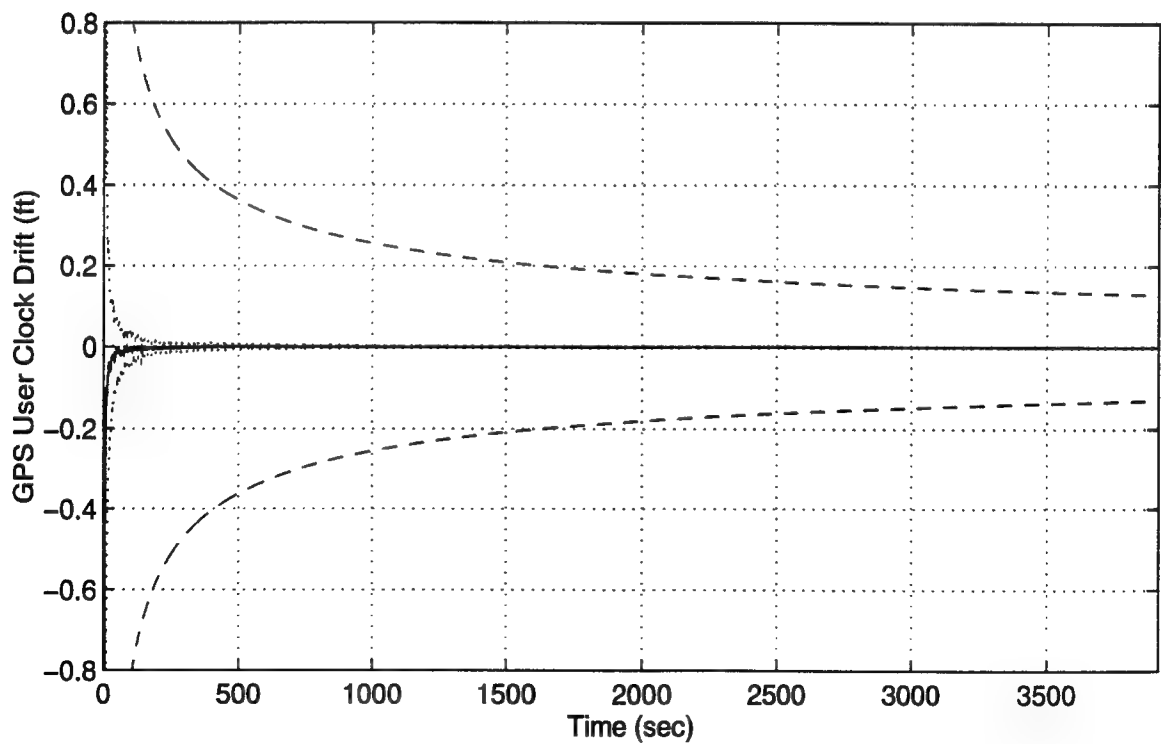
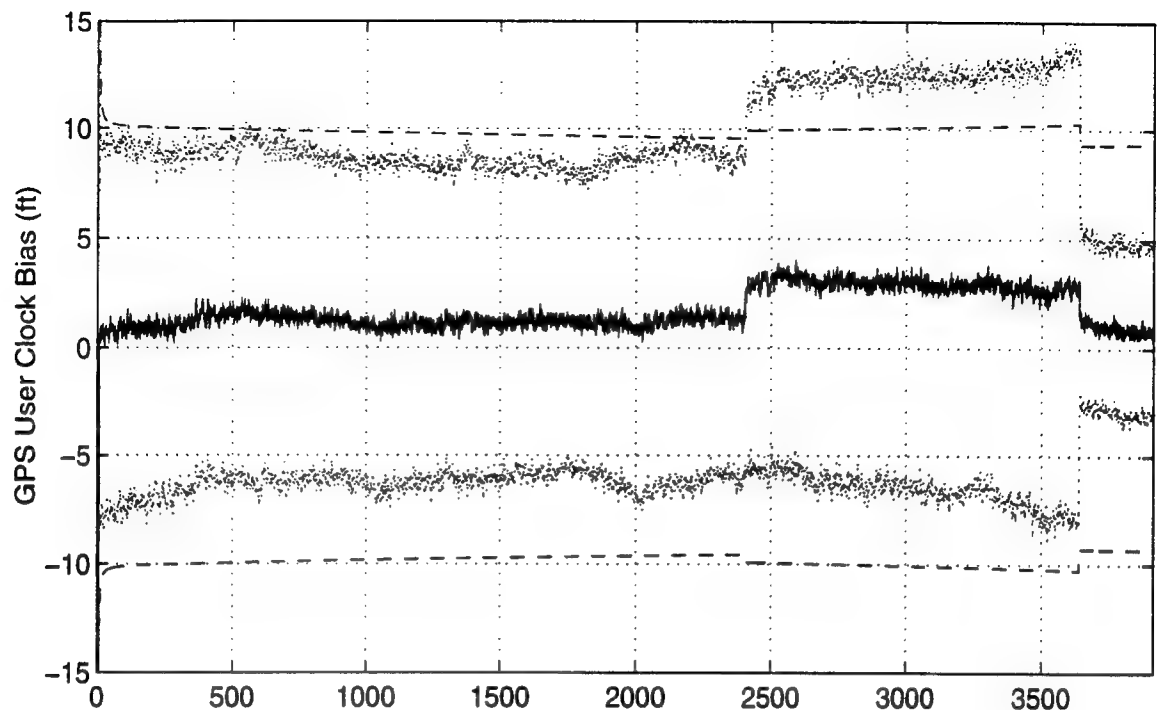
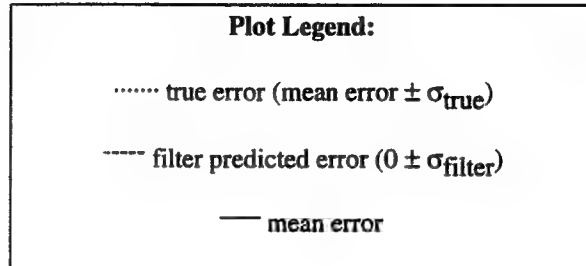


Figure P - 6 GPS User Clock Bias and GPS User Clock Drift

Appendix Q

Plots of Case X. Barometric Altimeter, 0.4 nm/hr INS, P-Code GPS, Single Pseudolite and Radar Altimeter Using the Tanker Flight Profile.



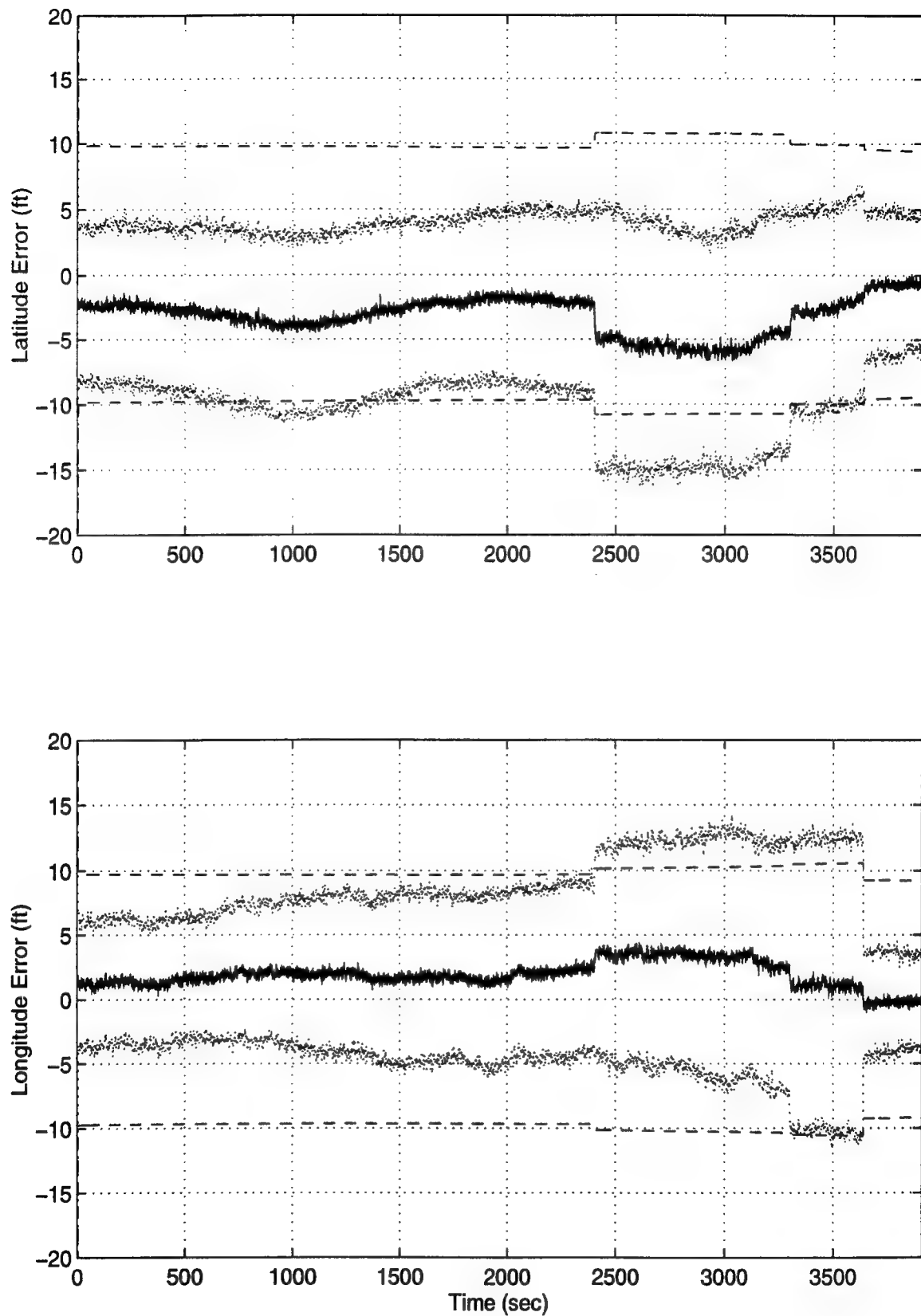


Figure Q - 1. Latitude and Longitude Error

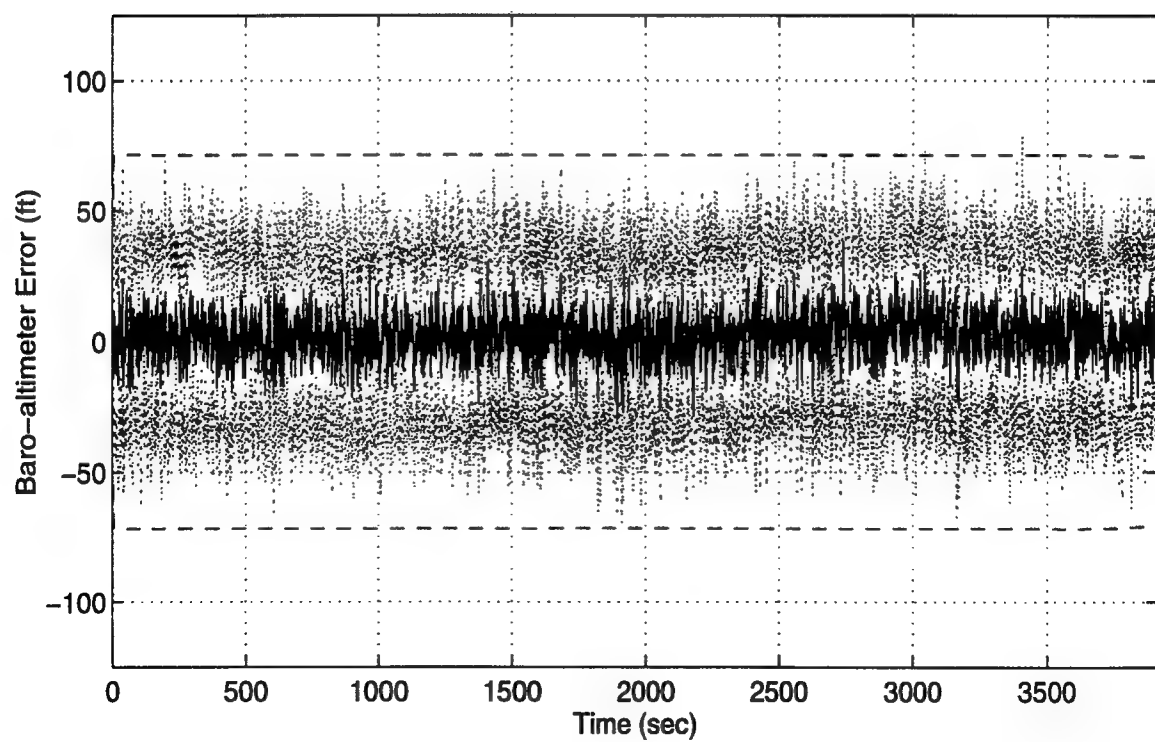
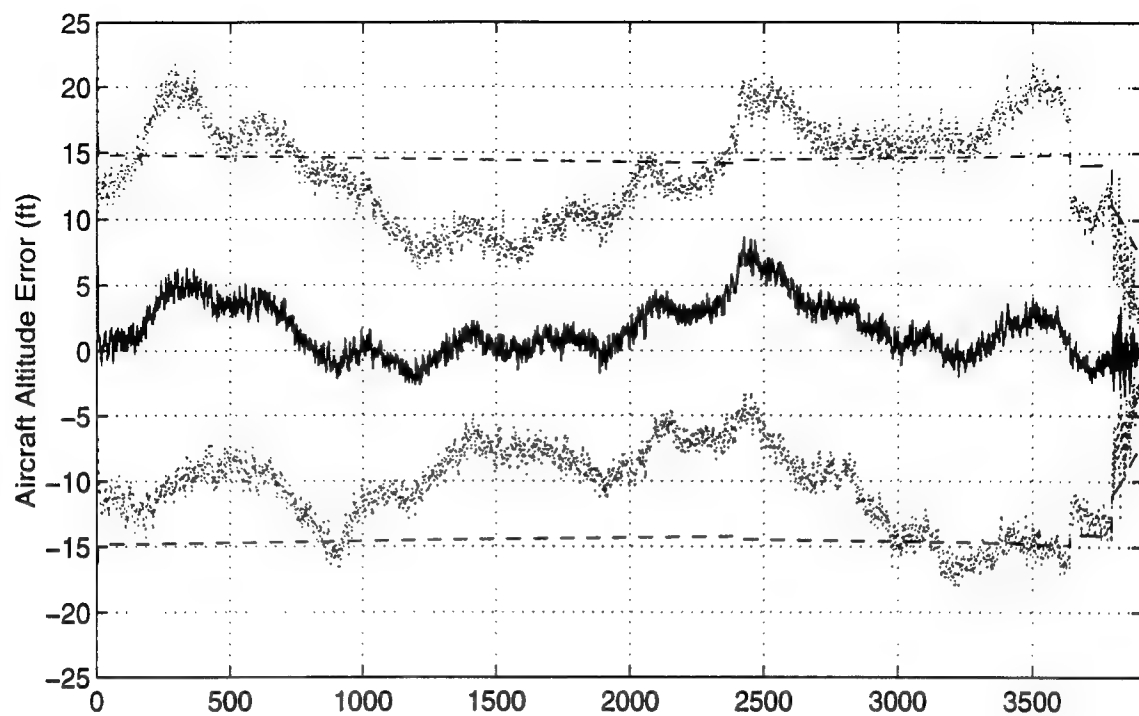


Figure Q - 2. Aircraft Altitude and Baro-Altimeter Error

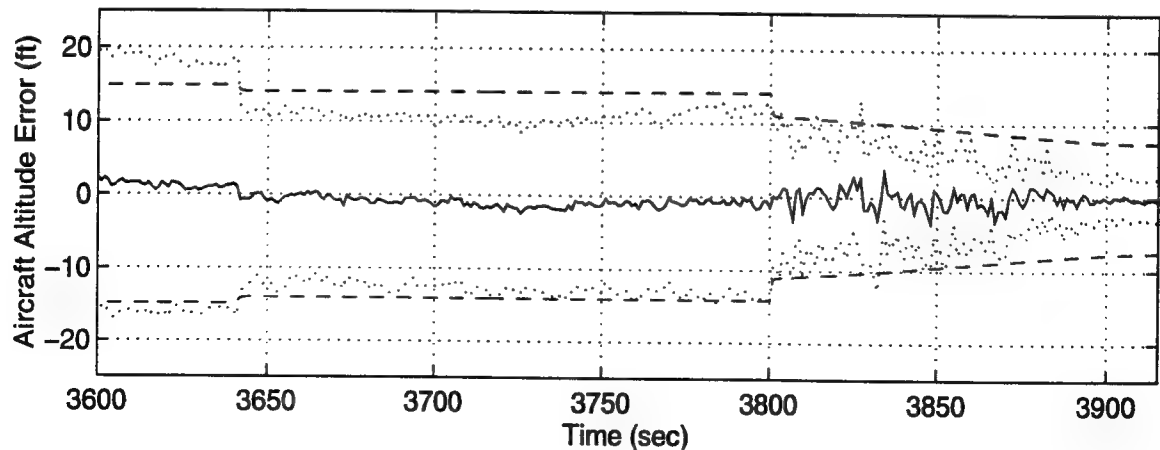
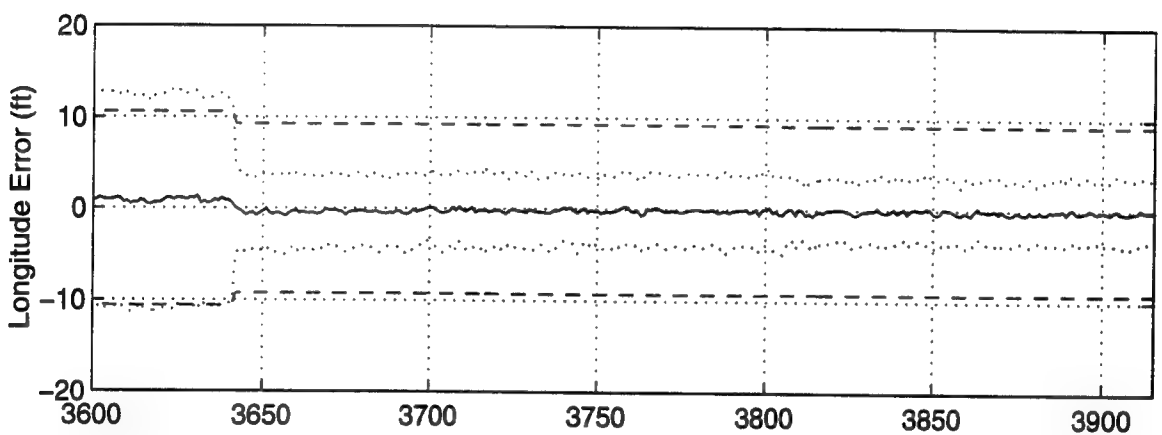
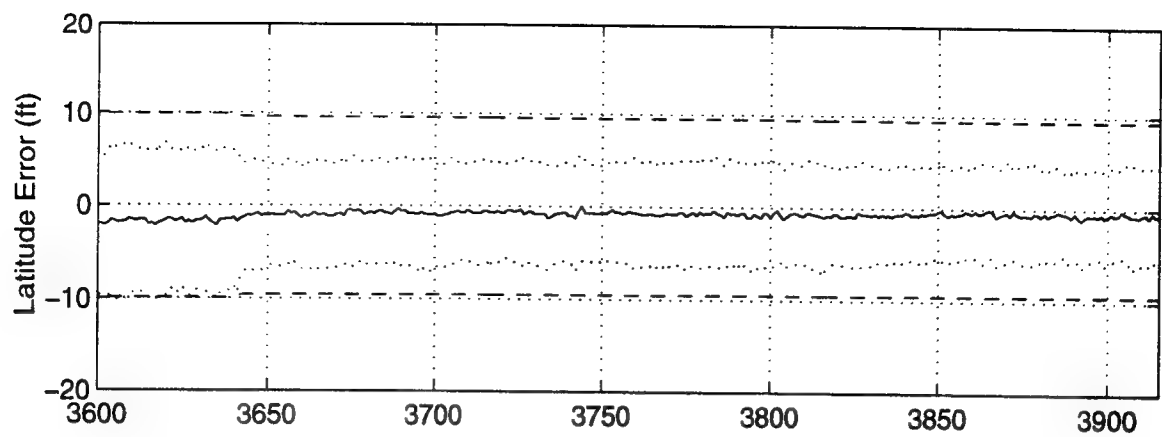


Figure Q - 3 Latitude, Longitude and Aircraft Altitude Error

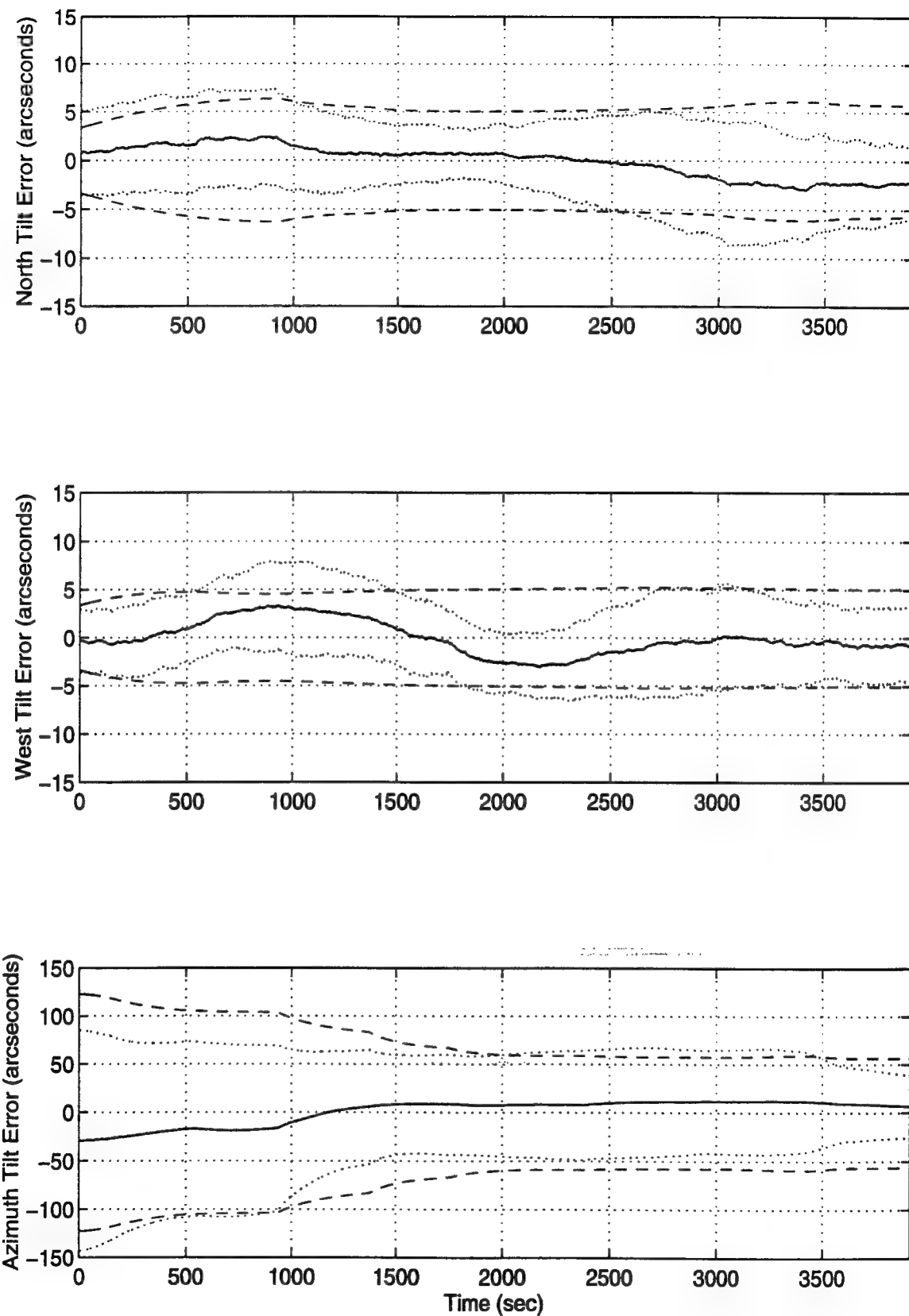


Figure Q - 4 North, West and Azimuth Tilt Errors

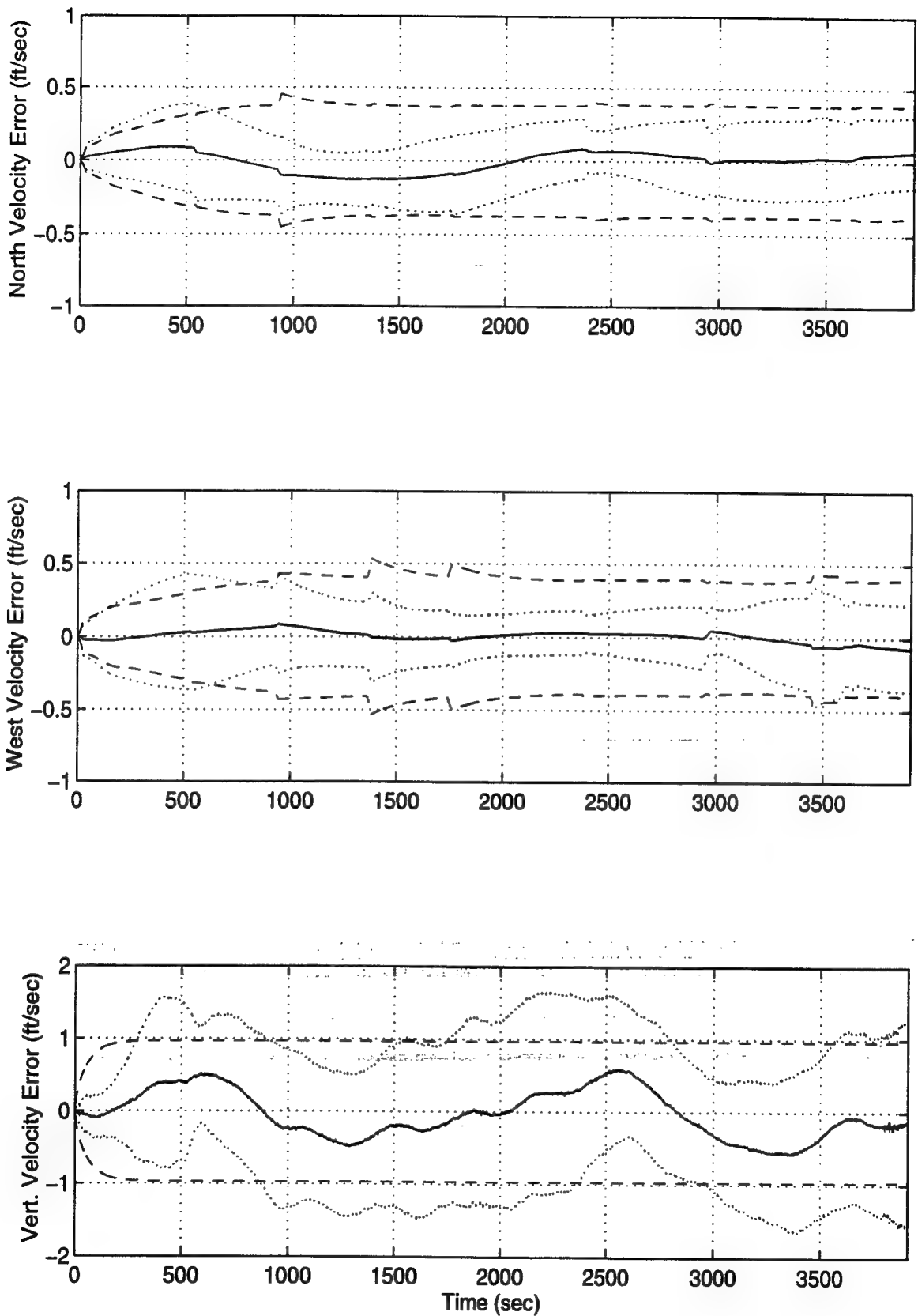


Figure Q - 5 North, West and Vertical Velocity Errors

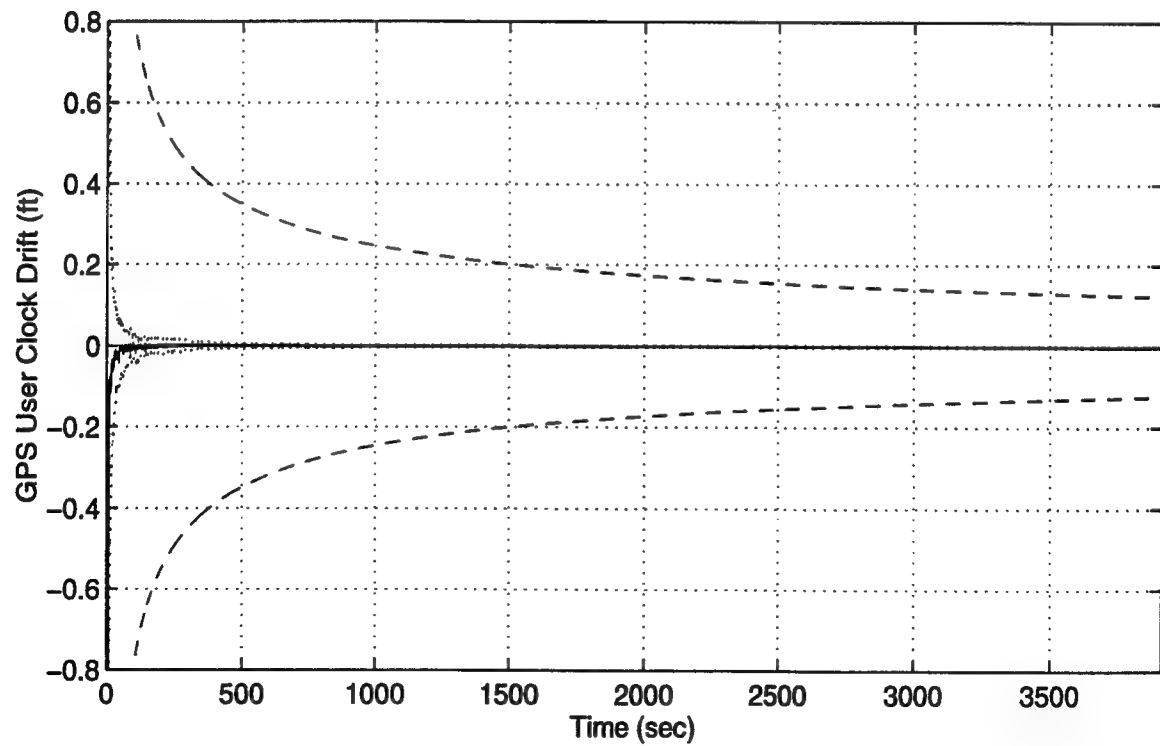
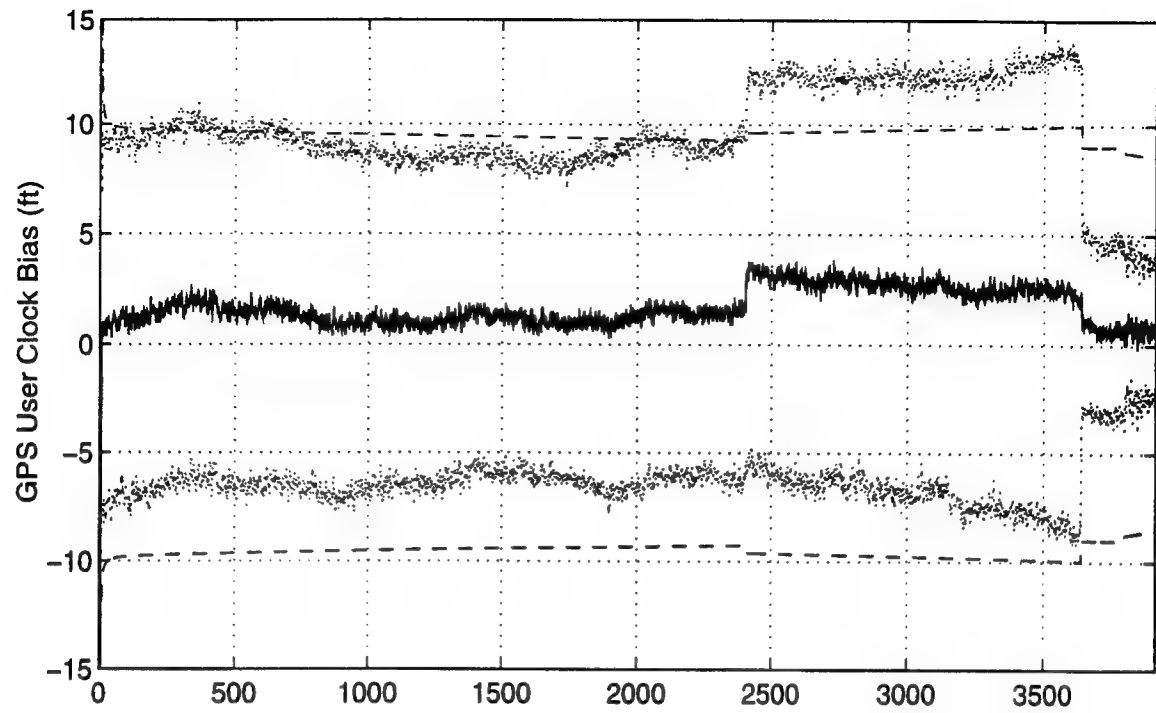
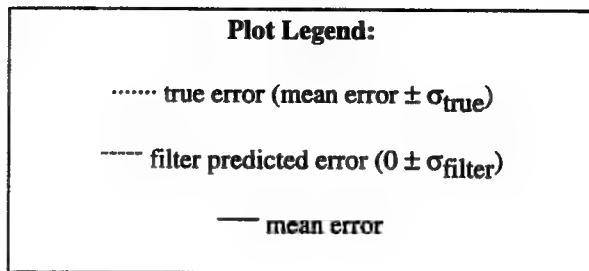


Figure Q - 6 GPS User Clock Bias and GPS User Clock Drift

Appendix R

Plots of Case XI: Barometric Altimeter, 2.0 nm/hr INS, P-Code GPS, Single Pseudolite and Radar Altimeter Using the Tanker Flight Profile.



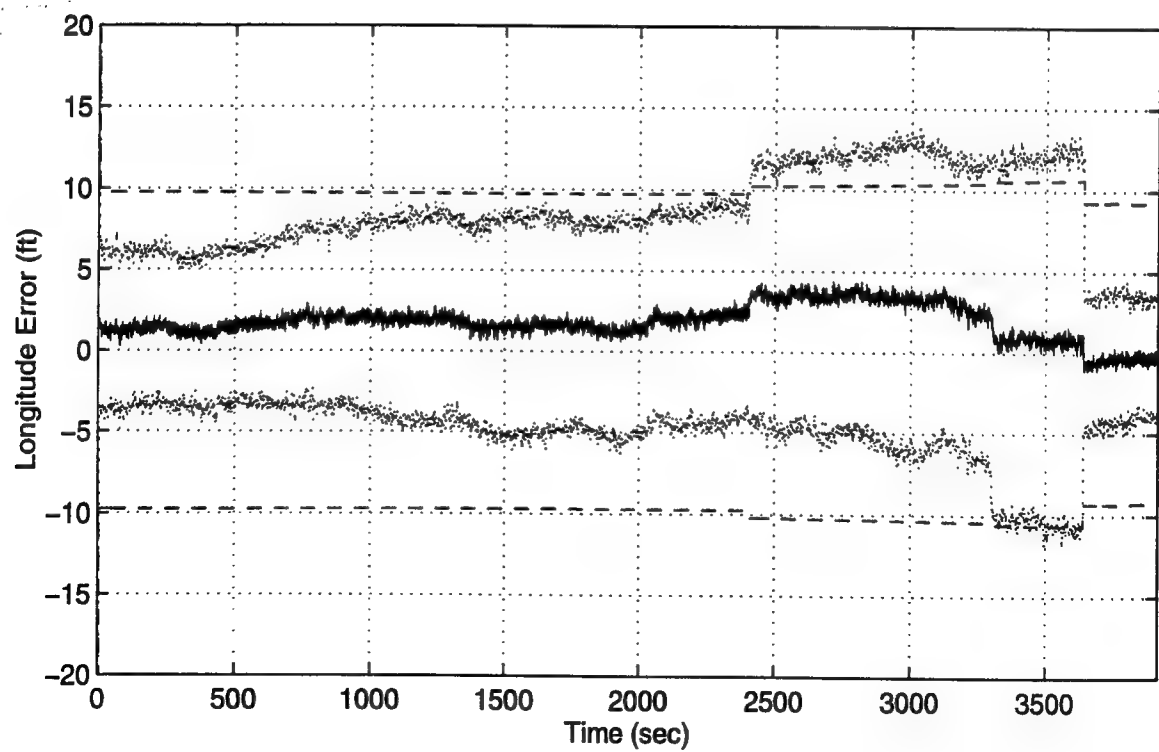
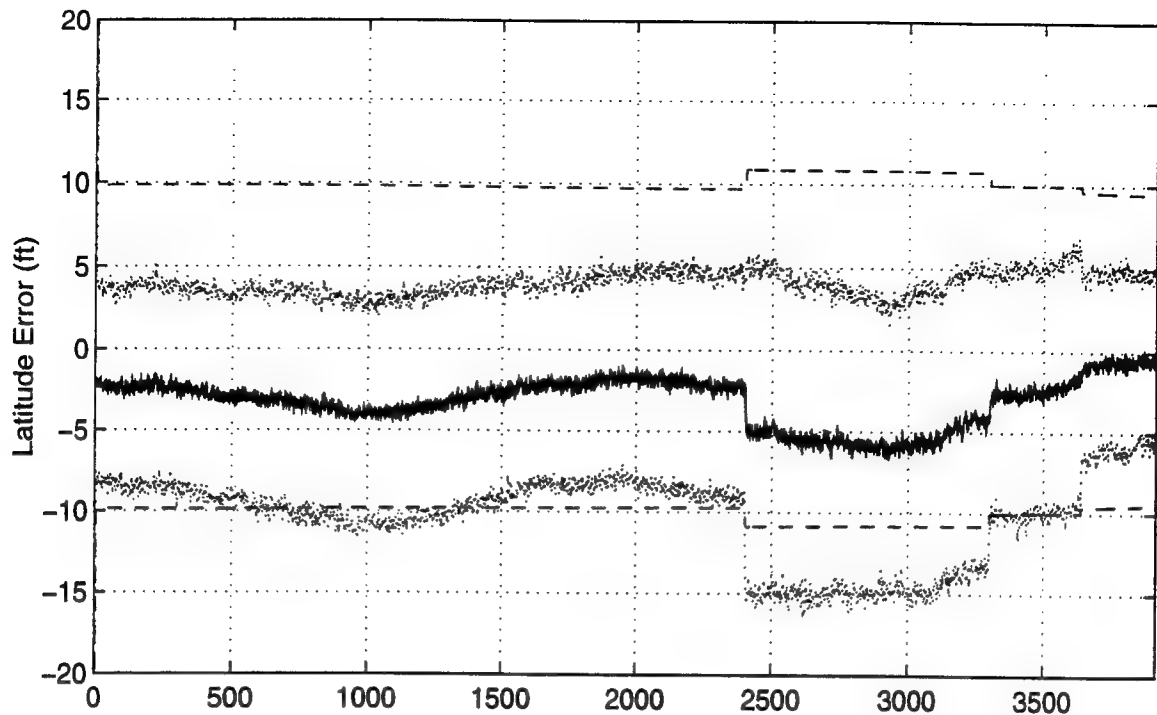


Figure R - 1. Latitude and Longitude Error

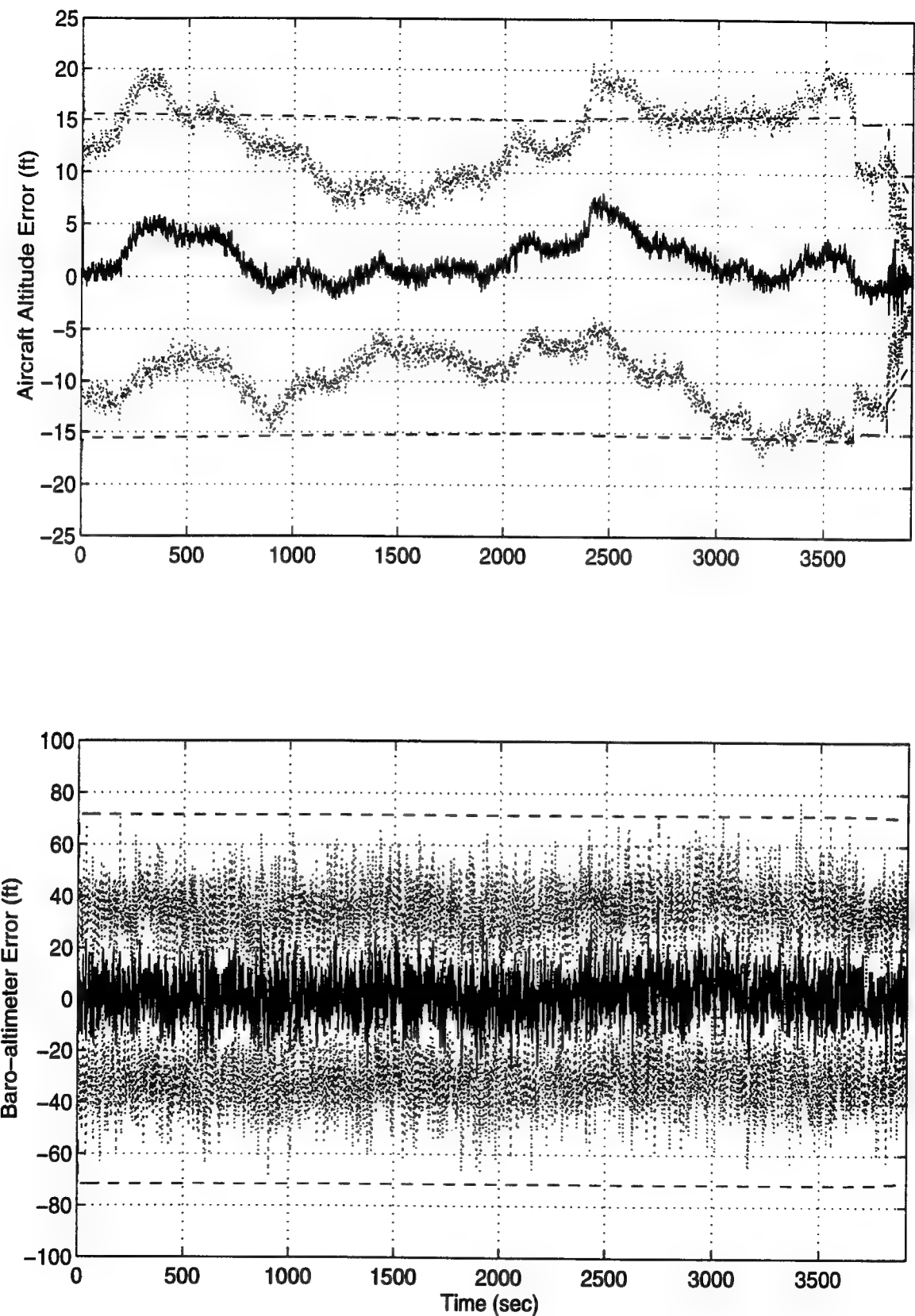


Figure R - 2. Aircraft Altitude and Baro-Altimeter Error

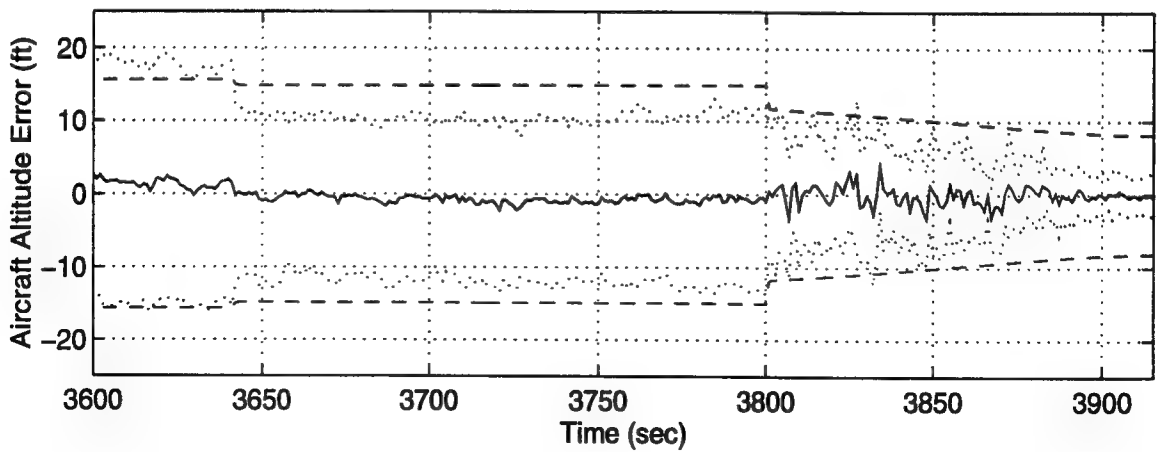
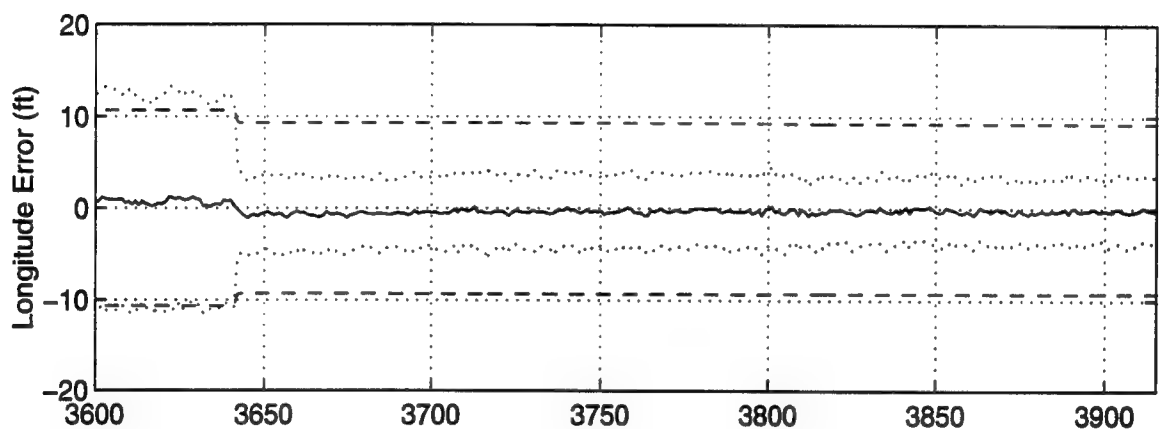
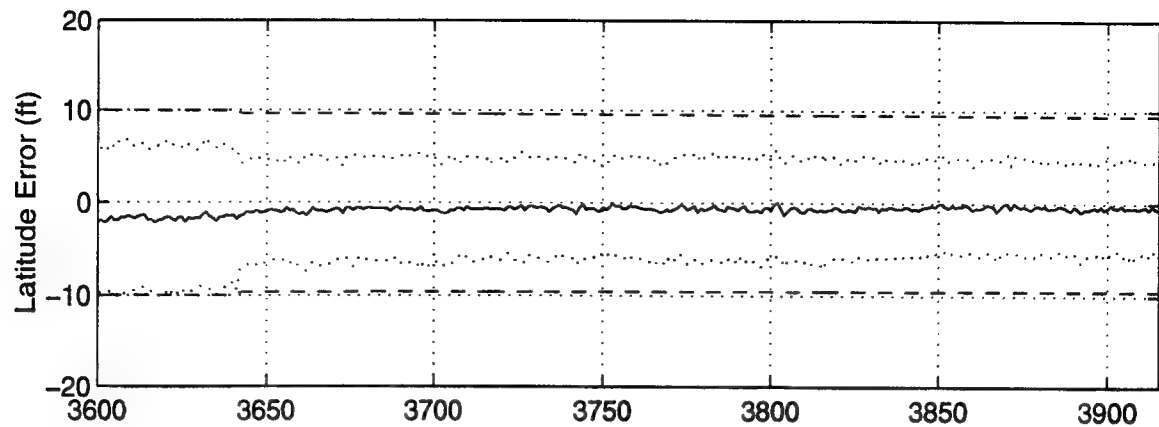


Figure R - 3 Latitude, Longitude and Aircraft Altitude Error

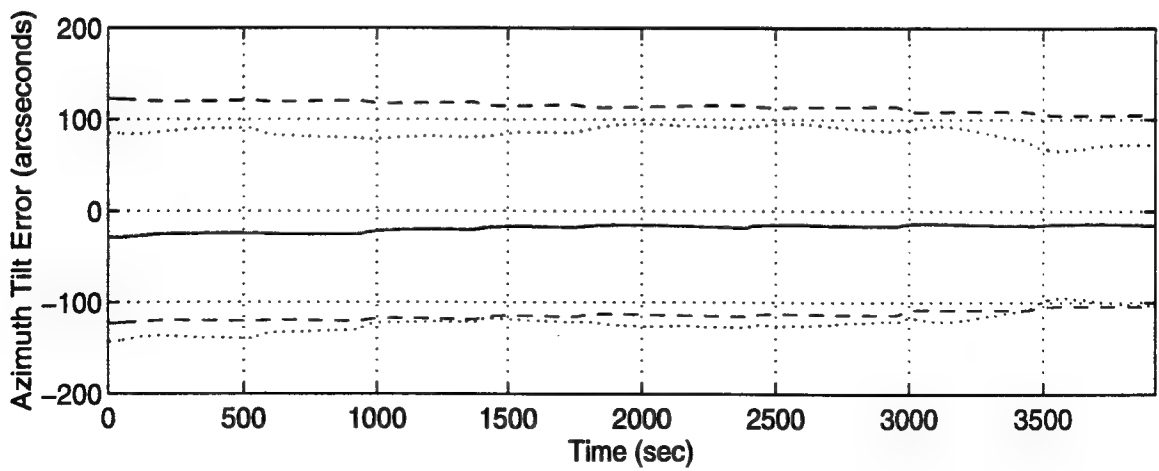
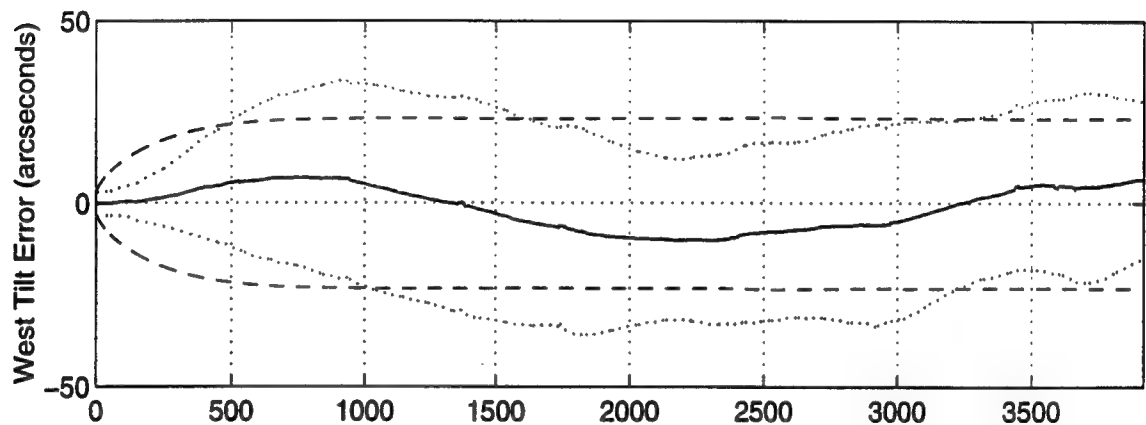
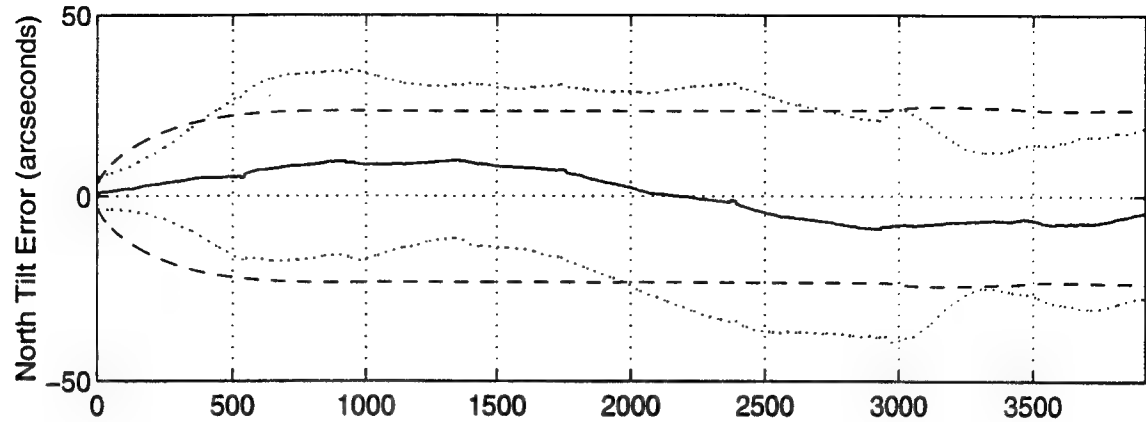


Figure R - 4 North, West and Azimuth Tilt Errors

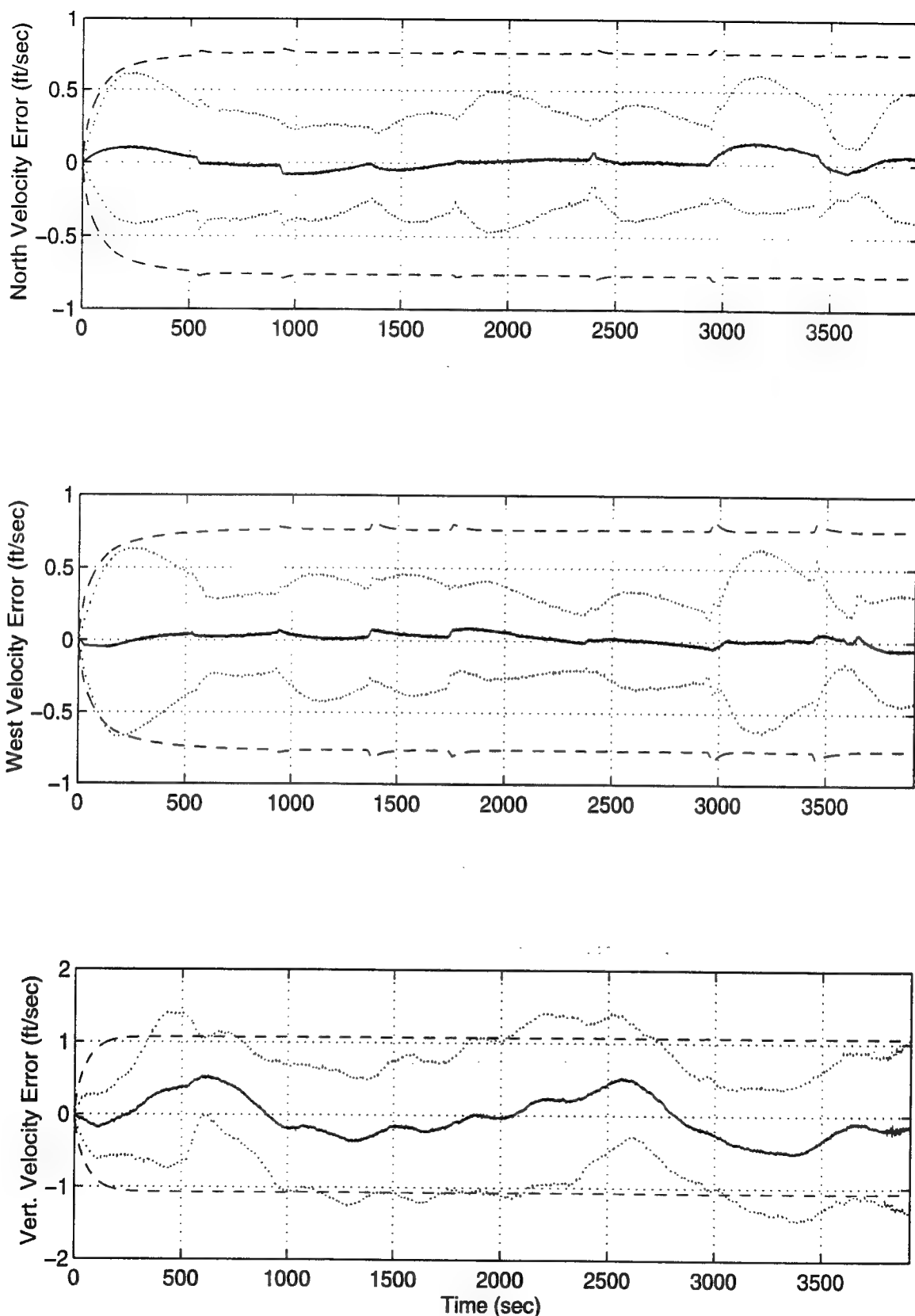


Figure R - 5 North, West and Vertical Velocity Errors

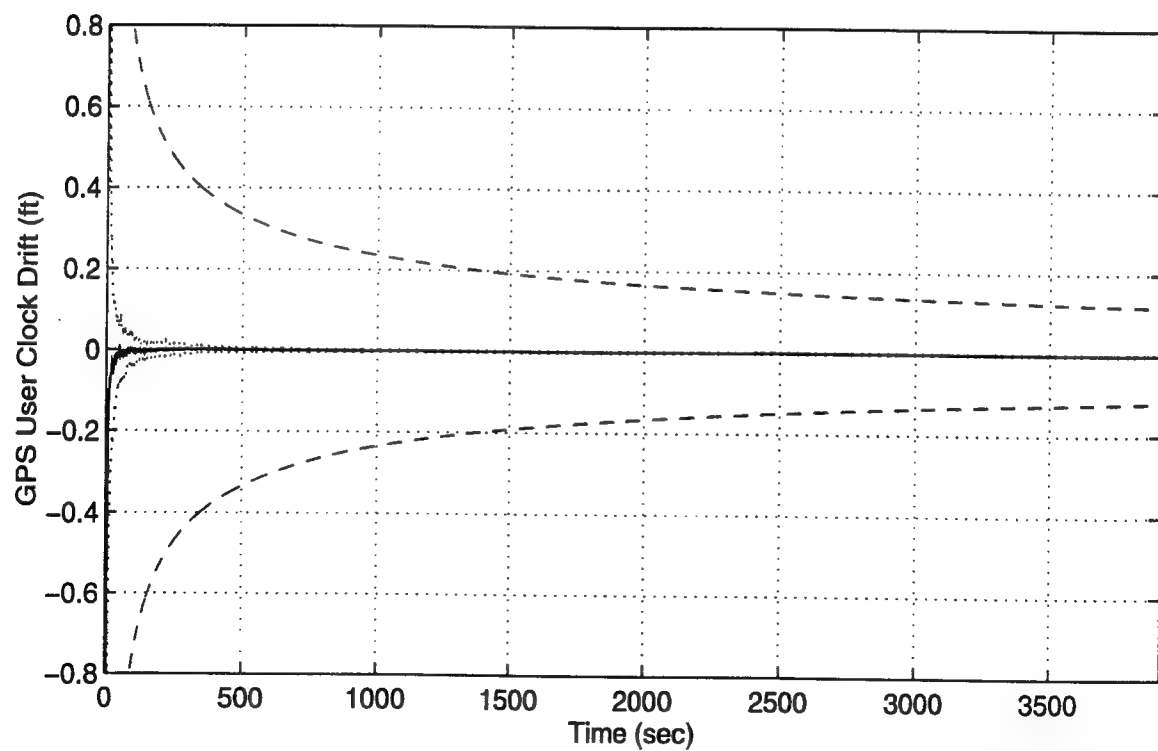
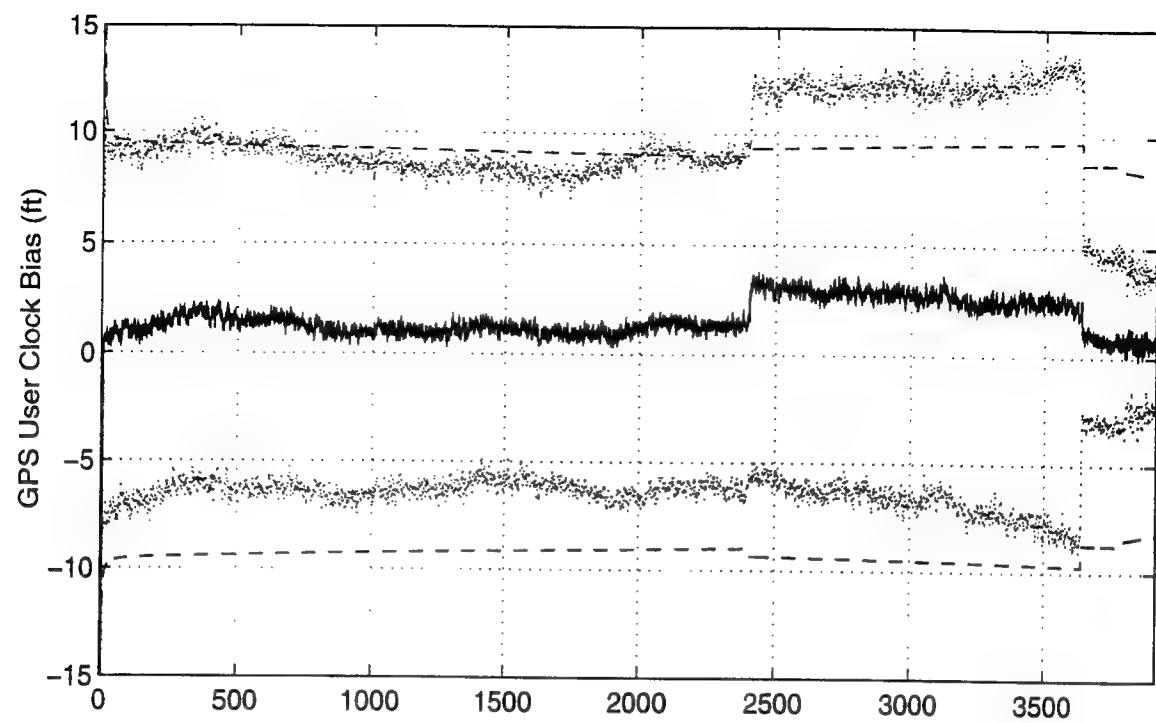
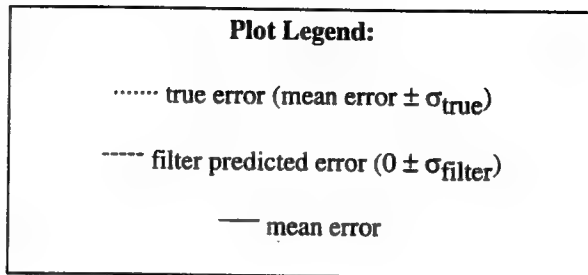


Figure R - 6 GPS User Clock Bias and GPS User Clock Drift

Appendix S

Plots of Case VII: Barometric Altimeter, 4.0 nm/hr INS, P-Code GPS, Single Pseudolite and Radar Altimeter Using the Tanker Flight Profile.



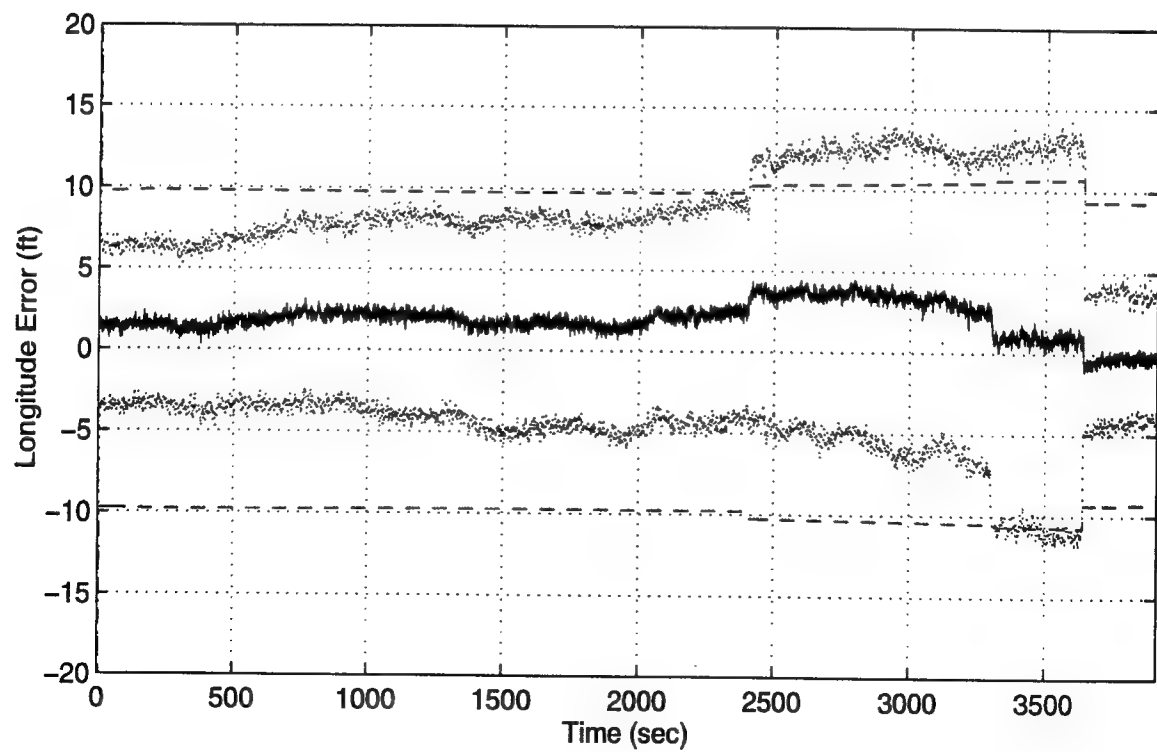
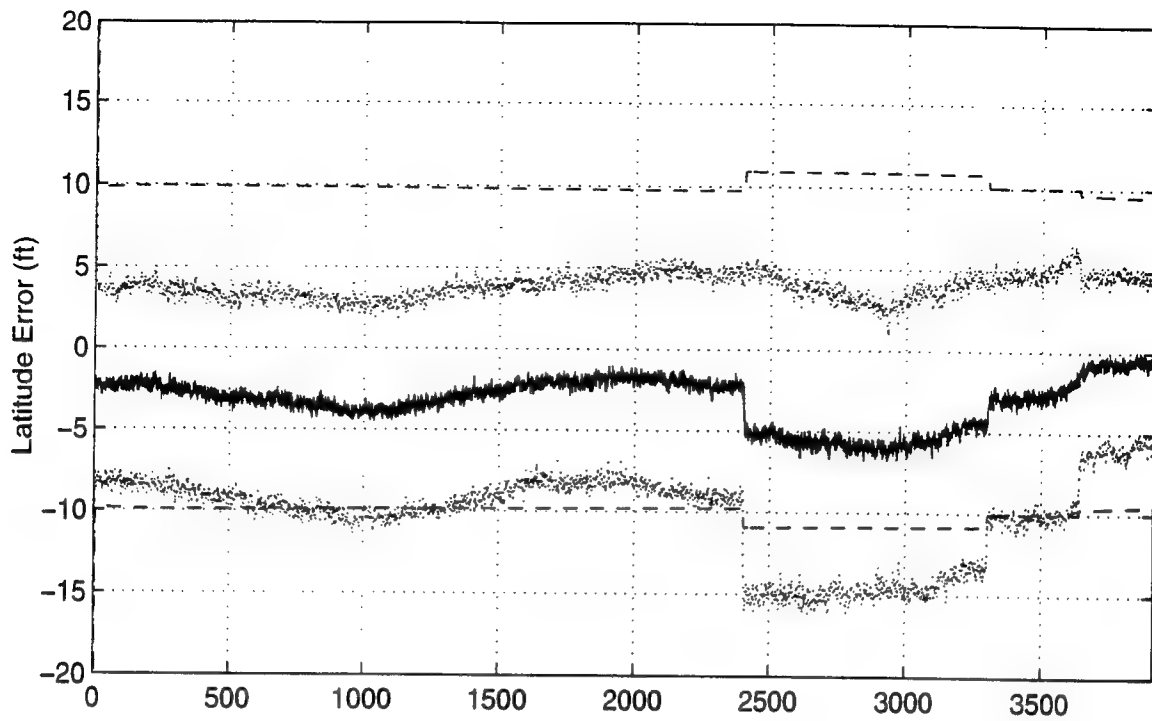


Figure S - 1. Latitude and Longitude Error

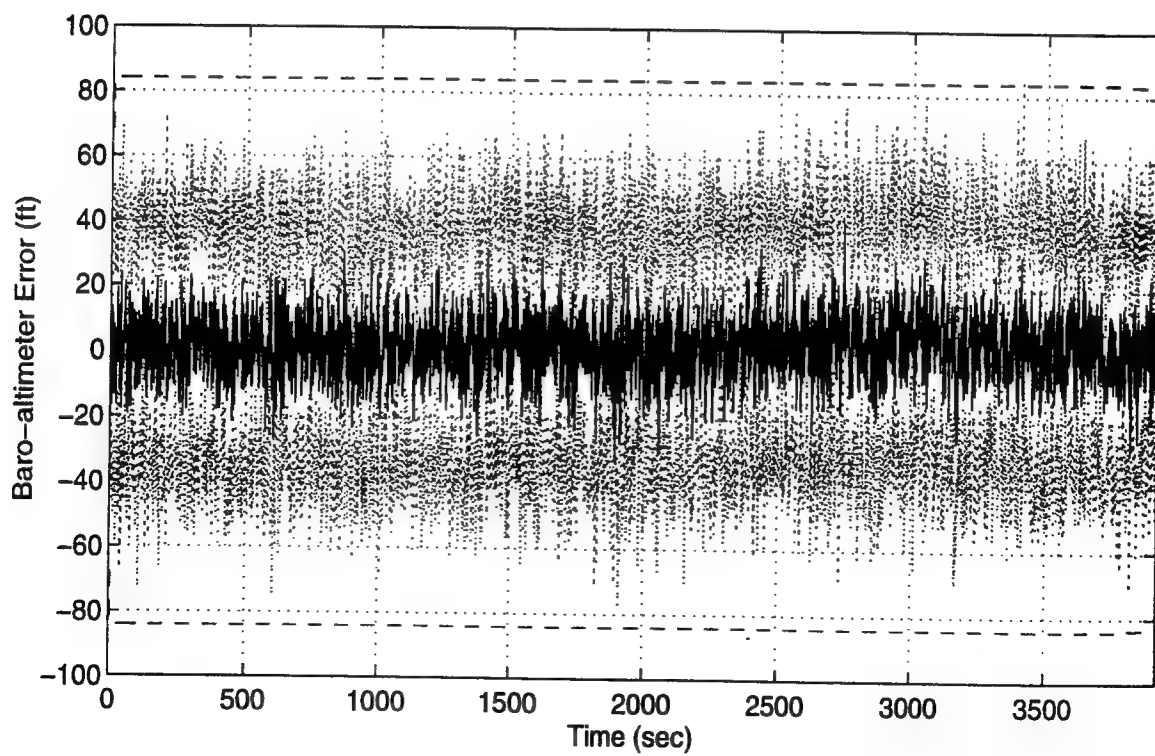
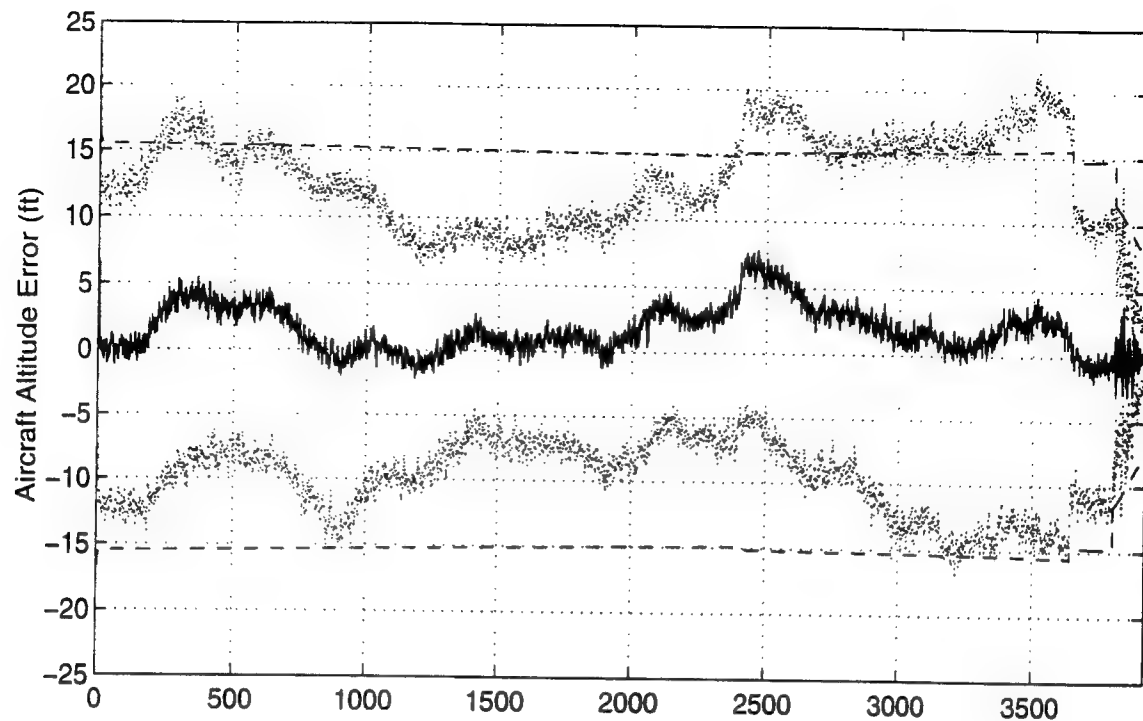


Figure S - 2. Aircraft Altitude and Baro-Altimeter Error

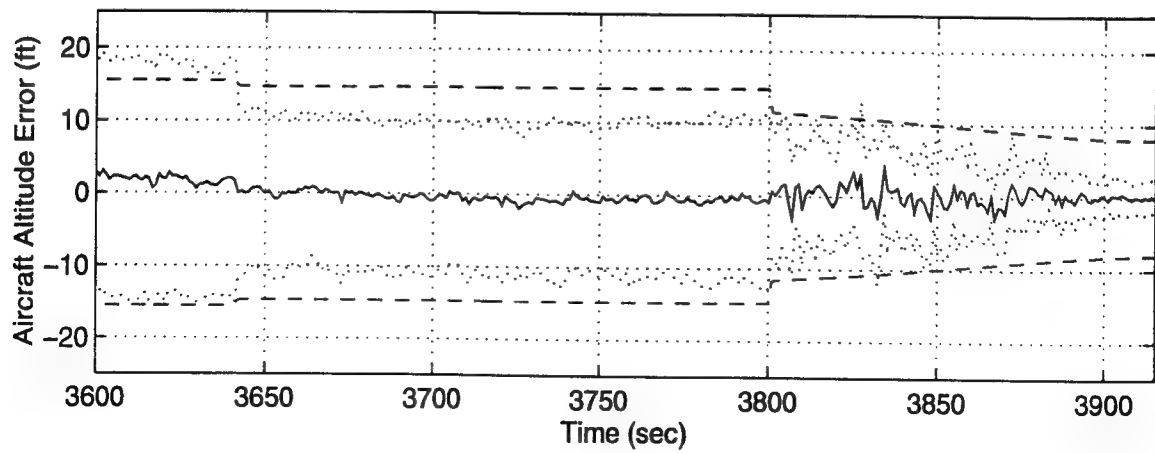
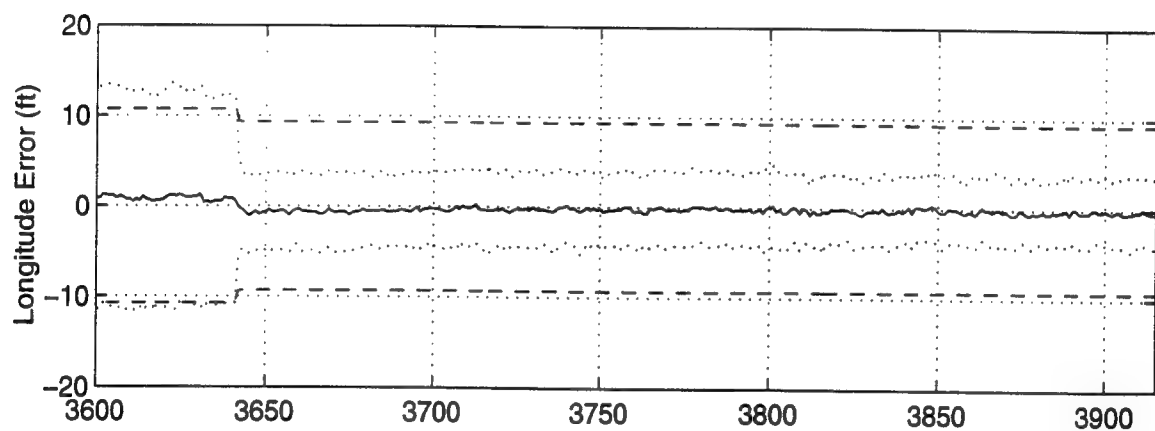
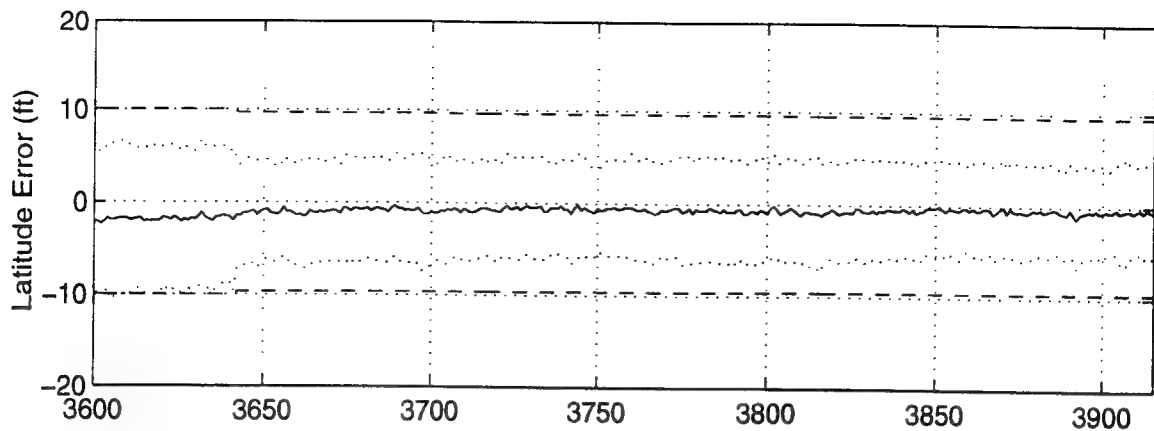


Figure S - 3 Latitude, Longitude and Aircraft Altitude Error

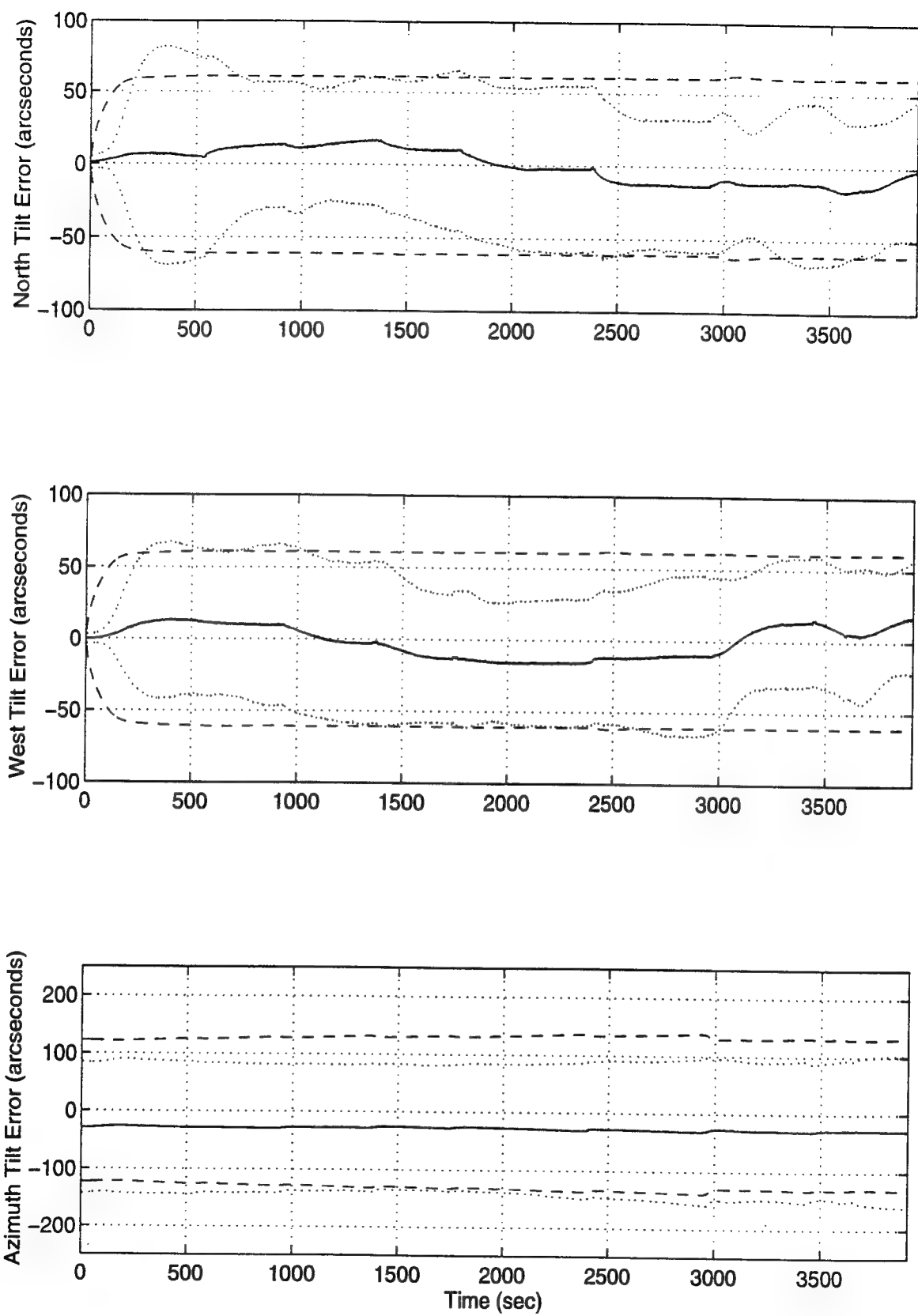


Figure S - 4 North, West and Azimuth Tilt Errors

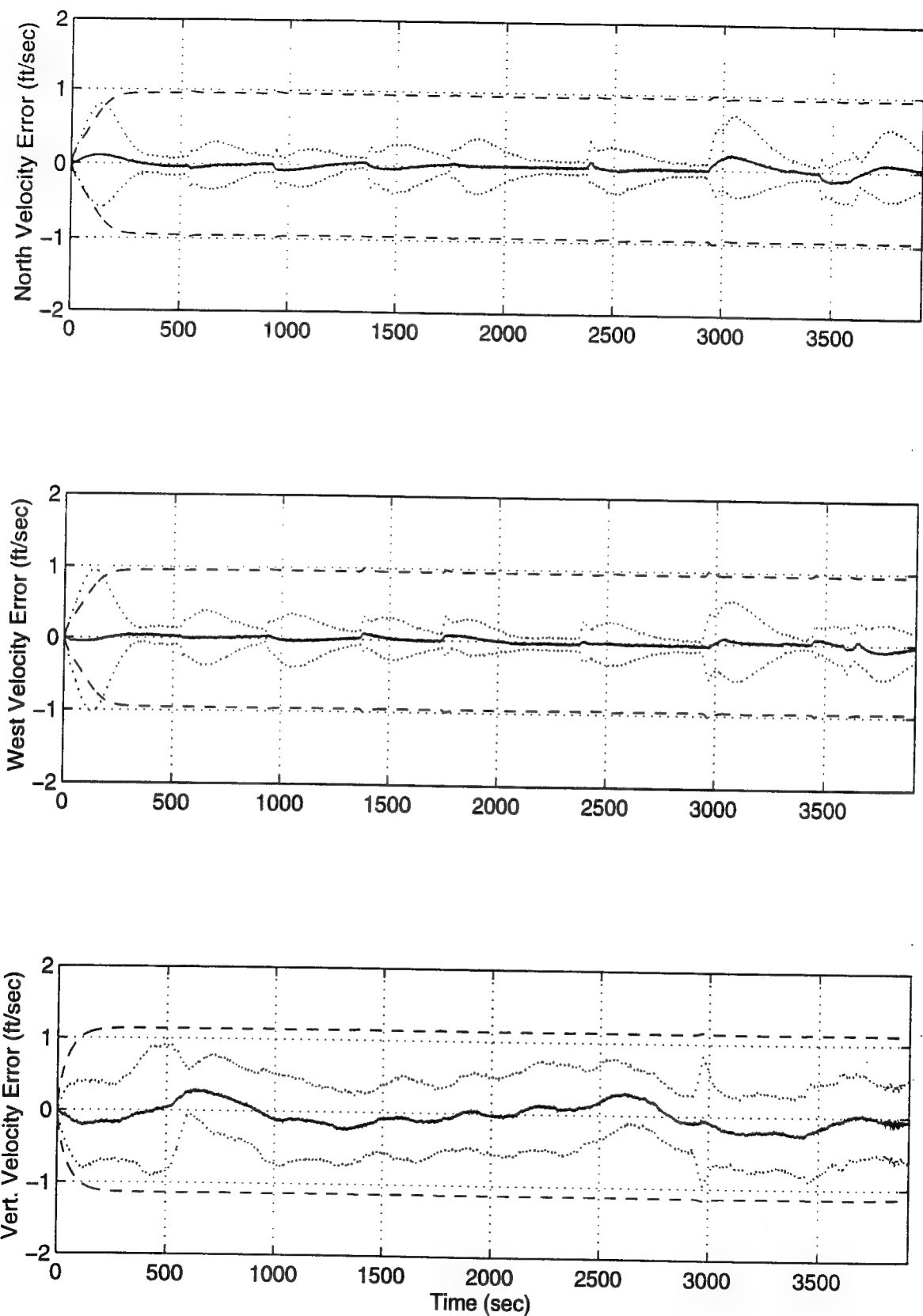


Figure S - 5 North, West and Vertical Velocity Errors

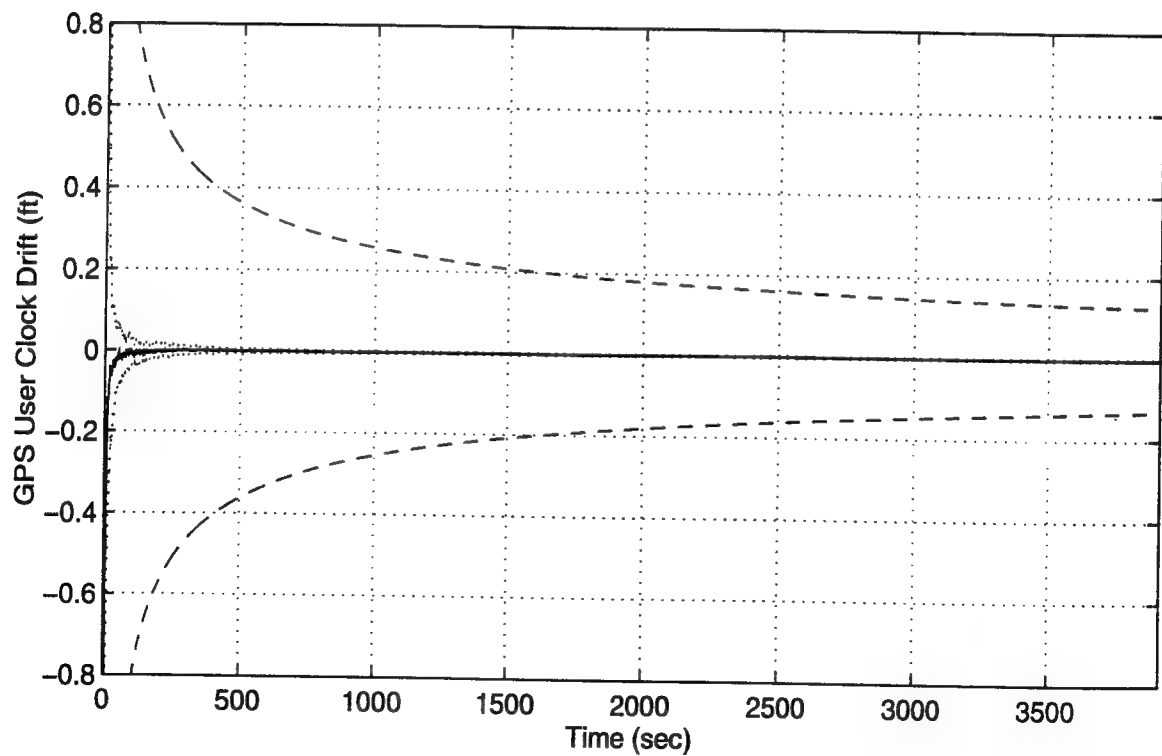
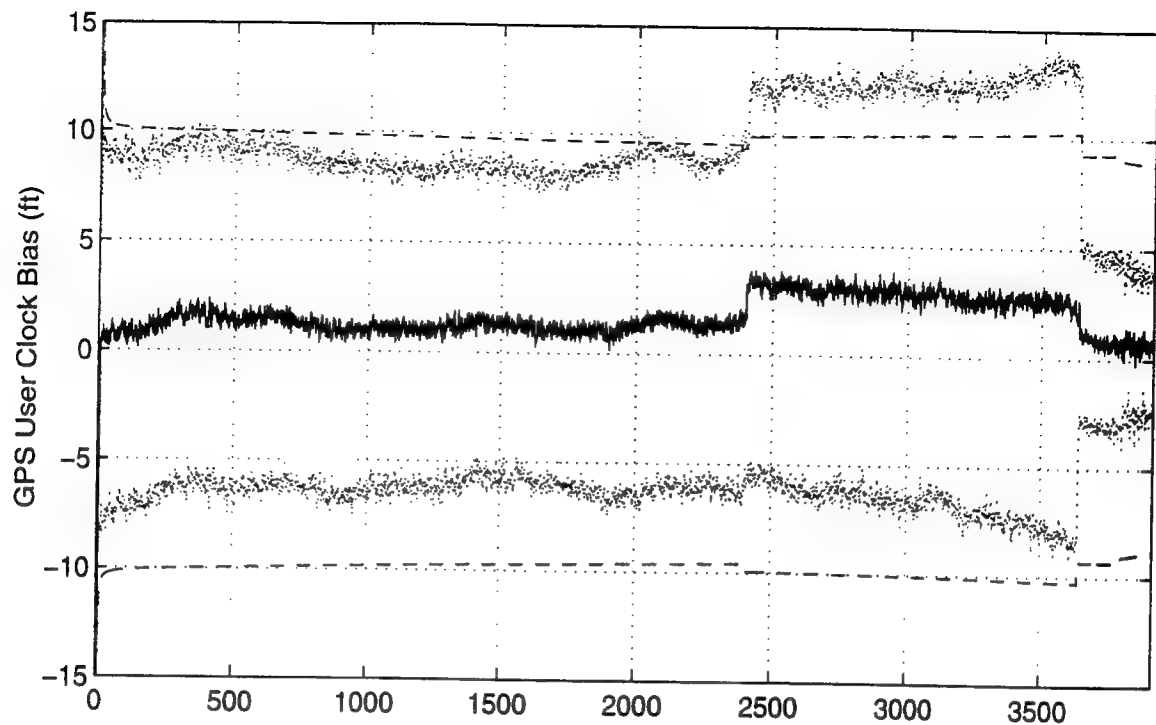


Figure S - 6 GPS User Clock Bias and GPS User Clock Drift

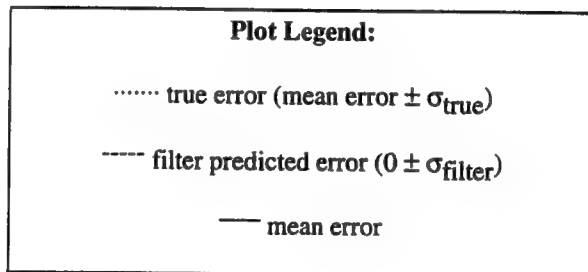
Appendix T

Plots of Cases XIII, XIV and XV: Barometric Altimeter, 0.4 nm/hr, 2.0 nm/hr and 4.0 nm/hr INS, P-Code GPS Using the Tanker Flight Profile with A Single GPS Outage.

Note that all three filters seem to believe the GPS clock bias error will blow-up during an outage, while the true GPS clock bias error seems to stay unchanged due to it being modeled as a random constant bias in the GPS truth model.

INS plot order for Figures T - 1 to T - 12 is as follows:

- 0.4 nm/hr (top plot)
- 2.0 nm/hr (middle plot)
- 4.0 nm/hr (bottom plot)



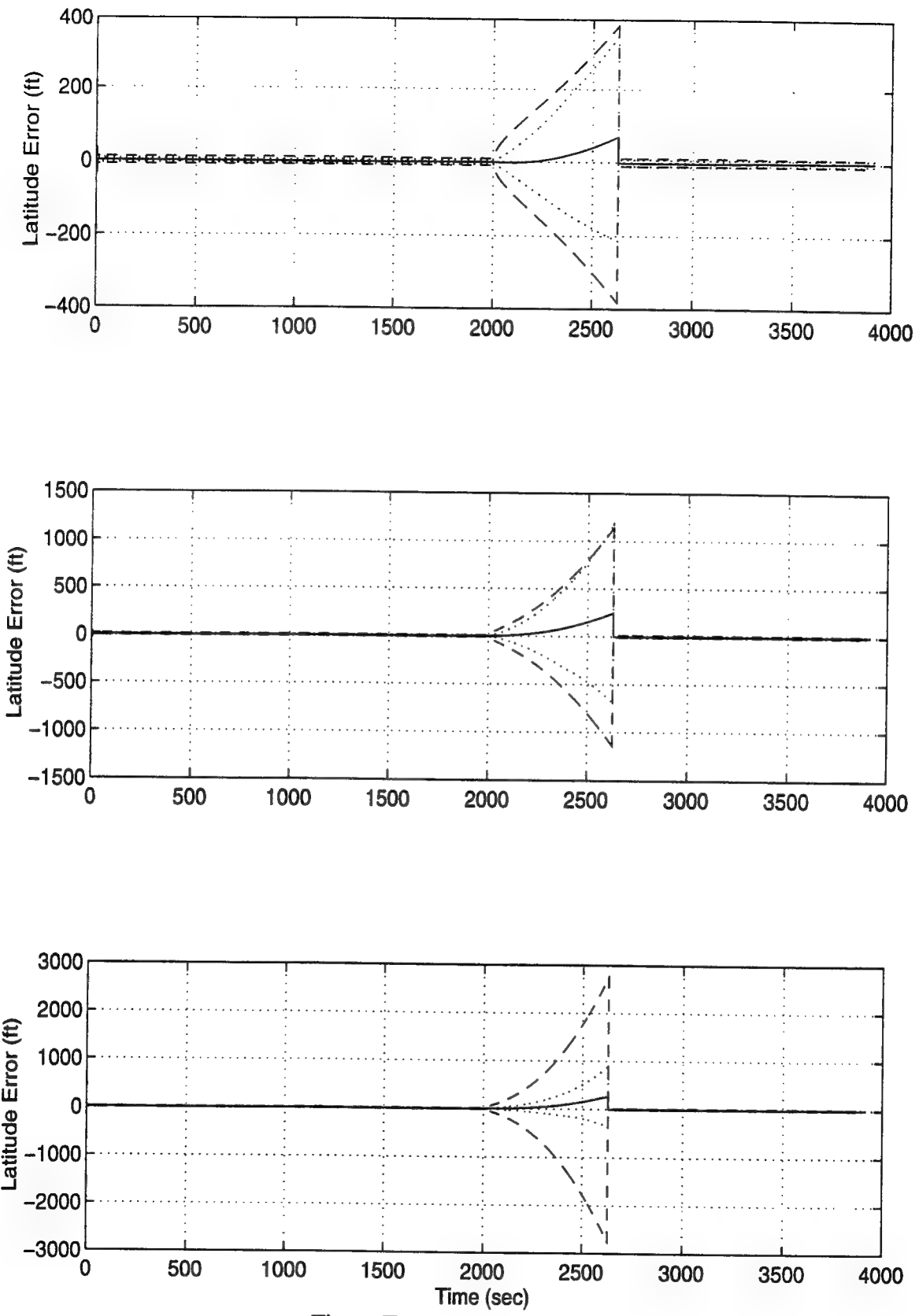


Figure T - 1. Latitude Error

T-2

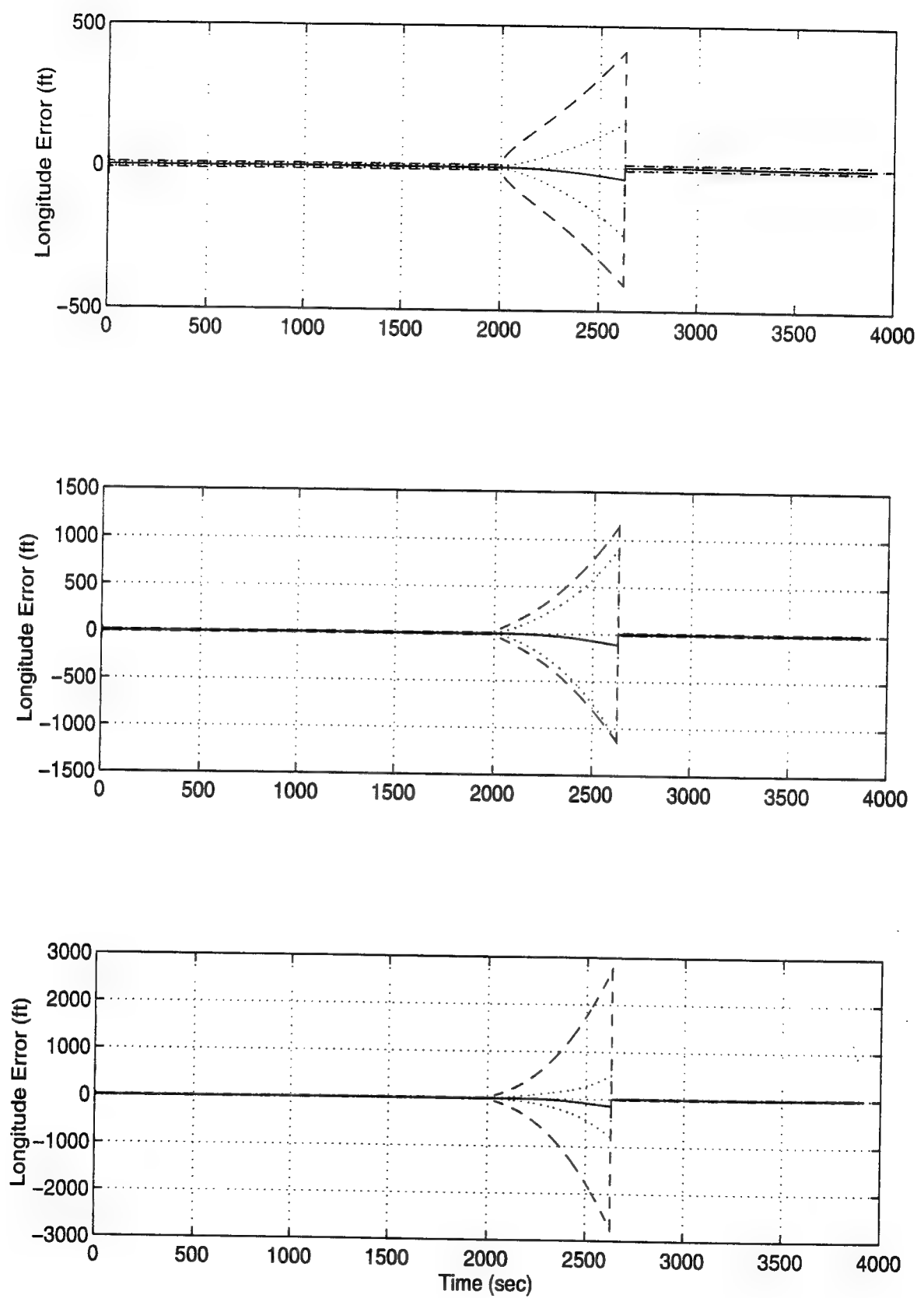


Figure T - 2. Longitude Error

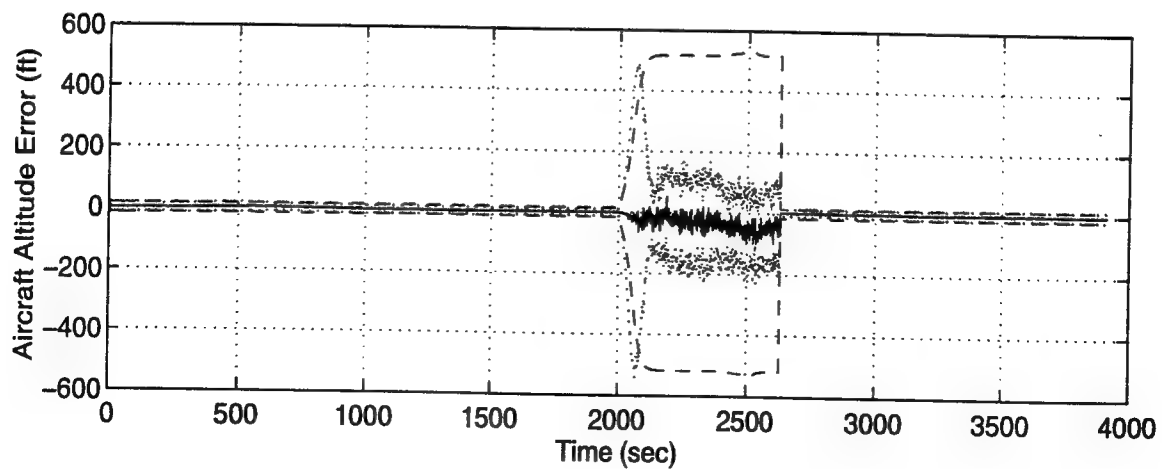
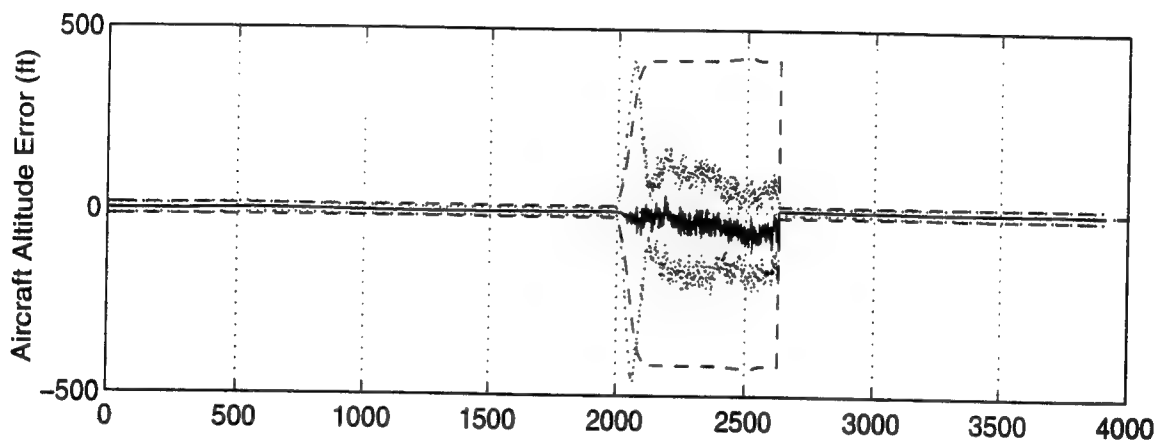
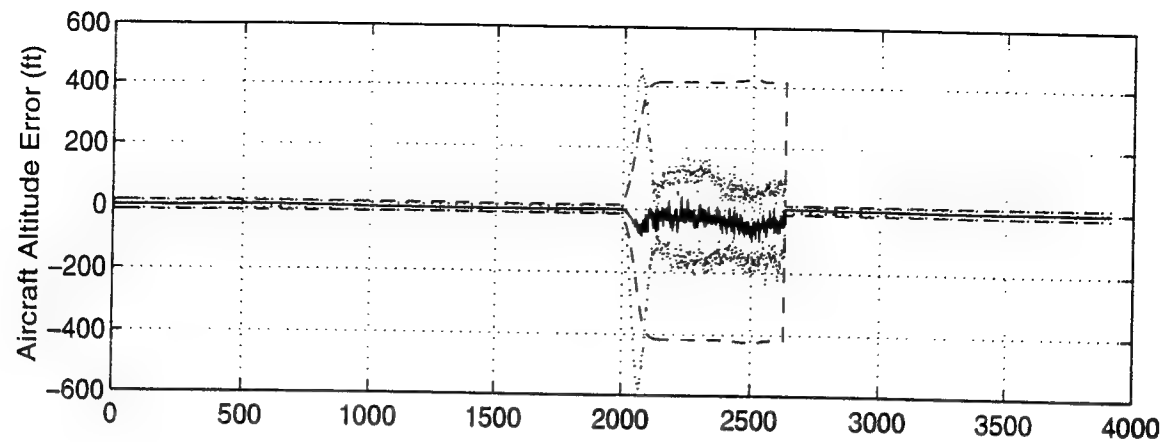


Figure T - 3. Aircraft Altitude Error

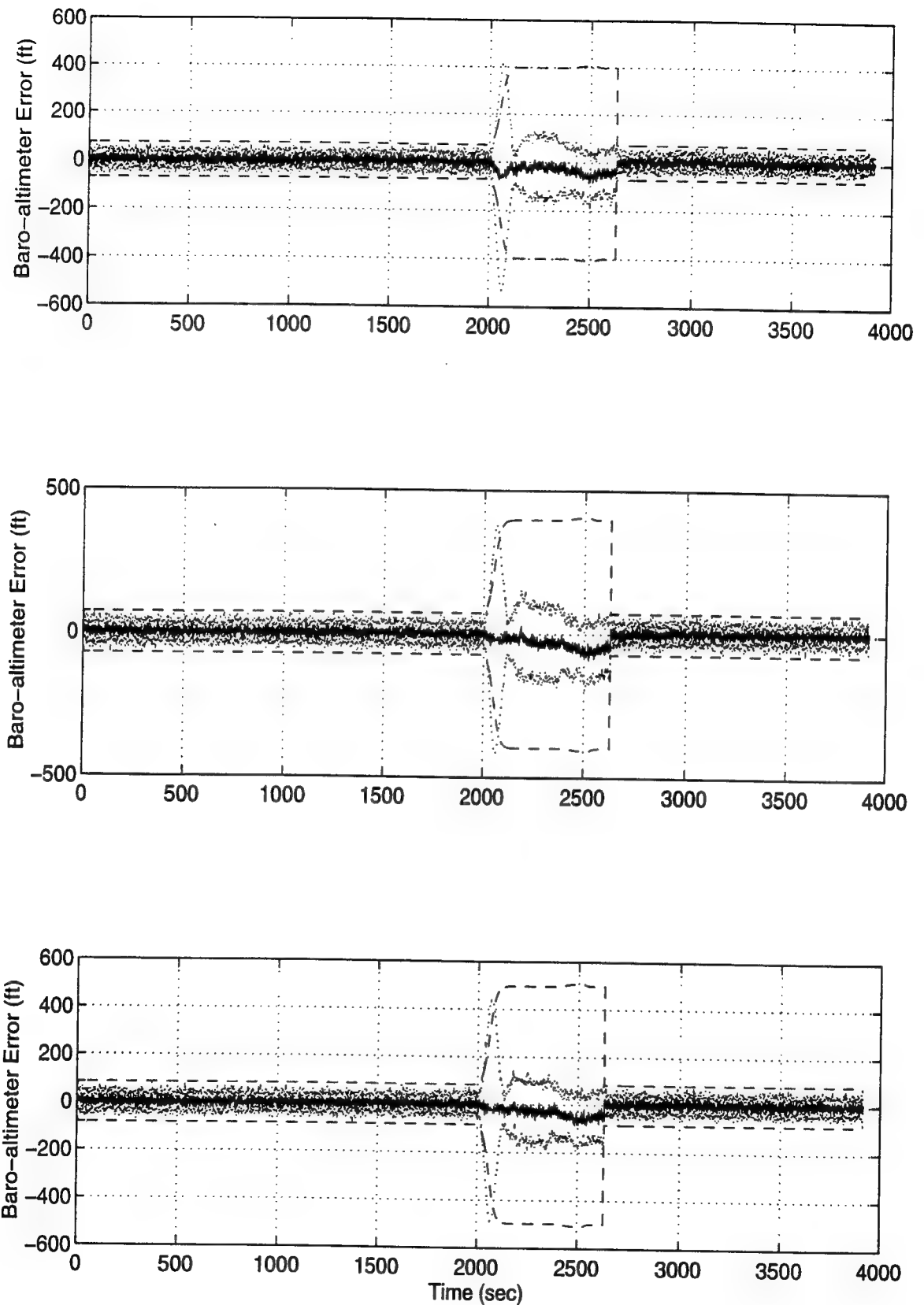


Figure T - 4. Baro-Altimeter Error

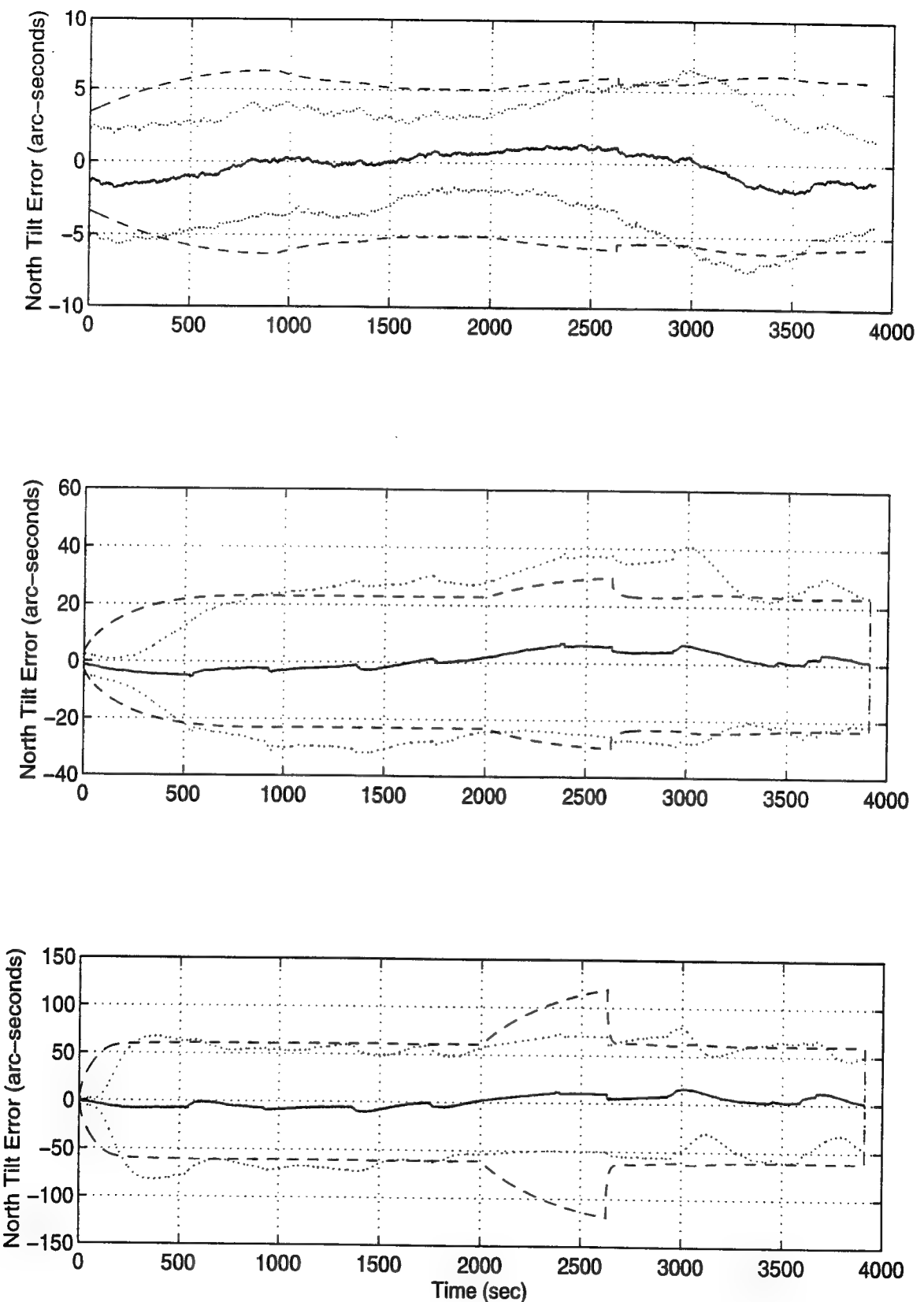


Figure T - 5 North Tilt Errors

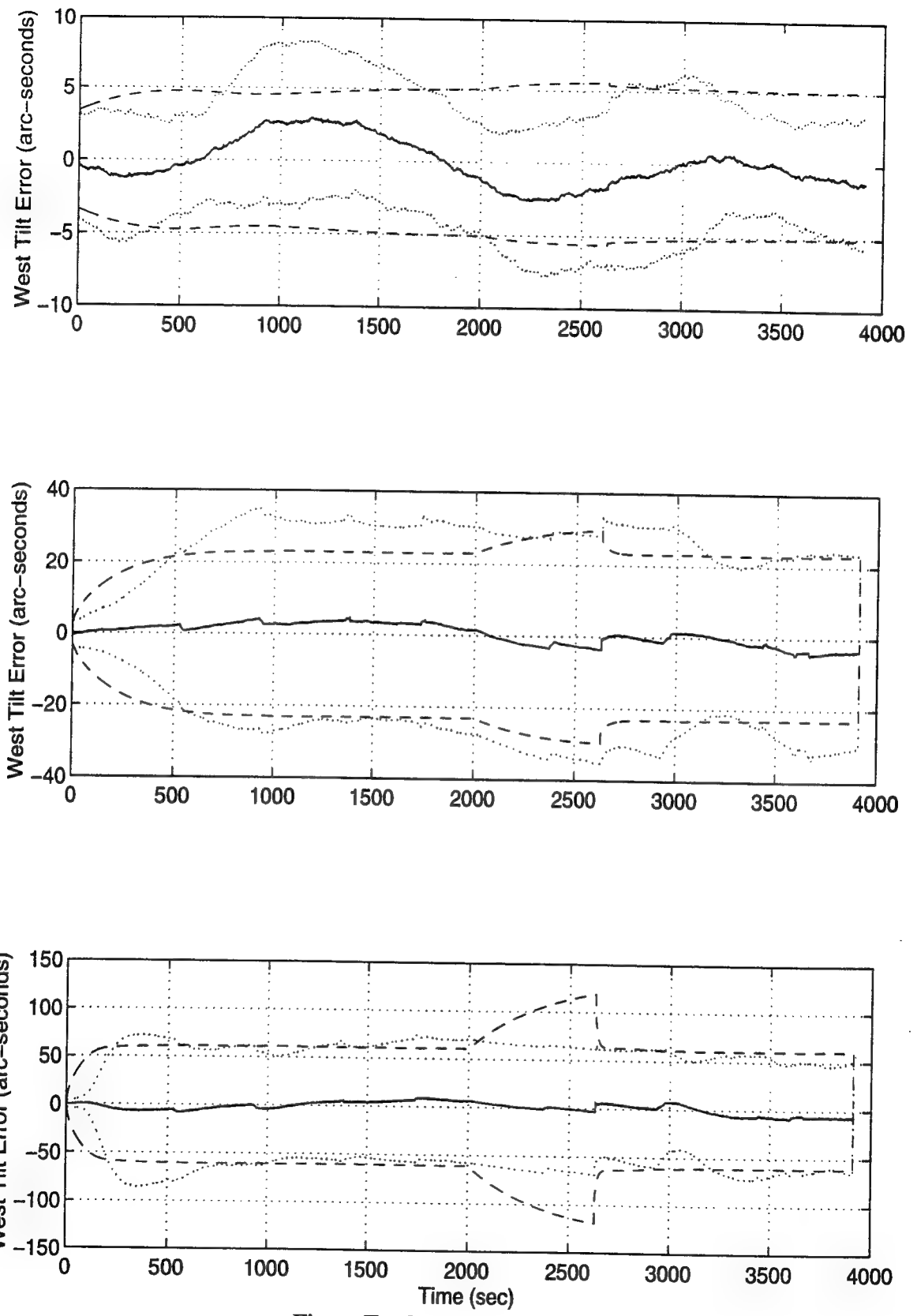


Figure T - 6 West Tilt Errors

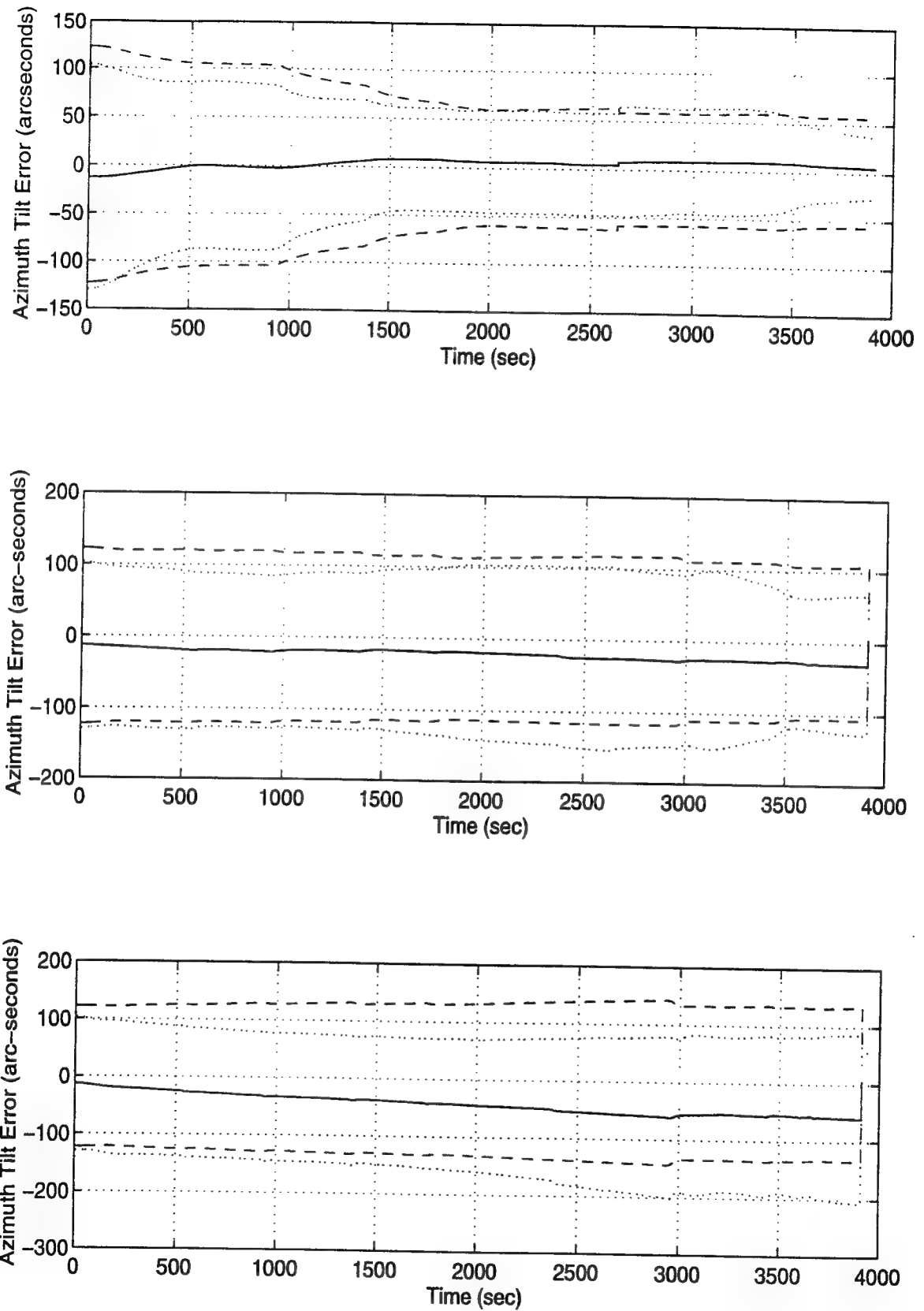


Figure T - 7 Azimuth Tilt Errors

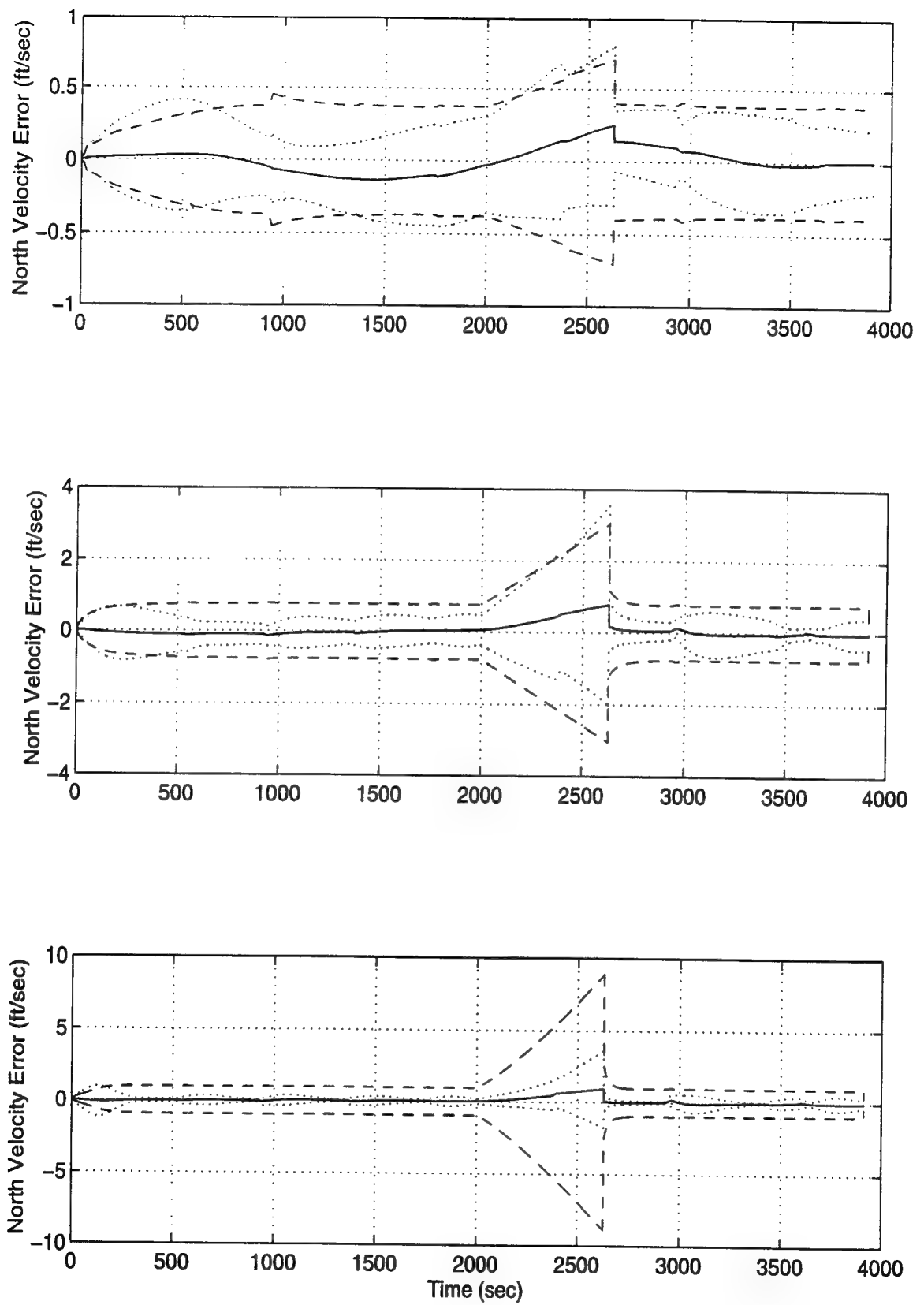


Figure T - 8 North Velocity Errors

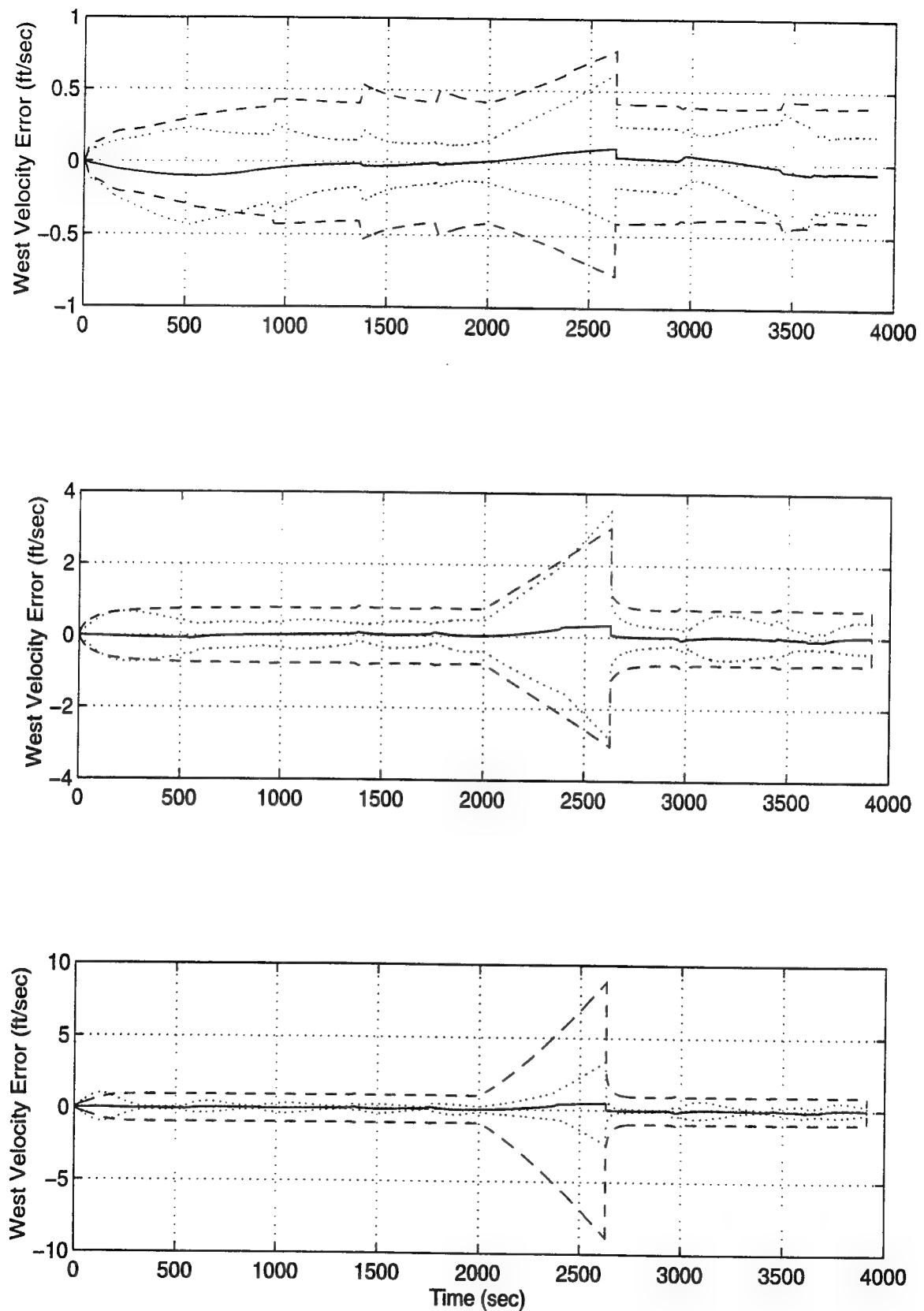


Figure T - 9 West Velocity Errors

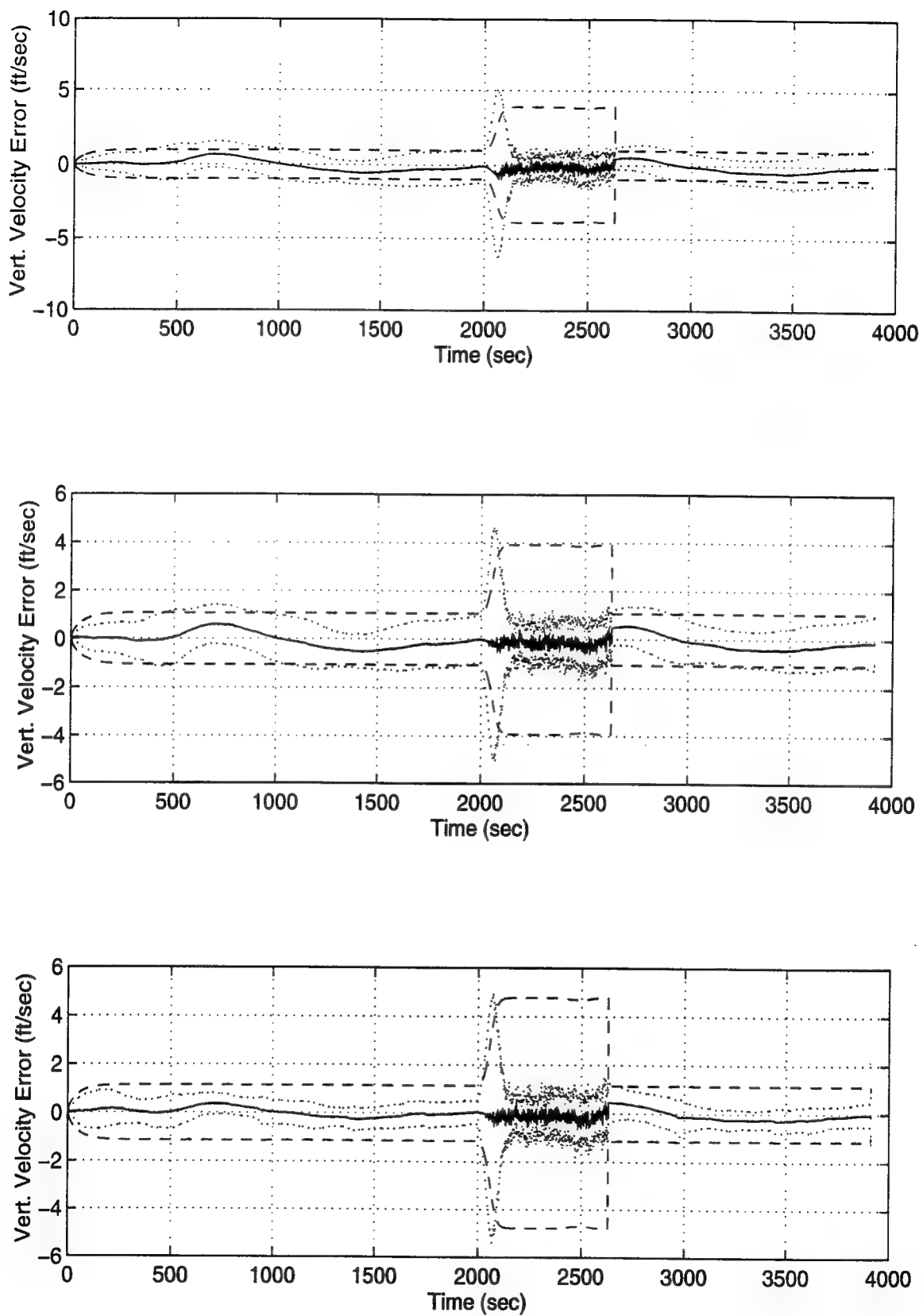


Figure T - 10 Vertical Velocity Errors

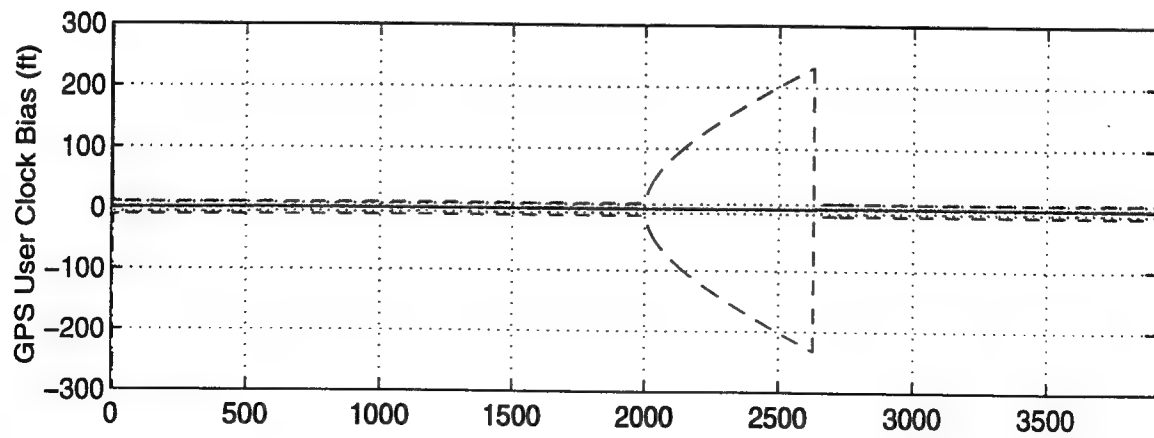
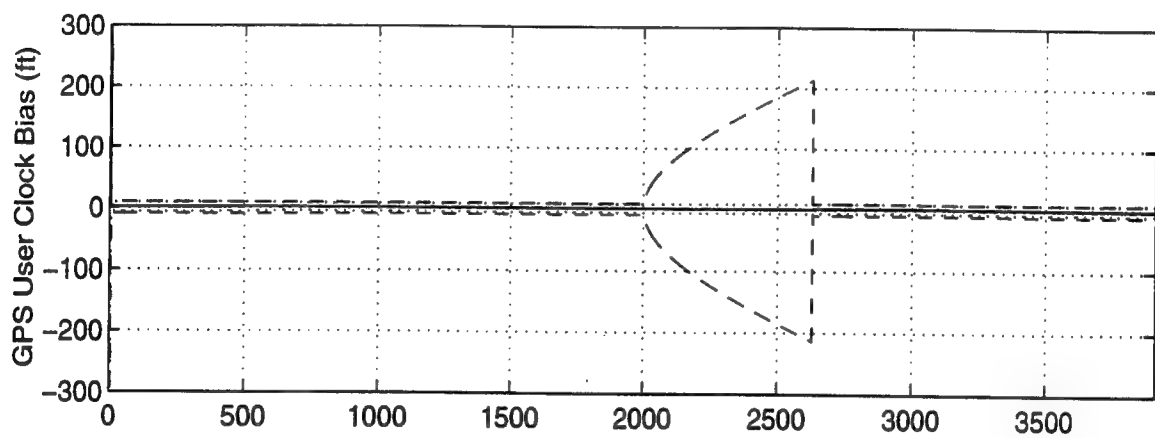
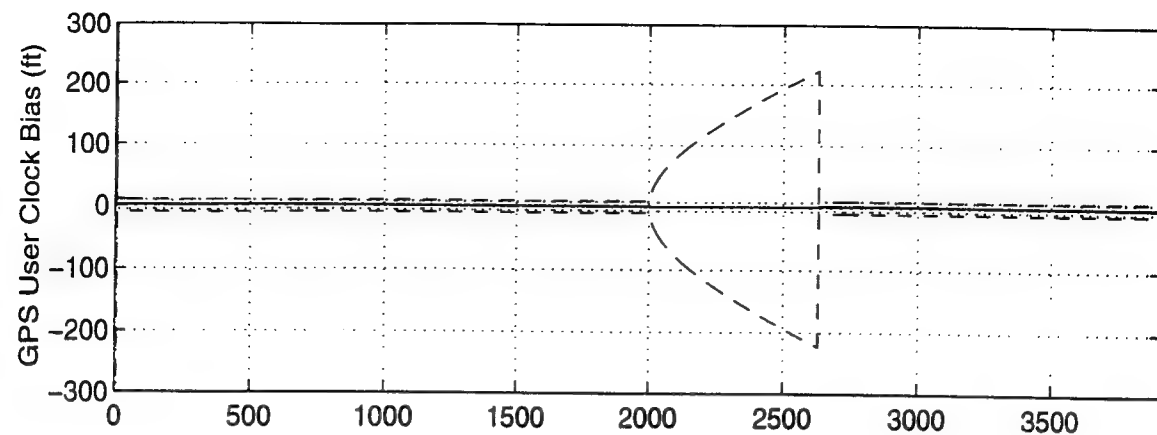


Figure T - 11 GPS User Clock Bias Error

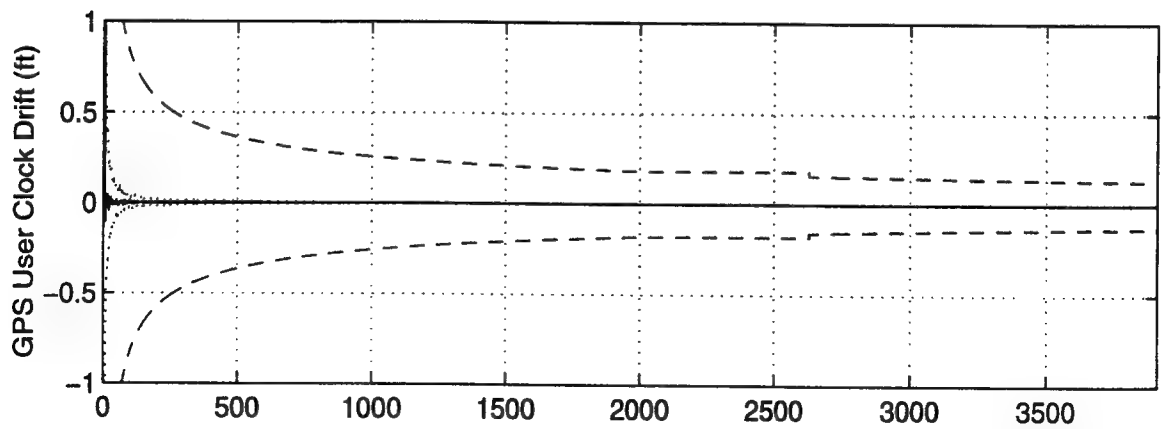
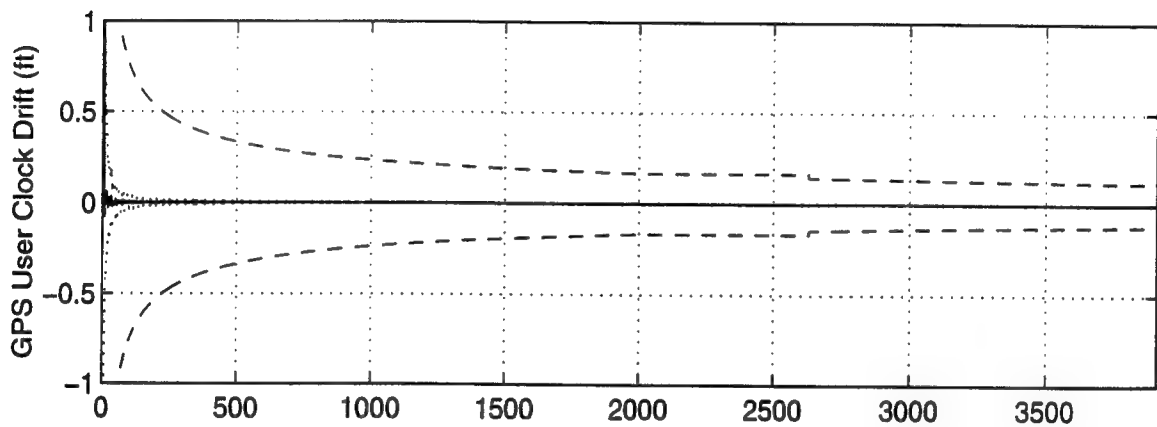
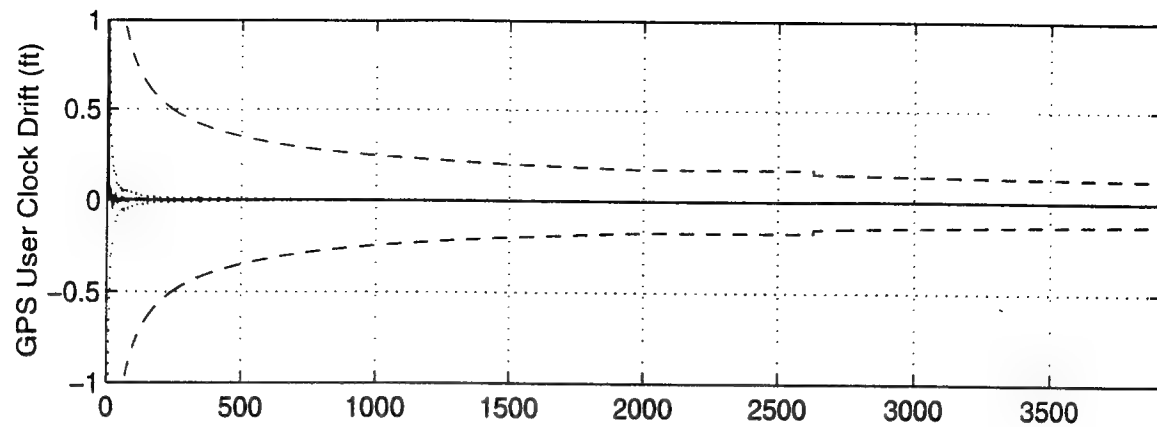
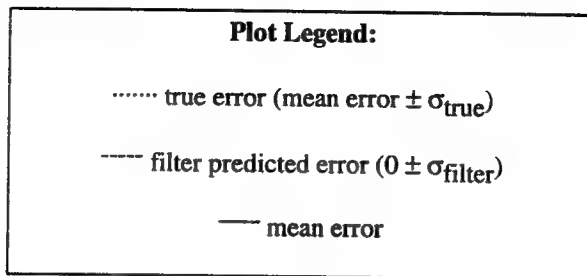


Figure T - 12 GPS User Clock Drift Error

Appendix U

Plots of Case XVI: Barometric Altimeter, 4.0 nm/hr INS, P-Code GPS, Single Pseudolite and Radar Altimeter Using the Tanker Flight Profile with Two GPS Outages.



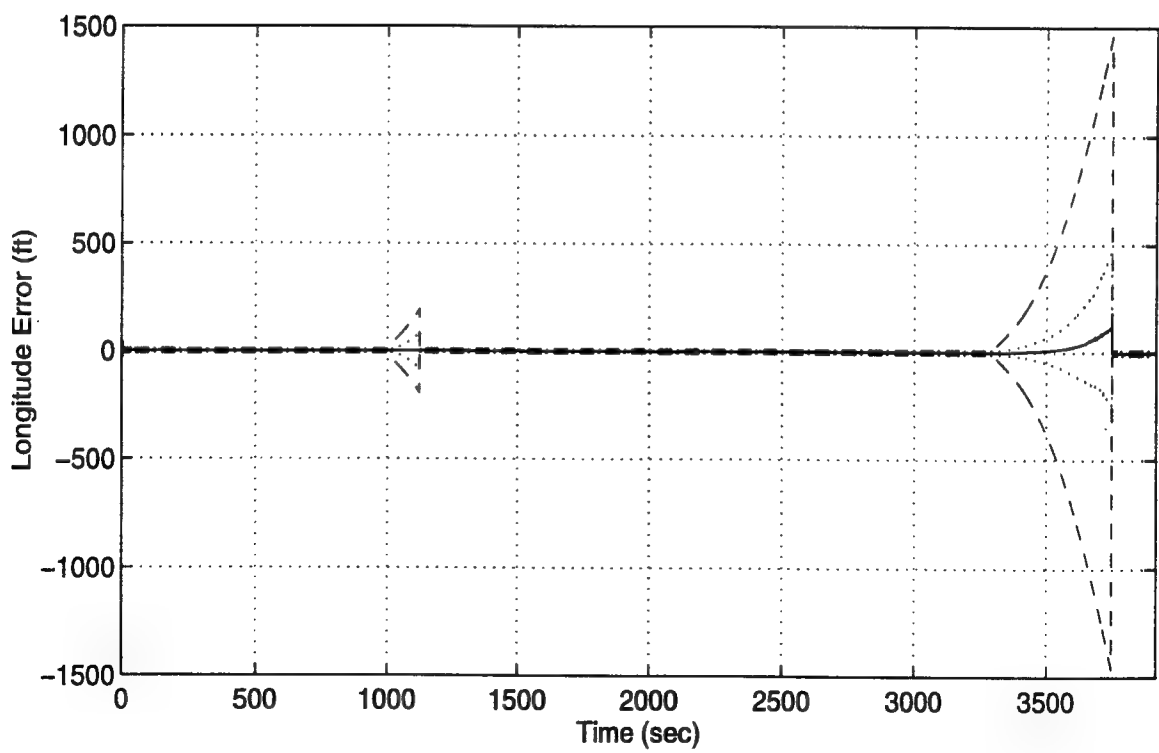
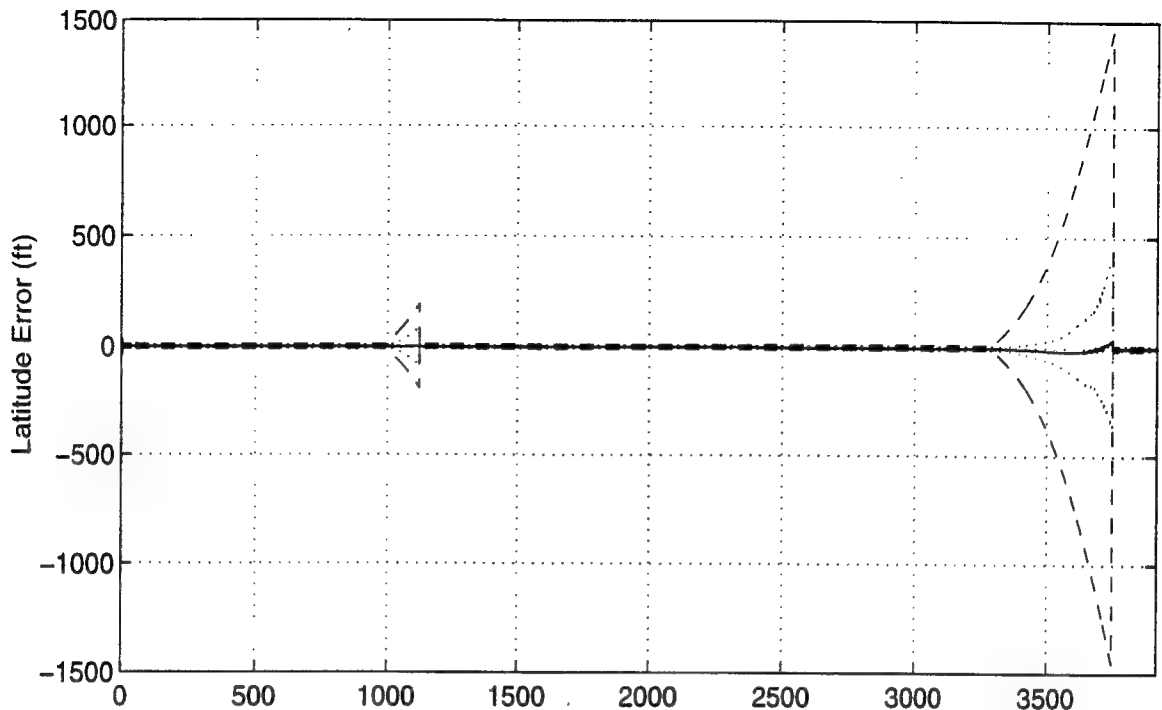


Figure U - 1. Latitude and Longitude Error

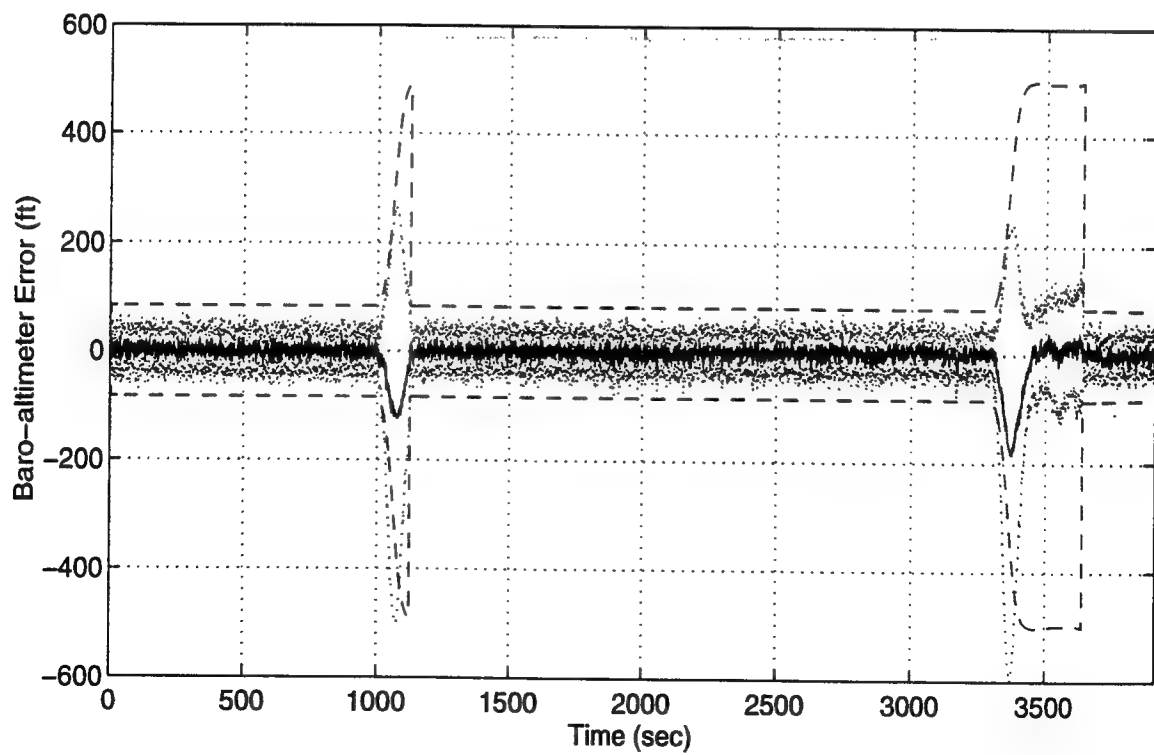
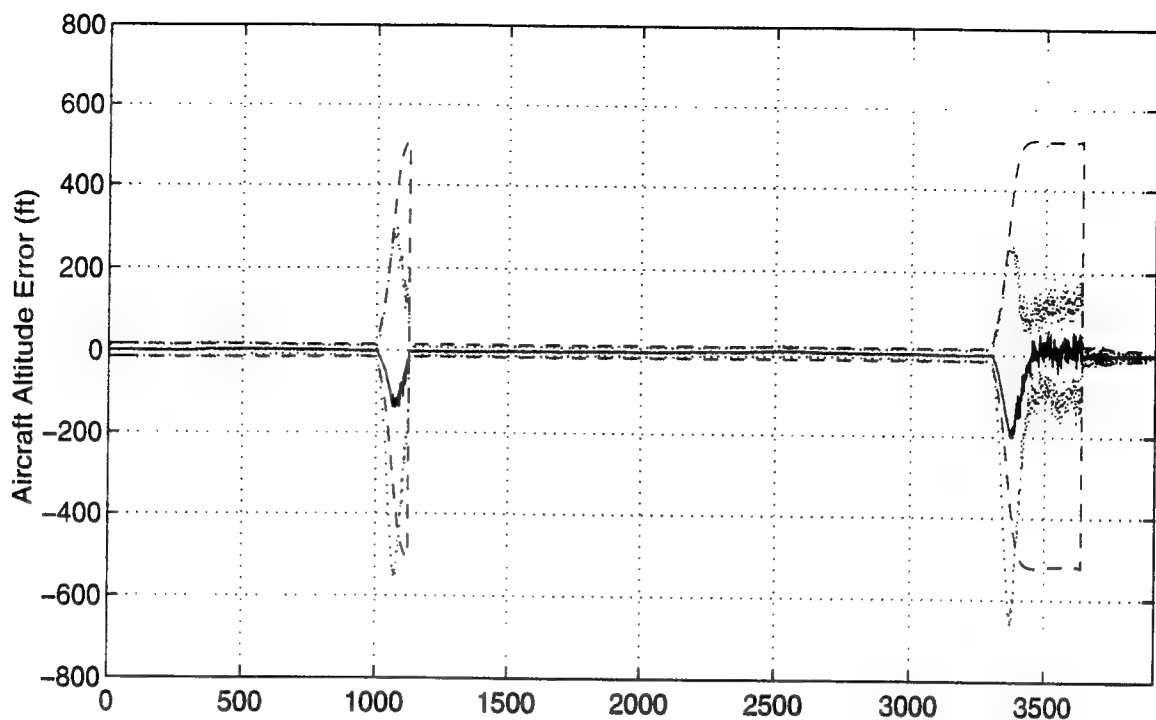


Figure U - 2. Aircraft Altitude and Baro-Altimeter Error

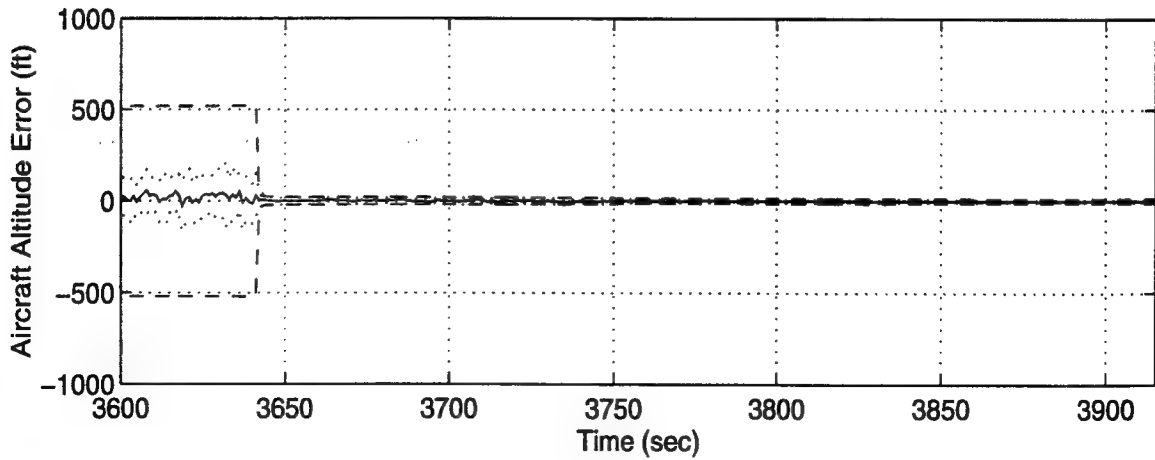
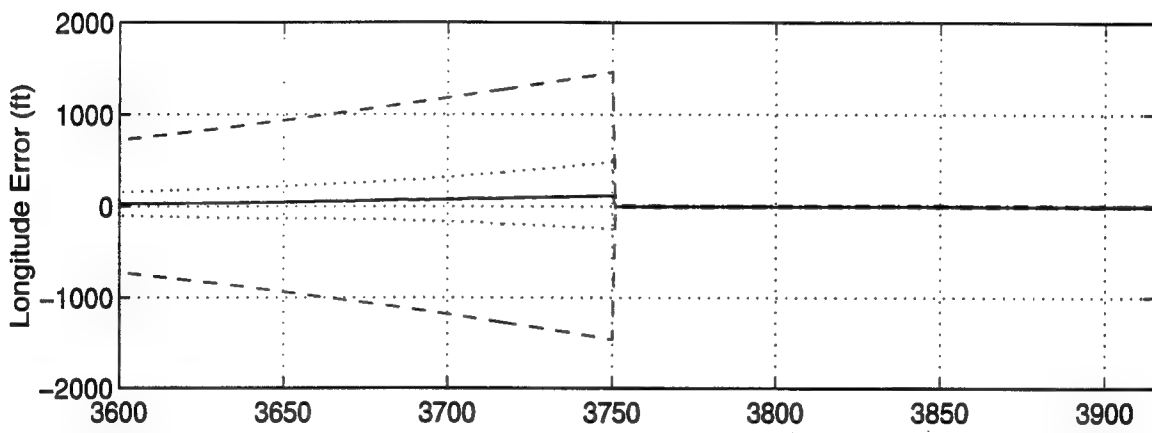
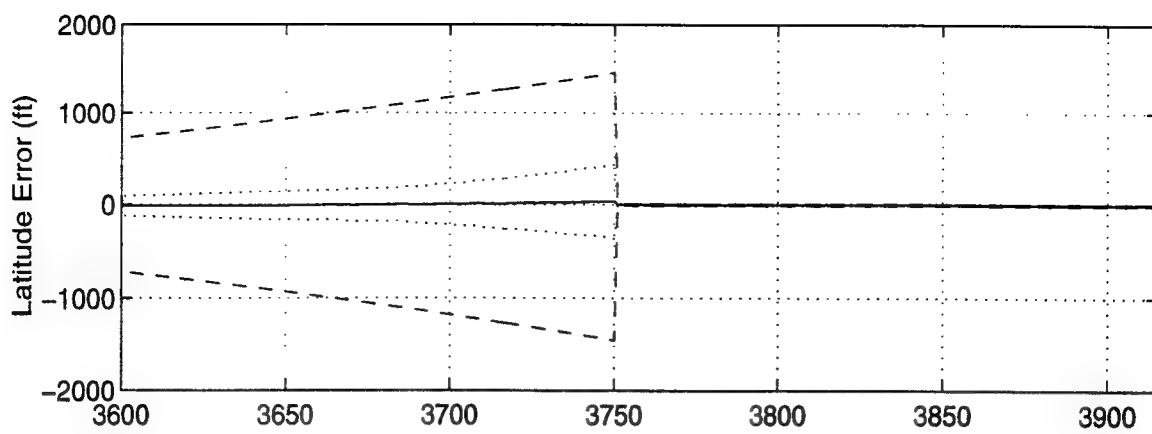


Figure U - 3 Latitude, Longitude and Aircraft Altitude Error

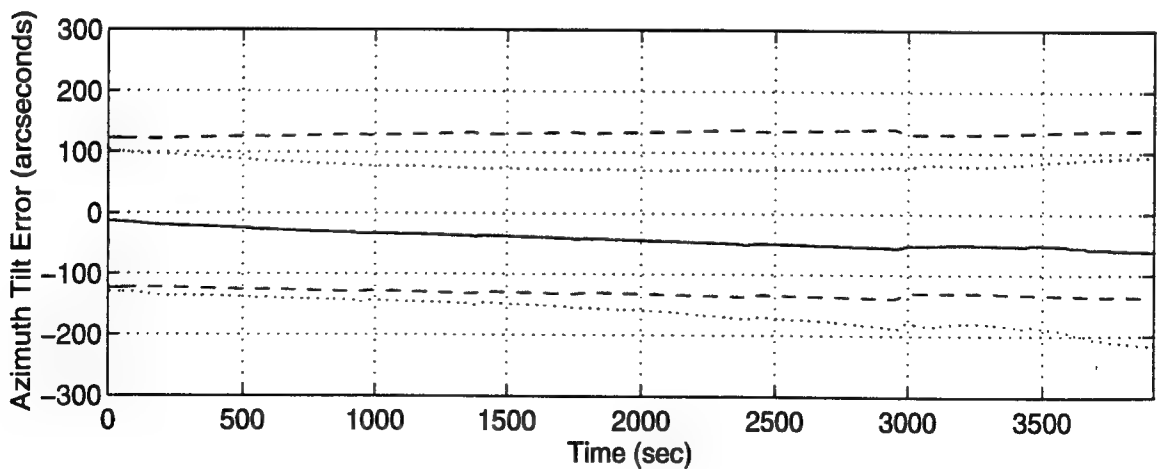
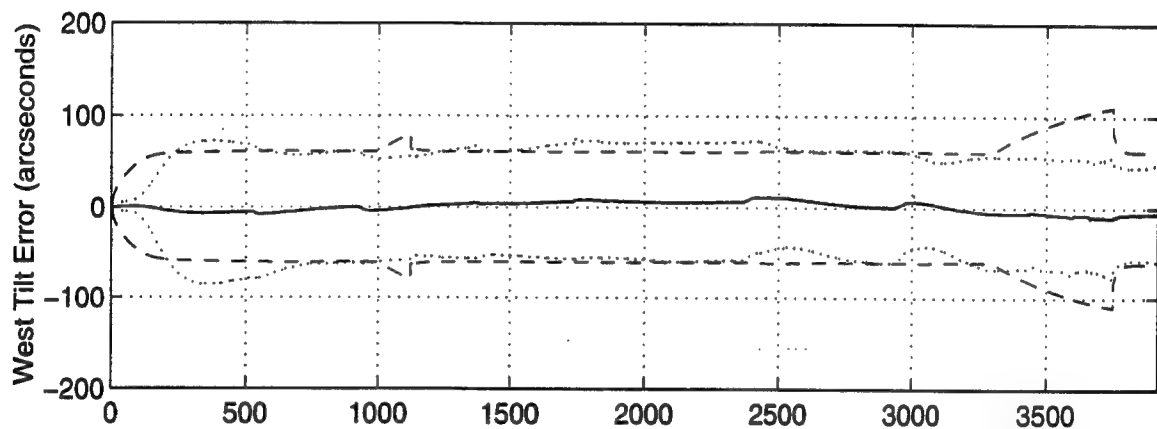
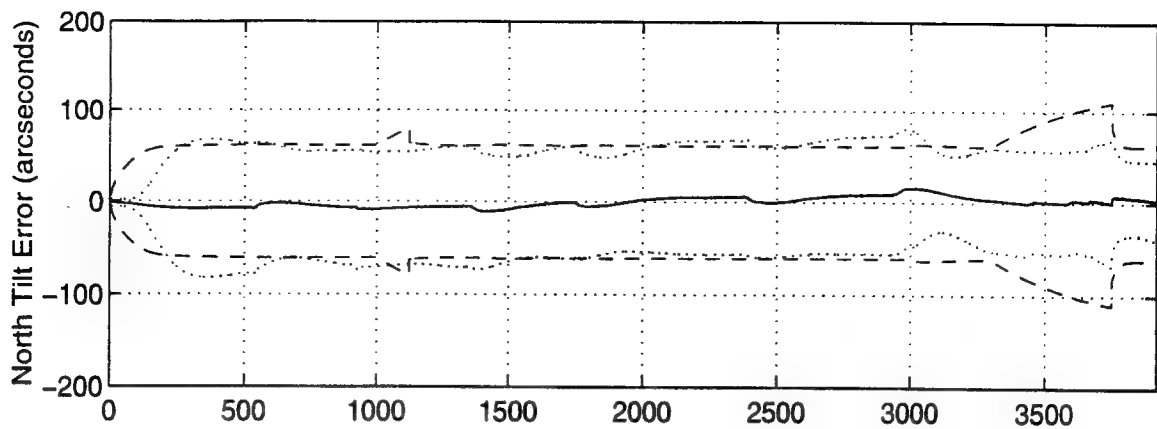


Figure U - 4 North, West and Azimuth Tilt Errors

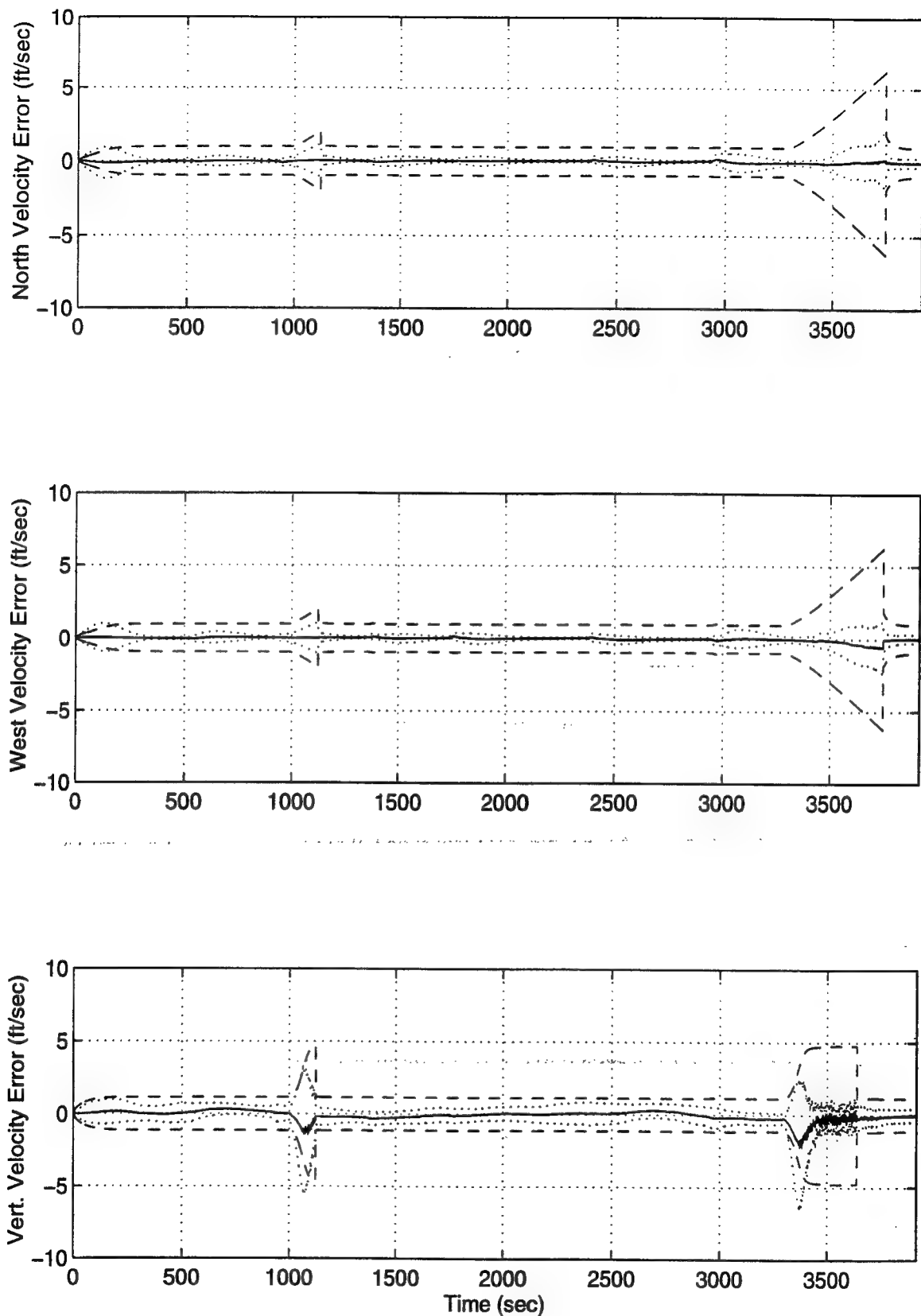


Figure U - 5 North, West and Vertical Velocity Errors

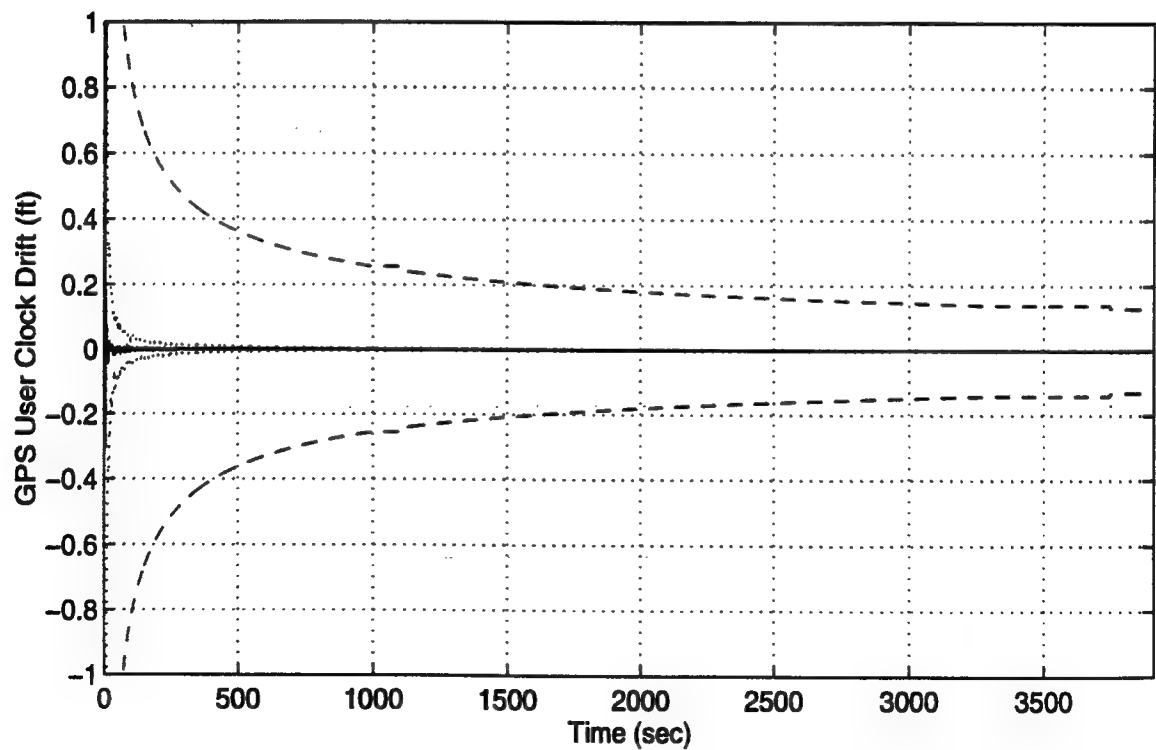
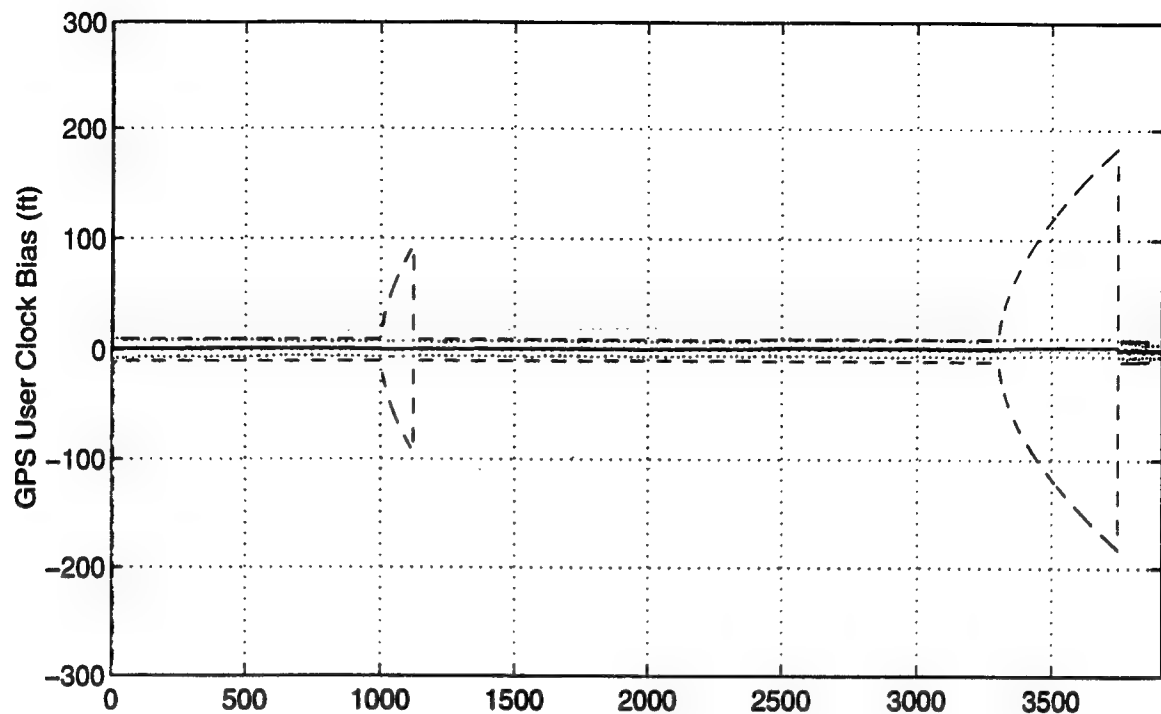


Figure U - 6 GPS User Clock Bias and GPS User Clock Drift

Bibliography

1. Aeronautical Systems Division, AFSC. *Specification for USAF Standard Form, Fit and Function (F3) Medium Accuracy Inertial Navigation Unit, F-16 Aircraft Application.* SNU84-1/F-16, Revision A, Change Notice 1, Wright-Patterson AFB, OH, 20 Aug 1991.
2. Alexander, Frank, Assistant Director of Flight Operations, Northwest Airlines, St. Paul, MN. Personal Correspondence. 12 September 1993.
3. Bagley, Daniel T. *GPS/INS Integration for Improved Aircraft Attitude Estimates.* MS Thesis, AFIT/GE/ENG/91D-04. School of Engineering, Air Force Institute of Technology, Wright-Patterson AFB OH, December 1992 (AD-A243947).
4. Blair, Lt Col Jesse (USAF retired). KC-135 Pilot, 121st Air Refueling Squadron, Rickenbaker ANG, OH, Personal Interview. August 1994.
5. Blomenhofer, Helmut, and others, "On-The-Fly Carrier-Phase Ambiguity Resolution for Precise Aircraft Landing," *Proceeding of the ION GPS-93 Sixth International Technical Meeting of the Satellite Division*, Salt Lake City, UT: 821-830 (22-24 Sep 93).
6. Bohenek, Brian J. *The Enhanced Performance of an Integrated Navigation System in a Highly Dynamic Environment.* MS Thesis, AFIT/GE/ENG/94D-01. School of Engineering, Air Force Institute of Technology, Wright-Patterson AFB, OH, December 1994.
7. Bose, Sam C. *Five Day Short Course on Inertial Navigation Systems (INS/GPS): Sensors, Systems, Mechanizations, Algorithms, Error Models, Kalman Filtering, System Analysis, Multisensor Integration, Sensor and System Testing with a Unified Treatment of the Similarities and Differences Between Gimbaled and Strapdown and Case Studies of Vertical Channel Stabilization and GPS/INS Kalman Integration.* Course Notes. Technalytics., Canoga Park, CA, 91303, 1994.
8. Bowditch, Nathaniel, LL.D., *American Practical Navigator*, Defense Mapping Agency/Topographic Center, Volume I, 1984.
9. Britting, Kenneth R. *Inertial Navigation Systems Analysis.* New York: Wiley-Interscience, 1971.
10. Burlinton, Richard Stevens, and Donald Curtis May. *Handbook of Probability and Statistics with Tables*, Handbook Publishers, Inc., Sandusky, OH, 1958.

11. Cohen, Clark. Avionics Research Engineer, Department of Aeronautics and Astronautics, Stanford University. Telephone Interview. November 1994.
12. Cohen, Clark, and others, "Real-Time Flight Test Evaluation of the GPS Marker Beacon Concept for Category III Kinematic GPS Precision Landing", *Proceeding of the ION GPS-93 Sixth International Technical Meeting of the Satellite Division*, Salt Lake City, UT: 841-849 (22-24 Sep 93).
13. Collins Government Avionics Division. Computer Program Product Specification for the GPS Radio Receiver R-2332D (RCVR 3-A) of the User Equipment Segment, NAVSTAR Global Positioning System. Part I of II, Code Ident: 13499, CP-RCVR-3010, Rockwell International Corporation, Cedar Rapids, IO, 9 January 1990.
14. Defense Mapping Agency. Department of Defense World Geodetic System 1984. DMA Technical Report, DMA TR 8350.2, 30 Sep 1987.
15. Department of Defense. *Flight Information Publication, (Terminal) Low Altitude United States Airport Diagrams, Instrument Approach Procedures*. Volume 8, Pages 339-340. 28 April 94.
16. Department of the Air Force. *Flying Training: Instrument Flying*. AFM 51-37. Washington: HQ USAF, 15 July 1986.
17. Department of the Air Force. *NAVSTAR GPS USER EQUIPMENT*. MZI0298.001, US Air Force Space Systems Division, NAVSTAR-GPS Joint Program Office, Los Angeles, CA. February 1991.
18. Department of the Air Force. *Single-Location User, System Effectiveness Model Demonstration Software (Version 3.6) Reference Manual*, Joint Program Office, Directorate of Systems Engineering, Los Angeles CA. March 1990.
19. Department of Transportation. *Automatic Landing Systems*, Federal Aviation Administration, AC 20-57A, Washington, D.C., 12 Jan. 1971.
20. Department of Transportation. *Engineering and Operational Issues Associated with the Application of Satellite-Based Navigation to Precision Approach and Landing*, Revision A, NAS System Engineering Service, Washington, D.C.: Federal Aviation Administration, February, 1992.
21. Department of Transportation. *FAA Satellite Navigation Program Master Plan, FY 93-98*. Washington, D.C.: Federal Aviation Administration, February 15, 1993.

22. Department of Transportation. *FAR-AIM (Federal Aviation Regulations and Airman's Information Manual) Part 1*, Aviation Supplies & Academics, Inc., Renton, WA., 1993.
23. Department of Transportation. *Federal Aviation Administration (FAA) Satellite Navigation Program Master Plan, ARD-70, FY 93-98*, Projected Civil Aviation GPS Operational Implementation Schedule, Washington, D.C.: Federal Aviation Administration, 15 Feb 93.
24. Department of Transportation. *Global Positioning System Information Center (GPSIC) Users Manual*. Bulletin Board Phone Number: (703) 313-5910. United States Coast Guard, Alexandria, VA, September 1992.
25. Farrel, James L. *Integrated Aircraft Navigation*. New York: Academic Press, 1976.
26. Gu, Xiaogang, "DGPS Positioning Using Carrier-Phase for Precision Navigation", *Proceedings of the Institute of Navigation 1994 National Technical Meeting*, San Diego, CA: 410-417 (24-26 Jan 94).
27. Hansen, Neil P. *Incorporation of Carrier-Phase Global Positioning System Measurements into the Navigation Reference System for Improved Performance*. MS Thesis, AFIT/GE/ENG/93D-40. School of Engineering, Air Force Institute of Technology, Wright-Patterson AFB OH, December 1993 (AD-A274136).
28. Honeywell Military Avionics Division. *Honeywell AN/APN-194 Pulse Radar Altimeter System*. Honeywell Technical Description, Minneapolis: June 1989.
29. Honeywell Military Avionics Division. *Ring Laser Gyro*. Honeywell LaserReady News, Vol 90, Number 2. 1990.
30. Huangqi, Sun, and others, "An Investigation of Airborne GPS/INS for High Accuracy Position and Velocity Determination," *Proceedings of the Institute of Navigation 1994 National Technical Meeting*, San Diego, CA: 801-809 (24-26 Jan 94).
31. Ignagni, Mario. Avionics Engineer, Honeywell Commercial Avionics, Minneapolis, MN. Personal Correspondence. May 1994.
32. Inertial Navigation System, STM 16-829 Vol I & II, *F-16 Block 40 Configuration, Training Manual*, General Dynamics, FortWorth, TX: 10 Jun 90.
33. Institute of Electrical and Electronics Engineers. *IEEE Standard Dictionary of Electrical and Electronics Terms*. IEEE Std 100-1972. New York.

34. Jacob, Thomas. "Landing System Using GPS/IMU System Integration," *Proceedings of the Institute of Navigation 1994 National Technical Meeting*, San Diego, CA: 298-305 (24-26 Jan 94).
35. Kalman, R.E., "A New Approach to Linear Filtering and Prediction Problems," *Transactions ASME, Series D: Journal of Basic Engineering*, 1960.
36. Kelly, Robert, and Jerry Davis, *RNP Tunnel Concept for Precision Approach and Landing*, RTCA, Inc., SC159 Working Group 4, MT/140, January 1993.
37. Knisely, Michael. Chief, Avionics Navigation Systems, F-16 System Program Office, ASC/YPVM, Wright-Patterson AFB, OH. Personal Interviews. 15 December, 1993.
38. Knudsen, L. *Performance Accuracy (Truth Model/Error Budget) Analysis for the LN-93 Inertial Navigation Unit*. Technical Report, Litton Guidance and Control Systems, Woodland Hills, CA: January 1985. DID No. DI-S-21433 B/T:CDRL No. 1002.
39. Martin, E.H. "GPS User Equipment Error Models," *The Institute of Navigation, Volume I*:109-118 (1980).
40. Maybeck, Peter S. *Stochastic Models, Estimation, and Control*. Volume 1. New York: Academic Press, Inc., 1979.
41. Maybeck, Peter S. *Stochastic Models, Estimation, and Control*. Volume 2. New York: Academic Press, Inc., 1982.
42. Maybeck, Peter S. *Stochastic Models, Estimation, and Control*. Volume 3. New York: Academic Press, Inc., 1982.
43. Meyer-Hilberg, Jochen, and Thomas Jacob. "High Accuracy Navigation and Landing System Using GPS/IMU System Integration," *IEEE Trans. Position Location and Navigation Symposium, Las Vegas*: 0-7803-1435-2/94, 298-305 (April 11-15, 1994).
44. Milliken, R.J., and C.J. Zoller. "Principle of Operation of NAVSTAR and System Characteristics," *Global Positioning System*, The Institute of Navigation, Volume I. Alexandria, VA 22314, 1980.
45. Mosle, William B. *Detection, Isolation, and Recovery of Failures in an Integrated Navigation System*. MS Thesis, AFIT/GE/ENG/93D-28. School of Engineering, Air Force Institute of Technology, Wright-Patterson AFB OH, December 1993 (AD-A274056).

46. Musick, Stanton H. Electronics Engineer, WL/AAAS-3, Air Force Avionics Laboratory, WPAFB, OH. Personal Conversations. August 1994.
47. Musick, Stanton H. *PROFGEN - A Computer Program for Generating Flight Profiles*. Technical Report, Air Force Avionics Laboratory, WPAFB, OH, November 1976. AFAL-TR-76-247, DTIC ADA034993.
48. Musick, Stanton H., and Neil Carlson. *User's Manual for a Multimode Simulation for Optimal Filter Evaluation (MSOFE)*. AFWAL-TR-88-1138, Wright-Patterson AFB OH: A.F. Avionics Laboratory, AFWAL/AARN-2, April 1990.
49. National Oceanic and Atmospheric Administration. *National Geodetic Survey GPS Orbital Formats*. National Geodetic Information Branch, Rockville, MD. August 1991.
50. Negast, William Joseph. *Incorporation of Differential Global Positioning System Measurements Using an Extended Kalman Filter for Improved Reference System Performance*. MS Thesis, AFIT/GE/ENG/91D-41. School of Engineering, Air Force Institute of Technology, Wright-Patterson AFB OH, December 1991 (AD-A243742).
51. Paielli, Russell, and others, "Carrier-Phase Differential GPS for Approach and Landing: Algorithms and Preliminary Results", *Proceeding of the ION GPS-93 Sixth International Technical Meeting of the Satellite Division*, Salt Lake City, UT: 831-840 (22-24 Sep 93).
52. Riggins, Lt Col Robert N., and Capt Ron Delap, . Assistant Professors of Electrical Engineering, Air Force Institute of Technology, Wright-Patterson AFB, OH. Course Notes EENG 534/635. 1993-94.
53. Rowson, Stephen V., and others, "Performance of Category IIIB Automatic Landings Using C/A Code Tracking Differential GPS," *Proceedings of the Institute of Navigation 1994 National Technical Meeting*, San Diego, CA: 759-767 (24-26 Jan 94).
54. Savage, Paul G. "Strapdown Sensors," *AGARD Lecture Series No. 95* (June 1978).
55. Scull, David, Director of Operations, The Institute of Navigation, 1800 Diagonal Road, Suite 480, Alexandria, VA 22314, Correspondence. 1 Aug 93.

56. Snodgrass, Faron Britt. *Continued Development and Analysis of a New Extended Kalman Filter for the Completely Integrated Reference Instrumentation System (CIRIS)*. MS Thesis, AFIT/GE/ENG/90M-5. School of Engineering, Air Force Institute of Technology (AU), Wright-Patterson AFB OH, March 1990 (AD-A220106).
57. Solomon, Capt Joseph , Research Scientist, Wright Laboratories, Wright-Patterson AFB, OH. Personal Interviews. April 1994 - November 1994.
58. Stacey, Richard D. *A Navigation Reference System (NRS) Using Global Positioning System (GPS) and Transponder Aiding*. MS Thesis, AFIT/GE/ENG/91M-04. School of Engineering, Air Force Institute of Technology, Wright-Patterson AFB OH, March 1991 (AD-A238890).
59. Sutcliffe, Don. Aeronautical Engineer, Boeing Military Aircraft Company. Wichita, KS. Telephone Conversation. August, 1994.
60. The MathWorks, Inc., 21 Elliot Street, Natick, MA 01760. *Matlab*. December 1992. Version 4.0a.
61. Thompson, Paul. Product Marketing, Litton Commercial Avionics. Washington DC. Telephone Conversation. March, 1994.
62. Unternaeher, Bill. Product Marketing, Honeywell Commercial Avionics. Pheonix, AZ. Telephone Conversation. April, 1994.
63. Urbanic, Robert J., and S.H. Musick, "Users' Manual for a Multimode Plotting Program (MPLOT)", Avionics Laboratory, WPAFB, OH, WRDC-TR-90-1077, to be published.
64. van Graas, Frank. Associate Professor of Electrical Engineering, Ohio University. Telephone Conversations. September 1994.
65. Vasquez, Juan R. *Detection of Spoofing, Jamming, or Failure of a Global Positioning System (GPS)*. MS Thesis, AFIT/GE/ENG/92D-37. School of Engineering, Air Force Institute of Technology, Wright-Patterson AFB OH, December 1992 (AD-A259023).
66. Wullschleger, Victor, and others, "FAA/Wilcox Flight Test Results of DGPS System for Precision Approach," *Proceedings of the Institute of Navigation 49th Annual Meeting*, Cambridge, MA: 111-118 (21-23 Jun 93).
67. Wullschleger, Victor. GPS Flight Test Manager, FAA Technical Center, Atlantic City, NJ. Personal Interview. January, 1993.

Vita

Robert Anthony Gray was born 12 Jan 63 in Erie, Pennsylvania. In 1981, he enlisted in the United States Air Force and was trained as an Avionics Inertial Navigation and Radar Systems Technician working primarily on RC-135s at Eielson AFB, AK, Shemya AB, AK and the KC-135 at McConnell AFB, KS. Mr Gray worked for Rockwell-Collins Avionics prior to his full-time studies at Ohio University where he graduated Summa Cum Laude in 1989 with a Bachelor of Science in Electrical Engineering. The collegiate experience was highlighted by a three year study as an avionics intern, studying the microwave landing system (MLS) and global positioning system (GPS) at the Ohio University Avionics Engineering Center, Athens, OH. Currently employed as an electrical engineer at Wright-Patterson AFB, OH, Mr Gray has been assigned various USAF avionics projects, primarily as a GPS/INS integration engineer while collocated at the F-16 System Program Office (SPO), and presently as a member of the Avionics Systems Integration and Research Team (ASIRT), Wright Laboratory, Wright-Patterson AFB, OH. Mr Gray earned the Master of Science in Electrical Engineering (MSEE) from the Air Force Institute of Technology (AFIT) in 1994 with primary studies in stochastic estimation, guidance (navigation) and controls. The engineering motto of Mr Gray is "Always keep in mind the pilot and maintenance personnel when making your (engineering) decisions."

Permanent Address:
3440 Crab Orchard Avenue
Beavercreek, OH 45430-1207

REPORT DOCUMENTATION PAGE

Form Approved
OMB No. 0704-0188

Public reporting burden for this collection of information is estimated to average 1 hour per response, including the time for reviewing instructions, searching existing data sources, gathering and maintaining the data needed, and completing and reviewing the collection of information. Send comments regarding this burden estimate or any other aspect of this collection of information, including suggestions for reducing this burden, to Washington Headquarters Services, Directorate for Information Operations and Reports, 1215 Jefferson Davis Highway, Suite 1204, Arlington, VA 22202-4302, and to the Office of Management and Budget, Paperwork Reduction Project (0704-0188), Washington, DC 20503.

1. AGENCY USE ONLY (Leave blank)	2. REPORT DATE	3. REPORT TYPE AND DATES COVERED	
	December 1994	Master's Thesis	
4. TITLE AND SUBTITLE AN INTEGRATED GPS/INS/BARO AND RADAR ALTIMETER FOR AIRCRAFT PRECISION APPROACH LANDINGS		5. FUNDING NUMBERS	
6. AUTHOR(S) Robert A. Gray			
7. PERFORMING ORGANIZATION NAME(S) AND ADDRESS(ES) Air Force Institute of Technology WPAFB, OH 45433-6583		8. PERFORMING ORGANIZATION REPORT NUMBER AFIT/GE/ENG/94D-13	
9. SPONSORING/MONITORING AGENCY NAME(S) AND ADDRESS(ES) Wright Laboratory WL/AAAS Wright-Patterson AFB, OH 45433-7301		10. SPONSORING/MONITORING AGENCY REPORT NUMBER	
11. SUPPLEMENTARY NOTES Approved for public release; Distribution Unlimited			
12a. DISTRIBUTION/AVAILABILITY STATEMENT		12b. DISTRIBUTION CODE	
13. ABSTRACT (Maximum 200 words) Currently, the Department of Defense (DOD) and the commercial airline industry are utilizing the Instrument Landing System (ILS) during aircraft landings for precision approaches. The replacement system for the aging ILS was thought to be the Microwave Landing System (MLS). Instead, use of the Global Positioning System (GPS) is now thought to be a viable replacement for ILS precision approaches. The majority of current precision landing research has exploited "stand-alone" GPS receiver techniques. This thesis instead explores the possibilities of using an extended Kalman filter (EKF) that integrates an Inertial Navigation System (INS), GPS, Barometric Altimeter, Pseudolite and Radar Altimeter for aircraft precision approaches. This thesis shows that integrating the INS, GPS, Barometric Altimeter and Radar Altimeter meets Federal Aviation Administration (FAA) requirements for a Category I precision approach and integrating the INS, GPS, Barometric Altimeter, Radar Altimeter and a single Pseudolite meets FAA requirements for a Category II precision approach.			
14. SUBJECT TERMS INS, GPS, Radar Altimeter, Precision, Landing, Kalman Filter ILS, MLS, Inertial Navigation System, Global Positioning System, Pseudolite		15. NUMBER OF PAGES 263	
		16. PRICE CODE	
17. SECURITY CLASSIFICATION OF REPORT Unclassified	18. SECURITY CLASSIFICATION OF THIS PAGE Unclassified	19. SECURITY CLASSIFICATION OF ABSTRACT Unclassified	20. LIMITATION OF ABSTRACT UL